N65-13847

NASA CR-54224
PWA-2320, Vol. 1

TOPICAL REPORT

ANALYTICAL STUDY OF LIQUID METAL CONDENSERS
Report PWA-2320
Vol. 1 - Design Study

prepared for
National Aeronautics and Space Administration

July 15, 1964

Contract NAS3-2335

Technical Management
NASA Lewis Research Center
Space Power System Division
Nuclear Power Technology Branch
Cleveland, Ohio
Martin Gutstein

Written by H. L. Hess — H. L. Hess, Sen. Anal. Engr.
H. R. Kunz — H. R. Kunz, Program Manager
S. S. Wyde — S. S. Wyde, Asst. Proj. Engr.

Approved by H. R. Kunz — H. R. Kunz, Program Manager
W. J. Lueckel — W. J. Lueckel, Chief, Space Power Systems

Pratt & Whitney Aircraft DIVISION OF UNITED AIRCRAFT CORPORATION

EAST HARTFORD • CONNECTICUT

FOREWORD

This report was prepared by the Pratt & Whitney Aircraft Division of United Aircraft Corporation, East Hartford, Connecticut, to describe in part the work conducted during the period June 1, 1963 to December 1, 1963 in fulfillment of Task III, Item A of Contract NAS 3-2335, Amendment 1, Experimental Investigation of Transients in Simulated Space Rankine Powerplants.

Task III consisted of an analytical and experimental study of convectively-cooled indirect condensers for Rankine-cycle space powerplants. This report summarizes the analytical part of the task which was directed towards identifying the most promising condenser concept based on considerations of heat transfer, fluid mechanics, structural integrity, fabrication and sealing, and systems integration. Volume 1 of this report contains the results of the analytical study except for the structural analysis which is presented in Volume 2*, because of the classified nature of some properties of columbium-1% zirconium.

Report PWA-2315 summarizes the experiment aspects of the task and deals with flow stability inside condensing tubes.

*Due to the classified and specialized nature of Volume 2, its distribution was limited. Copies may be obtained by qualified requesters from the NASA Office of Scientific and Technical Information, Washington 25, D.C., Attention AFSS-A

TABLE OF CONTENTS

	Page
Foreword	iii
Table of Contents	iv
List of Figures	vi
I. Summary	1
II. Introduction	3
III. Thermal Design Procedures	5
A. Introduction	5
B. Overall Heat Exchanger Design Relations	5
C. Single-Phase Convective Heat Transfer	8
1. State of the Art	8
a. Turbulent Flow	8
b. Laminar Flow	14
2. Recommended Relations	14
a. Fully Developed Turbulent Flow	15
1) Flow Through Circular Passages	15
2) Flow Through Annular Passages	15
3) Axial Flow Through Bundles of Circular Rods	16
b. Fully Developed Laminar Flow	17
D. Condensing Heat Transfer	18
1. State of the Art	18
a. Condensing Flow on Vertical Surfaces	18
b. Condensing Flow Inside Tubes	20
c. Comparison of Theory with Data	24
2. Proposed Methods of Estimating Condensing Heat Transfer Coefficients	26
a. Method of Carpenter and Colburn	27
b. Modified Film Conduction Method	30
c. Schrage Effect Method	31
d. Comparison between Methods	33
E. Pressure Drop Calculations	34
1. Contraction and Expansion Losses	35
2. Frictional Losses	35
3. Pressure Drop Due to Momentum Effects	36
4. Orifice Losses	36
5. Radial Pressure Loss	37
F. Critical Two-Phase Flow	37

TABLE OF CONTENTS (Cont'd)

		Page
IV.	Condenser Designs for a One-Megawatt (electric) Powerplant	39
	A. Introduction	39
	B. Shell-and-Tube Condensers	42
	1. Parallel Arrangements	43
	a. Constant Diameter Configurations	43
	1) Lithium-Cooled Configuration	45
	2) NaK - Cooled Configuration	49
	3) Lithium-Cooled, Annular-Shell, Bent-Tube Configuration	51
	b. Tapered Configurations	53
	1) Lithium-Cooled Configuration	55
	2) NaK - Cooled Configuration	57
	2. Series and Segmented-Shell Arrangements	58
	C. Concentric Tube Condenser	60
	D. Comparison of Condenser Configurations	63
	E. Conclusions	64
V.	Digital Computer Condenser Design Program	67
	A. Introduction	67
	B. Program Logic	67
	1. Constant-Diameter Case	69
	a. Condensing Section	70
	b. Subcooling Section	74
	c. Final Summation	76
	2. Tapered Tube Case	77
	a. Iteration Procedure	77
	b. Equations	78
Appendix A -	Materials and Fabrication	A1
Appendix B -	Nomenclature	B1
Appendix C -	References	C1
Appendix D -	Tables	D1
Appendix E -	Figures	E1
Appendix F -	Method of Calculating Incremental Lengths for Tapered Tube Condensers	F1
Appendix G -	Transition Criterion for a Condensing Film	G1
Appendix H -	Two-Phase Pressure Drop Calculations	H1
Appendix I -	Radial Pressure Losses	I1
Appendix J -	Critical Mass Velocity for Two-Phase Flow	J1

LIST OF FIGURES

Number	Title	Page
1	Generalized Velocity Profile	E2
2	Nusselt Number vs Peclet Number for Forced Convection Flow of Liquid Metals. Conditions: 1) Fully Developed Turbulent Pipe Flow 2) Uniform Wall Heat Flux	E3
3	Comparison of Theoretical Heat Transfer Results of Various Investigators for Forced Convection Flow of Liquid Metals. Conditions: 1) Fully Developed Turbulent Pipe Flow 2) Uniform Wall Heat Flux 3) Prandtl Number = 0.02	E4
4	$\left[\frac{\epsilon M}{\nu}\right]_{max}$ vs Reynolds Number	E5
5	Nusselt Number Ratio vs Heat Capacity Parameter (Koh, Sparrow and Harnett, Ref. 35)	E6
6	Film Reynolds Number vs Heat Transfer Parameter (Seban, Ref. 40)	E7
7	Transition Film Reynolds Number vs Shear Stress Parameter (Rohsenow et al, Ref. 41)	E8
8	Film Reynolds Number vs Heat Transfer Parameter (Rohsenow, et al, Ref. 41)	E9
9	Film Reynolds Number vs Heat Transfer Parameter. Comparison of Theoretical Results with Experimental Data of Misra and Bonilla (Ref. 47)	E10
10	Nusselt Number Ratio vs Acceleration Parameter. Comparison of Theoretical Results of Chen (Ref. 36) with Mercury Data of Misra and Bonilla (Ref. 47)	E11
11	Heat Transfer Parameter vs Film Reynolds Number. Comparison Between Theoretical Results of Seban (Ref. 40) and Nusselt (Ref. 32) and Experimental Data of Brooks and Sawochka (Ref. 48)	E12
12	Heat Transfer Parameter vs Wall Shear Stress Parameter. Comparison of Carpenter-Colburn Equation with Condensing Potassium Data	E13
13	Heat Transfer Parameter vs Dimensionless Film Thickness	E14
14	Typical Flow Pattern in Constant-Diameter Shell-and-Tube condenser for Parallel Arrangement	E15
15	Comparison Between the Critical Mass Velocities Predicted by Equation 41, the Theoretical Results of Fauske, and Experimental Data for a Steam-Water Mixture of 5-15% Quality	E16
16	Comparison Between the Critical Mass Velocities Predicted by Equation 41, the Theoretical Results of Fauske, and Experimental Data for a Steam-Water Mixture of 45-55% Quality	E17
17a	Schematic Diagram of 1 MW(e) Nuclear Rankine-Cycle Space Powerplant	E18
17b	Schematic Diagram of Condenser-Heat Rejection Loop Arrangements	E19
18	Detail of Tube-to-Tubesheet Joint for Columbium - 1% Zirconium Alloy	E20
19	Lithium-Cooled Potassium Condenser for 1MW(e) Nuclear Space Powerplant. Conventional Shell-Tube Configuration	E21
20	NaK-Cooled Liquid Metal Condenser for 1 MW(e) Nuclear Space Powerplant. Constant Diameter Configuration	E22
21	Lithium-Cooled Potassium Condenser for 1 MW(e) Nuclear Space Powerplant. Annular Shell, Bent Tube Configuration	E23
22	Lithium-Cooled Liquid Metal Condenser for 1 MW(e) Nuclear Space Powerplant. Tapered Configuration	E24
23	Detail of Hole Pattern in Orifice Plate	E25
24	Equilateral Triangular Tube Pitch	E26
25	Lithium-Cooled Constant-Diameter Condenser. Effect of Potassium Vapor Inlet Mach Number and Number of Tubes on Condenser Core Weight	E27
26	Lithium-Cooled Constant-Diameter Condenser. Effect of Potassium Vapor Inlet Mach Number and Number of Tubes on Shell Volume	E28
27	Lithium-Cooled Constant-Diameter Condenser. Effect of Potassium Vapor Inlet Mach Number and Number of Tubes on Tube Length	E29
28	Effect of Blockage on Condenser Core Weight for Lithium-Cooled and NaK-Cooled Constant-Diameter Configurations	E30
29	Effect of Blockage on Shell Volume for Lithium-Cooled and NaK-Cooled Constant-Diameter Configurations	E31
30	Effect of Blockage on Tube Length for Lithium-Cooled and NaK-Cooled Constant-Diameter Configurations	E32
31a	Variation of Heat Transfer Coefficient with Length for Lithium-Cooled Constant-Diameter Shell-and-Tube Configuration	E33
31b	Variation of Fluid Temperatures and Potassium Quality with Length for Lithium-Cooled Constant-Diameter Shell-and-Tube Configuration	E34
32a	Lithium-Cooled Constant-Diameter Condenser. Effect on Coolant Temperature Level on Shell Volume	E35
32b	Lithium-Cooled Constant-Diameter Condenser. Effect of Coolant Temperature Level on Condenser Core Weight	E36
33	Lithium-Cooled Constant-Diameter Condenser. Fluid Temperature Profile Curves	E37
34	Lithium-Cooled Constant-Diameter Condenser. Effect of Coolant Temperature Level on Temperature Driving Potential Distribution Along Condenser	E38
35	Effect of Blockage on Radial Pressure Loss for NaK-Cooled Constant-Diameter Condenser	E39
36	Effect of Gap Width and Blockage on Diameter of Coolant Inlet and Outlet Pipes for NaK-Cooled Constatn-Diameter Condenser	E40
37	Lithium-Cooled Tapered Condenser. Effect of Potassium Exit Temperature on Subcooling Length	E41

LIST OF FIGURES(Cont'd)

Number	Title	Page
38	Variation of Heat Transfer Coefficient with Length for Lithium-Cooled Tapered Shell-and-Tube Configuration	E42
39	Variation of Fluid Temperatures and Potassium Quality with Length for Lithium-Cooled Tapered Shell-and-Tube Configuration	E43
40	Lithium-Cooled Tapered Condenser. Comparison Between Local Mass Velocity and Critical Mass Velocity of Potassium	E44
41	NaK-Cooled Tapered Condenser. Comparison Between Local Mass Velocity and Critical Mass Velocity of Potassium	E45
42	Lithium-Cooled Potassium Condenser for 1 MW(e) Nuclear Space Powerplant with Condensing Flow in Annular Passages	E46
43	Concentric-Tube Condenser. Effect of Average Condensing Heat Transfer Coefficient and Number of Concentric Tube Sets on Inside Diameter of Central Tubes	E47
44	Concentric-Tube Condenser. Effect of Average Condensing Heat Transfer Coefficient and Number of Concentric Tube Sets on Inside Diameter of Outer Tubes	E48
45	Concentric-Tube Condenser. Effect of Average Condensing Heat Transfer Coefficient and Number of Concentric Tube Sets on Condenser Core Weight	E49
46	Concentric-Tube Condenser. Effect of Average Condensing Heat Transfer Coefficient and Number of Concentric Tube Sets on Tube Length	E50
47	Sketch of Counterflow Condenser	E51
48	Sketch of Condenser Increment	E52

I. SUMMARY

A study of liquid metal condensers was conducted for Rankine-cycle space powerplant applications in which single-phase heat rejection loops are used to transfer heat from the condensers to a segmented space radiator. The purpose of this study was to evaluate the present state of liquid metal technology, to formulate recommended thermal and mechanical design procedures for liquid metal condensers, and then using these procedures to determine the most suitable type of condenser for a nuclear Rankine-cycle space powerplant of one megawatt (electric) output using potassium as the two-phase working fluid. Since the study was restricted to condensers which employ fixed heat transfer surfaces, spray condensers and rotary disk condensers were not considered.

A method was formulated in this study which agrees with the available liquid metal condensing heat transfer data. This method was used for the comparative study of different types of condensers, together with other thermal and mechanical design techniques found to be most suitable.

The optimum condenser consisted of a constant-diameter shell-and-tube design operating in parallel with a number of similar units in such a manner that each condenser is associated with a separate radiator segment. Considering a 16-segment radiator using NaK as the coolant, the condensers consisted of 91 tubes of 0.375-inch outer diameter and 12.0-inch length, inside of shells of 8.17 inches outside diameter. The total weight of all sixteen of these condensers including fluid inventory was 740 pounds.

Columbium-1% zirconium was selected as the material of construction because of the desired 10,000-hour life. It was concluded that all joints should be welded under an inert gas cover using tungsten electrodes. In addition to being welded, all tube-to-tubesheet joints should be diffusion-bonded. Stress calculations indicated that the condenser structure was capable of withstanding all anticipated loads.

The initial portion of the study involved a detailed search of the available literature to select the best relations for heat transfer and pressure loss for several types of condensers. For calculating single-phase convective heat transfer coefficients for liquid metal flow, the theoretical approach proposed by Dwyer[1] and the method formulated by Lyon[2], based on the theory derived by Martinelli[3] were determined to be the methods most substantiated by carefully taken experimental

[1] See Appendix C for numbered references

data. All heat transfer theories for condensing flow obtained from the literature showed poor agreement with the scant amount of experimental data for condensing liquid metals. In spite of this fact, some methods were modified to conform with the available condensing liquid metal data in order to conduct the design studies. The condensing tube length for a particular design condition was found to be considerably different depending upon which of these methods was used. Therefore, one method was selected for the final design calculations which provided conservative estimates of tube lengths and thus resulted in condenser designs which would at least provide total condensation. The methods commonly used to calculate single-phase pressure losses were determined to be adequate for liquid metal flow. Also, the method of Lockhart and Martinelli[4] was determined to be adequate for calculating two-phase frictional pressure losses for the condensing liquid metal.

In the study to determine the most suitable type of condenser for a one-megawatt (electric) nuclear Rankine-cycle space powerplant, potassium was considered to be the condensing fluid. Both lithium and NaK were considered as coolants for the heat rejection loops of this powerplant. Three different condenser-heat rejection loop arrangements were considered as follows:

1) Parallel condenser operation with a separate heat rejection loop for each condenser,
2) Series condenser operation with a separate heat rejection loop for each condenser, and
3) Segmented-shell condenser operation with four separate heat rejection loops cooling each condenser segment.

A number of different condenser configurations were investigated. These included:

1) Constant-diameter shell-and-tube,
2) Tapered-diameter shell-and-tube,
3) Annular shell with bent tubes, and
4) Concentric tube with the condensing flow inside the annuli between the concentric tubes.

Design calculations were made on all of these configurations for at least one of the two coolants and at least one of the above condenser-heat rejection loop arrangements. A computer program was prepared to facilitate the calculations for the shell-and-tube configurations. Preliminary design drawings were prepared for the more desirable of these configurations.

The results indicated that neither the series nor the segmented-shell arrangement was practical. On the basis of size, weight, and fabrication considerations, the constant-diameter shell-and-tube configuration appeared to be the most practical configuration for the parallel arrangement.

II. INTRODUCTION

The design of indirect condensers for the heat rejection systems of nuclear Rankine-cycle space powerplants presents problems not usually encountered in ordinary condenser design. Both the condensing fluid and the coolant are liquid metals which are highly corrosive and have heat transfer characteristics much different from those of common engineering fluids. The condensers must be able to operate in any orientation, in gravity fields which range from zero to one or more. The condensers must operate leak-free in a vacuum environment at elevated temperatures for 10,000 hours or more. They must be designed to minimize system size and weight. As a result, the common procedures used in the design of condensers for more conventional applications are not adequate for the present purpose. A study was therefore conducted to determine the best thermal and mechanical design procedures for such condensers. Using these procedures, an additional study was performed to determine the most suitable type of condenser for a one-megawatt (electric) nuclear space powerplant. Since the most suitable condenser appeared to be some type of shell-and-tube condenser, a computer program was written to facilitate design calculations for shell-and-tube type condensers.

The main text of this report discusses the thermal design study, the prototype designs, and the computer program. The materials and fabrication study is summarized in Appendix A.

III. THERMAL DESIGN PROCEDURES

A. Introduction

This section contains discussions on overall heat exchanger design relations, methods of calculating condensing and single-phase convective heat transfer coefficients, pressure drop relations, and critical two-phase flow criteria. The state of the art on these topics is discussed and recommendations are made for relations to be used in designing liquid metal condensers.

B. Overall Heat Exchanger Design Relations

The approach used in this study to design condensers for a particular application involved the determination of tube length for any particular cross-sectional geometry. For a given set of flow rates and terminal temperatures a study was made to determine the effect on pressure losses of both fluids, of varying different parameters describing the cross-sectional geometry such as tube length, condenser weight, and condenser volume.

Various techniques are available to solve for tube length. Each of these can be derived by considering heat transfer across a differential element. These techniques differ due to the various assumptions made in the integration process.

The heat transferred per unit time across a differential element of a heat exchanger at steady state is *

$$dQ = U \ (T_{hot} - T_{cold}) \ dA \tag{1}$$

If the elemental heat transfer surface area dA refers to the surface adjacent to the cold fluid, then the overall heat transfer coefficient U is given by

$$U = \frac{1}{\frac{1}{h_{hot}} \ \frac{dA_{cold}}{dA_{hot}} + \frac{t}{k} \ \frac{dA_{cold}}{dA_{\substack{mean \\ wall}}} + \frac{1}{h_{cold}}} \tag{2}$$

As can be seen in Equation (2) the heat transfer coefficients of both fluids must be known in order to calculate U, especially if h_{hot} and h_{cold} are of the same order of magnitude. This is true for the design cases discussed later in this report.

* See Appendix B for nomenclature

The simplest case for which Equation (1) can be integrated to obtain the total surface area required for a given heat load Q is one in which U and cross-sectional dimensions are assumed constant with length. In this case, by also assuming an appropriate mean value for $(T_{hot} - T_{cold})$

$$A = \frac{Q}{U\,(T_{hot} - T_{cold})_{mean}} \tag{3}$$

Sometimes assuming a simple arithmetic mean temperature difference gives acceptable accuracy. However, in a high performance heat exchanger, the error caused by this assumption becomes significant. When the specific heats of both fluids, U and cross-sectional dimensions are assumed constant with length, Equation (1) can be integrated to yield the following form for parallel and counterflow heat exchangers

$$A = \frac{Q}{U\ \Delta T_{lm}} \tag{4}$$

where $$\Delta T_{lm} = \frac{\Delta T_{II} - \Delta T_{I}}{\ln \dfrac{\Delta T_{II}}{\Delta T_{I}}}$$

The term ΔT_{lm} is the familiar log-mean-temperature difference. The terms ΔT_{I} and ΔT_{II} refer to the temperature driving potentials at the terminals of the heat exchanger.

Equation (1) may also be integrated for a variable U. For the case where U is assumed to vary linearly with the temperature difference between the two fluids, and other conditions are the same as those assumed for Equation (4), the following equation presented in Reference 5 results

$$A = \frac{Q \ln\left(\dfrac{U_{I}\ \Delta T_{II}}{U_{II}\ \Delta T_{I}}\right)}{U_{I}\ \Delta T_{II} - U_{II}\ \Delta T_{I}} \tag{5}$$

Additional equations which account for variations of both U and cross-sectional dimensions with length are derived in Appendix F.

If only approximate answers are needed in the design of a liquid metal condenser, the equations listed above are useful despite the fact that the assumptions may not be completely satisfied. For instance, the log-mean-temperature approach may be applicable if the condensing section and the subcooled section of the condenser are treated separate-

ly, so that the specific heat of the condensing fluid can be considered constant in each section. These equations are also useful when the uncertainties in predicting local variations of the heat transfer coefficient or the static pressure (and consequently the temperature of the condensing fluid) outweigh the error introduced by the assumptions made. In general, however, greater accuracy is probably required in designing a liquid-metal condenser for space applications than that provided by the equations where the simple variations with length described above are considered. Methods which account for the local variation of the condensing heat transfer coefficient are necessary since heat transfer coefficients for condensing liquid metal flows vary considerably with quality and thus with length. Also, the temperature variation of the condensing fluid is dependent on the pressure drop along the condensing tube since local saturation temperature depends on local static pressure.

The most practical method of accounting for the effects of the local variations of the heat transfer coefficient and the static pressure of the condensing fluid is to divide the condenser into a number of smaller increments and employ a method of solution which uses an incremental marching procedure. Using such a procedure, changes across one increment are evaluated to determine the input values for the calculations on the next increment and so on. The increments can be chosen so that they would have the same heat load, the same coolant temperature rise, or the same change in the quality of the condensing fluid. The calculation would begin at the condensing fluid inlet end of the condenser where the temperatures and pressures of both fluids are known. The length of the first increment would be calculated using the appropriate relations. The changes of the quality, static pressure, and temperature of the condensing fluid across this increment would provide the additional information needed to solve for the length of the second increment. This procedure would be repeated until the desired condensing fluid condition at the end of the condenser was reached. Thus, the condenser length would be obtained by considering it to be composed of many smaller condensers operating in series. This method is particularly suited for solution by digital computer.

The accuracy of this numerical integration method increases as the condenser is subdivided into smaller and smaller increments. Also for a given number of increments, an increase of accuracy may result from using an integrated form of Equation (1) inside each increment, instead of using average values for U and the temperature difference.

The length of the individual increments can be calculated using the log-mean-temperature-difference approach. This can be done by assuming that the temperature of the condensing fluid remains constant at its

inlet value, and by evaluating the average condensing heat transfer coefficient using the average quality of the condensing fluid in the increment. However, since in reality the overall heat transfer coefficient U would vary across an increment of the condenser, relations which account for a variation of U are more desirable.

For counterflow condensers where the cross-sectional dimensions are constant with length, Equation (5) from McAdams[5] is recommended for the evaluation of the increment lengths. For tapered condensers where the cross-sectional dimensions of a condenser vary with length, the relations derived in Appendix F are recommended for the evaluation of increment lengths. These recommended procedures were programmed on a digital computer to facilitate design calculations for shell-and-tube condensers. This computer program is described in greater detail in Section V of this report. The program assumed increments of equal quality change in the condensing section and equal coolant temperature change in the subcooling section.

As indicated above, the heat transfer coefficients of both fluids must be known in order to calculate the overall heat transfer coefficient. The following two sections discuss the methods used to calculate the heat transfer coefficients for both the condensing fluid and the coolant for the condenser design of this study.

C. Single-Phase Convective Heat Transfer

1. State of the Art

During the past fifteen years considerable effort has been expended to develop methods that would adequately predict forced convection heat transfer coefficients for liquid metals. During this time the results of many studies, both analytical and experimental, have appeared in the literature. The major effort has been to resolve the differences that exist between the theoretical results and the experimental data for fully developed turbulent flow, while very little work has been done for flow in the laminar regime. The two regimes, turbulent and laminar flow, are discussed separately.

a. Turbulent Flow

The initial theoretical work on the turbulent flow of a liquid metal was done by Martinelli[3] who considered the case of fully-developed flow in a circular tube with uniform wall heat flux along the length of the tube. Martinelli attempted to account for the transport of heat by both molecular and turbulent transport mechanisms

across the fluid stream. He based his analysis upon the generalized velocity profile for fully-developed turbulent pipe flow obtained experimentally by Nikuradse [6] and Reichardt [7]. The universal velocity profile is illustrated in Figure 1 where the dimensionless velocity u^+ is shown to be a function of the dimensionless distance from the tube wall y^+. As can be seen in Figure 1, the velocity profile is broken up into three regions, the viscous sublayer, the buffer region and the turbulent core. Separate equations are fitted to the data in each region. Martinelli differentiated the generalized velocity profile with respect to the distance from the wall and combined the result with the momentum equation for turbulent pipe flow to obtain the variation of the eddy transport coefficient for momentum ϵ_M, across the fluid stream. He then expressed the eddy transport coefficient for heat ϵ_H in terms of ϵ_M and the ratio $\epsilon_H / \epsilon_M = \alpha$, which he assumed to remain constant across the fluid stream. Knowing ϵ_H in terms of ϵ_M, he solved the energy equation for turbulent pipe flow to obtain the temperature distribution across the fluid stream. He then obtained the heat flux at the wall q_w from the temperature gradient at the wall $\left(\frac{\partial T}{\partial y}\right)_{y=0}$ through the relation

$$q_w = -k \left(\frac{\partial T}{\partial y}\right)_{y=0} \tag{6}$$

Martinelli also integrated the temperature distribution across the fluid stream to obtain a mean fluid temperature T_m. He then defined a heat transfer coefficient h based upon the difference between the mean fluid temperature T_m and the wall temperature T_w using the equation

$$h = \frac{q_w}{(T_w - T_m)} \tag{7}$$

Martinelli presented his results in terms of nondimensional parameters. This result indicates that the Nusselt number of the flow Nu is dependent upon the Reynolds number of the flow Re, the Prandtl number of the fluid Pr, and the parameter α. Martinelli's final equations were very complex. However, he did present numerical results for the case of a constant $\alpha = 1.0$. These results indicate that the effect of the transport of heat by molecular conduction in the turbulent core of the fluid is much more significant for liquid metals which have very low Prandtl numbers than for common engineering fluids which have relatively high Prandtl numbers. This result also indicates that the heat transfer relations derived for common engineering fluids, which ignore the effect of molecular conduction in the turbulent core, cannot be used for liquid metal applications.

Lyon[2] investigated Martinelli's results and found that for Prandtl numbers less than 0.1 these results can be approximated reasonably well by the simple relation

$$Nu = 7.0 + 0.025 (\bar{a} Pe)^{0.8} \tag{8}$$

where $\bar{a}$ is a mean value of the ratio of eddy transport coefficients

Theoretical results similar to those of Martinelli and Lyon were also obtained by Seban and Shimazaki[8] for fully-developed turbulent flow through a circular tube with a constant wall temperature along the length of the tube and by Seban[9] and Bailey[10] for noncircular flow passages with uniform wall heat flux. However, when these early theoretical results were compared with the early experimental data very poor agreement was displayed. This is best exemplified by the work of Lubarsky and Kaufman.

Lubarsky and Kaufman[11] compiled the experimental results of the various studies of heat transfer to liquid metals performed prior to 1955. Since data were not always directly comparable because of differences in experimental apparatus or in methods of calculation, the experimental data were re-evaluated using as consistent assumptions and methods as possible. The results were then compared with each other and with the existing theoretical solutions. These results are illustrated in Figure 2 for the case of fully-developed turbulent pipe flow with uniform heat flux. As can be seen in Figure 2 this re-evaluated data has considerable scatter with the bulk of the data lying below Lyon's equation for the case of $a = 1.0$. The work of Lubarsky and Kaufman similarly showed disagreement between the theory and data for the cases of uniform wall temperature and noncircular flow passages.

In addition to the fact that this disagreement between the theory and the data existed, there was no conclusive explanation for this disagreement. As a consequence it was not known whether the theory or the data was more reliable. In spite of the fact that so little was actually known about liquid metal heat transfer, a relationship was needed to predict liquid metal heat transfer coefficients for design purposes. To provide such a relation Lubarsky and Kaufman fitted the following equation to the re-evaluated data presented in Figure 2

$$Nu = 0.625 Pe^{0.4} \tag{9}$$

However, this equation is an empirical correlation of experimental data whose reliability was questioned by Lubarsky and Kaufman. Subsequent efforts have been made to improve both the early theoretical solutions and the quality of experimental liquid metal heat transfer data.

In attempting to improve the early theoretical solutions, most investigators have tried to produce a rational method of evaluating the contribution of the turbulent transport mechanism for liquid metal heat transfer. Using modified forms of the Prandtl mixing length theory, a number of investigators have attempted to relate the ratio of eddy transport coefficients α to the Prandtl number of the fluid, and in some cases to the Reynolds number of the flow. These investigators, Jenkins [12], Deissler [13], Lykoudis and Touloukian [14], Rohsenow and Cohen [15], Mizushina and Sasano [16], Azer and Chao [17], and Dwyer[1], all assumed α was constant across the fluid stream. The results of some of these investigators are illustrated in Figure 3 for the case of fully-developed turbulent pipe flow through a circular tube with uniform wall heat flux, and a Prandtl number of 0.02.

As can be seen in Figure 3, these investigators obtained widely differing results. Those of Dwyer lie close to those obtained from Lyon's equation using an α of 1.0, while the results of the other investigators lie well below the Lyon equation. The results of these other investigators also show some agreement with the empirical relation of Lubarsky and Kaufman. However, in no case is this agreement complete. Since these theoretical results are so widely scattered and since the Lubarsky and Kaufman line cannot be relied upon, no conclusions can be drawn concerning the validity of these different theoretical results until they have been compared with reliable experimental data.

In seeking ways of improving the experimental data, investigators have sought to find reasons why the bulk of the early data lies below the theoretical results of Martinelli and Lyon. A number of investigators have hypothesized that this might be caused by an additional resistance to heat transfer at the interface of the liquid metal and the heat transfer surface. They suggested this resistance might be due to the presence of impurities at the liquid-wall interface or to the fact that the liquid metal may not totally wet the heat transfer surface, thus creating voids at the liquid-wall interface. In the more recent experiments, efforts have been made to eliminate the effects a resistance at the interface might have on liquid metal heat transfer data. Efforts have also been made to eliminate such a resistance by using an extremely pure liquid which completely wetted the heat transfer surface. Positive results appear to have been achieved by some of these investigators.

In an effort to eliminate the effects of a resistance at the liquid-wall interface from the experimental data, a number of investigators have obtained heat transfer coefficients from experimentally measured temperature distributions across the fluid stream instead of from the more common method of using experimentally measured wall temperatures.

Using the temperature distribution method, fictitious wall temperatures are obtained by extrapolating the experimentally measured temperature distributions to the wall. These extrapolated values of wall temperature did indicate that an additional resistance to heat transfer in the region of the wall might be present. Together with other experimentally measured quantities these extrapolated values of wall temperature can be used to calculate heat transfer coefficients which do not contain the effect of such a resistance. The temperature distribution method was originally employed by Isakoff and Drew[18] whose data for the turbulent flow of mercury through circular tubes showed agreement with the theoretical results of Martinelli and Lyon, as shown in Figure 2. Isakoff and Drew employed electrically heated tubes which approximated the condition of uniform heat flux at the wall. Their data also showed agreement with the more recent theoretical results of Dwyer[1]. Using the same technique, subsequent experiments by Brown, et al[19] have also shown similar agreement with these theoretical results for mercury flowing turbulently through a circular tube. The mercury in this case was cooled by water circulated through a cooling jacket. The flow rate of the water was adjusted to approximate the condition of uniform heat flux at the wall.

In more recent experiments, Subbotin, et al[20] have measured both temperature distributions and wall temperatures for both mercury and alkali metals flowing through circular electrically-heated tubes. For mercury they found that the heat transfer coefficients obtained from the temperature distributions were much higher than those obtained from the wall temperature measurements. The heat transfer coefficients calculated from the temperature distributions also agreed with the theoretical results of Martinelli and Lyon and of Dwyer. Subbotin, et al[20] attributed the difference between the heat transfer coefficients obtained by the two methods to an additional resistance to heat transfer caused by the presence of oxides in the viscous sublayer of the fluid stream. They showed this resistance to be a function of the Reynolds number with the resistance decreasing as Reynolds number increases. However, the same investigators found no additional resistance to heat transfer using alkali metals. The heat transfer coefficients obtained by both methods agreed well with the theoretical results of both Martinelli and Lyon and of Dwyer. This can be attributed to the fact that the alkali metals were very pure and also wetted the tube wall. In addition to the above results, the alkali metal data of Kirillov, et al[21] and Pirogov[22] for turbulent flow through electrically-heated tubes have also shown good agreement with the results of Martinelli and Lyon and Dwyer. These investigators also used the temperature distribution method to obtain heat transfer coefficients.

From these results it can be seen that there is a considerable amount of data showing reasonable agreement with the theoretical results of Martinelli and Lyon and Dwyer for the case of turbulent flow through circular tubes with a constant wall heat flux. However, this agreement is not complete for all flow regimes. For example, the data for turbulent flow near the transition region of Petukhov and Yushin [23] and the recent data of Subbotin, et al [24] using the temperature distribution method showed poor agreement with the theoretical results. However, the laminar regime data of these investigators compared favorably with the theory.

In addition to the above mentioned data taken by measuring the temperature distribution across the fluid stream, some data obtained using wall temperature measurements also agreed with the theoretical predictions of Dwyer for constant wall heat flux. This data was taken for fully developed turbulent flow through noncircular electrically-heated channels and includes the data of Petrovichev [25] for the flow of mercury through an annulus, the data of Maresca and Dwyer [26] for the axial flow of mercury through a bundle of rods, and the data of Winsche and Miles [27] for the axial flow of NaK through a bundle of circular rods. The agreement between the theory of Dwyer and the data of Maresca and Dwyer, and Winsche and Miles can probably be attributed to the fact that the liquid metals were kept as pure as possible and wetting occurred. As a result there was probably no additional resistance to heat transfer at the interface. However, according to Dwyer [1], wetting probably did not occur in the experiments of Petrovichev. The agreement between the theory and data, in this case, must be viewed in the light that some resistance at the interface may have been present.

In summary, there are a number of conclusions that can be drawn from these results for the turbulent flow of liquid metals:

1) The presence of impurities at the interface of the liquid metal and the heat transfer surface, or the inability of the liquid metal to wet the heat transfer surface can seriously affect the measured heat transfer coefficients for liquid metal flow.

2) Agreement between theory and some experimental data has been achieved for turbulent flow. However, this agreement is not complete for all flow regimes since some investigators showed disagreement for Reynolds numbers near the transition region. In addition, agreement has been achieved only for the case of uniform wall heat flux. In many heat exchanger applications this condition is not prevalent. A recent theoretical analysis by Stein [28] indicated that the wall boundary conditions in a heat exchanger can

seriously affect liquid metal heat transfer coefficients. Therefore additional work, both theoretical and experimental, is needed.

3) In light of the agreement that has been demonstrated between the recent experimental data and the theoretical relations of Martinelli and Lyon and of Dwyer, these relations are considered to be the most adequate of those available for use in design calculations. Although these relations were derived and validated for conditions of constant heat flux at the wall, their use is recommended for wall conditions other than constant heat flux until more suitable relations are developed for these other wall conditions.

b. Laminar Flow

In contrast to the extensive studies described above of liquid metal heat transfer for flow in the turbulent region, very few studies have been made of liquid metal heat transfer for flow in the laminar regime. Most authorities have felt that the theoretical laminar flow solutions found in heat transfer textbooks were adequate for predicting liquid metal heat transfer coefficients for flow in this regime. These theoretical solutions have been obtained for a number of flow geometries for both the constant wall heat flux and the constant wall temperature conditions. Very few experimental measurements have been made to verify these analyses. According to the textbook by Eckert and Drake[29], some of the early experimenters obtained heat transfer coefficients lower than the theoretical values. However, as in turbulent flow, this result may be due to the presence of an additional resistance to heat transfer at the interface of the liquid metal and the heat transfer surface. This is supported by the more recent data of Petukhov and Yushin[23] and Subbotin, et al[24] for laminar flow through circular electrically-heated tubes, which show excellent agreement with the theoretical laminar flow solutions. This agreement indicates the validity of these solutions for liquid metal applications.

2. Recommended Relations

In accord with the above discussion on the state of the art of liquid metal heat transfer technology, the following single-phase convective heat transfer relations are recommended for use in making design calculations for liquid metal condensers.

a. Fully-Developed Turbulent Flow

1) Flow Through Circular Passages - For flow through circular passages either the method of Martinelli and Lyon[3,2] or the method of Dwyer[1] can be used. Both give equally good results and are based on the same equation

$$Nu = 7.0 + 0.025\,(\bar{\alpha}\,Pe)^{0.8} \tag{10}$$

For the Martinelli and Lyon method, $\bar{\alpha}$ can be assumed constant and equal to one. For the method of Dwyer, $\bar{\alpha}$ must be calculated from the relation

$$\bar{\alpha} = 1.0 - \frac{1.82}{Pr\left(\frac{\epsilon_M}{\nu}\right)^{1.4}_{max}} \tag{11}$$

where the term $\left(\frac{\epsilon_M}{\nu}\right)_{max}$ can be evaluated as a function of Reynolds number using Figure 4. For a Reynolds number where the value of $\bar{\alpha}$ calculated from Equation (11) is less than zero, the Nusselt number is equal to 7.0.

Due to its simplicity the method of Martinelli and Lyon is preferable in making design calculations.

2) Flow Through Annular Passages - For flow through annular passages with heat transfer through either the inner wall or the outer wall, the following methods presented by Dwyer[1] are recommended.

For heat transfer through the inner wall the relation should be used

$$Nu = a_1 + b_1\,(\bar{\alpha}\,Pe)^{c_1} \tag{12}$$

where:
$a_1 = 4.63 + 0.686z$
$b_1 = 0.02154 - 0.000043z$
$c_1 = 0.752 + 0.01657z - 0.000883z^2$
z is the ratio of the outer to inner radius, r_2/r_1

The term $\bar{\alpha}$ in Equation (12) can be obtained from Equation (11) where $\left(\frac{\epsilon_M}{\nu}\right)_{max}$ is evaluated as a function of Reynolds number using Figure 4. If the value of $\bar{\alpha}$ calculated from Equation (11) is less than zero, the Nusselt number must be obtained from the relation

$$Nu = 4.92 + 0.686z \tag{13}$$

For the flow through an annular passage with heat transfer through the outer wall the following relation should be used

$$Nu = a_2 + b_2 (\bar{a} Pe)^{C_2} \tag{14}$$

where
$$a_2 = 5.26 + 0.050z$$
$$b_2 = 0.01848 + 0.003154z - 0.0001333z^2$$
$$c_2 = 0.780 - 0.01333z + 0.000833z^2$$

The term $\bar{a}$ in Equation (14) can be obtained from Equation (11) where $\left(\frac{\epsilon_M}{\nu}\right)_{max}$ is evaluated as a function of Reynolds number using Figure 4. If the value of $\bar{a}$ calculated from Equation (11) is less than zero, the Nusselt number must be obtained from the relation

$$Nu = 5.52 + 0.076z \tag{15}$$

3) Axial Flow Through Bundles of Circular Rods - For axial flow through bundles of circular rods with an equilateral triangular pitch the following relation presented by Dwyer[1] is recommended

$$Nu = 0.93 + 10.81 (P/D) - 2.01 (P/D)^2 + 0.0252 (P/D)^{0.273} (\bar{a} Pe)^{0.8} \tag{16}$$

The term P/D is the ratio of the distance between rod centers to the outside diameter of the rods. The term $\bar{a}$ in Equation (16) can be obtained from Equation (11). The term $\left(\frac{\epsilon_M}{\nu}\right)_{max}$ in Equation (11) can be evaluated as a function of Reynolds number and P/D using Figure 4. If the value of $\bar{a}$ calculated from Equation (11) is less than zero the following relation for Nusselt number must be used

$$Nu = 3.65 + 5.75 (P/D)^{1.27} \tag{17}$$

Due to the assumptions made in the derivation of Equations (16) and (17), they lose their validity for values of P/D less than 1.3. An upper limiting value of P/D for which these equations are valid has not been determined.

b. Fully-Developed Laminar Flow

The following tabulation of Nusselt numbers for fully-developed laminar flow conditions is recommended for use in liquid metal condenser design calculations.

Geometry	Condition at Wall	Nusselt Number
circular tube	q_w uniform	4.36
circular tube	T_w uniform	3.66
parallel plates	q_w uniform	8.23
parallel plates	T_w uniform	7.60
triangular duct	q_w uniform	3.00
triangular duct	T_w uniform	2.35

This tabulation, obtained from the textbook of Rohsenow and Choi[30], presents results for both uniform wall heat flux and uniform wall temperature for three different flow geometries. Since the Nusselt numbers for the two different wall conditions differ by an appreciable amount and since the wall conditions in liquid metal condensers frequently differ from both the uniform heat flux condition and the uniform temperature condition, judgment must be exercised in selecting the appropriate value of Nusselt number for a given application.

In addition to the above results, the relation of Friedland and Bonilla[31] is recommended for axial flow through a bundle of circular rods arranged in an equilateral triangular pitch

$$Nu = \left[144\,(R_m^2 - 1)(4\,R_m^4 \ln R_m - 3\,R_m^4 + 4\,R_m^2 - 1)^2\right] \Big/ \left[R_m^8\,(1{,}152 \ln^3 R_m - 2{,}592 \ln^2 R_m + 2{,}280 \ln R_m - 719) + R_m^6\,(1{,}152 \ln^2 R_m - 2{,}880 \ln R_m + 1{,}680) + R_m^4\,(720 \ln R_m - 1{,}296) + 368\,R_m^2 - 33\right] \qquad (18)$$

where $R_m = \sqrt{\frac{2\sqrt{3}}{\pi}}\left(\frac{P}{D}\right)$

This relation was derived for the case of uniform wall heat flux. An equivalent relation for the case of uniform wall temperature has not been found in the literature.

D. Condensing Heat Transfer

1. State of the Art

Numerous studies of condensing flow have been reported in the literature. These studies have resulted in a number of empirical, semi-empirical, and analytical relations for predicting the heat transfer coefficients of condensing films. These studies differ in the flow geometry and flow regime considered, and the degree of rigor with which they were conducted. In general these relations have shown reasonable agreement with the experimental heat transfer data taken for common engineering fluids which have relatively high Prandtl numbers. However, they have shown poor agreement with the limited amount of experimental heat transfer data taken for condensing liquid metals. These studies are summarized below and their results are considered for possible application in the liquid metal condenser design study.

a. Condensing Flow on Vertical Surfaces

The case of a condensing film flowing on a vertical surface under the influence of gravity has received considerable attention from many investigators. These investigators have considered the flow of the film in both the laminar and the turbulent regimes for the case of a stagnant vapor and the case where the flow of vapor in the downward direction imposes a shear stress on the film in the direction of flow.

The flow of a laminar condensate film on a vertical surface exposed to a stagnant vapor has been considered by Nusselt [32], Rohsenow [33], Sparrow and Gregg [34], Koh, et al [35], Chen [36], and Koh [37].

The initial studies were made by Nusselt [32] in 1916. He neglected acceleration and convection effects in the film and the interfacial shear stress between the film and the stagnant vapor. He derived his equations from a simple force balance between the liquid shear forces and the weight of the fluid and considered a linear temperature profile across the film. Nusselt obtained the following relation for the local and average Nusselt numbers of the film

Local

$$Nu = \frac{h\ell}{k_L} = \left[\frac{g_c \, \lambda \, (\rho_L - \rho_G) \, \ell^3}{4 \, \Delta T \, \nu_L \, k_L} \right]^{1/4} \tag{19}$$

Average

$$Nu_m = \frac{h_m L}{k_L} = \left[0.943 \, \frac{g_c \, \lambda \, (\rho_L - \rho_G) \, L^3}{\Delta T \, \nu_L \, k_L} \right]^{1/4} \tag{20}$$

Rohsenow[33] extended Nusselt's analysis to include convection effects on the temperature profile across the film. Sparrow and Gregg[34] included the effects of both acceleration and convection on the condensing film, but neglected the effect of the interfacial shear stress between the film and the stagnant vapor. Sparrow and Gregg employed a similarity transformation and a boundary layer type of solution. Koh, et al[35] extended the Sparrow and Gregg analysis to take into account shear stress between the film and the stagnant vapor at the vapor-liquid interface. Chen[36] and Koh[37] both considered the same case as Koh, et al[35]. However, Chen and Koh obtained their solutions using less exact integral techniques. Their results are in close agreement with those of Koh, et al[35]. These results indicate that the effects of acceleration, convection, and interfacial shear on the film can be significant for fluids which have low Prandtl numbers, such as liquid metals. These results are illustrated in Figure 5, where it can be seen that the solution of Koh, et al[35] can differ markedly from the Nusselt solution for fluids with low Prandtl numbers.

The case of a turbulent condensing film flowing on a vertical surface under the influence of gravity was first studied by Colburn[38] who reviewed the experimental data of Kirkbride[39] for condensation on the outside of vertical tubes. From this data Colburn reasoned that transition from laminar to turbulent flow took place at a film Reynolds number $4\Gamma / \mu_L$ of 2100. He also obtained the following empirical equation for local heat transfer coefficients of the condensing film from this data

$$\frac{h}{k_L}\left(\frac{\nu_L^2}{g_c}\right)^{1/3} = 0.056 \; Pr_L^{1/3} \left(\frac{4\Gamma}{\mu_L}\right)^{0.2} \tag{21}$$

The case of a turbulent condensing film flowing on a vertical plate under the influence of gravity and in the presence of a stagnant vapor was studied analytically by Seban[40]. Like Nusselt, Seban neglected the effects of acceleration, convection and interfacial shear on the film. He assumed that transition from laminar to turbulent flow occurred at a film Reynolds number of 1600. Seban assumed that the generalized velocity profile, obtained experimentally for fully-developed single-phase turbulent flow through circular pipes, could be applied to the turbulent condensing film. Using the generalized velocity profile, Seban solved for the case of a turbulent condensing film with methods similar to those Martinelli[3] used for fully-developed single-phase turbulent flow. Like Martinelli, Seban considered the transport of heat by both molecular conduction and the turbulent transport mechanism in the buffer layer and the turbulent

portion of the flow. Seban's results are illustrated in Figure 6 where the heat transfer parameter $\frac{h_m}{k_L}\left(\frac{\nu_L^2}{g_c}\right)^{1/3}$ is plotted as a function of the film Reynolds number and the Prandtl number of the fluid. These results indicate that for fluids with low Prandtl numbers the heat transfer coefficient for a given Reynolds number will be less for turbulent flow than the value predicted by Nusselt's theory for laminar flow.

Rohsenow, et al[41] extended the laminar flow solution of Nusselt and the turbulent flow solution of Seban to include the case where a downward flow of vapor imposes a shear stress on the film at the vapor-liquid interface. Based upon the experimental observations of a number of investigators, Rohsenow, et al reasoned that the film Reynolds number at the transition from laminar to turbulent flow depended on the vapor shear stress τ_V at the liquid-vapor interface. They developed expressions for this transition Reynolds number in terms of an interfacial shear parameter $\tau_V^* = \frac{\tau_V}{g_c\left(\rho_L - \rho_G\right)\left(\frac{\nu_L^2}{g_c}\right)^{1/3}}$.

The results of these expressions are illustrated in Figure 7 where it can be seen that the transition Reynolds number varies from a value of 1800 for τ_V^* equal to zero to 71.8 for high values of τ_V^*. Rohsenow, et al presented the results of their solution in terms of the heat transfer parameter $\frac{h_m}{k_L}\left(\frac{\nu_L^2}{g_c}\right)^{1/3}$ as a function of film Reynolds number, Prandtl number, and the shear stress parameter τ_V^*. Their results for a Prandtl number of 0.01 are illustrated in Figure 8. These results indicate that for a given film Reynolds number the heat transfer coefficient increases as the interfacial shear increases.

b. Condensing Flow Inside Tubes

Condensing flow inside vertical tubes was first studied by Carpenter and Colburn[42] who considered the downward flow of vapor and liquid for the case where the condensate formed a continuous film on the inside of the tube. This case differs from condensing flow on a vertical surface, as studied by Rohsenow, et al[41], since the film is not only affected by gravity and vapor shear, but also by a static pressure gradient in the axial direction. This static pressure gradient arises from frictional effects and momentum effects which are caused by the condensation of the vapor. Carpenter and Colburn studied the problem both experimentally and analytically. Their experimental data was taken for a number of common engineering fluids with high

Prandtl numbers. From the experimental data they concluded that for their experimental conditions the transition from laminar to turbulent flow occurred at a film Reynolds number near 240. This transition Reynolds number is considerably less than the value of 2100 observed for flow over a vertical surface in the presence of a stagnant vapor. They attributed this lower transition Reynolds number to the effect of vapor shear on the film. Carpenter and Colburn presented relations for local values of the heat transfer coefficient of the condensing film for flow in both the laminar and turbulent regimes.

For the flow of condensing films in the laminar regime Carpenter and Colburn presented the relation

$$h = k_L \left(\frac{\rho_L F}{2 \mu_L \Gamma} \right)^{1/2} \tag{22}$$

where F is the product of the wall shear stress τ_w and the gravitational constant g_c.

This relation was derived analytically, neglecting the acceleration and convection effects in the film.

Carpenter and Colburn also attempted an analytical solution of the turbulent condensing film and obtained a solution of the form

$$h = C_1 \; k_L \; \frac{(\rho_L F)^{1/2}}{\mu_L} \tag{23}$$

where C_1 is a constant to be empirically determined.

This solution, like that of Seban[40] and Rohsenow et al[41], assumed that the generalized velocity profile could be applied to the turbulent condensing film. However, unlike Seban and Rohsenow et al, Carpenter and Colburn assumed that only the laminar sublayer of the film offered a significant resistance to heat transfer. Consequently, they neglected the thermal resistances of the buffer layer and the turbulent region of the film. This assumption has been shown to be valid in the case of fully-developed single-phase turbulent pipe flow for fluids with high Prandtl numbers. Similarly, it is expected that this assumption is valid for condensing films only for the case of fluids with high Prandtl numbers. In an effort to account for the effect of Prandtl number, Carpenter and Colburn multiplied the right-hand side of Equation (23) by the square root of the Prandtl number with the result

$$h = C_1 \; k_L \; Pr_L^{1/2} \; \frac{(\rho_L F)^{1/2}}{\mu_L} \tag{24}$$

They then evaluated the constant C_1 empirically to obtain reasonable agreement with their experimental data. The resulting equation

$$\frac{h\,\mu_L}{k_L\,\rho_L^{1/2}} = 0.043\,Pr_L^{1/2}\;F^{1/2} \qquad (25)$$

is therefore a semi-empirical result which is only applicable for fluids with Prandtl numbers within the range of their experimental data, i.e. (Pr = 1.0 - 10.0).

Altman, Staub, and Norris[43] also studied condensing flow inside tubes. They performed experiments similar to those of Carpenter and Colburn[42] except that the tube was oriented in the horizontal direction. The experiments were conducted using refrigerant-22 as the test fluid. The results for the turbulent condensing film were correlated using an equation similar to that of Carpenter and Colburn

$$\frac{h\,\mu_L}{k_L\,\rho_L^{1/2}} = 0.057\,Pr_L^{1/2}\;F^{1/2} \qquad (26)$$

In addition to this correlation, Altman,et al[43] performed an analysis of the turbulent condensing film for flow inside a circular tube. This analysis, like those of Seban[40] and Rohsenow, et al[41] was based on the generalized velocity profile, and followed procedures similar to those used by Martinelli[3] in the solution of fully-developed single-phase turbulent pipe flow. This analysis also considered the thermal resistances of all three regions across the condensing film. However, unlike the analyses of Seban[40] and Rohsenow, et al[41] this analysis assumed that the Martinelli factor F_M was equal to 0.99. The Martinelli factor F_M is the ratio of the thermal resistance of the turbulent region of the film when both molecular and turbulent transport mechanisms are considered, to the thermal resistance when only the turbulent transport mechanism is considered. A value of 0.99 for F_M is valid for fluids with high Prandtl numbers, indicating that heat transport by molecular conduction is negligible compared to heat transport by the turbulent mechanism. However, F_M is considerably less for fluids with low Prandtl numbers, indicating the importance of molecular conduction in the turbulent region of the film for such fluids. Thus while this analysis of Altman, et al[43] has shown reasonable agreement with their experimental data, it cannot, in its present form, be applied to fluids with low Prandtl numbers such as liquid metals.

The various analyses described above assume that the film is either in true laminar flow or in fully-developed turbulent flow and that transition occurs at a definite value of the film Reynolds number. The laminar solutions have not taken into account small turbulent effects which might occur in the film. The turbulent solutions all depend upon the generalized velocity profile obtained with fully-developed single-phase pipe flow. With the exception of the work of Carpenter and Colburn, the turbulent analysis will follow the same procedure. The energy equation is solved using eddy transport coefficients obtained by differentiating the generalized velocity profile and combining this result with the differential form of the momentum equation. Recently Dukler [44] presented an analysis which appears to be a significant advance over the previously described methods. Dukler contended that neither true laminar flow nor fully-developed turbulent flow exists in a condensing film and that any theory studying momentum and heat transfer in a condensing film must account for both molecular and turbulent transport mechanisms at all points across the film profile. As a result, Dukler used the same set of equations to describe all flow regimes. Dukler solved both the momentum and the energy equations for a condensing film using methods similar to those developed by Deissler [45] for fully-developed single-phase turbulent pipe flow. The solution divides the film into two regions, a region near the wall and a region away from the wall. Different expressions for the turbulent transport coefficients are used in each region. The Deissler expression for the turbulent transport coefficient for momentum

$$\frac{\epsilon_M}{\nu_L} = n^2 u^+ y^+ (1 - e^{-n^2 u^+ y^+}) \tag{27}$$

was used for the region near the wall, $y^+ < 20.0$, while the von Karman expression

$$\frac{\epsilon_M}{\nu_L} = \mathcal{K} \frac{\left(\frac{du^+}{dy^+}\right)^3}{\left(\frac{d^2u^+}{dy^{+2}}\right)^2} \tag{28}$$

was used for the region away from the wall, $y^+ > 20.0$.

In his solution Dukler neglected acceleration and convection effects in the film and assumed that the ratio of turbulent transport coefficients $\alpha = \frac{\epsilon_H}{\epsilon_M}$ was equal to one. He also assumed that the transport of heat by molecular conduction was very small compared to the

transport of heat by the turbulent mechanism in the region away from the wall. His solution, therefore, neglected the effect of conduction in the region away from the wall. Since Martinelli's results for fully-developed pipe flow have demonstrated the importance of including the effect of molecular conduction in the turbulent region of the flow where $y^+ > 20.0$ for fluids with low Prandtl numbers, Dukler's method is not considered to be applicable to condensing liquid metal flow. Dukler's solution[46] of the momentum equation shows excellent agreement with film thickness data taken for the noncondensing two-phase annular flow through a circular tube and his heat transfer results show excellent agreement with the condensing heat transfer data of Carpenter and Colburn[42]. Dukler has also attempted to show agreement between the results of his solution and condensing liquid metal heat transfer data. The validity of this agreement is questionable and is discussed below in greater detail.

c. Comparison of Theory with Data

From the above discussion it can be seen that the literature contains many condensing flow analyses of various degrees of rigor. A number of these analyses have been derived using assumptions which are valid only for fluids with high Prandtl numbers. As a result they cannot be considered for application to the condensing flow of liquid metals. The validity of the remaining analyses, which have attempted to account for low Prandtl number effects, cannot be confirmed unless the results of these analyses show reasonable agreement with reliable condensing liquid metal heat transfer data. Unfortunately, at present there is little experimental data for condensing liquid metal flows available. The only such data found in the literature was that of Misra and Bonilla[47] and of Brooks and Sawochka[48].

The data of Misra and Bonilla[47] was taken for mercury and for sodium condensing on a vertical surface in the presence of a stagnant vapor. A number of comparisons between this data and the different solutions for condensing flow on a vertical surface have been presented in the literature. These results are illustrated in Figures 9 and 10. In Figure 9 both the sodium data and the mercury data are compared with Equation (21) derived by Nusselt, and Dukler's result[44] for a Prandtl number of 0.05 and no vapor shear. Both sets of data lie well below the Nusselt equation, while Dukler's result appears to show general agreement with the mercury data. However, since Dukler neglected the effect of molecular conduction in the turbulent portion of the condensing film, this agreement is apparently fortuitous. Sukhatme and Rohsenow[49] have performed sample calculations which indicate that when the effect of molecular

conduction is included in Dukler's analysis, the results fall very close to the Nusselt equation.

Some disagreement between the data and Nusselt's equation might be expected since Nusselt neglected the effects of acceleration, heat convection and interfacial shear on the condensing film, which were shown by several investigators to be important for low Prandtl number fluids. However, as illustrated in Figure 10, a comparison of the mercury data with the more rigorous analysis of Chen[36] still shows very poor agreement.

A number of ideas have been advanced to explain this disagreement between the existing theory and the data of Misra and Bonilla. Misra and Bonilla have suggested that this disagreement may be due to a resistance to heat transfer at the interface of the liquid metal and the heat transfer surface, similar to that observed in the single-phase convective heat transfer experiments. Chen[36] has suggested that instead of the vapor remaining relatively stagnant, the vapor may have been flowing upward in the region of the film. The upward flow of vapor would tend to thicken the film and thus reduce the heat transfer coefficient. Sukhatme and Rohsenow[49] have suggested that the disagreement might be caused by mass transfer effects at the vapor-liquid interface of the film. This suggestion is based on the work of Schrage[50] who has theorized that, due to mass transfer effects, a finite discontinuity in temperature exists at the vapor-liquid interface. According to Schrage, the temperature of the liquid at the interface is actually less than the saturation temperature. Estimates made by Sukhatme and Rohsenow indicate that this discontinuity would be sufficiently small to be neglected for common engineering fluids, but can be significant for liquid metals. As a consequence the commonly made assumption that the temperature of the liquid at the edge of the film is equal to the saturation temperature is probably incorrect for liquid metal applications. Any experimental condensing liquid metal heat transfer data evaluated making this assumption would,therefore, be incorrect. Misra and Bonilla attempted to correct some of their experimental data to account for this effect. However, as can be seen in Figure 9, their corrected data still does not show adequate agreement with the theory. Sukhatme and Rohsenow have re-examined this effect as a possible cause of the disagreement between the theory and data. They recently presented some experimental data[51] which tends to support their proposition. However, since this data is of a preliminary nature no definite conclusions can be drawn yet.

The experimental data of Brooks and Sawochka[48] was taken for the condensing flow of potassium through a circular tube oriented in the horizontal direction. Since none of the analyses derived for condensing flow inside circular tubes could be applied to fluids with very low Prandtl numbers, it was not possible to compare this data with an analysis derived specifically for the physical conditions of the data. Instead,the data was compared with the analyses of Nusselt[32] and Seban[40] which were derived for the case of condensing flow on a vertical surface, but which can be applied to fluids with low Prandtl numbers. This comparison is illustrated in Figure 11 where it can be seen that the experimental data lies well below the theoretical predictions.

There are a number of possible explanations for this disagreement between the theory and the experimental data:

1) No attempt was made to correct the data for the Schrage effect. If the effect of a temperature discontinuity at the vapor-liquid interface were taken into account in evaluating the data, the experimental heat transfer coefficients might be higher and thus show better agreement with the theory.

2) The experimental data was of a preliminary nature. Improved measurements might yield results showing closer agreement with the theory.

3) The theoretical solutions with which the data was compared were not derived specifically for the case of condensing flow inside tubes. The solutions neglected the effects of acceleration, heat convection in the condensing film, vapor shear, and static pressure gradient. In addition, the turbulent solution assumed that the ratio of turbulent transport coefficients α was equal to one. The single-phase convective heat transfer studies have indicated that this is probably a poor assumption for liquid metals. Improved theoretical solutions might show closer agreement with the experimental data.

2. Proposed Methods of Estimating Condensing Heat Transfer Coefficients

While the state of the art indicated that there were no relations that would adequately predict condensing liquid metal heat transfer coefficients, some means of predicting such coefficients was required for design purposes in this study. Since it was not within the scope of the study to perform an analysis on the condensing liquid metal film, no attempt was made to advance the state of the art. However, methods

were investigated which would provide condensing heat transfer coefficients of the same order of magnitude as those measured experimentally, and which could be used to extrapolate these results beyond the range of the experimental conditions. These empirical methods are described below. They are no more accurate than the data upon which they are based and their validity beyond the range of experimental conditions cannot presently be substantiated. However, these methods do provide relations useful for design purposes until improved relations are available.

At present, the only experimental heat transfer data available for condensing liquid metals are limited to the cases of condensing flow on a vertical plate and condensing flow through circular horizontal tubes. Since the data taken for condensing flow on a vertical plate is dependent upon a one-gravity field and since the liquid metal condensers in this study were designed to operate in zero-gravity fields, this data was not considered applicable to the design applications of this study. Therefore, only the data taken by Brooks and Sawochka[48] for condensing flow through horizontal tubes was considered.

a. Method of Carpenter and Colburn

In an effort to find a method of correlating the data of Brooks and Sawochka the experimental data was plotted in terms of the variables $\frac{h\,\mu_L}{k_L\,(\rho_L\,Pr_L)^{1/2}}$ and F. These variables were shown by Carpenter and Colburn[42] and by Altman, et al[43] to be important for turbulent condensing flow through circular tubes for fluids with Prandtl numbers of the order of one.

The term F was calculated using the equation

$$F = \tau_w g_c = \frac{g_c\,D}{4}\left(\frac{dP}{d\ell}\right)_{tpf} \tag{29}$$

The two-phase frictional pressure gradient $\left(\frac{dP}{d\ell}\right)_{tpf}$ was calculated using the method of Lockhart and Martinelli[4] which is described in greater detail in Section III.E. of this report. The plot is illustrated in Figure 12. As can be seen in Figure 12, both the equations of Carpenter and Colburn[42] and Altman, et al[43] predict condensing heat transfer coefficients of the same order of magnitude as the experimental liquid metal data. However, the equation of Carpenter and Colburn appears to show closer agreement with the experimental data.

Because of the apparent agreement between the experimental data and the equation of Carpenter and Colburn for a turbulent condensing film, it was decided to employ the general method by Carpenter and Colburn as one method of estimating condensing heat transfer coefficients for the liquid metal condenser design study. The following relations were therefore used to predict condensing heat transfer coefficients.

Laminar Film, Equation (22)

$$h = k_L \left(\frac{\rho_L F}{2 \mu_L} \right)^{1/2}$$

Turbulent Film, Equation (25)

$$\frac{h \mu_L}{k_L \rho_L^{1/2} Pr_L^{1/2}} = 0.043 F^{1/2}$$

To differentiate between the laminar and turbulent flow regimes the following transition criterion was employed

$$\tau_{w_{trans}} = \frac{2.37 \times 10^4}{\rho_L g_c} \left(\frac{\mu_L}{D} \right)^2 \qquad (30)$$

where $\tau_{w_{trans}}$ is the wall shear stress for turbulent flow at the transition point. This transition criterion employs a wall shear stress instead of the more commonly used film Reynolds number. Equation (30) was developed using methods similar to those suggested by Carpenter [52] and is described by Rohsenow, et al [41]. The details of the development of Equation (30) are outlined in Appendix G.

Since all of the data points of Brooks and Sawochka were taken for turbulent films, as determined by the above criterion, the validity of Equation (22) for the laminar film cannot presently be confirmed by comparison with experimental data. In addition, while Equation (25) for the turbulent film shows apparent agreement with the experimental data, it neglects an important effect that should be brought to the attention of anyone using this relation for design calculations.

As discussed above under state of the art, the Carpenter and Colburn solution of the turbulent film was derived for liquids with high Prandtl numbers and therefore only considered the thermal resistance of the viscous sublayer of the film. This assumption caused the calculated condensing heat transfer coefficient to be independent of the film thickness for a given wall shear stress. The thermal resistances of

the buffer layer and the turbulent region of the film were assumed to be negligible. However, since these latter resistances are not negligible for fluids of low Prandtl number, the heat transfer coefficient of a condensing liquid metal film must be a strong function of the thickness of the film. As a consequence, Equation (25) does not correctly account for the effects of the film thickness.

The fact that Equation (25) does not adequately account for the effect of the film thickness is illustrated in Figure 13 where the heat transfer parameter $\frac{5\mu_L h}{k_L(\rho_L F)^{1/2}}$ is plotted against the dimensionless film thickness δ^+. The results of Equation (25) are compared with those of the equation

$$h = \frac{k_L}{\delta} \tag{31}$$

where δ = film thickness

This can be derived for thin films by neglecting convection effects and assuming heat is transferred only by molecular conduction. Since Equation (31) neglects the effect of heat transfer by the turbulent transport mechanism, it represents the lowest heat transfer coefficient that is theoretically possible for a liquid film. The results of the Carpenter and Colburn equation are shown as a function of Prandtl number. As can be seen,these results are represented by a family of horizontal lines indicating that for a given wall shear stress, the results of Equation (25) are independent of the film thickness. In contrast the results of Equation (31) are steeply sloped, indicating that the heat transfer coefficient of the film can be strongly dependent upon the film thickness. For purposes of comparison, the data of Brooks and Sawochka was also plotted in Figure 13. The film thickness δ was calculated for the data using the relation

$$\delta = \frac{D}{2}\left[1 - \sqrt{1 - R_L}\right] \tag{32}$$

The liquid fraction R_L was obtained from the correlation of Lockhart and Martinelli [4]. As can be seen in Figure 13, the data points show general agreement with the heat transfer coefficients predicted using Equation (25) with a Prandtl number of 0.003. However, as can be seen in Figure 13, the bulk of the data lies substantially below the minimum theoretical values predicted using Equation (31). There are a number of possible explanations for this result:

1) The data may require correction to account for the Schrage effect.

2) The data itself may not be accurate.

3) The friction and liquid fraction correlations of Lockhart and Martinelli[4] used to calculate F and δ for the data points on this plot were obtained experimentally for the isothermal two-phase flow of common engineering fluids. These relations may not be valid for the condensing flow of liquid metals.

It can also be seen in Figure 13 that Equation (25) predicts heat transfer coefficients substantially below the minimum theoretical values. This result is caused by the term $Pr^{1/2}$ in Equation (25) which was included by Carpenter and Colburn. Thus while Equation (25) predicts condensing heat transfer coefficients of the same order of magnitude as the experimental data, this agreement is fortuitous. The agreement might well be due to a combination of a Schrage effect in the data and the term $Pr^{1/2}$ in Equation (25).

b. Modified Film Conduction Method

To obtain an expression that would predict condensing heat transfer coefficients of the same order of magntitude as the experimental data of Brooks and Sawochka and also reflect the importance of the film thickness, it was decided to multiply the coefficient obtained from Equation (31) by a correction factor. This correction factor was used to bring the coefficient into agreement with the experimental data. As can be seen in Figure 13, a correction factor of 0.3 gave results that agreed reasonably with the bulk of the data. This resulted in the relation

$$h = 0.3 \frac{k_L}{\delta} \tag{33}$$

which was used as a second method of estimating condensing heat transfer coefficients for design purposes in this study. The film thickness δ was calculated from Equation (32) where the liquid fraction correlation of Lockhart and Martinelli[4] was used to obtain R_L. Since this liquid fraction correlation is valid for both laminar and turbulent films, this method was applied to film flow in both regimes. To use this correlation it is necessary to determine the flow regime of both the vapor core and the liquid film. The transition criterion presented by Lockhart and Martinelli was used to determine the flow regime of the vapor core, while calculations were made

using both Equation (30) and the criterion presented by Lockhart and Martinelli[4] to determine the flow regime of the film.

Since all the data points of Brooks and Sawochka were taken for turbulent films, as determined using both of the above criteria, the validity of this method for laminar films cannot presently be confirmed by comparison with experimental data. While this method does show apparent agreement with the experimental data for a turbulent film, its use for conditions that differ from those of the experimental data is dependent upon the validity of the constant correction factor, 0.3, and validity of the friction and liquid fraction correlations of Lockhart and Martinelli for use with condensing liquid metal flows has not been definitely established. In addition, the very strong dependency of the condensing heat transfer coefficient on the film thickness predicted by Equations(31) and (33) is approximately valid only for fluids which have very low Prandtl numbers, such as high temperature potassium. For fluids such as mercury, which have Prandtl numbers an order of magnitude higher, turbulent effects in the film become more important and the heat transfer coefficient becomes less dependent upon the film thickness.

c. Schrage Effect Method

An effort was also made to determine whether the difference between the experimental data points and the results of Equation (31) shown in Figure 13, could be related to the Schrage effect. If such a relation existed, it could be used together with Equation (31) to predict condensing liquid metal heat transfer coefficients for design purposes.

On the basis of the kinetic theory of gases, Schrage[50] has theorized that, due to mass transfer effects, a temperature discontinuity exists at the vapor-liquid interface of a condensing film. His theory predicts that the temperature of the liquid at the vapor-liquid interface T_{int}, is actually less than the saturation temperature of the fluid T_{sat}. Based on Schrage's work, Sukhatme and Rohsenow[49] have presented the following equation which relates the mass flux at the liquid-vapor interface m to the temperature difference $T_{sat}-T_{int}$.

$$m = \left(\frac{\sigma}{2-\sigma}\right)\left(\frac{2g_c}{\pi}\right)^{1/2}\left(\frac{M}{R}\right)^{3/2}\frac{(P_{sat}\lambda J)}{(T_{sat}+460)^{5/2}}(T_{sat}-T_{int}) \qquad (34)$$

As can be seen in Equation (34) the mass flux is directly proportional to this temperature difference.

The term σ in Equation (34) is known as the condensation coefficient or accommodation coefficient. Very little is known about this condensation coefficient. It is felt that σ is a function of the condition of the liquid-vapor interface and the fluid being condensed. According to Sukhatme and Rohsenow[49], many investigators have measured a value of σ near 0.04 for water. Sukhatme and Rohsenow also indicate that values of σ have been measured for mercury which range from 0.0005 to 1.0. A value of 0.1 for σ is the most consistently reported value for mercury. Knudsen[53] measured a value of 1.0 for σ using very pure mercury and a value of 0.0005 for mercury when the surface was contaminated with a scum. There are no measurements of σ available for other condensing liquid metals.

For heat transfer considerations, the temperature difference T_{sat}-T_{int} can be treated by assuming an additional resistance to heat transfer at the vapor-liquid interface. Thus the heat transfer coefficient of a condensing flow is defined by the relation

$$h \equiv \frac{q_w}{(T_{sat}-T_w)} \tag{35}$$

where q_w is the heat flux at the wall

This heat transfer coefficient can be expressed in terms of the heat transfer coefficient of the condensing film h_{film} and the equivalent heat transfer coefficient of the resistance at the interface h_{int} using the relation

$$h = \frac{1}{\frac{1}{h_{film}} + \frac{1}{h_{int}}} \tag{36}$$

where

$$h_{film} \equiv \frac{q_w}{T_{int}-T_w} \tag{37}$$

$$h_{int} \equiv \frac{q_w}{(T_{sat}-T_{int})} \tag{38}$$

The true heat flux at the liquid-vapor interface q_{int} can be related to the mass flux m through the relation

$$q_{int} = m\lambda \tag{39}$$

where λ is the latent heat of vaporization

However, if the subcooling of the liquid in the film is neglected, q_{int} can be assumed equal to q_w and Equations (34), (35), and (39) can be combined to yield the following relation for h_{int}

$$h_{int} = \left(\frac{\sigma}{2-\sigma}\right)\left(\frac{2g_c}{\pi}\right)^{1/2}\left(\frac{M}{R}\right)^{3/2}\frac{(P_{sat}\ \lambda^2\ J)}{(T_{sat}+460)^{5/2}} \tag{40}$$

Using the above relations, an attempt was made to relate to the Schrage effect the difference between the experimental heat transfer coefficients and those predicted by Equation (31). It was assumed that for each data point the heat transfer coefficient of the condensing film was equal to the value predicted by Equation (31). Values of σ that would account for the difference between the experimental heat transfer coefficients and the film heat transfer coefficients were then determined. It was hoped that these values of σ would show a consistent trend. If such a trend could be correlated in terms of physical parameters, it could be used together with Equations (31), (36), and (40) to provide a rational method of predicting condensing liquid metal heat transfer coefficients for the design study. However, the values calculated for σ varied from 0.00635 to 0.1984, with an average value of 0.045. No consistent trend was apparent and it was therefore not possible to correlate σ in terms of any physical parameters. In addition, since the values varied over such a wide range, little significance can be attached to the average value of 0.045. As a result, no positive conclusions can be drawn concerning the significance of the Schrage effect in the experimental data of Brooks and Sawochka. Nevertheless, the use of Equations (31), (36), and (40) with assumed values of σ was considered as a third method of predicting condensing liquid metal heat transfer coefficients for the liquid metal condenser design study.

d. Comparison Between Methods

The above discussion describes a number of methods developed to estimate condensing liquid metal heat transfer coefficients for the liquid-metal condenser study. Since many design calculations were needed to conduct this study, it was not practical to repeat these calculations using each different method of estimating the condensing heat transfer coefficients. A comparison was therefore made to investigate the effect of these different methods on the calculated size and weight of a typical liquid metal condenser considered in this study. On the basis of this comparison, one of these methods was selected for use in most of the design calculations.

This comparison was made for the lithium-cooled constant-diameter shell-and-tube condenser described in Section IV of this report. The thermodynamic design conditions are listed in Table 1, Appendix D. The configuration that was considered employed ninety-one tubes of 3/8-inch outside diameter arranged in an equilateral triangular pattern with a pitch-to-diameter ratio of 1.350. Calculations of tube length and condenser core weight were made for this configuration using these different methods for predicting condensing heat transfer coefficients. The results are shown in Table 2.

As can be seen in this table, the size and weight calculated for the given condenser configuration is strongly dependent upon the method used to predict condensing heat transfer coefficients. These results show that the shortest tube lengths and lightest core weights are predicted using the film conduction method, while the longest tube lengths and heaviest core weights are predicted using the Schrage effect method. The Carpenter and Colburn method predicts tube lengths and core weights half-way between those predicted by the film conduction method and the Schrage effect method, using a value of 0.045 for σ. These results also show that tube length and core weight are only slightly affected by the different transition criteria used with the film conduction method, but that tube length and core weight are strongly affected by the value assumed for σ using the Schrage effect method.

In selecting a method to use for the design calculations it was desired to choose one that predicted long tube lengths and high core weights. Such a method would probably predict answers that were conservative in terms of size and weight. As can be seen in Table 2, the Schrage effect method predicts the longest tube lengths and the highest core weights. However, since the results obtained using the Schrage effect method are so strongly dependent upon the condensation coefficient σ, and since so little is actually known about σ, it was decided that this method was not sufficiently reliable for use in the design calculations. As a result, the Carpenter and Colburn method, which predicts more conservative results than the modified film conduction method, was selected for most of the design calculations.

E. Pressure Drop Calculations

A literature survey was conducted to obtain methods for calculating the different types of pressure drop encountered by flow through the various condenser designs considered in this study. These pressure drops can be classified into the general categories of contraction and expansion

losses, frictional losses, pressure drop due to momentum effects, orifice losses, and radial pressure loss. The methods employed for calculating these different types of pressure drop and their applicability to the condenser designs of the study are discussed below.

1. Contraction and Expansion Losses

Pressure losses due to sudden contractions and expansions are encountered whenever a fluid flows between passages of different cross-sectional area without a gradual transition section. Typical examples are the flow from a feed pipe into an inlet manifold, flow from an inlet manifold feeding a number of tubes, and flow from a shell into an exit manifold. Reference 30 contains a summary of the general equations and coefficients for calculating expansion and contraction losses for single-phase flow through typical heat exchanger geometries. In addition, some information has been presented for calculating these losses for two-phase flow. Lottes [54] reviewed several methods of calculating the static pressure drop due to a sudden expansion for two-phase flow, while Straub and Silberman [55] presented methods for calculating static pressure drops due to both sudden expansion and sudden contraction for two-phase flow. Their equations are empirical and are based on experimental data taken for air-water mixture at low quality flow.

In making the design calculations the equations presented in Reference 30 were used for the case of single-phase flow. However, for the conditions of this study, two-phase flow contractions and expansions occurred only at high quality (83 per cent) conditions. Since the methods presented by Lottes [54] and Straub and Silberman [55] were obtained empirically for low quality flows, it was felt that these methods were not applicable for this study. As a result the design calculations for two-phase contractions and expansions were made using the equations of Reference 30 and assuming the flow to be a single-phase vapor. This method is arbitrary, but it is felt to give a reasonable estimate of these losses.

2. Frictional Losses

The frictional pressure losses for the condenser designs of this study are associated with flow through circular tubes and annular passages, and with the axial flow of the coolant through the shell for shell-and-tube condenser designs. The relations for predicting frictional pressure losses for the flow of single-phase fluids through passages with both circular and noncircular cross-sections are well established. The equations presented in the textbook of Binder [56] were employed in making the calculations for this study.

Relations for predicting frictional pressure losses for two-phase flow in a circular pipe have been presented by Lockhart and Martinelli[4]. Hays[57] indicated that a pressure drop prediction based upon the Lockhart and Martinelli correlation agreed reasonably well with condensing mercury data. Altman, et al[43] also indicated that calculated values of pressure drop using the method of Martinelli and Nelson[58] (an integrated version of the Lockhart and Martinelli correlation) gave good results in comparison with data for refrigerant-22 condensing in horizontal tubes. A recent paper by Dukler et al[59] indicated that the Lockhart and Martinelli correlation showed the best agreement with a set of carefully culled adiabatic two-phase pressure drop data when compared with four other correlations.

The method of Lockhart and Martinelli was employed in making the calculations for the design study. The Lockhart and Martinelli correlation was adapted for use in a computer program to facilitate calculations. A discussion of this calculation procedure is found in Appendix H.

3. Pressure Drop Due to Momentum Effects

This type of pressure drop was considered in calculations involving the working fluid in the two-phase flow regime. This pressure drop is due to the large changes in velocity head of the fluid as condensation occurs. In order to calculate this type of pressure drop a method is needed to calculate an average velocity head which in turn involves a method of obtaining relative volumes (or velocities) of vapor and liquid as the two phases flow concurrently in the passages. These relative volumes depend upon flow regime. The method used in the design calculations to determine relative volumes of the two phases was based on empirical data obtained by Lockhart and Martinelli[4] for the different flow regimes. The general equations and the Lockhart and Martinelli correlation of liquid volume fractions were programmed for a computer and are discussed in Appendix H. A recent paper by Dukler, et al[59] indicated that the Lockhart and Martinelli correlation showed good agreement with a set of carefully culled experimental data on liquid volume fraction with annular two-phase flow.

4. Orifices Losses

In some condenser designs orifices were included in order to cause better flow distribution for both the coolant and the working fluid. Since in all cases, the orifices were in a regime of single-phase liquid flow, calculations of pressure losses through orifices were based on standard equations for liquid flow through orifices, such as those discussed in McCabe and Smith[60].

5. Radial Pressure Loss

In the shell-and-tube designs of this study, passages were formed between the tubesheets and plates containing orifices to distribute the coolant (see Figure 14). These passages were located at both ends of the shell. At the inlet end of the shell the coolant entered these passages at the outer periphery, flowed radially inward, and was dispersed through the orifices into the main shell section. Thus, the flow rate diminished as the coolant flowed towards the center. A reverse procedure occurred at the exit passageway. Similar radial flow patterns were obtained by the flow of the working fluid between adjacent tubesheets as it entered and left the annular passages of the concentric tube design (see Figure 52). The pressure drop encountered by this radial flow was thus a combination of friction, expansion, and contraction type losses as the fluid flowed across a tube bank.

No direct method of calculating this type of loss was found in the literature survey. A method of approximating the radial loss for the particular condensers designed in this study was devised. The method is described in Appendix I, and is based on methods for flow across staggered tube banks. However, adaptations had to be made for variations of mass flow velocity and number of tubes in the direction of flow.

F. Critical Two-Phase Flow

In the two-phase flow of a liquid and a gas through a duct, a condition can occur when for a fixed inlet pressure a further decrease in exit pressure will not produce an increase in the mass velocity of the fluid through the duct. This condition, known as the critical condition, corresponds to the sonic choking phenomenon of single-phase gas flow. However, in critical two-phase flow, sonic choking of the gas phase does not necessarily occur. Critical two-phase flow is significant in condenser design because it places an upper limit on the mass velocity of the condensing fluid. This is a particularly important consideration in the design of tapered condensers since the mass velocity of the condensing fluid can increase in the direction of the condensing flow.

Using an annular flow model and following an approach similar to that of Fauske [61], the following equation has been derived for the critical mass velocity of a two-phase fluid

$$G_{cr} = \left[\frac{-g_c}{\left\{ v_L \left[(k-1)(1-2x)-1 \right] + \frac{v_G}{k} \left[2x(k-1)+1 \right] \right\} \left\{ \frac{v_{fg}}{S_{fg}\lambda} \left[xC_{pG} + (1-x)C_{pL} \right] + \frac{xR}{S_{fg}P} \right\} + \frac{x}{k} \left[x(k-1)+1 \right] \frac{v_G}{P} \left(\frac{Pv_{fg}}{\lambda} - 1 \right)} \right]^{1/2} \tag{41}$$

where $k = \left(\frac{v_G}{v_L} \right)^{1/2}$

A detailed derivation of this equation is given in Appendix J. As can be seen in Equation (41), the critical mass velocity is dependent only upon the thermodynamic properties of the two phases and upon the dynamic quality of the two-phase flow.

The results using Equation (41) were compared with the available critical two-phase flow data of Moy[62], Faletti[63], Fauske[61], and Cruz[64] and with the theoretical results of Fauske. As can be seen in Figures 15 and 16, the results using Equation (41) show reasonable agreement with the experimental data taken for steam-water mixtures. In addition it can be seen that the results using this analysis and that of Fauske are identical. However, Equation (41) is of a more convenient form to use than the method presented by Fauske.

Equation (41) was used to check whether two-phase choking would occur in the tapered condenser designs presented in Section IV of this report.

IV. CONDENSER DESIGNS FOR ONE-MEGAWATT (ELECTRIC) POWERPLANT

A. Introduction

The recommended analytical design procedures described in the preceding section were employed in a study to determine the most suitable type of liquid metal condenser for a one-megawatt (electric) Rankine-cycle space powerplant. Three different arrangements for the heat rejection system of the powerplant were considered as well as two different radiator fluids, lithium and NaK. A number of different condenser configurations were investigated. Parametric studies were conducted for these different configurations and preliminary designs were made on the basis of these parametric studies.

The one-megawatt Rankine-cycle powerplant used as the basis of this study was originally investigated by Pratt & Whitney Aircraft for NASA under Contract NASw-360 and is described in detail in Reference 65. The powerplant is shown schematically in Figure 17a. It consists of a lithium-cooled nuclear reactor supplying heat to four power systems. Each power system consists of a power loop and four heat rejection loops. The power loop consists of a boiler, a turbine, one or more condensers, a jet pump, a turbine-driven pump and a control valve. Potassium is used as the working fluid in the power loops. Heat is removed from the condensers of each power loop using the four heat rejection loops which operate independently of each other for improved reliability. The heat rejection loops consist of the condensers, a radiator and a circulation pump, and employ a liquid metal coolant.

There are a number of possible condenser arrangements that can be used with the four independent heat rejection loops. Of these the following three arrangements, illustrated in Figure 17b, were considered in this study.

1) Four condensers connected in parallel on the potassium side, each connected to a different heat rejection loop.

2) Four condensers connected in series on the potassium side, each connected to a different heat rejection loop.

3) One condenser with the coolant side divided into four segments which are sealed from each other. Each segment is connected to a different heat rejection loop.

Arrangements 2 and 3 are similar thermodynamically and differ primarily in the mechanical construction of the condensers and piping.

In the event of failure of one of the heat rejection loops, the power output of the system will be reduced to the point that the heat removed from the three remaining active heat rejection loops will be sufficient to completely condense the working fluid. In Arrangements 2 and 3 the working fluid can be completely condensed within the three active condensers themselves. However, due to the parallel connection used in Arrangement 1 some of the working fluid would bypass the three active condensers, flow through the inactive condenser, and enter the collecting pipe as an uncondensed vapor. Condensation would therefore be completed in the collecting pipes as the vapor mixes with the subcooled condensate from the three active condensers and flows to the jet pump. In designing condensers for Arrangement 1 it is necessary to restrict the amount of vapor passing through the inactive condenser to a sufficiently low flow rate so that it can be completely condensed by the subcooled condensate from the three active condensers. This can be done by placing small-diameter orifices in the condensate flow path of each condenser.

The powerplant as described in Reference 65 employs liquid lithium in the heat rejection loop. However, since NaK has a much lower freezing temperature than lithium, there is also interest in using NaK as the coolant in the heat rejection loops of Rankine-cycle space powerplants. For this reason both lithium and NaK were considered as coolants in the condenser design study.

The condenser design conditions for the case where lithium is used as the coolant are given in Table 1. The potassium enters the condenser as a wet mixture and leaves as a subcooled condensate, while the lithium coolant takes a 152°F temperature rise. These conditions were obtained from Reference 65 and are the result of an optimization study performed on the system.

The design conditions for the case where NaK is used as the coolant are also given in Table 1. They are identical to those of the previous case except for the coolant temperature rise and coolant flow rate. The 205°F temperature rise specified is considered typical of that to be expected for an NaK-cooled system and is not the result of an optimization of this particular system.

The reader is cautioned that the subcooling length for the non-tapered diameter designs presented in this report are minimal in order to comply with the specified potassium outlet tem-

perature. It is recommended that additional length be added to the constant-diameter cases in order to insure complete condensation in the tubes, to account for off-design conditions. This would result in a lower value of potassium outlet temperature. The tapered designs included additional subcooling length and resulted in a lower value of potassium outlet temperature. This was done because of difficulties involved in adding length to tapered designs.

In the initial phase of the design study, plate-fin, shell-and-tube, and concentric-tube heat exchangers were considered for possible use as liquid metal condensers to operate in a space environment. Plate-fin heat exchangers were found impractical from a fabrication standpoint, since all joints should be welded (see Appendix A). Shell-and-tube and concentric-tube condensers appeared to be the most practical types for this application, and therefore were given detailed consideration in the study.

The effect of varying the important geometrical parameters was studied in order to arrive at the most desirable design for each individual condenser configuration considered. Design configurations were then selected on the basis of the size and weight of the condenser, the relative ease of fabrication, and the degree of reliability that would be expected. Preliminary design drawings were made for the most promising of these design configurations. These preliminary design drawings appear as Figures 19 to 22 and Figure 52 of this report. Comprehensive stress analyses were performed in the preparation of these preliminary designs. These analyses were similar to that presented in Volume II of this report for a constant-diameter shell-and-tube configuration, and indicated that these designs could withstand the thermal stresses expected in normal operation for a period exceeding the 10,000-hour design life of these condensers.

In addition, a study was conducted in order to determine the best material of construction for either a lithium or an NaK-cooled potassium condenser operating at a maximum temperature of 1200°F. This study concluded that the refractory alloy columbium-1% zirconium was the best material from the overall standpoints of corrosion resistance, strength, machinability, and ability to be joined. The details of this study are presented in Appendix A. In addition, this study describes different joining techniques for tube-to-tubesneet joints for heat exchangers using Cb-1% Zr. The recommended method of joining tubes to tubesheets consists of seal-welding the tube ends to the sheets and diffusion-bonding the tubes to the mating holes, using vanadium

inserts (see Figure 18). The thicknesses of tubes and tubesheets used in the design study were selected to conform with the requirements of this fabrication procedure. All welding in the fabrication of the condenser is to be done in an argon or helium atmosphere with tungsten electrodes. Welding the tubes to the tubesheets should be done using a high speed process such as the cone-arc method.

A detailed description of the design features and the design selection procedure is given below for each condenser configuration considered.

B. Shell-and-Tube Condensers

The shell-and-tube condenser is particularly attractive for space powerplant applications. The cylindrical shell serves as a good pressure vessel, while the basic construction provides a minimum number of metal-to-metal joints, thereby improving reliability. For this reason, the major portion of this study was devoted to various types of shell-and-tube condenser configurations. Three basic types of shell-and-tube condensers were considered, 1) constant diameter, 2) tapered diameter, and 3) annular shell. These are illustrated in Figures 19 to 22 and are described in greater detail in the sections that follow.

All of the shell-and-tube condensers used a counterflow arrangement with the condensing fluids flowing through the tubes and the coolant flowing axially through the shell as illustrated in Figure 14. The counterflow arrangement is required to meet the temperature design conditions, since the coolant exit temperature is considerably higher than the condensate exit temperature. Condensing inside the tubes was chosen instead of the more conventional method of condensing outside the tubes, because the condenser must be designed to operate in a zero-gravity environment. With the condensing flow inside the tubes, fluid pressure and shear effects instead of gravity can be used to drive the liquid condensate from the condenser. Since the heat transfer coefficient on the shell side was sufficiently high with straight axial flow, cross-flow baffling was not employed in the shell. In addition, the use of cross-flow baffling would have resulted in a large number of passes in order to obtain the required heat exchanger performance, and a very large shell diameter in order to keep the shell-side pressure losses within the required 1.2 psi.

Shell-and-tube condensers were considered for use with all three heat rejection arrangements. The constant-diameter, tapered-diameter, and annular-shell configurations were studied for the series and segmented-shell arrangements.

1. Parallel Arrangements

For the parallel arrangements constant-diameter shell-and-tube configurations and tapered shell-and-tube configurations were designed for both lithium-cooled and NaK-cooled cases. In addition, an annular-shell, bent-tube configuration was designed for the lithium-cooled case. The design calculations were made using the computer program described in Section V of this report.

a. Constant-Diameter Configuration

The constant-diameter shell-and-tube configurations are illustrated in Figures 19 and 20. They consist of a bundle of circular tubes attached to tubesheets at either end. The tube bundles are arranged in a hexagonal pattern using an equilateral triangular pitch. The tube bundles are enclosed in cylindrical shells employing hexagonal liners to direct the flow through the tube bundles. The shells are joined to the tubesheets at both ends through toroidal type manifolds. These manifolds are sufficiently flexible to relieve the stresses caused by the differential thermal expansion between the shell and the tubes. Orifice plates are used at both ends of the shell since the frictional pressure loss of the fluid through the shell is insufficient to maintain a uniform distribution of the coolant across the shell. The resulting shell fluid flow pattern is illustrated in Figure 14. The potassium enters through the inlet pipe and is distributed to the tubes from the potassium inlet manifold. The potassium enters the tubes where it is condensed and subcooled. The potassium condensate leaves the tubes and is collected by the potassium exit manifold before leaving through the exit pipe.

Small-diameter orifices are placed at the exit of each tube. These orifices minimize the amount of vapor that would pass through the condenser if the heat rejection loop of that condenser failed. They also reduce the amplitude of the pressure oscillations that would occur during such a loss of cooling. These oscillations are caused by vapor entering the exit manifold and were observed in tests conducted under this contract and reported in Reference 66. In addition, these orifices are sized so that the static pressure drop across them is greater than the static pressure rise of the condensing flow through the tubes. This helps to insure a uniform distribution of potassium to all tubes, particularly when the condenser is operating in a horizontal orientation within a gravity field.

The coolant enters from the inlet pipe and is distributed circumferentially by the coolant inlet manifold. The lithium then flows radially inward through the circumferential gap between the shell and the tubesheet and enters the passage between the tubesheet and the adjacent orifice plate. The coolant flows radially inward through this passage and is dispersed through the holes in the orifice plate into the main shell section. Thus the flow rate of the coolant is diminished as it flows towards the center. The coolant flows axially through the main shell section and then through the holes in the orifice plate at the exit end of the shell. The coolant is collected in the passage between this orifice plate and the adjacent tubesheet where it flows radially outward. The coolant continues to flow radially outward through the circumferential gap between the tubesheet and the shell and is collected by the coolant exit manifold before leaving through the exit pipe.

In order to obtain high thermal performance, the coolant flow must be distributed uniformly in the radial direction as it flows through the main shell section of the condenser. This coolant distribution is strongly influenced by the relative pressure drops across various portions of the coolant flow path. As the pressure drop across an orifice plate increases relative to the radial pressure loss for the flow between this orifice plate and the adjacent tubesheet, the coolant distribution becomes more uniform across the shell. It was felt that the drop across the orifice plate must be at least ten times the radial pressure loss to obtain an acceptably uniform coolant distribution in the main shell section.

The hole pattern in the shell orifice plates is illustrated in Figure 23. The tubes are fitted through circular holes in the plate. An average clearance of 0.006 inch is maintained between the tubes and the mating plate hole to permit ease of assembly. This clearance forms annular orifices through which a portion of the fluid passes. The remainder of the fluid passes through circular orifice holes located at the centers of the equilateral triangular tube arrangements.

A uniform distribution of the coolant flow in the main shell section of the condenser is also promoted by a uniform distribution of the flow through the circumferential gaps between the shell and the tubesheets (see Figure 14). As the pressure drop across each gap increases relative to the other pressure drops in the coolant flow path, the flow through the gap becomes more uniform in the circumferential direction.

The equilateral triangular tube arrangement is illustrated in Figure 24. There are two parameters which are convenient for describing the relative spacing of these tubes. These are the pitch-to-diameter ratio P/D and the blockage B. The blockage is the fraction of the total shell frontal area that is blocked to shell side flow, or $1.0 - \frac{\text{free flow area}}{\text{total frontal area}}$. The pitch-to-diameter ratio is related to the blockage through the equation

$$B = \frac{\pi}{2\sqrt{3}\left(\frac{P}{D}\right)^2}$$

which can be derived from geometrical considerations. Thus as the tubes are spaced closer together P/D decreases while B increases.

1) Lithium-Cooled Configuration - Both lithium and NaK-cooled configurations were considered for the constant-diameter condenser. The lithium-cooled configuration is shown in Figure 19. The effect of the following parameters on core weight, shell volume and tube length was considered in sizing this condenser:

1) Number of tubes
2) Inlet Mach number of the potassium vapor
3) Blockage

The condenser core weight is calculated as the sum of the weights of the tubes, the tubesheets, the shell, and the potassium and lithium inventories. It does not contain the weight of the manifolds nor fluid inventories within the manifolds. The shell volume is calculated as the cylindrical volume enclosed within the shell and the tubesheets.

Although the potassium enters the tubes as a two-phase mixture of vapor and liquid, the inlet Mach number used in the parametric study was calculated on the basis of the vapor flow alone. While a Mach number calculated in this manner is not a rigorously defined physical quantity, it does serve as a useful measure of the mass velocity of the vapor. For high quality two-phase flows this Mach number also gives an indication of the magnitude of compressibility effects that might be expected in the actual two-phase flow. This is particularly important since there is, at present, no adequate theory describing two-phase compressible flow effects. The equations used in the condenser analysis are not adequate for describing two-phase compressible flow effects. A maximum inlet Mach number of 0.5 was chosen for the parametric study since compressible effects become significant for single-phase vapor flow near this Mach number.

The effects of varying the number of tubes and the inlet Mach number of the potassium vapor were studied for a blockage of 0.5. The results are illustrated in Figures 25, 26, and 27. As can be seen from these figures, core weight and shell volume decrease as both the number of tubes and the inlet Mach number increase. Thus, weight and volume are lowest at the upper limit of inlet Mach number and largest number of tubes considered in this study. However, while weight and volume decrease as the number of tubes increases, the number of tubes that can be employed is limited by reliability and fabrication considerations. As the number of tubes increases, the number of tube-to-tubesheet joints increases accordingly. This increases the possibility of leakage, thus reducing the reliability. In addition, as the number of tubes increases at a given inlet Mach number, the tube diameters must decrease to maintain a constant potassium flow area. At present, tubes with outside diameters less then 3/16 inch cannot be used due to difficulties in fabricating the tube-to-tubesheet joints. This places an upper limit on the number of tubes that can be used for a given inlet Mach number. The following design conditions were chosen as a compromise between size, weight, reliability and ease of fabrication:

number of tubes	91
tube outside diameter	0.375 inch
tube wall thickness	0.020 inch
inlet Mach number	0.46

A reasonable degree of reliability can be obtained with ninety-one tubes and tube-to-tubesheet joints can be fabricated without difficulty for tubes of 3/8 inch outside diameter. In addition, the inlet Mach number of 0.46 is sufficiently high to provide low weight and volume without exceeding the limit of 0.5.

Since the parametric study described above was performed for a blockage value of 0.5, the effect of blockage on the selected ninety-one tube condenser was investigated. The results of this investigation are illustrated in Figures 28, 29 and 30, where core weight, shell volume and tube length are all shown to decrease with increasing blockage, making high blockages desirable. However, it was found that a blockage of 0.5

represents an upper limit for practical condenser design. At values of B greater than 0.5 the tube spacing P-D (see Figure 23), becomes so tight that it is difficult to fabricate the individual tube-to-tubesheet joints without interfering with the neighboring joints. In addition, the validity of the relations for predicting the heat transfer coefficient of the shell fluid becomes questionable for values of B greater than 0.5.

In designing shell-and-tube heat exchangers it is desirable to distribute the fluid to each tube as uniformly as possible in order to keep the heat exchanger performance as high as possible. Since the flow rate in each tube is strongly dependent upon the heat transfer rates along each tube, it is desirable to keep the heat transfer rates from each tube as uniform as possible at any axial position. Since the radial cross-flow between the tubesheets and their adjacent orifice plates represents an area where there are nonuniform heat transfer rates from each tube, it is desirable to keep the length of tube exposed to this radial cross-flow to a minimum. This is particularly important at the potassium inlet end of the tube where the condensing film is just developing. However, as the distance between a tubesheet and the adjacent orifice plate is decreased, the pressure loss resulting from this radial cross-flow increases.

In calculating the pressure loss for the shell fluid, it was found that the 1.2 psi pressure drop requirement for the coolant would be exceeded at a blockage of 0.5 unless the distances between the tubesheets and their adjacent orifice plates were made unacceptably large. This was due to the magnitude of the radial pressure loss. In order to obtain a design where the radial pressure loss and the distances between the tubesheets and their adjacent orifice plates were reasonable it was necessary to decrease the blockage, thus taking a weight and volume penalty. It was felt that a maximum distance of 3/4 inch between the tubesheets and their adjacent orifice plates could be tolerated. This necessitated a blockage of 0.354 and a relatively wide circumferential gap width of 1/2 inch in order to meet the 1.2 psi pressure drop requirement for the coolant.

The final design conditions for the constant-diameter lithium-cooled condenser are summarized in Table 3. Figures 31a and 31b show variations of heat transfer coefficients, fluid temperatures and quality with length, for this final design configuration.

The temperature level of the coolant in the condensers is an important consideration in optimization studies of Rankine-cycle space powerplants. For this reason a study was performed to determine how the size and weight of a typical constant-diameter shell-and-tube condenser would change as the coolant temperature level was changed from the original design conditions. For this study the potassium state and the lithium temperature rise were the same as specified in the design conditions, while the lithium outlet temperature was varied from 1130°F to 1165°F. The results are illustrated in Figures 32a and 32b where shell volume and core weight are plotted against lithium outlet temperature. The shell volume and core weight are relatively insensitive to the lithium temperature level until the lithium outlet temperature approaches the potassium inlet temperature. This is caused by the unusual fluid temperature distributions found in this type of condenser. Typical temperature distributions for this study are plotted in Figure 33. In this figure the potassium temperature changes very little along the length of the condensing section. It rises slightly in the direction of potassium flow due to the effect of static pressure on the saturation temperature. In the subcooling section, however, the potassium temperature decreases at a very rapid rate over a short distance. The reverse is true of the lithium temperature distribution. In the subcooling section the lithium temperature rises only slightly in the direction of lithium flow while it rises significantly in the condensing section. These fluid temperature distributions give rise to the axial distribution of the temperature driving potential ΔT shown in Figure 34. In the condensing section ΔT rises steadily with distance in the direction of the potassium flow, while in the subcooling section it falls rapidly with distance. In Figure 34 ΔT is much less at the potassium inlet end of the condenser than it is over the greater portion of the condenser. Therefore as the lithium temperature level is increased, ΔT decreases by a much lower percentage over the greater portion of the condenser than it does at the potassium inlet end. As a result it is only when the temperature difference at the potassium inlet end becomes very small that condenser size must increase greatly in order to transfer the required heat load.

2) NaK-Cooled Configuration - The NaK-cooled constant-diameter condenser design is illustrated in Figure 20. It is similar in construction to the lithium-cooled design. Both configurations employ ninety-one tubes of 3/8 inch outside diameter arranged in a hexagonal pattern, expansion joint manifolds, orifice plates to maintain uniform axial flow in the shell, and small diameter orifices in the tube exits. The primary difference between these two designs is in their dimensions. The NaK-cooled design has a longer tube length, a larger shell diameter, and a lower blockage than the lithium-cooled design. The construction using ninety-one tubes of 3/8 inch outside diameter was selected for the NaK-cooled configuration on the basis of the same considerations employed in the case of the lithium-cooled configuration. Since the number of tubes and inlet Mach number should affect the size and weight of an NaK-cooled condenser in the same manner as they do the lithium-cooled condenser, it was not necessary to perform a second parametric study in order to arrive at this selection.

The larger size of the NaK-cooled design results primarily from the fact that the physical properties of NaK cause it to be a poorer coolant than lithium. Table 4 compares the physical properties of NaK and lithium and lists the properties of potassium used. The thermal conductivity of NaK is considerably less than that of lithium. Since the heat transfer coefficient of the liquids is strongly dependent upon thermal conductivity, the heat transfer coefficient on the shell side is less for the NaK-cooled case than for the lithium-cooled case at a given blockage. This reduces the overall heat transfer coefficients along the length of the condenser and thus more tube area is required for the NaK-cooled case to transfer the same quantity of heat. This is reflected in a longer length for the NaK-cooled condenser as illustrated in Figure 30. In addition, Table 4 shows that the specific heat of NaK is much less than that of lithium. Therefore, a much greater flow rate is needed for a given coolant temperature rise. Table 2 shows that the flow rate required for the NaK case is approximately four times that of the lithium case. This higher flow rate requires a lower blockage to maintain the shell fluid pressure drop within 1.2 psi. Figures 28, 29 and 30, show that shell volume, core weight, and length increase as blockage decreases.

Because of this higher flow rate the shell fluid pressure loss was the principle consideration in sizing the NaK-cooled constant diameter condenser. The problem was to size the various components of the shell fluid flow path so that the pressure loss would not exceed the required 1.2 psi while condenser weight and volume was kept to a minimum. Therefore, the effects of the various parameters controlling the individual shell fluid (NaK) pressure drops were studied to arrive at a suitable compromise.

In performing this study the following basic tenets were adhered to:

1) Only one inlet and one outlet pipe for the shell fluid was to be used

2) The inside diameters of the inlet and outlet pipes for the shell fluid were equal

3) The distance between an orifice plate and its adjacent tubesheet was 3/4 inch

4) The pressure loss across the orifice plate at a given end was ten times the radial pressure loss at the end

5) The widths of the circumferential gaps between the shell and the tubesheets were equal at both inlet and exit manifolds

The results of this parametric study are shown in Figures 35 and 36. In Figure 35 radial pressure loss decreases with decreasing blockage. Figure 36 shows the diameter of the inlet and outlet pipes that is required to meet the 1.2 psi coolant pressure loss for a given blockage and circumferential gap width. Since the diameter of the inlet and outlet pipes influences the size and structural integrity of the expansion joint manifolds, it was desirable to keep them as small as possible. However, as can be seen in Figure 36, a reduction in the pipe diameter for a given gap width requires a blockage decrease, which in turn results in an increase in core weight and shell volume (see Figures 28 and 29). A 2.0-inch pipe diameter was chosen as a compromise between practical design considerations and condenser core weight and shell volume.

The width of the gap between the shell and the tubesheet controls the pressure drop of the flow between the manifolds and the shell. As this gap width decreases, the pressure loss increases. As the pressure loss increases relative to other pressure losses in the system, the flow through the gap becomes more uniform in the circumferential direction. However, as shown in Figure 36, as the gap width decreases for a given pipe diameter, the blockage must also decrease with a resultant increase in condenser weight and volume. A gap width of 0.30 inch and a pipe diameter of 2.0 inches with a resultant blockage of 0.227 were selected as a compromise between flow distribution and core weight.

The final design conditions for the constant-diameter lithium-cooled condenser are summarized in Table 3.

3) Lithium-Cooled Annular-Shell Bent-Tube Configuration - In order to relieve the stresses that develop from differentials in the thermal expansion of individual tubes, many shell-and-tube heat exchangers are built so that individual tubes can flex independently of the others. This has been accomplished in a number of different ways. Some heat exchangers employ long thin tubes which bow under the action of thermal stresses. Others use tubes bent into a U shape which are free to grow in the axial direction. For liquid metal heat exchangers many designers have found it expedient to bend the tubes approximately 45 degrees instead of into a complete U. Such a bend still provides sufficient flexibility to relieve the stresses.

In designing liquid metal condensers for this study it was found that the calculated tube lengths were too short to employ any of the above-mentioned conventional methods of allowing the tubes to flex. However, a flexible tube construction was found possible in an annular-shell arrangement, with tubes that were so bent as to be perpendicular to the radial direction. Such a condenser is illustrated in Figure 21 where the tube bundle is seen to be enclosed in an annular passage between two concentric shells. The tubes are of equal length and are equally spaced along three concentric circles. The tubes are bent in the middle to permit flexibility. They are also bent to conform with the same circle when viewed in the axial direction as shown in Section BB of Figure 21.

Like the other condensers in this study, the annular-shell bent-tube configuration employs a counterflow arrangement. However, the flow patterns for this configuration (Figure 21) differ from those described for the more conventional constant-diameter configurations. Also, the potassium vapor enters through an inlet pipe and is distributed uniformly in the radial direction by a flow divider. The potassium then enters the tubes where it is condensed. At the tube exits the condensed potassium is collected by a toroidal type manifold and leaves through an outlet pipe. The lithium enters from an inlet pipe and is distributed uniformly in the radial direction by the lithium flow divider. The lithium enters the annular shell area through the gap between the inner shell and the tubesheet. The lithium then flows axially through the tube bundle and leaves the annulus through the gap between the outer shell and the opposite tubesheet. The lithium is then collected in the same type of toroidal manifold employed by the other shell-and-tube configurations and leaves through an outlet pipe. Flexible manifolds are shown in Figure 21 although they are not required to relieve stresses due to differential thermal expansion between the tubes and the shell. Since the sum of the total radial pressure loss is approximately equal for all fluid paths through the annular shell, orifice plates are not needed to insure uniform axial flow. Because this type of bent-tube arrangement is not commonly used, there are no methods presently available for predicting the heat transfer coefficients on the shell side of this configuration. The method of Dwyer, derived for axial flow through a bundle of straight tubes, was therefore used in order to obtain an estimate. It was thus possible to apply the results presented in Figure 30 for the lithium-cooled constant-diameter configuration to the annular-shell bent-tube configuration.

In designing this configuration, consideration was given to size, weight, and reliability, as well as to the factors involved in fabricating a bent flexible tube. A ninety-one tube bundle of tubes 3/8 inch in outside diameter was selected on the basis of the size, weight, and reliability considerations discussed above for the lithium-cooled constant-diameter configuration. In order to obtain a tube sufficiently long to be bent without difficulty it was necessary to decrease the blockage, thus

sacrificing size and weight. A ten-inch tube length with a resulting blockage of 0.165 was selected for the design. Because of this low blockage and the absence of orifice plates, shell-side pressure losses were very low and parametric studies were not required to keep the shell-side pressure loss within the 1.2 psi limit. The final design conditions for the annular-shell bent-tube condenser are summarized in Table 3.

b. Tapered Configurations

The tapered configuration may offer some advantages over the constant-diameter configuration. Since the cross-sectional area of the tubes decreases with length, the tapered tubes maintain a higher average vapor velocity than can be obtained with a constant-diameter tube. This results in a higher average heat transfer coefficient for the condensing flow. In addition, there is some evidence that condensing flow is more stable inside tapered tubes, as observed for the case of mercury[67]. However, subsequent experiments performed with condensing water as a part of this study and reported in Reference 66, showed no apparent increase in stability for condensing flow inside tapered tubes.

While there may be some advantages to tapered designs, they are also more difficult to manufacture. This arises from the basic tapered construction of the shell and the tubes, and from the problems of aligning the tubes during the assembly of the condenser.

The tapered shell-and-tube condenser configuration designed in this study is illustrated in Figure 22. It is similar in construction to the constant-diameter configurations except that the cross-sectional dimensions decrease with length in the direction of the potassium flow. Both configurations employ the following basic features:

1) The tube bundle is arranged in a hexagonal pattern using an equilateral triangular pitch.

2) A hexagonal liner is used to direct the shell fluid through the tube bundle.

3) The shell is attached to the tubesheets through toroidal expansion joint manifolds.

4) Orifice plates are used to maintain uniform axial flow through the shell.

As a result, the flow pattern for the tapered configuration is similar to that described above for the constant-diameter configurations.

The tapered condensers considered in this study were designed so that cross-sectional dimensions would vary linearly with length. This was accomplished by tapering the tubes and shell according to the following relations

$$D_{i\ tube} = D_{i\ tube_o} \ (1 - \gamma_t \ell) \tag{43}$$

$$D_{i\ shell} = D_{i\ shell_o} \ (1 - \gamma_s \ell) \tag{44}$$

where ℓ = axial distance measured from the potassium inlet of the tube

$D_{i\ tube_o}$ = initial inside diameter of the tube

$D_{i\ shell_o}$ = initial inside diameter of the shell

γ_t = tube taper

γ_s = shell taper

Since the tube diameter and the shell diameter can have different tapers, the blockage is not necessarily constant with length, but varies in a manner dependent upon both the tube and shell tapers.

In order to provide sufficient spacing, P-D, between the outside of the tubes so that individual tube-to-tubesheet joints could be fabricated without difficulty, the following basic rules were followed:

1) Maximum allowable blockage was 0.5

2) Tube spacing P-D was constant with length

The first rule is the same as that applied to the constant-diameter configuration.

The second rule insures adequate spacing to facilitate welding at the potassium outlet end of the condenser when the blockage is high at the potassium inlet end.

In order to meet the requirement that P-D remain constant with length, γ_t and γ_s must be related through the equation

$$\gamma_s = \frac{\sqrt{\frac{2\sqrt{3}}{\pi} \; Bo}}{\left(1 + \frac{2t_w}{Di\ tube_o}\right)} \gamma_t \tag{45}$$

where

Bo = initial blockage

t_w = tube wall thickness

This equation can be derived from geometrical considerations assuming that the tube wall thickness remains constant with length.

In view of the criteria set forth in the above paragraphs, the geometrical variables for a tapered configuration are the number of tubes, the tube inside diameter at the inlet, the tube wall thickness, the tube taper, the initial blockage, and the tube length. Some of these variables are interrelated and in turn define other interesting dimensions. The following paragraphs describe limitations selected for these variables in order to limit the scope of this study.

Knowledge of the desired range for the tube diameter at the exit and the tube taper can help define the range of the number of tubes. The inside diameter at the tube exit should not be greater than approximately 0.30 inch in order to provide any possible advantage of flow stability. Also, this dimension should not be smaller than approximately 0.180 inch due to welding considerations.

The tube taper should be high enough to provide a substantial difference between a tapered and a constant-diameter configuration. However, the tube taper should not be so high as to either cause tube manufacturing difficulties or cause excessively high mass velocities in two-phase flow.

With the considerations mentioned above for the limits on tube exit diameter and tube taper, limits for the number of tubes can be determined. In order to keep a hexagonal tube pattern, the number of tubes must be 1, 7, 16, 37, 61, 91, etc. The constant-

diameter lithium-cooled design configuration contains 91 tubes, 0.335 inch in inside diameter. It is apparent that use of 91 or more tapered tubes would mean that the tube diameter at the exit would be unreasonably small if the tube taper were high enough to make this type configuration different from the constant-diameter configuration. Even 61 tubes would not provide an adequate difference. On the other hand 16 or less tubes would mean that excessive two-phase mass velocities would occur if a reasonably low tube diameter were provided at the exit. Thus use of 37 tubes provides a reasonable compromise.

The potassium Mach number at the inlet is defined once the number of tubes and the inside diameter at the tube inlet are selected. The maximum Mach number of 0.5 was selected for the constant-diameter configurations in order to avoid compressibility effects due to high mass velocities. For a constant-diameter configuration the maximum ratio of local mass velocity to critical mass velocity occurs at the tube inlet. However, for a tapered configuration with sufficiently high tube tapers an inlet Mach number of 0.5 would probably cause the two-phase flow mass velocity to reach the critical mass velocity at some location further downstream of the entrance. Therefore, the maximum inlet Mach number to be studied for the tapered configurations was arbitrarily selected as 0.30. With 37 tubes this Mach number results in a tube diameter at the inlet of 0.72 inch, which appears to be a reasonable dimension.

A tube wall thickness of 0.020 inch was used for the constant-diameter configuration since the tubes would only be 0.335 inch in inside diameter. However, the tapered tubes would be over twice this diameter at the entrance. Therefore, a tapered tube wall thickness of 0.035 inch was selected for this study.

A high blockage is desirable to provide high heat transfer coefficients for the shell fluid. However, the shell fluid pressure loss increases as the blockage increases. In designing the condenser the highest blockage that can be obtained without exceeding the shell fluid pressure loss limits should be used.

1) Lithium-Cooled Configuration - A design study was conducted for the lithium-cooled configuration based on the limits discussed in the previous paragraphs. Table 5 lists the results of this study. The first case studied was for a geometry of 37 tubes, inside diameter of tubes at the inlet 0.68 inch, initial blockage 0.500, tube taper 0.500, and tube wall thickness 0.035 inch. The potassium exit temperature of 1053°F, which

was set as the criterion for the lithium-cooled constant-diameter configurations, provided a subcooling length of only 0.59 inch. Such a short subcooling length could result in uncondensed vapor entering the exit manifold if inadvertent changes in flow rates or inventory occur. In designing a condenser with constant cross-section a minimum length can be calculated for a design and added length provided upon fabrication with no serious consequences. This is due to the fact that manifolds and welding dimensions would be unchanged. However, for tapered configurations there is no design freedom for adding length. Therefore, sufficient subcooling length is needed before designing a tapered configuration.

It was apparent in this study that the only way to establish a sufficient subcooling length and yet maintain the desired criteria was to lower the potassium outlet temperature requirements. The tapered geometry for the first cases studied was used to determine a potassium exit temperature to obtain a reasonable subcooling length. The results of this study are shown in Figure 37, and Cases 1-7 of Table 5. Case 7 gave a reasonably long subcooling length of 3.39 inches as well as a reasonable inside diameter at the tube exit and pressure losses for a potassium outlet temperature of 996°F. Additional cases were run at this potassium outlet temperature with variations of inside diameter at the tube inlet and tube taper (see Cases 8-15, Table 5). Of the nine cases (7-15) run for this study, Cases 7, 9, 11, 12, and 14 were within the desired criteria range. The differences between these five cases were slight and therefore Case 7 was arbitrarily selected for a design layout.

Since the tapered lithium-cooled condenser configuration employed fewer tubes than the constant-diameter configuration, radial pressure losses were much less severe. It was therefore possible to keep the total shell-side pressure loss within the required 1.2 psi using the maximum initial blockage of 0.5. Consequently, the effects of lower initial blockage on condenser size and weight were not investigated for the tapered lithium-cooled condenser. The tapered lithium-cooled condenser configuration is shown in Figure 22. The final design numbers are listed in Table 3. Figures 38 and 39 show variations of heat transfer coefficient, fluid temperature and quality with length, for this final design configuration.

In addition to meeting the specified requirements, this design

was checked to determine whether two-phase flow choking would occur under the design conditions. Using the methods outlined in Section III. F. it was found that the local mass velocities were below the local critical mass velocity at all points in the condenser. These results are illustrated in Figure 40.

2) NaK-Cooled Configuration - A study was conducted for the NaK-cooled configuration using 37 tubes and a tube wall thickness of 0.035 inch. The results of this study are presented in Table 6. In the first three cases which involved an inside diameter at the tube inlet of 0.72 inch, a tube taper of 0.350 and a potassium outlet temperature of 960°F, initial blockage was varied as in the case of the NaK-cooled constant-diameter case. The subcooling length increased as the blockage decreased. Also the inside diameter at the tube exit decreased towards a more desirable value. In Cases 4 through 8, tube taper and inlet Mach number were varied at an initial blockage of 0.437 and a potassium outlet temperature of 960°F. Of these cases, Nos. 5 and 8 were the best since the exit diameters were near the desired size and the subcooling lengths were the longest. Cases 9-14 were similar to Cases 3-8 except that the potassium outlet temperature was set at 950°F. For this latter set of cases, the subcooling length showed an increase. Of the fourteen cases tabulated, No. 11 gave the most desirable results. This case was selected to be listed in Table 3 as the final design. Since the tapered NaK-cooled configuration would employ the same basic construction features as the tapered lithium-cooled configuration, a design drawing was not made.

This design was also checked to determine whether two-phase choking would occur under the design conditions. The results are illustrated in Figure 41, where the local mass velocities are seen to be well below the local critical mass velocity at all points in the condenser.

2. Series and Segmented-Shell Arrangements

Since the series and segmented-shell arrangements are similar thermodynamically and differ primarily in physical construction, only the segmented-shell arrangement was analyzed. The design conditions are shown in Table 2. Each segment is designed to remove an equal amount of heat from the potassium. As a result, the coolant

weight flow for any segment is equal to that for a single condenser in the parallel arrangement, while the potassium weight flow is four times that for a single condenser in the parallel arrangement. Consequently the segmented condenser requires many more tubes and a larger shell diameter than condensers in the parallel arrangement.

In order to estimate the size of the segmented-shell condenser, an analysis was performed on a segment using the log-mean-temperature-difference method described in Section III.B. The analysis was based on the NaK-cooled conditions. The temperature of the condensing potassium was assumed to remain constant at 1175°F and the condensing heat transfer coefficient was assumed to be 5000 Btu/hr ft^2°F. The NaK heat transfer coefficient was calculated using the method of Dwyer described in Section III.C. Orifice plates were used to maintain uniform axial flow through the shell. The tubes were spaced so that the radial pressure drop would be one-tenth of the pressure drop across the orifice plate.

The analysis was performed for a configuration employing tubes of 3/8 inch outside diameter with 0.020-inch walls. The results are tabulated below for inlet Mach numbers of 0.20 and 0.40.

Inlet Mach No.	No. of Tubes	Blockage	Shell Diameter	Tube Length
0.20	721	0.325	20.00 inches	1.25 inches
0.40	397	0.382	13.29	2.04

The shell has a relatively large diameter while the tube length for a segment is very short. It would be virtually impossible to design a condenser segment with these dimensions and yet maintain uniform axial flow in the shell. The only alternative would be to cool the tubes using cross flow in the shell. However, due to pressure loss and heat transfer considerations a cross-flow arrangement would result in a much larger heat exchanger. For these reasons, it was felt that a condenser employing a segmented-shell arrangement was not practical for the design conditions of this study. In addition, since the results of the above analysis could be applied directly to the series arrangement, it was also felt that the series arrangement was impractical.

C. Concentric-Tube Condenser

During the course of the condenser design study it was desired to investigate some type of condenser employing a swirl device in the condensing flow to remove liquid from the heat transfer surface, thus thinning the film and increasing the condensing heat transfer coefficient. Since swirl devices throw the liquid radially outward, the most practical arrangement was to condense the potassium inside an annular flow passage where heat would be removed at the inner wall. Such an arrangement is readily obtained with two concentric tubes to form the annular passage. Swirl flow can be induced by placing a helical ribbon between the tubes. Thus heat can be removed at the inner wall by passing a coolant through the central tube.

In studying this condenser concept, only the lithium-cooled situation with a parallel condenser arrangement was considered. The series arrangement was not considered due to the difficulties in manifolding two-phase flow for this type of condenser. The condenser design which evolved from this investigation is illustrated in Figure 42. It consists of a bundle of concentric tubes with manifolding arrangements to direct the lithium through the central tubes and the potassium through the annular passages between the outer tubes and the central tubes. Separate tubesheets are provided at each end for the outer tubes and the central tubes. The tubesheets at each end are separated to permit the potassium to flow between them and are connected to each other through the potassium manifold. The potassium manifolds are sufficiently flexible to relieve the stresses caused by the differential in thermal expansion of the central and outer tubes.

Due to higher frictional pressure losses assumed for the swirl flow, a pressure drop instead of a pressure rise was taken by the condensing flow through the annular passages. As a result, uniform distribution of the potassium to all annular passages could be obtained without using orifices at their exits. Since no orifices were used, the potassium outlet pipe was sized sufficiently small to restrict the vapor flow rate, in the event that the heat rejection loop of the condenser failed.

Figure 42 shows that the flow patterns for the concentric-tube condenser are considerably different from those of the shell-and-tube configurations. The potassium enters a large toroidal-shaped manifold from the potassium inlet pipe. This manifold distributes the

potassium flow uniformly around the circumference of the gap between the tubesheet for the central tubes and the tubesheet for the outer tubes. The potassium then flows radially inward between these two tubesheets and enters the annular passages between the concentric tube sets. The potassium flows through these annular passages where it is condensed and subcooled. Swirl flow is maintained in the annular passages by the use of helical ribbons. The subcooled potassium leaves the annular passages and flows radially outward between the two tubesheets at the potassium outlet end of the condenser. The potassium is then collected by a toroidal-shaped manifold and leaves through the potassium exit pipe.

The lithium enters a header from the lithium inlet pipe and is distributed radially by the lithium flow divider. From the header the lithium enters the central tubes where it cools the condensing potassium. The lithium is then collected in a second header and leaves through the lithium exit pipe.

At present there is very little knowledge of the effect of swirlers on heat transfer and fluid friction for condensing flow. As a result it is not possible to accurately predict local values of the condensing heat transfer coefficient, the static pressure, and the temperature for the potassium flow through the annular passages. It was therefore necessary to make a number of approximations and use the less rigorous log-mean-temperature-difference method to analyze the concentric-tube condenser. Since the heat transfer process is different for condensing flow and single-phase flow, it was necessary to divide the condenser into a condensing section and a subcooling section which were analyzed individually by the log-mean-temperature-difference method.

In analyzing the condensing section the potassium temperature was assumed to remain constant with length. Equation (10) with $\alpha = 1.0$ was used to predict the lithium heat transfer coefficient, while the methods dicussed in Section III.E. were used to predict the frictional pressure loss for the lithium. The potassium pressure loss was analyzed using the method outlined in Appendix H. However, the frictional term in Equation (H1) was arbitrarily multiplied by a factor of three in an effort to account for the higher frictional pressure loss arising from the swirl flow. No attempt was made to predict the condensing

heat transfer coefficient or to relate it to the frictional pressure loss of the potassium. Instead, values were assumed for an average condensing heat transfer coefficient h_{cond}, and the effect of varying h_{cond} was investigated as part of the parametric study.

In analyzing the subcooling sections, Equation (10) with $\alpha = 1.0$ was used to predict the lithium heat transfer coefficients, while a Nusselt number of 8.23 derived for laminar flow through parallel plates with uniform heat flux at the wall was used to predict the heat transfer coefficients for the potassium. The methods discussed in Section III.E. were used to predict the frictional pressure losses for both fluids. No attempt was made to account for the effects of swirl flow on heat transfer and fluid friction for the potassium flow through the subcooling section.

For the condenser as a whole the lithium pressure drop was calculated as the sum of the tube entrance loss, the condensing section frictional loss, the subcooling section frictional loss, and the tube exit loss. The condenser was designed for a lithium pressure loss of 1.2 psi. The potassium pressure drop was calculated as the sum of the various pressure drops from the potassium inlet pipe and to the potassium pipe. A design value of 0.540 psi was selected. In order to maintain a uniform distribution of potassium it was necessary to design the condenser so that the pressure drop across the annular passages was greater than any other pressure drops in the potassium flow path. The pressure drop across the annular passages, including the inlet and outlet pressure drops, was therefore set equal to 0.440 psi.

In order to size the condenser, a parametric study was performed to investigate the effect of varying the number of concentric tube sets and the condensing heat transfer coefficient on condenser size and weight. The results are illustrated in Figures 43 and 44. In Figures 43 and 44 the inside diameters of the central and outer tubes decrease as the number of concentric tube sets increases, and are relatively insensitive to the value assumed for the condensing heat transfer coefficient. Figures 45 and 46 show that while weight and length also decrease as the number of concentric tube sets increases, they are strongly dependent upon the value assumed for the condensing heat transfer coefficient. As a result, a condensing heat transfer coefficient of 10,000 Btu/hr ft^2°R was assumed since it was felt to be representative of values that could be obtained with swirl flow.

In sizing the condenser a large number of concentric tube sets is desirable to keep size and weight to a minimum. However, as the number of concentric tube sets increases, the number of tube-to-tubesheet joints must also increase, thus reducing the reliability. A configuration employing nineteen concentric tube sets was selected as a compromise between weight, size, and reliability considerations. The other components of the potassium flow path were sized to keep the potassium pressure drop within the specified 0.540 psi. As a result it was necessary to employ a large potassium inlet pipe, a large potassium inlet manifold, and a wide space between the tubesheets at the potassium inlet end, in order to keep the pressure drop of the incoming potassium vapor to a minimum. The final design conditions for the concentric-tube condenser are summarized in Table 3.

D. Comparison of Condenser Configurations

Four different types of condenser design were investigated by means of a design study:

1) Constant-diameter shell-and-tube configuration with condensing inside of the tubes,

2) Tapered shell-and-tube configuration with condensing inside of the tubes,

3) Annular-shell bent-tube configuration with condensing inside of the tubes, and

4) Concentric-tube configurations with condensing in the annular passages.

All four types were investigated with lithium as the coolant while only the first two types were investigated with NaK as the coolant. All designs considered the condensers operating in parallel, since series operation was found to be unfeasible.

The following tables show a relative rating of these different designs with respect to various considerations based on the results of the design study of each configuration. In these tables a lower number signifies better rating.

Lithium-Cooled Configurations

Design	Weight	Volume	Relative Accuracy of Design	Relative Reliability	Ease of Mani-folding	Ease of Fabri-cation
constant-diameter	2	2	1	2	1	1
tapered	1	1	2	1	1	2
annular-shell, bent-tube	4	3	3	3	2	4
concentric-tube	3	4	4	4	4	4
NaK-Cooled Configurations						
constant-diameter	2	2	1	2	1	1
tapered	1	1	2	1	1	2

The important design values including total volumes and weights are listed in Table 3 for each of these configurations. The lengths obtained for these designs except the two tapered designs were minimum lengths to achieve the specified thermal design conditions. However, in these designs with minimal lengths, condensing ends fairly close to the exit manifolds and in the event of inadvertent changes in flow rate or inventory, the potassium might not be fully condensed at the tube ends. Therefore, the tube lengths should be increased to allow for a safety factor. An increased length would not affect differential expansion between the shell and the tube since the tube and shell temperatures would be very close over the added length. Special consideration was given to the tapered configurations by decreasing the potassium exit temperature requirements to increase subcooling length. This was done since minimal length designs could not be changed later without major changes in the design of manifolds. However, the tables above account for this change of thermal design conditions.

E. Design Conclusions

In comparing the different condenser configurations, a number of conclusions can be reached:

1) The parallel flow arrangement is the only practical arrangement of the three considered. The condensers for the series and segmented-shell arrangements are too short to design without extreme difficulties.

2) There is apparently no advantage in using either the annular-shell bent-tube configuration or the concentric tube configuration. Both configurations are much heavier, occupy more volume, and are much harder to manifold and fabricate than either tapered or constant-diameter shell-and-tube lithium-cooled configurations. In addition, stress calculations showed that it is not necessary to employ bent tubes in order to relieve thermal stresses for the design conditions of this study.

3) The tapered designs show advantages over the constant-diameter design due to weight, size, and reliability. However, the weight and size advantages are not very great. The possible advantage of increased stability in condensing flow with tapered tubes is somewhat doubtful. The main advantage of a tapered design is therefore that of increased reliability resulting from fewer tube welds. However, the more difficult fabrication procedure needed for the tapered case probably offset all of the possible advantages. The manufacture of tapered tubes, tapered shell, and the difficult aligning of the tubes in the tubesheet (note in Figure 22 that the tubes must be canted at the ends in order to have the tubes perpendicular to the tubesheets) are some of the difficult fabrication problems for the tapered design.

4) The NaK-cooled shell-and-tube configurations are heavier and occupy a larger volume than the corresponding lithium-cooled shell-and-tube configurations. This is due to the poorer thermodynamic and heat transfer properties of NaK.

5) On the basis of the factors stated above, the constant-diameter shell-and-tube condensers operating in parallel are considered to be the most desirable designs for both NaK-cooled and lithium-cooled operations.

V. DIGITAL COMPUTER CONDENSER DESIGN PROGRAM

A. Introduction

The condenser design procedures recommended in Section III were programmed for a high speed digital computer (IBM 7090)*. The primary purpose of the program was to calculate condenser tube lengths, pressure drops, and temperature profiles for shell-and-tube condensers having liquid metals for both coolant and condensing fluid. The program was made to assist in sizing condensers for a specific set of design conditions and was not written to obtain the effects of operating a known condenser at off-design conditions. The program can only handle cases in which condensation takes place inside the tubes with a single-pass counterflow coolant arrangement. Other restrictions on the program are that the tubes must be arranged in an equilateral triangular pattern and the condensing fluid cannot be superheated at the condenser entrance. However, the program is flexible enough to handle either tapered or constant-diameter tube cases in which the condensing fluid leaves the condenser as a wet mixture of liquid and vapor, as saturated liquid, or as subcooled liquid. Also the program offers the option of calculating condensing heat transfer coefficients either by the Carpenter and Colburn method or the modified film conduction method described in Section III. D. When using the second method, there is also a choice between two different criteria for transition from laminar to turbulent flow. In addition, provision is made to account for the Schrage effect described in Section III. D. Condensing heat transfer coefficients which take this effect into account can be calculated according to Equations (36) and (40). The term h_{film} in Equation (36) can be calculated either by Equation (31) or by the Carpenter and Colburn method.

The following sections describe the general logic used in the program and outline the specific calculation procedures used.

B. Program Logic

The main purpose of the program was to calculate lengths of tubes, pressure drops, and temperature profiles for shell-and-tube condensers. To accomplish this, the main physical dimensions of the

*Copies of a manual describing this computer program, Report NASA CR-54252, are on file at the NASA Office of Scientific and Technical Information, Washington 25, D. C.

condenser except for tube length must be known, as well as the overall quantity of heat to be transferred. In addition, the flow and inlet thermodynamic state of both fluids must be specified. The necessary thermal and physical properties of the fluids and structural materials also must be defined in the form of curves.

The main calculation procedure is essentially an incremental marching procedure, where the changes across one increment are evaluated to determine input values to begin calculations for the next increment, and so on. In performing the program calculations, the condenser is considered to be comprised of two distinct sections, the condensing section and the subcooling section, each having a distinct set of equations. A sketch showing the general arrangement of the condensing and subcooling sections of a condenser appears in Figure 47. The condensing section is subdivided into an integral number of increments having equal quality changes and the subcooling section is subdivided into an integral number of increments having equal condensate temperature drops.

The calculation procedure starts in the condensing fluid inlet manifold. A contraction type pressure drop is calculated for the fluid entering the tube to obtain the pressure at the tube entrance. The computer continues calculations in a stepwise fashion through both the condensing and subcooling sections of the tubes to the condensing fluid exit manifold. An expansion type pressure drop is then calculated from the tube exit to the exit manifold. The program also calculates expansion and contraction losses for the coolant at the inlet and outlet regions.

Figure 48 shows the notation used for each increment in the condenser core. At the beginning of an increment, Station I, the condensing fluid enters and the coolant leaves. At the end of an increment, Station II, the coolant enters and the condensing fluid leaves.

The length of an increment is first calculated and then the pressure drop and inventory of that increment are determined. Calculation of incremental length is dependent upon values of fluid temperature, fluid properties, heat transfer coefficient, and tube dimensions along the increment. The temperatures at the inlet and exit of each subcooling section increment are easily evaluated since the increments are divided in equal condensate temperature drops, and coolant

temperature can be evaluated from a heat balance. The fluid properties are evaluated as a function of temperature from input curves. In calculation of local quantities such as heat transfer coefficient, local property values were used. In calculations of overall increment quantities, such as coolant temperature change, average property values were used. For condensing section increments the problem is more complex since temperature and pressure of the condensing fluid are mutually dependent. The present program avoids this problem mathematically by assuming condensing fluid pressure and temperature to be constant across each increment. The deviations caused by this assumption are small if the number of increments chosen is sufficiently large. The program calculates heat transfer coefficients only at the two end points of an increment, and uses averaging techniques which are discussed in detail later, to determine increment length. The tube and shell diameters used in the calculation procedure for a constant-diameter condenser are input items. However, these diameters vary with length for a tapered condenser. Therefore, both the shell and tube diameters at the inlet of the first increment and the rate of taper are input values for a tapered condenser, but tube length and tube exit diameter are not. Since the tube and shell diameters at the exit of the first increment and the length of the first increment are mutually dependent, the program undergoes an iterative procedure to determine these dimensions. The tube and shell diameters at the exit of the first increment are used as the tube and shell diameters at the inlet of the next increment. This iteration procedure continues for all increments. Since an iterative procedure is required for tapered condensers and not for constant-diameter condensers, two separate logical paths are used in the program for these two cases. The calculation to determine pressure drop and inventory are straightforward and do not require any iteration.

The next sections describe the calculation procedure along an increment in more detail for the computer paths of both constant-diameter and tapered condensers.

1. Constant-Diameter Case

The calculation procedures for the condensing section and the subcooling section are discussed separately.

a. Condensing Section

The program calculates the length, the temperature change, and pressure drop of both the coolant and the condensing fluid as well as the condensing fluid liquid and vapor inventory, for each condensing section increment. The quality decrement Δx across each increment is equal to the difference between the condensing section inlet quality x_{in} and the condensing section exit quality x_{out} divided by the arbitrarily chosen number of condensing section increments I_{cond}

$$\Delta x = \frac{x_{in} - x_{out}}{I_{cond}}$$

When performing calculations for a condensing section increment the following items are known:

$$P_{cond_I},\ T_{cond_I},\ T_{cool_I},\ W_{cond},\ W_{cool},\ x_I,\ x_{II}$$

The sequence of calculations performed for each condensing section increment is:

Step I - Calculate the coolant temperature at the increment exit $T_{cool_{II}}$ from a heat balance across the increment, assuming that the coolant specific heat $C_{p\ cool}$ and latent heat of vaporization of the condensing fluid λ are constant within the increment.

$$Q_{cond} = Q_{cool}$$

which can be expressed as

$$W_{cond}\ \lambda\ \Delta x = W_{cool}\ C_{p_{cool}}\ (T_{cool_I} - T_{cool_{II}})$$

or

$$T_{cool_{II}} = T_{cool_I} - \frac{W_{cond}\ \lambda\ \Delta x}{W_{cool}\ C_{p_{cool}}}$$

Step II - Calculate a local condensing heat transfer coefficient h_{cond}, at both the entrance and exit of the increment in accordance

with one of the methods described in Section III. D. The calculation for condensing coefficients is a complete subroutine of the program and can be replaced easily in the event a better method is found.

The condensate film thickness is a byproduct of the heat transfer coefficient calculation and is stored for the inventory calculations performed in a later step.

Step III - Evaluate a mean thermal conductivity of the tube wall k_{tw}.

Step IV - Calculate a local heat transfer coefficient of the coolant h_{cool} at both the entrance and exit of the increment using Equation (16) or (17). This calculation is a complete subroutine of the program.

Step V - Calculate a local overall heat transfer coefficient U_o at both the increment end points from the following equation

$$U_o = \frac{1}{\dfrac{D_o}{D_i\, h_{cond}} + \dfrac{D_o \ln (D_o/D_i)}{2\, k_{tw}} + \dfrac{1}{h_{cool}}}$$

Step VI - Calculate the increment heat transfer area based on tube outside diameter from the following equation

$$A = \frac{Q \ln \left(\dfrac{U_{o_I}\ \Delta T_{II}}{U_{o_{II}}\ \Delta T_I} \right)}{U_{o_I}\ \Delta T_{II} - U_{o_{II}}\ \Delta T_I}$$

where

$\Delta T_I = T_{cond_I} - T_{cool_I}$

$\Delta T_{II} = T_{cond_{II}} - T_{cool_{II}}$

Q = The heat lost by the condensing fluid across the increment

$= W_{cond}\, \lambda\, \Delta x$

This equation assumes a linear variation of U with length.

Step VII - Calculate the incremental length $\Delta \ell$ needed to satisfy the heat transfer area requirements from the following equation

$$\pi D_o N \quad \Delta \ell = A$$

where
N = number of condenser tubes

Step VIII - Calculate the condensing fluid static pressure drop and total pressure drop across the increment using the two-phase flow pressure drop equations described in Appendix H. This calculation is a complete subroutine of the program.

Step IX - Calculate the coolant total pressure loss across the increment using the methods described in Section III.E.

Step X - Calculate the condensing fluid inventory assuming that the liquid forms an annular film with a linearly varying thickness (see sketch below). The vapor in an increment is thus considered to be contained in a truncated cone.

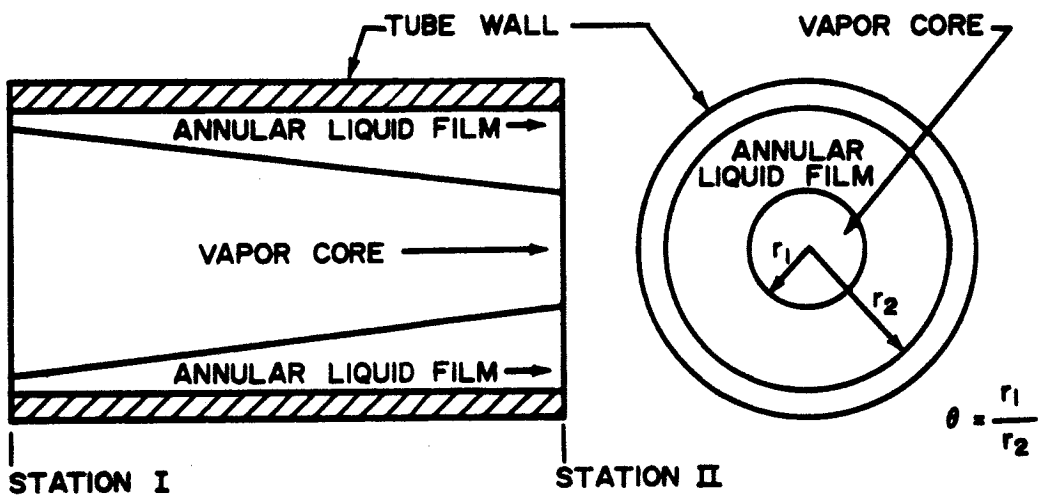

The film thicknesses at Stations I and II were obtained in Step II and are subtracted from the tube inside radius r_2 to obtain r_1. The ratio of vapor-core diameter to tube inside diameter θ is

calculated at both the entrance and exit of each increment by the subroutine which calculates the condensing heat transfer coefficients. The tube vapor inventory is the product of the volume of each truncated cone, the number of tubes, and the vapor density.

$$W_G = N \rho_G V_G = N \rho_G \Delta \ell \frac{\pi}{12} D_i^2 \left[\theta_I^2 + \theta_I \theta_{II} + \theta_{II}^2 \right]$$

Step XI - Calculate the condensate inventory in an increment from

$$W_L = N \rho_L (V_{tube} - V_G) = N \rho_L \frac{\pi}{12} \Delta \ell D_i^2 \left[3 - (\theta_I^2 + \theta_I \theta_{II} + \theta_{II}^2) \right]$$

This equation subtracts the total vapor volume of the condensing fluid from the total volume inside the tubes for the increment to obtain the liquid volume, and then multiplies this value by the condensate density.

At this point, all calculations have been completed for the increment under consideration. Prior to indexing to the next increment, the fluid conditions must be evaluated at the inlet of the next increment.

Step XII - The static pressure at the entrance of the next increment is equal to that of the previous increment minus the static pressure drop across the previous increment.

Step XIII - The corresponding saturation temperature T_{cond_I} of the condensing fluid in the succeeding increment is evaluated from the input curve of saturation temperature vs vapor pressure.

Step XIV - The quality of the condensing fluid and the coolant temperature at the entrance of the succeeding increment are set equal to their respective values at the exit of the preceding increment. The quality of the condensing fluid is considered to be unaffected by the pressure drop through the condensing section. This assumption causes insignificant error if the static pressure drop across the condensing section is small relative to the pressure level.

Steps I through XIV are repeated for each successive increment. Upon completion of these calculations on all N condensing section

increments, the program proceeds to perform calculations on the subcooling section. However, if the input exit quality of the condensing section is greater than zero, the program ignores the subcooling section and proceeds to the final summation routine.

b. Subcooling Section

The program calculates the length, temperature of both fluids, and pressure drops of both fluids for each of the arbitrarily chosen number of subcooling section increments M.

The condensate and coolant conditions at the entrance of the first subcooling section increment are equal to the corresponding values at the exit of the last condensing section increment, and the exit temperature of the condensate leaving the condenser is an input item. Thus the overall condensate temperature change can be determined as well as the equal decrements of condensate temperature drop ΔT_{cond} across each subcooling section increment.

When performing calculations for a subcooling section increment, the following is known data:

$$T_{cond_I},\ T_{cond_{II}},\ T_{cool_I},\ W_{cond},\ W_{cool}$$

The subcooling section calculations are performed in the following order:

Step I - Calculate the coolant temperature at the increment exit $T_{cool_{II}}$ from a heat balance across the increment

$$Q_{cond} = Q_{cool}$$

This can be expressed as:

$$W_{cond}\, C_p\, (T_{cond_I} - T_{cond_{II}}) = W_{cool}\ C_{p_{cool}}\, (T_{cool_I} - T_{cool_{II}})$$

or

$$T_{cool_{II}} = T_{cool_I} - \frac{W_{cond}\ Cp_{cond}\ (T_{cond_I} - T_{cond_{II}})}{W_{cool}\ \ C_{p_{cool}}}$$

Step II - Calculate tube fluid Reynolds numbers at both the entrance and exit of the increment. If the local tube fluid Reynolds number is less than or equal to 2300 the flow is considered to be laminar. If it is greater than 2300, the flow is considered to be turbulent. The Reynolds number is equal to $4\ W_{cond}/\pi\ D_i\ \mu\ N$.

Step IIa - Calculate a local condensate heat transfer coefficient, h_{cond}, at both the entrance and exit of the increment using the appropriate one of the following equations:

$$h_{cond} = 4.36 \quad \frac{k_{cond}}{D_i} \quad \text{for laminar flow}$$

$$h_{cond} = (7.2 + 0.025\ Pe^{0.8}) \quad \frac{k_{cond}}{D_i} \quad \text{for turbulent flow}$$

where Pe denotes the Peclet number (see Section III. D. for detailed discussion of condensate heat transfer coefficients).

Step III - Evaluate a mean thermal conductivity of the tube wall k_{tw}.

Step IV - Calculate the local heat transfer coefficient of the coolant h_{cool}, at both the entrance and exit of the increment, using Equations (16) and (17). This calculation is a complete subroutine of the program.

Step V - Calculate the local overall heat transfer coefficients U_o at both the increment entrance and exit from the following equation

$$U_o = \frac{1}{\dfrac{D_o}{D_i h_{cond}} + \dfrac{D_o \ln (D_o/D_i)}{2k_{tw}} + \dfrac{1}{h_{cool}}}$$

Step VI - Calculate the increment heat transfer area based on tube outside diameter from the following equation

$$A = \frac{Q \ln \left(\dfrac{U_{o_I} \quad \Delta T_{II}}{U_{o_{II}} \quad \Delta T_I} \right)}{U_{o_I} \quad \Delta T_{II} - U_{o_{II}} \quad \Delta T_I}$$

where

$$\Delta T_I = T_{cond_I} - T_{cool_I}$$

$$\Delta T_{II} = T_{cond_{II}} - T_{cool_{II}}$$

$$Q = \text{heat lost by the condensate across the increments}$$

$$= W_{cond} \; (C_p \; \Delta T)_{cond}$$

This equation which is discussed in detail in Section II is based on the assumption that U_o varies linearly with ΔT.

Step VII - Calculate the incremental length $\Delta \ell$ from

$$N D_o \pi \; \Delta \ell = A$$

where
N = number of condenser tubes

Step VIII - Calculate the condensate total pressure loss across the increment using the method described in Section III.E.

Step IX - Calculate the coolant pressure loss across the increment using the methods described in Section III.E.

Step X - Complete the calculations for the increment under consideration. The condensate and coolant temperatures at the entrance of the next increment are set equal to the respective values at the exit of the increment just described.

Steps I through X are repeated for each successive increment. Upon performing these calculations on all M subcooling section increments, the program proceeds to the final summation equations.

c. Final Summation

Upon completion of the calculations for each increment in the condensing and subcooling sections, the program calculates the total tube length by performing a summation of all incremental lengths.

Total pressure drops for both the coolant and condensing fluids are calculated by adding all of the incremental pressure drops and the expansion and contraction pressure drops. Section III.E. describes the methods used to obtain contraction and expansion losses.

The program also calculates the weights of condensate in the subcooling section, the coolant, tube wall, shell wall, and tubesheet. These values are added to the sum of the weights of the tube fluid in the condensing section. Weights of the manifolds and the other miscellaneous items are not calculated by the computer and must be calculated separately to obtain total condenser weight.

2. Tapered Case

The calculation procedures outlined for the constant-diameter case apply in general to the tapered case. However, some equations were modified to account for variation of tube and shell dimensions with length for the tapered case. Since this case requires an iterative procedure, a method of starting the procedure was also required. The modifications to the equations for the constant-diameter case and the iteration procedure are discussed in this section.

a. Iteration Procedure

In order to calculate the length of an increment, the program calculates local values of heat transfer coefficient at both end points of an increment. This calculation requires knowledge of the tube and shell diameters and coolant flow area at both points. For a tapered case, the dimensions at the beginning of an increment would be known either from the calculations from the preceding increment or would be input items for the first increment. However, the dimensions at the end of the increment are dependent upon the length of the increment. The program starts the calculation procedure by assuming the dimensions at the end of the increment are the same as those of the beginning of the increment. The program continues the procedure and calculates a length of the increment. Dimensions at the end of the increment can then be determined from this value of length. The sketch shown below illustrates how the tube diameter at the exit of an increment is determined from the incremental length.

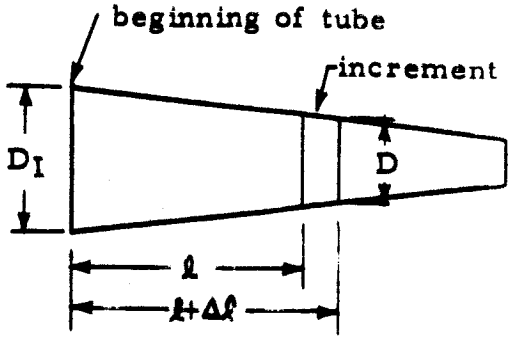

D_I = diameter of beginning of tube (input item)

D = diameter at end of increment

ℓ = length from beginning of tube to beginning of increment

$\Delta\ell$ = length of increment

γ_T = fractional decrease in tube diameter per unit length based on tube inlet diameter (input item)

$$D = D_I \left[1 - \gamma_T(\ell + \Delta\ell) \right]$$

The newer values of dimensions at the end of the increment are used in turn to calculate a more accurate value of incremental length, and so on, until the difference between two successive values of incremental length is within a specified relative tolerance. Convergence of this iteration process is obtained in a few steps by use of a point slope iteration routine. Then the program continues to calculate pressure drops and inventories for that increment before proceeding to the next increment.

b. Equations

Step II of the calculation procedure for both condensing and subcooling section increments for a constant-diameter case calculated overall heat transfer coefficients based on the outside diameter of the tubes. For the tapered case the overall heat transfer coefficients are based on the inside diameter of the tubes.

The modifications to other equations used to obtain a value of incremental length are complex and are discussed in detail in Appendix F. The equations for calculating fluid inventory are modified slightly to account for variation of diameter with length.

Condensing fluid momentum differentials across a condensing section increment are based on the local diameters at the beginning and end of the increment. The friction drop calculations across an increment consider the increment to have a constant diameter, namely, that at the midpoint of the increment. The calculation to determine the static pressure differential for an increment also included the effect of the wall force due to change of cross-sectional area. All other calculations are essentially the same for the tapered case as for the constant-diameter case.

APPENDIX A

Materials and Fabrication

APPENDIX A

Materials and Fabrication

Columbium-1% zirconium was chosen as the best available material for fabricating the liquid metal condenser. This material has good corrosion resistance to all the liquid metals studied, high strength at elevated temperatures, and good machinability.

Cb-1% Zr was determined to be the most suitable material as a result of a study made of various materials and fabrication techniques for application over a temperature range from 1200 to 2200°F in the presence of lithium, potassium, sodium, and the eutectic mixture of potassium and sodium, NaK. The high temperatures encountered in liquid metal condensers and the corrosive nature of liquid metals impose stringent requirements on any material or fabrication technique to be used in the construction of such devices. At high temperatures, many materials have relatively low yield and ultimate strength, high creep rate, or low corrosion resistance. These factors coupled with a 10,000-hour desired life and the high stresses due to differential thermal expansion eliminated many materials as candidates for the applications under study. Also, due to the need for a leakproof system, the metal joints must have a high reliability. The topics covered in this study are corrosion resistance of metals, physical properties of the better materials, and metal-joining techniques.

A. Corrosion by Liquid Metals

Corrosion of a material in contact with a liquid metal can occur by different mechanisms. For a system containing a pure solid metal in contact with a liquid metal, the following modes of corrosion are possible[A1] :

1) Solution of solid metal into the liquid metal by uniform solution or intergranular penetration,

2) Intergranular or uniform diffusion of the liquid metal into the solid metal lattice,

3) Formation of an intermetallic compound at the solid-liquid interface, and

[A1] Numbered references for this appendix are listed on page A24

4) Mass transfer due to temperature or composition gradient within the system.

In addition, corrosion may occur in systems containing alloys by the leaching of a constituent from the alloy surface due to selective solution. The result may be phase transformations of the material structure or formation of subsurface voids.

The principal parameters influencing corrosion in a liquid metal system are: temperature level, temperature gradient, extent of thermal cycling, internal surface area-to-volume ratio, purity of solid and liquid metals, flow velocity of the liquid metals, and number of different structural materials in contact with the liquid metal. Temperature is the most influential of these parameters since increasing temperature increases the solubility of solid metal in liquid metal, the diffusion rate of the liquid metal into the wall materials, and the rate of formation of intermetallic compounds at the solid-liquid interface. Thermal cycling due to either fluid temperature fluctuation or transient temperature changes during starting can also accelerate the rate of corrosive attack. The greater quantity of container material dissolved at high temperatures may result in a supersaturated liquid during the low temperature part of a cycle. The excess metal may subsequently precipitate in the liquid or deposit on the container walls. This phenomenon also can result from temperature gradients within a loop. The liquid metal can dissolve solid metal from the hotter portion of the system and deposit it in the cooler portion of the system.

Many investigators have found that the purity of the liquid metals is an important factor in corrosion. The oxygen and nitrogen levels of the liquid metals should be maintained at the lowest possible levels. Also hot traps should be included in all liquid metal loops which operate above 1500°F to prevent mass transfer and carburization (when applicable) in cold-leg portions of the loop. Such traps can be made using zirconium, Cb-1% Zr, or titanium chips to getter any carbon, oxygen, or nitrogen leached from the structural material. This practice prevents the gettered elements from being deposited in the colder sections of the loop and embrittling the structural material [A2].

The number of different materials in contact with the liquid metal within a system is a factor in determining the type and rate of corrosion. Mass transfer can occur under isothermal conditions due to composition gradients.

The flow velocity or Reynolds number is important in mass transfer for forced convection systems since increased flow velocity increases the diffusion rate of wall materials dissolved in the liquid metal.

Techniques used by the different investigators for determining corrosion of metal in liquid metals can be divided into the general classifications of static and dynamic tests[A3]. In static tests, the specimen is contained in a chamber of the same material (two-component system), or a different material (three-component system) filled with liquid metal. For a two-component system test, the specimen may be the chamber itself. Dynamic tests include a relative movement of liquid metal with respect to the specimen. This can be accomplished either by agitating the liquid or by maintaining a flowing current of liquid metal by forced or free convection in a circuit (loop test). A temperature gradient is normally maintained between sections of the loop. Due to the close simulation of actual operating conditions, data generated from loop tests are most reliable.

The following three sections contain a discussion of the compatibility of the several liquid metals with various structural materials.

1. Lithium Compatibility

Of all the liquid metals studied, lithium is considered the most corrosive to most of the structural materials[A4]. Contamination by nitrogen, oxygen, or hydrogen dissolved in lithium presents some problems in interpreting test results, since there is very little information on the effects of these elements.

Over the entire temperature range from 1200 to 1500°F, the only materials known to be suitable for containment of pure lithium are: pure iron, chromium, Types 316, 347, and 430 stainless steels, and the refractory metals columbium, molybdenum, tantalum, tungsten, zirconium, titanium and rhenium, and some refractory alloys such as columbium-1 per cent zirconium and molybdenum-0.5 per cent titanium[A4, 5, 6, 7].

The nickel-base alloys Inconel, Inconel X, Nichrome 5, Monel, Hastelloy B, and Hastelloy C, plus the cobalt-base alloy L605 are all severely attacked at a temperature of 1500°F in static tests[A7]. Day and Brasunas[A8] also found that L605 alloy was subject to pronounced intergranular attack and mass transfer in loop tests at 1500°F.

Even those materials considered suitable over the temperature range from 1200 to 1500°F showed some amounts of corrosion. At close to 1500°F, zirconium is subjected to uniform solution due to mass transfer in a three-component static system [A7]. In austenitic stainless steels such as Type 316, lithium selectively leaches nickel from the surface in the areas adjacent to the grain boundaries with the subsequent transformation of these areas to ferrite. This leaching action leads to intergranular attack and void formation at the surface [A4].

The refractory metals molybdenum, columbium, rhenium, tantalum, zirconium, and the refractory alloys Mo-0.5% Ti and Cb-1% Zr are the only materials reported that could be considered to have suitable corrosion resistance at temperatures up to 1832°F for even short periods. Cunningham [A9] investigated the corrosion resistance of the refractory metals chromium, columbium, molybdenum, vanadium, tantalum, and tungsten at 1832°F in static tests. Arc-melted chromium is subject to solution attack and intergranular penetration. Columbium and tantalum have good resistance to lithium at 1832°F for as long as 400 hours. However, continuous carbide films were reported to be present after 400 hours' exposure. Molybdenum showed resistance to lithium for only 4 hours' exposure. Longer exposures resulted in greater amounts of solution and mass transfer of molybdenum to the capsule wall. Tungsten resists the corrosive effects of lithium for only short periods at 1832°F. Vanadium does not have outstanding resistance to lithium at 1832°F.

Rhenium has not been extensively investigated and available data is insufficient to be used for design criteria. However, static tests at 1500°F showed no corrosion of rhenium in lithium [A7].

Other investigators rated molybdenum as having good corrosion characteristics at temperatures of 1832°F in both static and dynamic tests [A5]. At 1832°F graphite-melted zirconium had good corrosion resistance to lithium in static tests [A9].

Pratt & Whitney Aircraft has accumulated more than 4000 hours of operation on a test loop constructed of Cb-1% Zr containing lithium. The thermal and flow conditions were realistic for an actual 5MW powerplant operation with lithium temperatures as high as 2000°F [A10].

2. Potassium Compatibility

Potassium is also very corrosive to structural materials at elevated temperatures. Numerous investigators have tested materials in contact with potassium under various conditions. Some of the more pertinent results of these tests are discussed in this section.

Hoffman [A11] investigated the behavior of Type 316 stainless steel while containing potassium at 1600°F for 3,000 hours in a dynamic system. The sample showed uniform attack to a depth of 2 mils with no detrimental effects on the mechanical properties of the alloy. However, extensive mass transfer of carbon and chromium carbide ($Cr_{23}C_6$) occurred.

Potassium has a high affinity for carbon and will leach out carbon and carbides from an alloy. Therefore, stainless steels cannot be used for extensive durations at temperatures over 1500°F.

Kovacevick [A12] found that at a temperature of 1800°F intergranular penetration of Hastelloy X tubing proceeded to a depth of 4 mils with heavy surface roughening, and nickel deposits were observed in the cold leg of the loop. Since nickel is also readily attacked by potassium, nickel-base alloys can be used only for short durations at 1500°F.

Semmel [A2] investigated L 605 (Haynes alloy No. 25) in a potassium thermal loop at 1850°F for 1,000 hours. He found excellent resistance to both uniform surface attack and intergranular attack. However, he did observe an internal transformation (aging reaction) which decreased room temperature ductility.

Kovacevick [A12] found the refractory alloys Mo-0.5% Ti and Cb-1% Zr had excellent corrosion resistance to potassium under a static test condition of 1800°F. Chandler [A13] found that Cb-1% Zr alloy in static tests at 2100°F for 100 hours showed no evidence of a reaction layer, intergranular penetration, or other corrosion.

The Rocketdyne Division of North American Aviation [A13, 14, 15] has tested refractories and refractory alloys with these results: 1) Columbium and Cb-1% Zr when coupled with nickel-base alloys in static tests above 1450°F will corrode rapidly and form a film of columbium nitride and columbium carbide on the columbium surface. In addition, the potassium decarburized the nickel-base alloys and carburized the columbium alloys. 2) When there are no nickel-base alloys in the system, both columbium and Cb-1% Zr alloy show no corrosion at temperatures up to 2000°F. 3) Dynamic tests at 1800°F indicate that materials in order

of favorable corrosion resistance are molybdenum, Cb-1% Zr, columbium, and tantalum. North American Aviation has also conducted static tests on molybdenum and columbium-base alloys in Cb-1% Zr capsules with temperatures as high as 2200°F. Materials tested included F-48 (15% W-5% Mo-1% Zr - balance Cb), FS alloy 83 (33% Ta - .75% Zr - balance Cb), and TZC (1.26% Ti-.29% Zr-.3% C - balance Mo). These specimens showed no reaction layer and small weight changes after 140 hours of testing [A16].

Semmel et al [A17] reported on a technique for high temperature brazing. Mo-0.5% Ti and L 605 were brazed with braze alloy H-33 (or J-8400) using a tongue-and-groove joint. H-33 is a cobalt base alloy which has the composition 21% Cr - 21% Ni - 8% Si - 3.5% W - 0.4% C - 0.8% B - balance Co. The brazed joint was exposed to potassium at 1850°F for 100 hours and showed no corrosion effects. Thermal cycling tests between 400°F and 1850°F for 250 hours indicated some cracking along the external surface, but the joint remained helium leak-tight.

The General Electric Company [A18] is investigating the strength, fabrication techniques, and corrosion resistance to potassium of some columbium-base alloys. The work is in the early stages. The National Aeronautics and Space Administration [A19] is screening a number of refractory alloys for alkali metal containment from 1800°F to 2400°F. Included in these plans are static corrosion tests on Fansteel FS-85, Westinghouse B-33 and B-66, General Electric AS-55, and DuPont X-110, using potassium as the test fluid.

In summary the following materials are resistant to potassium corrosion for long durations:

1) The refractory metals molybdenum, columbium, tantalum, and tungsten up to a temperature of 2000°F,

2) The refractory base alloys Cb-1% Zr and Mo-0.5% Ti up to a temperature of 2000°F, and

3) The cobalt-base alloy Haynes L 605 up to a temperature of 1800°F.

Several other refractory-base alloys are presently being investigated, some of which may be found suitable for long duration, high temperature applications.

Stainless steels can be used up to 1500°F for moderate lengths of time. Also, the braze alloy H-33 has suitable corrosion resistance to potas-

sium at 1850°F for limited time exposure, and might be practical for long periods at 1500°F.

3. Sodium and NaK Compatibility

Many of the common structural materials have been found suitable for use with sodium and NaK at high temperature. The austenitic stainless steels, cobalt-base alloys, and nickel-base alloys are among the materials with good corrosion resistance. Columbium, molybdenum, tantalum, tungsten, and chromium are suitable for use with sodium and NaK up to 1690°F [A20].

Tables A1 and A2 summarize dynamic testing conducted by Perlow and Crosby [A21]. In general, molybdenum, Hastelloy N, Hastelloy C, Inconel X,

TABLE A1

1200°F NaK Corrosion Data (Ref. A18)

Specimen	Duration (hrs)	Type and Rate of Attack
Stainless Steel 304	1500	No apparent attack
	2500	0.0014-in. intergranular corrosion
	3500	Evidence of general corrosion
	4500	0.0015-in. pitting
Stainless Steel 316	1000	0.0026-in. general corrosion
	2000	0.0025-in. intergranular corrosion
	3000	0.0010-in. general corrosion
Stainless Steel 347	1500	0.0007-in. intergranular corrosion
	2500	0.0020-in. general corrosion
	3500	0.0019-in. intergranular corrosion
	4500	0.0020-in. pitting
Hastelloy N	1500	Slight evidence of general corrosion
	2500	No apparent attack
	3500	No apparent attack
	4500	0.0014-in. intergranular corrosion
Columbium*	1000	No evidence of intergranular attack or general corrosion

*This specimen at 1300°F

TABLE A2

1400°F NaK Corrosion Data (Ref. A18)

Specimen	Duration (hrs)	Type and Rate of Attack
Stainless Steel 304	1500	No apparent attack, slight evidence of decarburization
	2500	0.0014-in. pitting
	3500	0.0013-in. intergranular corrosion
	4500	0.0023-in. decarburization
Stainless Steel 316	1000	Slight evidence of general corrosion
	2000	0.0004-in. decarburization
	3000	0.0008-in. decarburization
Stainless Steel 347	1500	0.0006-in. intergranular corrosion
	2500	0.0004-in. pitting
	3500	General corrosion to a depth of 0.0006 in.
	4500	0.0025-in. decarburization
Hastelloy N	1500	Slight evidence of intergranular attack
	2500	General corrosion to a depth of 0.0005 in.
	3500	No apparent attack
	4500	Very slight surface attack
Haynes 25	1000	0.0002-in. pitting
	2000	Very slight evidence of general corrosion
	3000	0.0011-in. decarburization
Molybdenum	1000	No apparent attack
	2000	No apparent attack
	3000	Slight pitting, no depth
Inconel X	1000	No apparent attack
	2000	Very slight general corrosion
	3000	Very slight pitting, no depth
Hastelloy C	1000	0.0010-in. pitting
	2000	0.0017-in. decarburization

and Haynes 25 (L 605) showed good corrosion resistance to NaK at 1200 and 1400°F for long durations, while stainless steel Types 304, 316, and 347 showed moderately good resistance at these temperatures. Columbium showed excellent resistance to NaK at 1300°F for 1000 hours.

Perlow and Page [A22] conducted NaK dynamic corrosion tests on Type 316 stainless steel, Hastelloy N, Hastelloy C, and Haynes 25 (L 605) at temperatures of 1200 and 1400°F for a continuous test exposure of 5000 hours with the tests interrupted at specified intervals for metallographic examinations. In general, more corrosion was found on the specimens from the interrupted tests than the specimens from the continuous tests. The four materials tested showed only slight corrosion effects for 5000-hour continuous operation at 1400°F.

Simons [A23] reported that molybdenum, columbium, rhenium, tantalum, vanadium, tungsten, zirconium, Hastelloy B, Inconel X, Kanthal, Stellite 6, and Thermenol suffered less than 1-mil penetration in a screening test with NaK at 1600°F. The test was for 5000 cycles in 110 hours.

Teitel [A14] reported that a sodium boiling loop operating at temperatures up to 1860°F indicated no corrosion on Haynes 25 (L 605), 321 stainless steel, Inconel, and molybdenum.

North American Aviation [A24] reported on sodium static corrosion tests conducted at 1652°F for 168 hours. Materials in order of decreasing resistance to corrosion are molybdenum, tungsten, Type 347 stainless steel, L 605, tantalum, Kennametal - 138A, and titanium. All of these materials showed at least good corrosion resistance to sodium.

Brasunas [A25] conducted static capsule tests of various materials in sodium at 1832°F for 40 to 400 hours. Austenitic stainless steels, chromium, molybdenum, tantalum, tungsten, titanium, cobalt, and Inconel had good corrosion resistance under these conditions, while nickel had excellent resistance. Inconel X was found to have some-

what less than good resistance to sodium. Columbium was found very sensitive to the oxygen level in sodium or NaK.

Semmel [A26] reported on 300-hour static corrosion tests with sodium at 1700°F for F-48 columbium alloy and Mo-.5% Zr alloy. The most serious evidence of corrosion was pitting along one of the edges of an F-48 specimen. Other F-48 specimens did not exhibit this pitting.

Brookhaven National Laboratory [A27] has run a Cb-1% Zr capsule for 720 hours at 2200°F which indicated that the alloy has good corrosion resistance to sodium.

In summary, the materials which were compatible with potassium are compatible with sodium and NaK. Other materials including nickel and nickel base alloys which are not compatible with potassium are compatible with sodium and NaK. However, in a potassium condenser cooled by sodium or NaK it would be impractical to have a dual alloy system by cladding tubes, due to fabricating difficulties and differential thermal expansion.

B. Properties of Candidate Materials

The nonrefractory metals which were determined to be suitable in the temperature range of 1200 - 1500°F are conventional structural materials and thus properties of these materials are readily available. Cb-1% Zr and Mo-.5% Ti are presently the most suitable refractory-base structural materials for use with liquid metals at high test temperatures for long durations. The pure refractory metals which were suitable for long durations at high temperatures do not have as high strength characteristics as either Cb-1% Zr or Mo-.5% Ti. The following section contains curves and tables of the more pertinent properties of these two materials and their unalloyed base metals. Some properties were not available for all of these materials. Other properties are contained in References A28 to A47.

Table A3 contains the densities at 70°F and melting temperatures for Cb-1% Zr, Mo-.5% Ti and their base metals [A28].

TABLE A3

Density and Melting Temperature of
Candidate Materials (Ref. A28)

Material	Density (lbs/in^3)	Melting Temperature (°F)
Molybdenum	.37	4730
Mo-.5% Ti	.369	4750
Columbium	.31	4474
Cb-1% Zr	.31	4350

Figure A1 shows thermal conductivity as a function of temperature for molybdenum, columbium, Mo-.5% Ti and Cb-1% Zr [A29, 30, 31]. Figure A2 shows specific heat as a function of temperature for the two pure refractory metals [A32]. Specific heat data is not available for Cb-1% Zr and Mo-.5% Ti. However, specific heats are expected to be similar for the alloys and pure metals.

Table A4 contains mean coefficients of thermal expansion for molybdenum, Mo-.5% Ti, and columbium over various temperature ranges [A30, 31 - 32]. Table A5 contains modulus of elasticity data for molybdenum, Mo-.5% Ti, annealed columbium, and recrystallized Cb-1% Zr [A28, 34, 35, 36].

Table A6 contains values of tensile strength and yield strength for columbium and recrystallized Cb-1% Zr at various temperatures [A28, 36]. Comparative curves of ultimate strength and yield strength as a function of temperature are shown in Figures A3 and A4 respectively for molybdenum and Mo-.5% Ti [A34]. Vacuum conditions were used for these last two curves on wrought, stress-relieved material. These curves and tables indicate that alloyed materials are stronger than pure metals.

Figure A5 contains curves of stress to rupture and elongation as a function of time for 1600°F, 1800°F, and 2000°F for the Mo-.5% Ti alloy [A37]. However, the data does not extend to the desired 10,000 hours' duration.

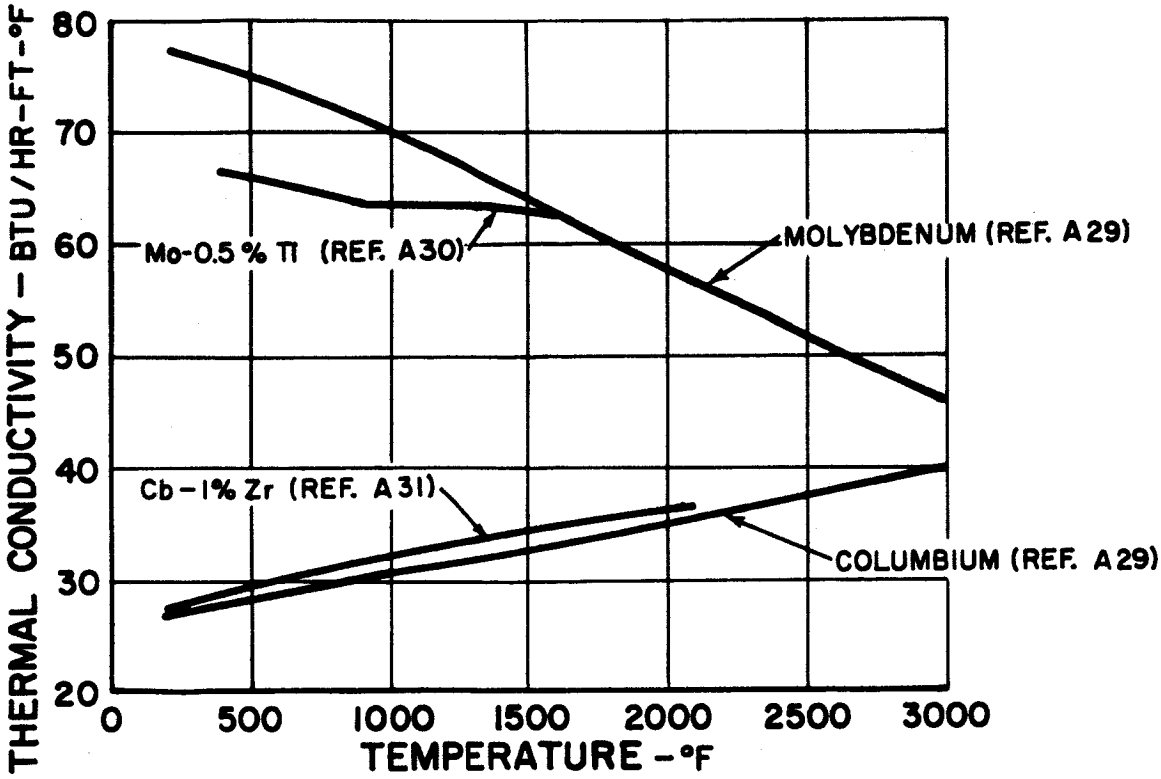

Figure A1 Thermal Conductivity vs Temperature for Molybdenum, Columbium, Columbium-1% Zirconium, and Molybdenum -0.5% Titanium

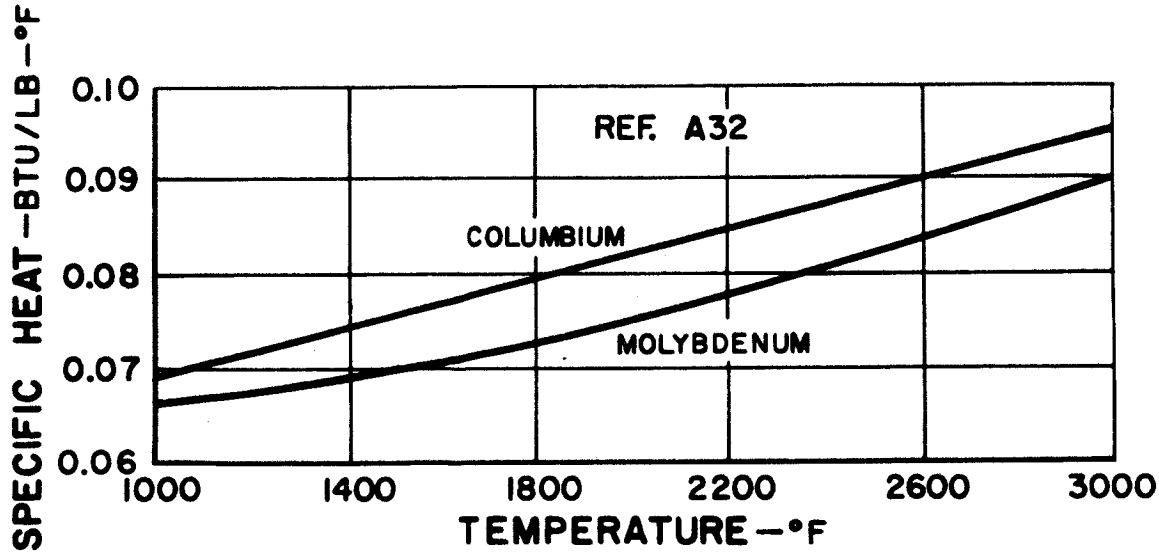

Figure A2 Specific Heat vs Temperature for Molybdenum and Columbium

TABLE A4

Mean Coefficient of Thermal Expansion
Molybdenum (Ref. A32)

Temperature Range (°F)	Mean Coefficient of Thermal Expansion (in/in. per °F)
68-300	3.02×10^{-6}
68-600	2.89
68-900	2.88
68-1200	2.98
68-1500	3.08
68-1800	3.23
68-2100	3.37
68-2400	3.49
68-2700	3.61
68-2900	3.70
68-3000	3.75 (Extrapolated)

Mo-0.5% Ti (Ref. A30, 32)

Temperature Range (°F)	Thermal Expansion (in/in. per °F)
68-212	3.06×10^{-6}
68-392	3.06
68-572	3.09
68-752	3.14
68-932	3.19
68-1112	3.24
68-1292	3.28
68-1472	3.32
68-1652	3.36
68-1832	3.41

Columbium (Ref. A33)

Temperature Range (°F)	Thermal Expansion (in/in. per °F)
70-570	4.06×10^{-6}
70-750	4.10
70-930	4.15
70-1110	4.20
70-1290	4.24
70-1470	4.29
70-1650	4.33
70-1830	4.38

TABLE A5

Modulus of Elasticity for Molybdenum and Mo-.5% Ti (Ref. A34)

Temperature (°F)	Modulus of Elasticity for Molybdenum	Modulus of Elasticity for Mo-.5% Ti
70	40.8×10^6 psi	37.1×10^6 psi
400	35.1	36.5
600	36.1	38.5
800	34.9	33.5
1000	31.0	33.7
1200	32.9	32.2
1400	27.2	28.5
1600	25.6	29.9
1800	25.4	27.8
2000	21.4	25.5
2200	17.4	18.9
2400	8.5	8.5

Modulus of Elasticity for Annealed Columbium (Ref. A28, 35)

Temperature (°F)	Modulus of Elasticity
68	15.2×10^6 psi
392	14.7
572	14.5
752	14.6
932	14.2
1600	13.6

Modulus of Elasticity for Recrystallized Cb-1% Zr (Ref. A36)

Temperature (°F)	Modulus of Elasticity
75	11.5×10^6 psi
2500	2.7
2700	2.0
3000	0.8

TABLE A6

Tensile Properties of Recrystallized Cb-1% Zr (Ref. A36)

Temperature °F	Tensile Strength 1000 psi	Yield Strength (0.2% offset) 1000 psi
75	48.0	37.1
	45.5	33.7
2000	22.9	21.4
	22.8	20.0
2500	8.65	7.0
	8.15	6.24
2700	5.9	4.6
	6.16	5.0
3000	2.95	2.34
	3.47	2.94

Tensile Properties of Columbium (Ref. A28)

Temperature °F	Tensile Strength 1000 psi	Yield Strength 1000 psi
70	40	35
1600	20	10
2400	5	2

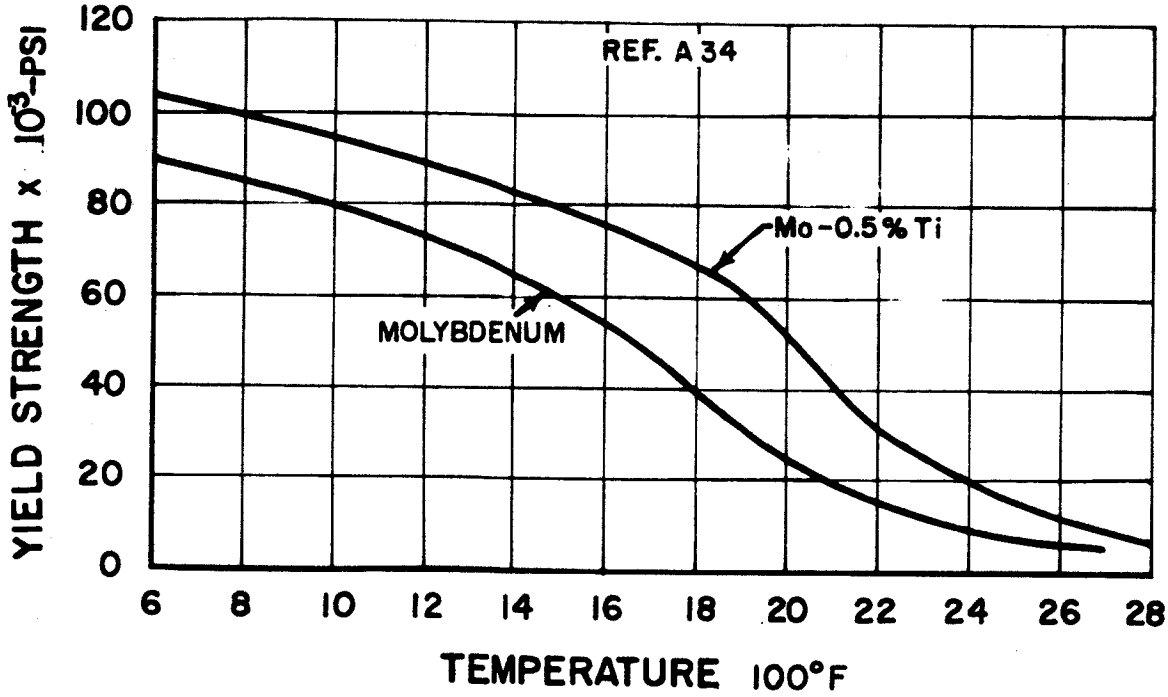

Figure A3 0.2% Yield Strength vs Temperature for Molybdenum and Molybdenum-0.5% Titanium under 10^{-5}mm Hg Vacuum

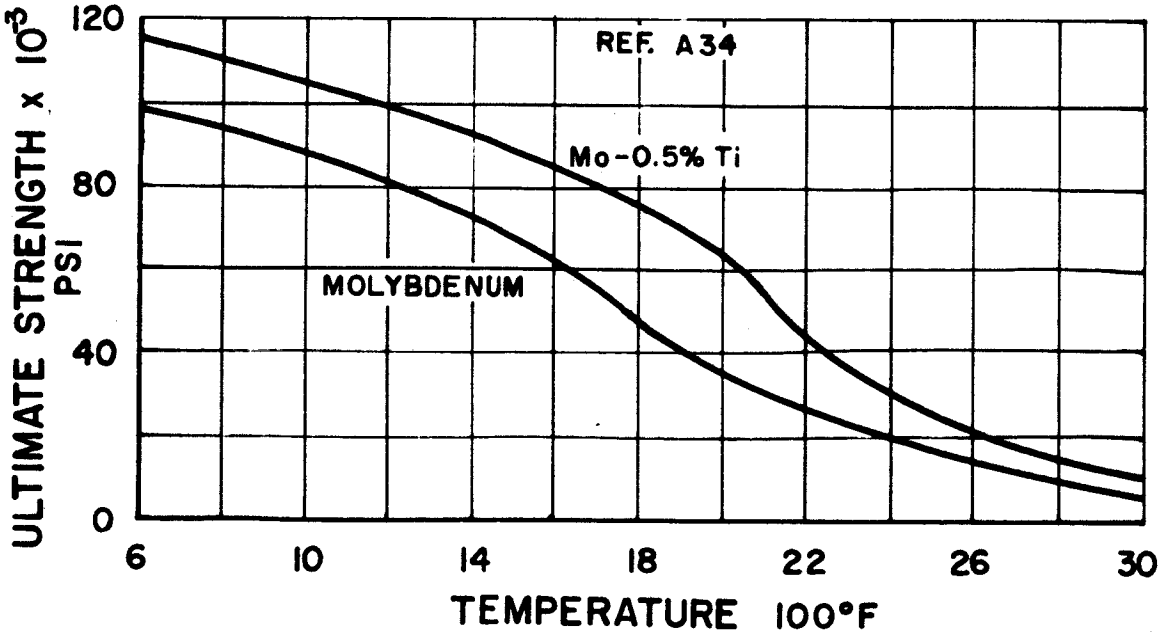

Figure A4 Ultimate Strength vs Temperature for Molybdenum and Molybdenum - 0.5% Titanium under 10^{-5} mm Hg Vacuum

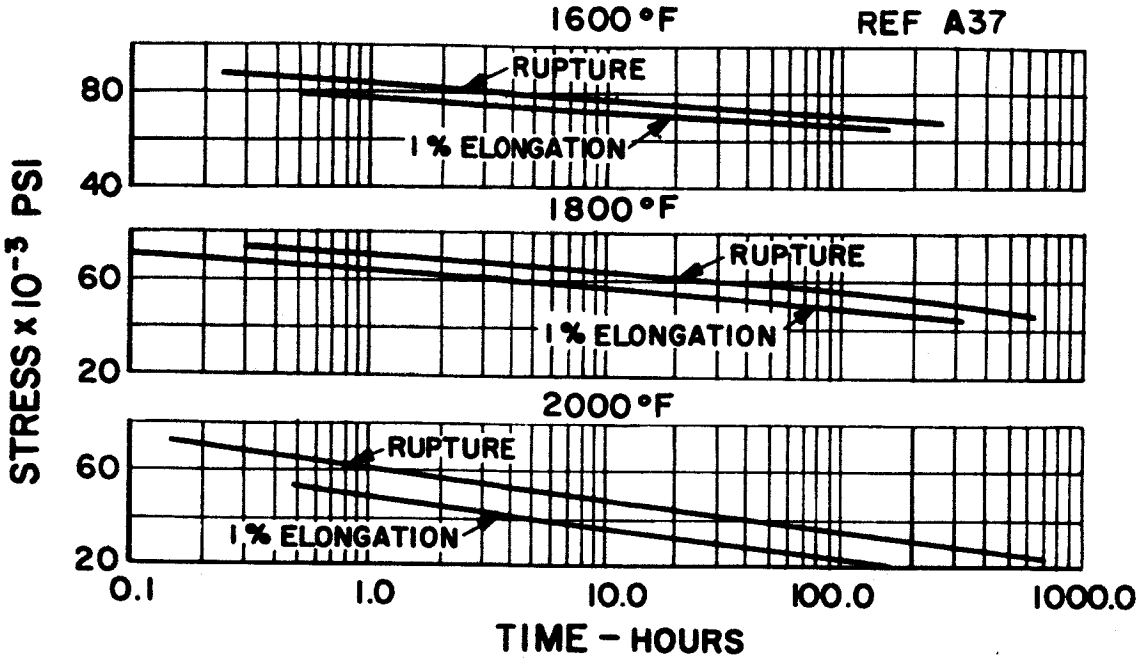

Figure A5 Rupture and Elongation vs Time for Molybdenum-0.5% Titanium in Stress-Relieved Condition

Machining molybdenum, columbium and Cb-1% Zr is not extremely difficult. Usually these materials cut like stainless steel [A28, 38]. However joining and forming molybdenum must be done at elevated temperatures because of lack of room-temperature ductility [A38].

For any extended time operation at elevated temperature, columbium or molybdenum-base alloy components should be protected from oxidation by operation in vacuum or inert gas.

No noticeable reaction occurs in Mo-.5% Ti exposed to air up to about 350°F. At 500°F the rate of oxidation is low and increases only moderately up to 1300°F. At this point, the protective molybdenum trioxide (MoO_3) layer starts to volatilize, resulting in a sharp rise in oxidation rate. At 1550°F MoO_3 melts and combines with molybdenum dioxide, MoO_2, the reaction product formed at the metal-oxide interface. The resulting eutectic has a melting point of 1525°F, accounting for a further increase in oxidation rate at this temperature.

Cb-1% Zr begins to oxidize in air at approximately 200°F [A39]. The rate increases rapidly with increasing temperature up to 900°F. A discon-

tinuity exists at this temperature as oxidation rate immediately falls to 1/10 its value. The curve resumes its positive slope with further increases in temperature.

Columbium alloys and molybdenum-base alloys in sheet form can be obtained from primary producers of the materials. Tubing of either material with dimensional tolerances required for this application can be produced by a specialty tubing fabrication facility from ingot supplied by the primary producers.

C. Joining Techniques

In a liquid metal condenser application, it is required that all joints be leak-tight, corrosion resistant, and capable of withstanding high stresses. Most joints can be fabricated merely by using careful welding techniques. However, in shell-tube type condensers for liquid metal applications, the joints at the tube ends require special techniques.

The tubes are joined at each end to common sheets which separate the tube fluid in the manifolds from the shell fluid. If welding alone were used to form these joints, a space would exist between the tubes and their mating holes in the tubesheet since complete penetration of the weld is impractical. Also, the tube wall would have a sharp change in contour or notch where the weld area ends, thus causing an area of stress concentration. Thermal cycling of the tube could cause fatigue failure at the notch area. This type of failure was evidenced at Oak Ridge National Laboratory [A48]. In subsequent work at Oak Ridge [A49, 50], the tube joints were welded and then the spaces between the tubes and their mating holes were brazed from the side of the tubesheet opposite the weld (back surface). This back brazing process eliminated the notch at the ends of the tubes, increased the strength of the joints by bonding the tubes to the full thickness of the tubesheet, and provided more uniform stress distribution by forming fillets between the tubes and back surfaces of the tubesheets. The shallow-depth welds act as seals, but require reinforcement to prevent cracking.

These seal-welded and back-brazed joints have been used with success in various liquid metal heat exchanger programs in the temperature range of 700° - 1500°F with NaK as a coolant. However, at present there is no braze alloy that has been reported as being corrosion-resistant to lithium at high temperatures. Several investigators are investigating possible braze alloys that would be suitable for use with lithium. Table A7 contains a list of some possible high temperature braze alloys for Cb-1% Zr and their melting points [A51]. Table A8 lists

TABLE A7

Brazing Alloys for Service With Cb-1 Zr (Ref. A51)

Nominal Composition Wt. %	Expected Melting Range, (°F) Solidus	Liquidus
Ti - 5 Fe	2680	2780
Ti - 10 Fe	2390	2600
Ti - 20 Fe	2060	2280
Ti - 10 Cr	2910	2980
Ti - 20 Cr	2710	2800
Ti - 2 Be	--	2730
Zr - 12 Ag	2280	2280
Zr - 11 Al	2460	2460
Ti - 13 Fe - 8 Cr	--	--
Ti - 6 Fe - 4 Cr	2060	2280
Zr - 28 V - 16 Ti	2220	2350

TABLE A8

Brazing Alloys for Mo-.5% Ti (Ref. A46)

Braze Alloy (%)	Melting Point (°F)	Tensile Strength at 1800°F (psi)
84 Ni - 16 Ti	2350	15,800
52 Co - 48 Ni	2212	17,000
80 Ni - 14 Cr - 6 Fe	2540	6,700
55 Co - 20 Cr - 15 W - 10 Ni	2600	20,100

alloys successfully used in brazing Mo-.5% Ti, plus their melting points and tensile strengths at 1800°F [A46]. No information was available on the corrosion resistance to liquid metals for these braze alloys listed in Tables A7 and A8.

Another good method of bonding the tube joints is to first seal-weld the tubes to the tubesheet, swage the tube out to make a force fit between the tubes and tubesheet holes, and then to diffusion-bond the tube to the mating hold surfaces of the tubesheets. In the case of stainless steel fabrication, the tube end would first be plated with a suitable metal such as nickel. Nickel has a high solubility with stainless steels and thus, upon heating the plated area to the bonding temperature for a required length of time, an intimate bond is formed between the two mating surfaces. A similar technique is used with columbium-base alloys at Pratt & Whitney Aircraft. However, instead of plating the tube ends, an intermediate element in the form of a foil or sleeve is inserted between the mating surfaces. This material is usually one of the more reactive metals which has a 100 per cent solid solubility with columbium-base alloys, such as titanium, zirconium, or vanadium. A temperature of 2200°F is held for 2 to 3 hours for bonding titanium or vanadium. This technique has been used successfully for fabricating heat exchangers for use with lithium at temperatures up to 2000°F. Columbium has also been diffusion bonded without any filler material under an inert gas pressure of 10,000 psi at 2200°F [A52]. These joints were found to be ductile and to have room temperature tensile strengths of 40,000 psi, or about the same as the annealed parent material.

The welding of the tube joints and other joints must be done with care to prevent impurities from contaminating the weld. This contamination is avoided by performing the welding in an inert gas atmosphere. One of the most common methods is the tungsten-inert gas (TIG) process which uses a tungsten electrode and either helium or argon as the inert gas.

Since welding the tube ends to the tubesheet presents a problem due to the different heat absorption rates of the two parts and manual operation of the tungsten electrode which can lead to uneven stress distribution around each joint, a method called the cone-arc process was developed [A53, 54, 55]. In this process a magnetic field induces high speed rotation of the welding arc about the periphery of a circle, thus decreasing the time necessary to complete the weld and providing a more even temperature distribution around the weld periphery.

Electron-beam welding is another method that can be used to produce high reliability tube-to-tubesheet joints [A56]. This method offers an advantage of high depth-to-width ratio in the weld (up to 25 to 1). Adequate seal welds can be achieved by this method with no major problems, but to achieve welds which penetrate the full thickness of the tubesheet would require a considerable development to overcome heat transfer and eccentricity problems.

Figures A6 and A7 compare properties of ultimate tensile strength and bend ductility as functions of temperature for Mo-.5% Ti base metal with those of electron-beam weldments of this material [A57]. The data indicate that electron-beam weldments in Mo-0.5% Ti have relatively good mechanical properties.

D. Conclusions

The refractory alloy Cb-1% Zr was chosen as the most favorable material presently available for the condenser applications under study. This choice was made for the cases where either lithium or NaK would be used as coolants. Although the condenser itself can operate effectively for long durations with other more conventional engineering materials, a refractory alloy is needed for the boiler due to temperatures of approximately 2000°F. As indicated above, Cb-1% Zr is susceptible to mass transfer type corrosion when other materials are present within the system.

The refractory metals and alloys were the only materials that could satisfactorily resist lithium corrosion at high temperatures. Columbium appears to be the best of the refractory metals for corrosion resistance. The alloy Cb-1% Zr has similar resistance to corrosion and has higher strength at elevated temperatures than its base metal.

Other columbium-base alloys which have higher strength characteristics than Cb-1% Zr are being investigated for corrosion resistance. However, at present, considerable experience on corrosion resistance and on fabrication techniques is available only for Cb-1% Zr.

The most favorable method of joining Cb-1% Zr tubes to tubesheets is to seal-weld the tubes ends to the sheets and diffusion-bond the tubes to the mating holes using vanadium inserts. The welding must be done in an inert gas atmosphere and preferably using a high speed process such as the cone-arc method. All other joints can be TIG-welded manually.

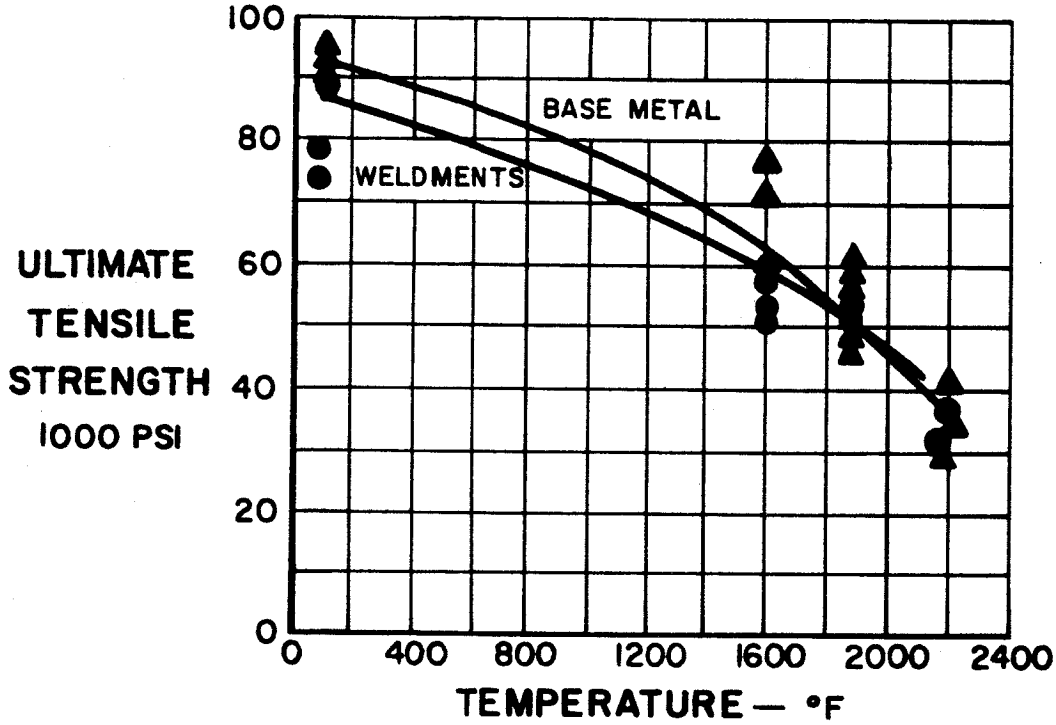

Figure A6 Ultimate Tensile Strength vs Temperature for Electron-Beam Weldments and Base Metal of Molybdenum-0.5% Titanium (Ref. A57)

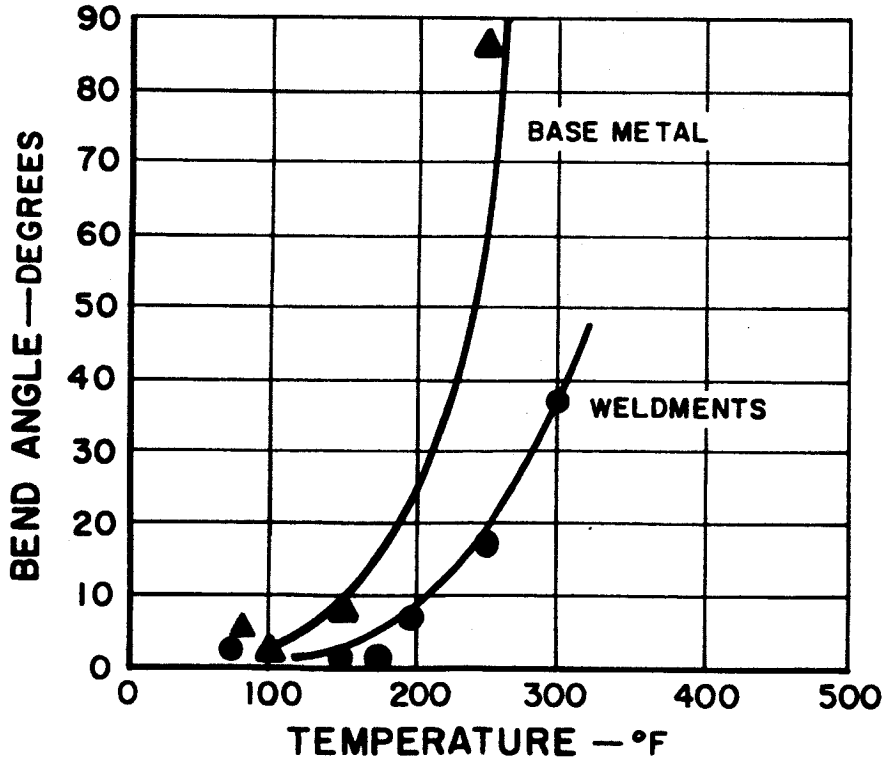

Figure A7 Bend Ductility vs Temperature for Electron-Beam Weldments and Base Metal of Molybdenum-0.5% Titanium (Ref. A57)

APPENDIX A
References

A 1. Brasunas, A., Liquid Metal Corrosion, Corrosion, May 1953, pp. 78-84

A 2. Semmel, J. W., Liquid Metal Investigation, Presented at NASA-AEC Liquid Metals Corrosion Meeting, Dec. 1961

A 3. Vrieland, D. C., E. E. Hoffman and W. D. Manley, Corrosion Tests for Liquid Metals, Fused Salts at High Temperatures, Nucleonics, Nov. 1953, pp. 36-39

A 4. Amateau, M. F., The Effect of Molten Alkali Metals on Containment Metals and Alloys at High Temperature, Battelle Memorial Institute, DMIC 169, May 1962

A 5. Anderson, R. C., and H.R. Stephan, Program Report on Materials Tested in Lithium, NEPA-1652, August 1950

A 6. Jesseman, D.S., and G.D. Robin, Preliminary Investigation of Metallic Elements in Molten Lithium, NEPA-1465, June 8, 1950

A 7. Hoffman, E. E., Corrosion of Materials by Lithium at Elevated Temperatures, ORNL-2924, Oct. 1960

A 8. Day, R. B., and A. Brasunas, Testing and Examination of Thermal Convection Loop Operated with Lithium and Lead, Y-F 31-4, Aug. 1951

A 9. Cunningham, J. E., Resistance of Metallic Materials to Corrosion Attack by High Temperature Lithium, CF-51-7-135, July 1951

A10. Kelly, K. J., Sheet No. 1, Nucleonics Panel Discussion 11/19/63, Corrosion of High Temperature Materials in Alkali Metals

A11. Hoffman, E. E., Boiling Alkali Metals and Related Studies, Presented at NASA-AEC Liquid Metals Corrosion Meeting, Dec. 1960, NASA TN D-769

A12. Kovacevick, E. A., Potassium Corrosion Studies, Presented at NASA-AEC, Liquid Metals Corrosion Meeting, Dec. 1961

A 13. Chandler, W. J., Alkali-Metal Corrosion Studies, Presented at NASA-AEC Liquid Metals Corrosion Meeting, Dec. 1961

A 14. Teitel, R. J., Alkali Metal Corrosion Studies, Presented at NASA-AEC Liquid Metals Corrosion Meeting, Dec. 1960, NASA TN D-769

A 15. Compatibility of Materials with High Temperature Potassium, Third Quarterly Progress Report, NP-10147, Nov. 1960, Rocketdyne Division

A 16. Compatibility of Materials with High Temperature Potassium, Second Quarterly Progress Report, NP-10005, August 1 to October 31,1960, Rocketdyne Division

A 17. Semmel, J. W., W. R. Young, and W. H. Kearns, Alkali Metals Boiling and Condensing Investigations, Volume II Materials Support, G. E. 63FPD66, Jan. 14,1963

A 18. Evaluation of AS-55 and Other High Strength Columbium Alloys for Alkali Metal Containment, General Electric Company, March 25, 1963 to April 25, 1963

A 19. Lewis, J. P., Liquid Metal Research at NASA-Lewis,Proceedings of 1962 High-Temperature Liquid-Metal Heat Transfer Technology Meeting, Brookhaven National Laboratory, BNL 756 (C-35), May 1962

A 20. Miller, E. C., Corrosion of Materials by Liquid Metals, Liquid-Metals Handbook, NAVEX05-P-733 (Rev.), June 1962, p. 158, Washington, D. C.

A 21. Perlow, M. A., and J. R. Crosby, Liquid-Metal Corrosion Research in the SNAP Developmental Program, Presented at NASA-AEC Liquid Metals Corrosion Meeting, Dec. 1960, NASA TN D-769

A 22. Perlow, M. A., and J. P. Page, Liquid Metal Corrosion Research in the SNAP Development Program, Presented at AEC-NASA Liquid Metals Corrosion Meeting, Dec. 1961

A 23. Simons, E. M., Liquid and Vapor Alkali-Metal Corrosion, Presented at NASA-AEC Liquid Metals Corrosion Meeting, Dec. 1960, NASA TN D-769

A 24. The Corrosion of Refractory Materials in Sodium, North American Aviation, NAA-SR-126, Nov. 20, 1951

A 25. Brasunas, A., Interim Report on Static Liquid-Metal Corrosion, ORNL-1647, July 1954

A 26. Semmel, J. W., Liquid-Metal Investigation, Presented at NASA-AEC Liquid Metals Corrosion Meeting, Dec. 1960, NASA TN D-769

A 27. Fleitman, A., A. Romano, and C. Klamut, Vapor-Liquid Corrosion Studies in Mercury and Sodium Systems, Presented at NASA-AEC Liquid Metals Corrosion Meeting, Dec. 1961

A 28. Materials in Design Engineering, Materials Selector Issue, 10/63

A 29. Goldsmith, Waterman, and Hirschhorn, Handbook of Thermophysical Properties of Solid Materials, Vol. 1, The Macmillan Company, New York, 1961

A 30. Engineering Data for 0.5 Titanium-Molybdenum Alloy, Climax Molybdenum Company, April 1956

A 31. Deem, H. W., and J. Matolich, The Thermal Conductivity and Electrical Resistivity of Liquid Potassium and the Alloy Niobium - 1 Zirconium, Battelle Memorial Institute BATT-4673-16, April 30, 1963

A 32. Physical and Mechanical Properties of Molybdenum and the Mo-0.5 Ti Alloy, Battelle Memorial Institute, DMIC Memorandum 14, April 10, 1959

A 33. Tottle, C. R., The Physical and Mechanical Properties of Niobium, J. Inst. Metals, 85, 377, April 1957

A 34. Arc-Cast Molybdenum and its Alloys, Universal-Cyclops Steel Corporation, AVC-Mol-862, 1962

A 35. Heal, T. J., The Mechanical and Physical Properties of Magnesium and Niobium Canning Materials, Second U.N. International Conference of the Peaceful Uses of Atomic Energy, Geneva, 1958

A 36. Columbium and Tantalum Base Alloys for Structural and Nuclear Applications, Wah Chang Corp., Vol. 1, Rev 2, 1962

A 37. Creep-Rupture Data on the 0.5% Titanium Molybdenum Alloy at 1000 to 2400°F, Climax Molybdenum Co., Sept. 1957

A 38. Levy, A. V. and S. E. Bramer, Molybdenum-Vanguard Material for Space Vehicles, p 41-46, SAE Journal, August 1959

A 39. Brady, J. F. and J. N. Ong, Oxidation Rate of Columbium as a Function of Temperature and Pressure, Columbium Metallurgy, pp. 719-739, Interscience Publishers, New York, 1961

A 40. Briggs, J. Z., and R. R. Freeman, Molybdenum for High Strength at High Temperatures, Jet Propulsion, Vol. 27, No. 2, Part I, pp. 138-147, Feb. 1957

A 41. Schmidt, F. F., and H. R. Ogden, The Engineering Properties of Molybdenum and Molybdenum Alloys, Battelle Memorial Institute, DMIC Report 190, Sept. 20, 1963

A 42. Houck, J. A., Physical and Mechanical Properties of Commercial Molybdenum-Base Alloys, Battelle Memorial Institute, DMIC Report 140, November 30, 1960

A 43. Schmidt, F. F., and H. R. Ogden, The Engineering Properties of Columbium and Columbium Alloys, Battelle Memorial Institute, DMIC Report 188, Sept. 6, 1963

A 44. Bartlett, E. S. and J. A. Houck, Physical and Mechanical Properties of Columbium and Columbium-Base Alloys, Battelle Memorial Institute, DMIC Report 125, February 22, 1960

A 45. Williams, L. R., and J. J. Heal, The Consolidation, Fabrication and Properties of Niobium, Third Plansee Proceedings, 1958

A 46. Northcott, L., Molybdenum, Butterworths Scientific Publications, London, 1956

A 47. Lucks, C. F., and H. W. Deem, The Thermal Conductivities, Heat Capacities, and Linear Expansion of Five Materials, WADC Technical Report 55-496, August 1956

A 48. Patriarca, P., G. M. Slaughter, and W. D. Manly, Heat-Exchanger Fabrication, Welding Journal, 36, (12), 1172-78, 1957

A 49. Slaughter, G. M. and P. Patriarca, Welding and Brazing of High-Temperature Radiators and Heat Exchangers, ORNL-TM-147, Feb. 20, 1962

APPENDIX B

Nomenclature

APPENDIX B

Nomenclature

Symbol	Definition	Dimensions
A	surface area	ft^2
B	blockage	--
C_f	coefficient of skin friction	--
C_p	specific heat at constant pressure	$Btu/lb_m\ °F$
C_s	specific heat at saturated conditions	$Btu/lb_m\ °F$
D	diameter	ft
F	wall shear stress parameter = $\tau_w g_c$	$lb_m/ft\ hr^2$
f	friction factor	--
G	mass velocity of fluid	$lb_m/hr\ ft^2$
G_{cr}	critical mass velocity	$lb_m/hr\ ft^2$
g_c	Newton's conversion factor	$lb_m ft/lb_f\ hr^2$
h	heat transfer coefficient	$Btu/hr\ ft^2\ °F$
J	thermal conversion factor (778 ft-lb_f/Btu)	--
k	thermal conductivity	$Btu/hr\ ft\ °F$
k	slip ratio	--
L	total length	ft
ℓ	length	ft
M	molecular weight	lb_m/lb-mole
M_i	initial Mach number of vapor entering condensing passage	--
m	mass flux	lb_m/hr
N	number of condenser tubes	--
n	Deissler constant, 0.124	--
n	number of tube rows	--
Nu	Nusselt number	--
P	pitch (center-to-center distance between adjacent tubes)	ft
P	static pressure	lb_f/ft^2
P_T	total pressure	lb_f/ft^2
ΔP	change in pressure	lb_f/ft^2

Symbol	Definition	Dimensions
Pe	Peclet number	--
Pr	Prandtl number	--
Q	overall heat transferred	Btu/hr
q	velocity head	lb_f/ft^2
q_w	local heat flux at wall	Btu/hr ft^2
r	radius	ft
r_1	radius from tube center to liquid-vapor interface	ft
r_2	tube inside radius	ft
Re	Reynolds number	--
R	universal gas constant	ft-lb_f/lb-mole °R
R_G	local volume fraction of vapor in condensing passage	--
R_L	local volume fraction of liquid in condensing passage	--
S	entropy	Btu/lb_m °F
T	temperature	°F
ΔT	driving potential or change of fluid temperature	°F
t	thickness of wall	ft
U	overall heat transfer coefficient	Btu/hr ft^2 °F
u	velocity	ft/hr
u^+	$u/\sqrt{\tau_w/\rho_L}$	--
V	average velocity	ft/hr
V	volume	ft^3
v	specific volume	ft^3/lb_m
W	total flow rate	lb_m/hr
X	Lockhart and Martinelli two-phase flow parameter	--
x	quality	--
y	distance measured radially inward from tube wall	ft
y^+	$\frac{y}{\nu}\sqrt{\frac{\tau_w}{\rho_L}}$	--
α	ratio of eddy transport coefficients, ϵ_H/ϵ_m	--

Symbol	Definition	Dimensions
$\bar{a}$	mean ratio of eddy transport diffusivities	--
β	increment taper	1/ft
Γ	mass flow rate of condensate per unit of wetted tube circumference	lb_m/hr ft
γ	condenser taper	1/ft
δ	liquid film thickness	ft
δ^+	dimensionless liquid film thickness	--
λ	latent heat of vaporization	Btu/lb_m
μ	dynamic viscosity	lb_m/hr ft
ν	kinematic viscosity	ft^2/hr
ρ	density	lb_m/ft^3
σ	$\frac{\text{no. of molecules striking interface which condense}}{\text{total no. of molecules striking interface}}$	--
τ_v	vapor shear stress	lb_f/ft^2
τ_w	wall shear stress	lb_f/ft^2
ϕ	Lockhart and Martinelli two-phase flow parameter	--
$\varkappa$	von Karman mixing length constant	--
ϵ_H	eddy transport coefficient for heat	ft^2/hr
ϵ_M	eddy transport coefficient for momentum	ft^2/hr

Subscripts

cold	cold fluid
cond	condensing fluid
cool	coolant fluid
cr	critical
film	condensate film
fg	difference between conditions of saturated vapor and saturated liquid
G	gas
hot	hot fluid
i	inside or inlet

Symbol	Definition	Dimensions
	Subscripts	
initial	initial conditions	
int	conditions at the liquid-vapor interface	
k	at constant slip ratio (Appendix J)	
L	liquid	
lm	logarithmic mean	
m	mean	
mw	mean wall	
o	outside or initial	
out	outlet conditions	
p	at constant pressure (Appendix J)	
s	shell	
S	at constant entropy (Appendix J)	
sat	saturation conditions	
T	total or tube	
t_p	two phase	
tpf	two phase friction	
tt	turbulent liquid-turbulent vapor	
tv	turbulent liquid-viscous vapor	
vt	viscous liquid-turbulent vapor	
vv	viscous liquid-viscous vapor	
w	conditions at the wall	
x	at constant quality (Appendix J)	
I	refers to the beginning point of an increment	
II	refers to the end point of an increment	

APPENDIX C

References

APPENDIX C

References

1. Dwyer, O. E., AIChE Journal, Vol. 9, No. 2, p. 261, March 1963

2. Lyon, R. N., Liquid Metal Heat Transfer Coefficients, Chemical Engineering Progress, Vol. 47, No. 2, February 1951, pp 75-79

3. Martinelli, R. C., Trans. ASME, Vol. 69, No. 8, pp 947-959, Nov. 1947

4. Lockhart, R. W. and R. C. Martinelli, Chem. Eng. Prog. Symp. Series, Vol. 45, No. 1, p. 39, 1949

5. McAdams, W. H., Heat Transmission, 3rd ed., McGraw-Hill, New York, 1954

6. Nikuradse, J., Gesetzmassigkeiten der Turbulenten Stromung in Glatten Rohren, Forschungsheft 356, 1932

7. Reichardt, H. , Heat Transfer through Turbulent Friction Layers, NASA Technical Memorandum No. 1047, September 1943

8. Seban, R. A., and T. T. Shimazaki, Heat Transfer to a Fluid Flowing Turbulently in a Smooth Pipe with Walls at Constant Temperature, Paper No. 50-A-128, ASME, 1950

9. Seban, R. A., Heat Transfer to a Fluid Flowing Turbulently Between Parallel Walls with Asymmetric Wall Temperatures, Trans. ASME, Vol. 72, No. 6, August 1950, pp. 789-795

10. Bailey, Raymond V., Heat Transfer to Liquid Metals in Concentric Annuli, ORNL 521, Tech. Div., Eng. Res. Section, Oak Ridge Nat. Lab., June 13, 1950 (Contract No. W-7405, eng. 26)

11. Lubarsky, B., and S. J. Kaufman, NACA Tech. Note 3336, March 1955

References (Cont'd)

12. Jenkins, R., Heat Transfer and Fluid Mechanics Institute, p. 147, Stanford University Press, 1951

13. Deissler, R. G., NACA Research Memo E52 F05, 1952

14. Lykoudis, P. S. and T. S. Touloukian, Trans. ASME, Vol. 80, No. 3, 653, 1958

15. Rohsenow, W. M. and S. Cohen, The Influence of the Ratio of Eddy Diffusivities on Heat Transfer to Liquid Metals, MIT Heat Transfer Lab. Report, June 1960

16. Mizushina, T. and T. Sasano, Paper No. 78 presented at 1961 International Heat Transfer Conference, Boulder, Colorado

17. Azer, N. Z. and B. T. Chao, Int. Journal Heat and Mass Transfer, Vol. 1, No. 1, 121, 1960

18. Isakoff, E., and T. B. Drew, Heat and Momentum Transfer in Turbulent Flow of Mercury, General Discussion on Heat Transfer, Inst. Mech. Eng. and ASME, 1951, pp. 405-409

19. Brown, H. E., B. H. Amstead, and B. E. Short, Trans. Am. Soc. Mech. Engrs., Vol. 79, No. 2, p. 279, 1957

20. Subbotin, V. I., M. Kh. Ibraginov, M. N. Ivanovskii, M. N. Arnol'bov, and E. V. Nomofilov, Heat Transfer from the Turbulent Flow of Liquid Metals in Tubes, Soviet Journal of Atomic Energy, Vol. 11, pp 769-775

21. Kirillov, P. L., V. I. Subbotin, M. Ya. Suvorov, and M. F. Troyanov, Heat Transfer in Pipes to a Sodium-Potassium Alloy and to Mercury, Journal of Nuclear Energy, Part B - Reactor Technology, Vol. 1, No. 2, Aug. 1959, pp. 123-129

22. Pirogov, M. S., Atomnaya Energiya, Vol. 8, No. 4, p 367, 1960

23. Petukhov, B. S., and A. Y. Yushin, Soviet Physics - Doklady, Vol. 6, No. 2, p. 159, 1961

References (Cont'd)

24. Subbotin, V. I., M. Kh. Ibraginov, Y. V. Nomofilov, Atomnaya Energiya, Vol. 14, p. 414, 1963

25. Petrovichev, V. I., Heat Transfer in Mercury Flow through Annular Channels, Soviet Journal of Atomic Energy, Vol. 7, No. 4, pp. 844 - 847

26. Maresca, M. W., and O.E. Dwyer, Heat Transfer to Mercury Flowing In-Line Through a Bundle of Circular Rods, ASME Paper No. 63-HT-29, 1963

27. Winsche, W. E., and F. T. Miles, Brookhaven National Laboratory Progress Report for Nuclear Engineering Department, BNL 782 (S-63), Brookhaven National Laboratory, Upton, New York, September 1 to December 31, 1962

28. Stein, R. P., Heat Transfer Coefficients in Liquid Metal Co-Current Flow Double Pipe Heat Exchangers, paper presented at Third Annular AEC High-Temperature Liquid-Metal Heat Transfer Conference, ORNL, September 1963

29. Eckert, E. R. G. and R. M. Drake, Jr., Heat and Mass Transfer, McGraw-Hill, New York, 1959, p. 301

30. Rohsenow, W. M. and H. Choi, Heat, Mass, and Momentum Transfer, Prentice-Hall, Englewood, Cliffs, N. J., 1961

31. Friedland, A. J. and C. F. Bonilla, Analytical Study of Heat Transfer Rates for Parallel Flow of Liquid Metals Through Tube Bundles II, AIChE Journal, Vol. 7, No. 1, March 1961, pp. 107-112

32. Nusselt, W., Zeitsch, d. ver. deutch Ing. 60, 541-9, 1916

33. Rohsenow, W. M., Trans. ASME 78, 1645-8, 1956

34. Sparrow, E. M. and J. L. Gregg, Trans. ASME Journal of Heat Transfer, Ser. C. 81, 13-18, 1959

References (Cont'd)

35. Koh, J. C. Y., E. M. Sparrow and J. P. Hartnett, Int. Journal of Heat and Mass Transfer, 2, 69-82, 1961

36. Chen, M. M., Trans. ASME, Journal of Heat Transfer, 83, 48-60, 1961

37. Koh, J. C. Y., Trans. ASME, Journal of Heat Transfer, 83, 359-62, 1961

38. Colburn, A. P., Trans. AIChE., 30, 187, 1933

39. Kirkbride, C. G., Trans. AEChE, 30, 170, 1933

40. Seban, R. A., Trans. ASME, 76, 299, Feb. 1954

41. Rohsenow, W. M., T. H. Weber, and A. T. Ling, Trans. ASME, 78, 1637-43, 1956

42. Carpenter, E. F., and A. P. Colburn, Proc. General Disc., Heat Transfer Inst. of Mech. Engr. and ASME, pp. 20-26, July 1951

43. Altman, M., F. W. Staub and R. H. Norris, Chem. Eng. Progr., Symp. Vol. 56, No. 36, p. 151, 1960

44a. Dukler, A. E., Chem Eng. Prog. Symp. Series Vol. 56, No. 30, pp. 1-10, 1960

44b. Dukler, A. E., Appendix to 44a Document 6058. American Documentation Inst., Photoduplication Service, Library of Congress, Washington, D. C.

45. Deissler, R. G., NACA Tech. Notes 2129 (1950) and 2138 (1952) and NASA Tech. Note 3145 (1959)

46. Dukler, A. E., Comparison of Theoretical and Experimental Film Thickness, ARS Journal, Jan. 1961, p. 86

47. Misra, B. and C. F. Bonilla, Chem. Eng. Progr. Symp., Vol. 52, No. 2, pp. 7-21, 1956

References (Cont'd)

48. Brooks, R. D. and S. G. Sawochka, Alkali Metal Two-Phase Heat Transfer for Space Power - Present Status, ARS Preprint 2547-62, 1962

49. Sukhatme, S. P. and W. M. Rohsenow, Heat Transfer During Film Condensation of a Liquid Metal Vapor, Paper presented at the Third Annual High Temperature Liquid Metal Heat Transfer Meeting, Oak Ridge National Lab., Sept. 4-6, 1963, AEC Contract No. AT(30-1)-2995

50. Schrage, R. W., A Theoretical Study of Interphase Mass Transfer, Columbia University Press, New York, 1953

51. Sukhatme, S. P. and W. M. Rohsenow, AEC Contract AT(30-1)-2995, Report No. 10, 224, Nov. 1963

52. Carpenter, F., Heat Transfer and Pressure Drop for Condensing Pure Vapors Inside Vertical Tubes at High Vapor Velocities, PhD Thesis, University of Delaware, 1948

53. Knudsen, M., Kinetic Theory of Gases, pp. 13-51, Methuen Company, London, 1934

54. Lottes, P. A., Nuclear Science and Eng. 9, p. 26-31, 1961

55. Straub, L. G. and E. Silberman, Air-Water Mixture Flow Through Orifices, Bends, and Other Fittings in a Horizontal Pipe, Project Report No. 63, St. Anthony Falls Hydraulic Laboratory, University of Minnesota, Sept. 1960

56. Binder, R. C., Fluid Mechanics, Third Edition, Prentice Hall, Englewood Cliffs, 1955

57. Hays, L., Investigations of Condensers Applicable to Space Power Systems, Part I, Direct Condensers, Electro-Optical Systems, Inc. Report 1588, Final, Aug. 15, 1962

58. Martinelli, R. C. and D. D. Nelson, Prediction of Pressure Drop During Forced Circulation Boiling of Water, Trans. ASME, Vol. 70, 1948

59. Dukler, A. E., Moye Wicks, III, and R. G. Cleveland, Frictional Pressure Drop in Two-Phase Flow, A.I.Ch.E Journal, Jan. 1964

References (Cont'd)

60. McCabe, W. L. and J. C. Smith, Unit Operations of Chemical Engineering, McGraw-Hill, New York, 1956, p. 108

61. Fauske, H. K., Contribution to the Theory of Two-Phase One-Component Critical Flow, PhD. Thesis, University of Minnesota, 1961

62. Moy, J. E., Critical Discharges of Steam-Water Mixtures, M. S. Thesis, Univ. of Minnesota, 1955

63. Faletti, D. W., Two-phase Critical Flow of Steam-Water Mixtures, PhD. Thesis, Univ. of Washington, 1959

64. Cruz, A. J. R., Critical Discharges of Steam-Water Mixtures, M. S. Thesis, Univ. of Minnesota, 1953

65. Design Report, Advanced Nuclear-Electric Power Generator Systems Study, Rankine-Cycle Nuclear Space Powerplant, Pratt & Whitney Aircraft, Report PWA-2233, Oct. 15, 1963

66. Wyde, S. S. and H. R. Kunz, Experimental Condensing-Flow Stability Studies, Pratt & Whitney Aircraft, Report PWA-2315, 1964

67. Government - Industry Conference on Mercury Condensing, NASA Technical Note D-1188, April 18, 1961, pp. 2-45

APPENDIX D

Tables

TABLE 1

Design Conditions

Design Life - 10,000 hours

A. Parallel Arrangement -- Design Conditions for a single condenser in parallel arrangement

	Lithium-Cooled	NaK-Cooled
Potassium flow rate	1593 lb/hr	1593 lb/hr
Potassium temperature		
inlet	1175°F	1175°F
outlet	1053°F	960°F
Potassium pressure		
inlet	3.95 psia	3.95 psia
outlet	3.41 psia	3.41 psia
Potassium dynamic quality		
inlet	0.83	0.83
outlet	0.00	0.00
Coolant flow rate	7841 lb/hr	28,450 lb/hr
Coolant temperature		
inlet	998°F	945°F
outlet	1150°F	1150°F
Coolant pressure loss	1.2 psi	1.2 psi

B. Series and Segmented-Shell Arrangements

Potassium flow rate	6372 lb/hr	6372 lb/hr
Potassium temperature		
inlet of first condenser or segment	1175°F	1175°F
outlet of last condenser or segment	1053°F	960°F

TABLE 1 (Cont'd)

Potassium pressure		
inlet of first condenser or segment	3.95 psia	3.95 psia
outlet of last condenser or segment	3.41 psia	3.41 psia
Potassium dynamic quality		
inlet of first condenser or segment	0.83	0.83
outlet of last condenser or segment	0.00	0.00
Coolant flow rate for each condenser or segment	7841 lb/hr	28450 lb/hr
Coolant temperature		
inlet of each condenser or segment	998°F	945°F
outlet of each condenser or segment	1150°F	1150°F
Coolant pressure loss of each condenser or segment	1.2 psi	1.2 psi

TABLE 2

Comparison Between Tube Lengths and Core Weights Calculated for a Lithium-Cooled Constant-Diameter Shell-and-Tube Condenser Using Different Methods for Predicting Condensing Heat Transfer Coefficients

Method	Tube Length-Inches	Core Weight-Pounds
1) Carpenter and Colburn	5.58	9.68
2) modified film conduction		
a) film transition criterion of Equation (30)	3.59	7.37
b) film transition criterion of Lockhart and Martinelli	3.56	7.34
3) Schrage effect		
a) $\sigma = 0.0168$	19.31	23.02
b) $\sigma = 0.045$	8.33	12.09

Note: Core weight = tube weight + shell weight + tubesheet weight + weight of fluid inventories inside of the shell and the tubes

TABLE 3

Condenser Designs For Parallel Arrangement

List of Condenser Designs

1. Lithium-Cooled Constant-Diameter Configuration
2. Lithium-Cooled Tapered Configuration
3. NaK-Cooled Constant-Diameter Configuration
4. NaK-Cooled Tapered Configuration
5. Lithium-Cooled Annular-Shell Bent-Tube Configuration
6. Lithium-Cooled Concentric-Tube Configuration

Design Number	Material	Number of Tubes	Tube ID at Inlet (inch)	Tube ID at Exit (inch)	Tube Wall Thickness (inch)	Shell ID at Inlet (inch)	Shell ID At Exit (inch)	Shell Wall Thickness (inch)	Tubesheet Thickness (inch)
1	Cb-1% Zr	91	0.335	0.335	0.020	6.54	6.54	0.035	0.420
2	Cb-1% Zr	37	0.680	0.240	0.035	7.30	4.01	0.035	0.560
3	Cb-1% Zr	91	0.335	0.335	0.020	8.10	8.10	0.035	0.420
4	Cb-1% Zr	37	0.720	0.247	0.035	7.96	4.67	0.035	0.560
5	Cb-1% Zr	91	0.335	0.335	0.020	10.54-5.70	Annulus	0.035	0.420
6	Cb-1% Zr	19	1.057 x .020 and 0.300 x .020 Concentric Tubes						0.420

Design Number	P/D at Inlet	P/D at Exit	Condensing Length (inch)	Tubesheet-To-Tubesheet Length (inch)	Coolant Side Inlet and Exit Pipe Dia. (inch)	Potassium Inlet Pipe Inside Dia. (Inch)	Potassium Exit Pipe Inside Dia. (Inch)	Tubesheet to Orifice Plate Distance (inch)	Orifice Plate Thickness (inch)
1	1.60	1.60	6.55	6.80	1.39	3.29	0.430	0.75	0.02
2	1.35	1.84	12.09	15.48	1.30	3.29	0.430	0.50	0.02
3	2.00	2.00	11.03	12.00	2.00	3.29	0.430	0.75	0.02
4	1.44	2.10	16.97	19.71	2.00	3.29	0.430	1.25	0.02
5	**		-	9.00	1.00	3.29	0.430	-	-*
6	**		-	25.91	1.40	3.29	0.430	-	-*

Design Number	Height of Shell-Side Annular †Orifices (inch)	Orifice Hole Diameter ‡ (inch)	Gap Width (inch)	Tube Orifice Dia. (inch)	Approx. Dry Weight (lbs)	Approx. Total Weight*** (lbs)	Approx. Total Volume (ft^3)	Blockage at Inlet	Blockage at Exit
1	0.006	0.083	0.50	0.052	14.8	20.4	0.59	0.354	0.354
2	0.006	0.130	0.30	0.101	20.7	25.3	0.74	0.500	0.268
3	0.006	0.150	0.30	0.054	29.0	46.2	1.45	0.226	0.226
4	0.006	0.132/0.152	0.3/0.5	0.101	29.5	41.2	1.83	0.437	0.205
5	-	-	0.30	0.054	-	43.2	1.54	-	-
6	-	-	1.50/1.00	-	-	37.9	2.46	-	-

* No orifice plate required
** No meaning for P/D
*** Total weight includes weight of manifolds and manifold inventories
† Number of annular orifices equals number of tubes
‡ Number of orifice holes equals twice number of tubes

TABLE 4

Liquid Metal Coolant Properties at 1150°F

	Lithium	NaK (5)
specific heat, Btu/lb °F	0.995(1)	0.2096
dynamic viscosity, lb/ft hr	0.695(2)	0.402
thermal conductivity, Btu/hr ft °F	29.5(3)	14.93
density, lb/ft^3	29.48(4)	45.14

Potassium Properties at Condenser Entrance (1175°F)

	Liquid(5)	Vapor(5)
specific heat, Btu/lb °F	0.1833	0.208
dynamic viscosity, lb/ft hr	0.36	0.04385
thermal conductivity, Btu/hr ft °F	19.72	0.0076
density, lb/ft^3	43.02	0.0078
latent heat of vaporization, Btu/lb	874	

[1] Douglas, T. B., L. F. Epstein, J. L. Dever, and W. H. Howland, Lithium: Heat Content from 0 to 900, Triple point and Heat of Fusion, and Thermodynamic Properties of the Solid and Liquid, JACS 77, 2144, 1955

[2] Andrade, E.N. daC., and Dobbs, The Viscosities of Liquid Lithium, Rubidium, and Cesium, Proc. Roy. Soc. London 211, 12, 1952

[3] Kapelner, S. M., The Electrical Resistivity of Lithium and Sodium Potassium Alloy, PWAC-349, June 30, 1961

[4] U.S. Navy Department, Liquid Metals Handbook, June 1952

[5] Properties of Organic Energy-Conversion and Heat-Transfer Fluids for Space Application, WADD Technical Report 61-96, November 1961

TABLE 5

SUMMARY OF RESULTS FOR LITHIUM-COOLED TAPERED CONDENSER

Case Number	Potassium Temp. out, °F	Inlet Mach Number	Tube I. D. Inches Inlet	Tube I. D. Inches Exit	γ_T, Tube Taper	γ_S, Shell Taper	Total Tube Length, Inches	Condensing Length, Inches	Subcooling Length, Inches	Pressure Loss in Tubes, psi	Pressure Loss in Shell, psi	Initial Blockage
1	1053	0.250	0.680	0.321	0.500	0.336	12.68	12.09	0.59	0.348	0.007	0.500
2	1045	0.250	0.680	0.319	0.500	0.336	12.74	12.09	0.65	0.348	0.007	0.500
3	1030	0.250	0.680	0.314	0.500	0.336	12.91	12.09	0.82	0.348	0.007	0.500
4	1015	0.250	0.680	0.307	0.500	0.336	13.18	12.09	1.09	0.348	0.007	0.500
5	1000	0.250	0.680	0.286	0.500	0.336	13.90	12.09	1.81	0.348	0.007	0.500
6	997	0.250	0.680	0.268	0.500	0.336	14.53	12.09	2.44	0.349	0.007	0.500
7	996	0.250	0.680	0.241	0.500	0.336	15.48	12.09	3.39	0.351	0.008	0.500
8	996	0.250	0.680	0.397	0.400	0.269	12.47	11.79	0.68	0.318	0.007	0.500
9	996	0.250	0.680	0.223	0.600	0.404	15.89	12.62	3.27	0.418	0.010	0.500
10	996	0.225	0.720	0.421	0.400	0.270	12.45	11.78	0.67	0.252	0.006	0.500
11	996	0.225	0.720	0.218	0.500	0.338	16.72	12.01	4.71	0.280	0.007	0.500
12	996	0.225	0.720	0.245	0.600	0.406	15.89	12.38	3.51	0.328	0.008	0.500
13	996	0.300	0.626	0.311	0.400	0.268	15.10	11.93	3.17	0.451	0.009	0.500
14	996	0.300	0.626	0.224	0.500	0.334	15.41	12.44	2.97	0.499	0.011	0.500
15	996	0.300	0.626	0.402	0.600	0.158	16.78	13.66	3.12	0.719	0.016	0.500

TABLE 6

SUMMARY OF RESULTS FOR NaK-COOLED TAPERED CONDENSER

Case Number	Potassium Temp. Out, °F	Inlet Mach No.	Tube I. D. Inches Inlet	Tube I. D. Inches Exit	Tube Taper	Shell Taper	Total Tube Length Inches	Condensing Length Inches	Subcooling Length Inches	Pressure Loss In Tubes, psi	Pressure Loss In Shell, psi	Initial Blockage
1	960	0.225	0.72	0.391	0.350	0.237	15.68	14.15	1.53	0.257	0.039	0.500
2	960	0.225	0.72	0.350	0.350	0.224	17.60	15.87	1.73	0.269	0.027	0.450
3	960	0.225	0.72	0.338	0.350	0.221	18.17	16.38	1.79	0.272	0.024	0.437
4	960	0.225	0.72	0.310	0.370	0.233	18.45	16.59	1.86	0.279	0.026	0.437
5	960	0.225	0.72	0.265	0.400	0.252	18.96	16.97	1.99	0.291	0.029	0.437
6	960	0.250	0.68	0.314	0.350	0.220	18.43	16.62	1.81	0.346	0.031	0.437
7	960	0.250	0.68	0.285	0.370	0.230	18.84	16.94	1.90	0.356	0.032	0.437
8	960	0.250	0.68	0.241	0.400	0.252	19.37	17.34	2.03	0.372	0.037	0.437
9	950	0.225	0.72	0.324	0.350	0.221	18.86	16.38	2.48	0.272	0.025	0.437
10	950	0.225	0.72	0.295	0.370	0.233	19.16	16.59	2.57	0.280	0.026	0.437
11	950	0.225	0.72	0.247	0.400	0.252	19.71	16.97	2.74	0.292	0.029	0.437
12	950	0.250	0.68	0.301	0.350	0.220	19.12	16.62	2.50	0.346	0.031	0.437
13	950	0.250	0.68	0.270	0.370	0.230	19.55	16.94	2.61	0.356	0.033	0.437
14	950	0.250	0.68	0.224	0.400	0.252	20.12	17.34	2.78	0.373	0.037	0.437

APPENDIX E

Figures

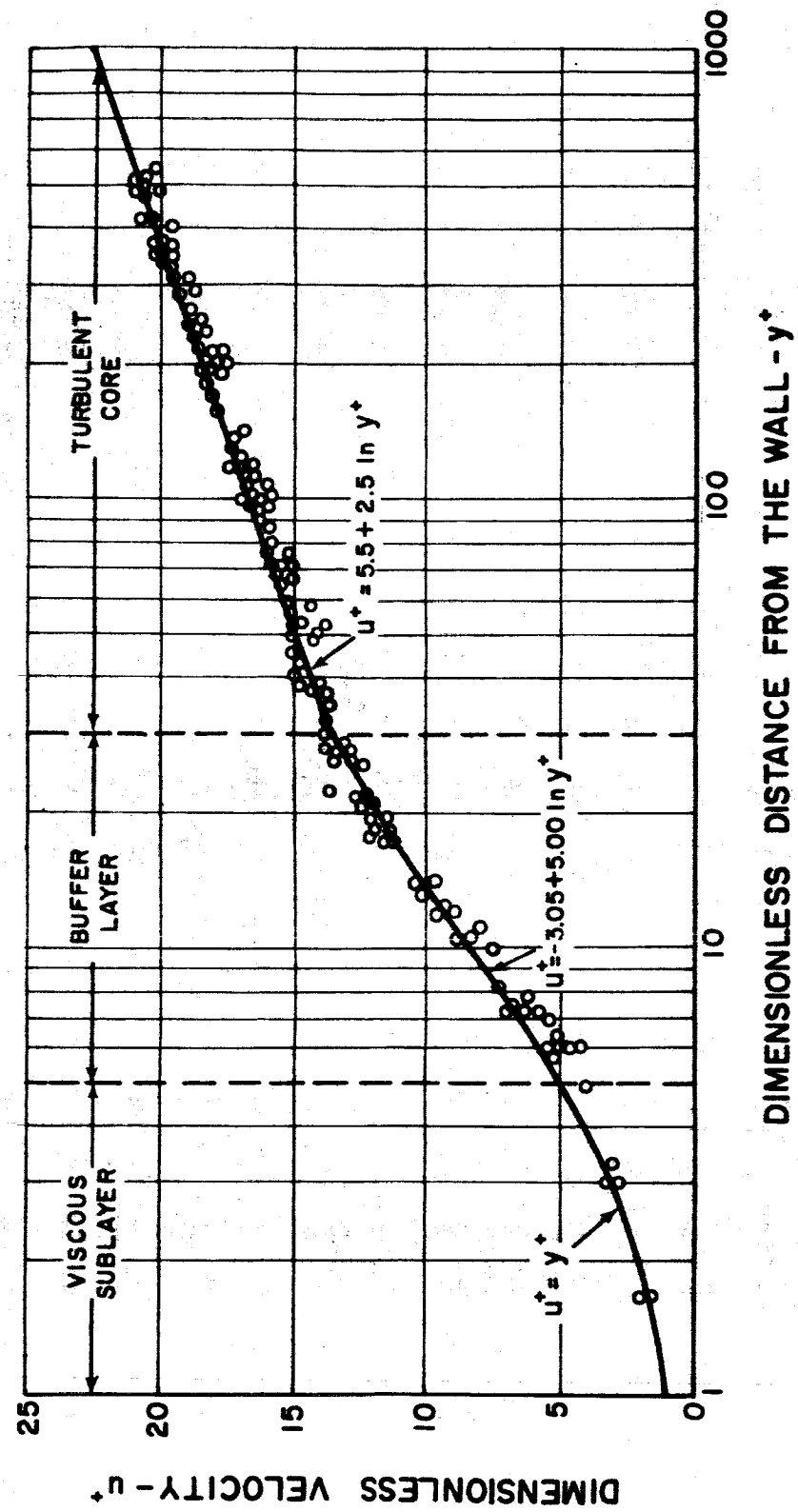

Figure 1 Generalized Velocity Profile

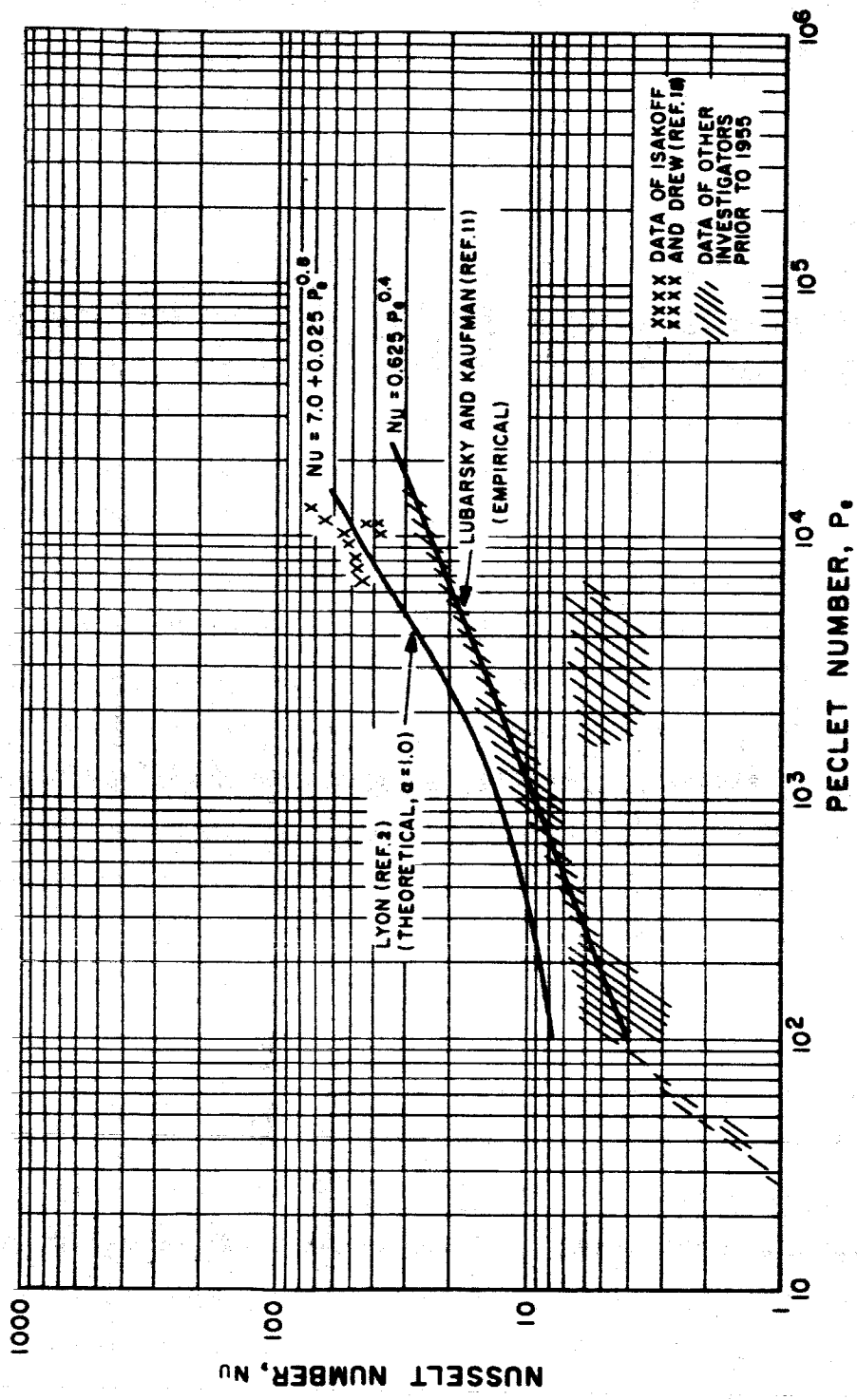

Figure 2 Nusselt Number vs Peclet Number for Forced Convection Flow of Liquid Metals.
Conditions: 1) Fully Developed Turbulent Pipe Flow
2) Uniform Wall Heat Flux

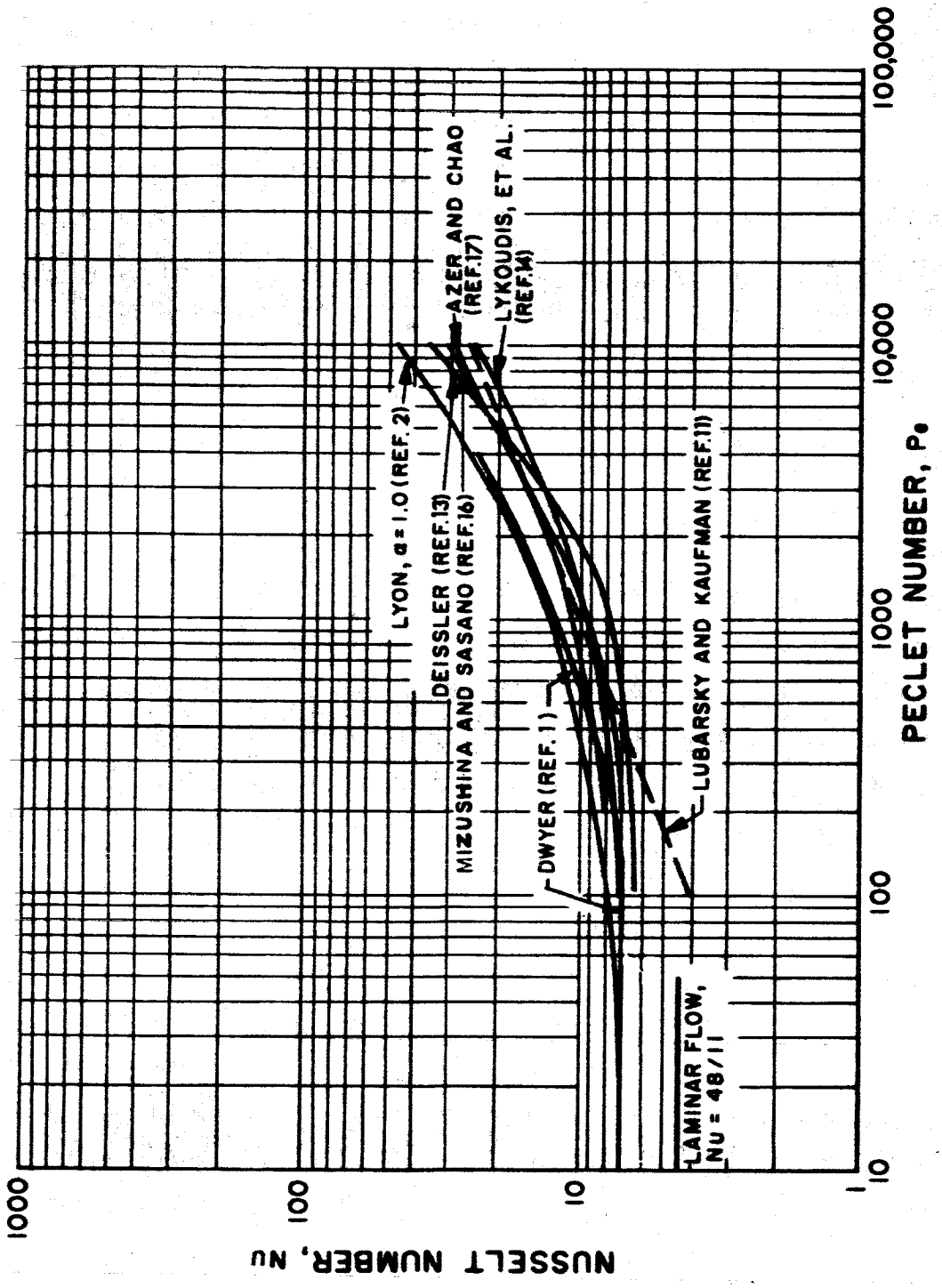

Figure 3 Comparison of Theoretical Heat Transfer Results of Various Investigators for Forced Convection Flow of Liquid Metals.
Conditions: 1) Fully Developed Turbulent Pipe Flow
2) Uniform Wall Heat Flux
3) Prandtl Number = 0.02

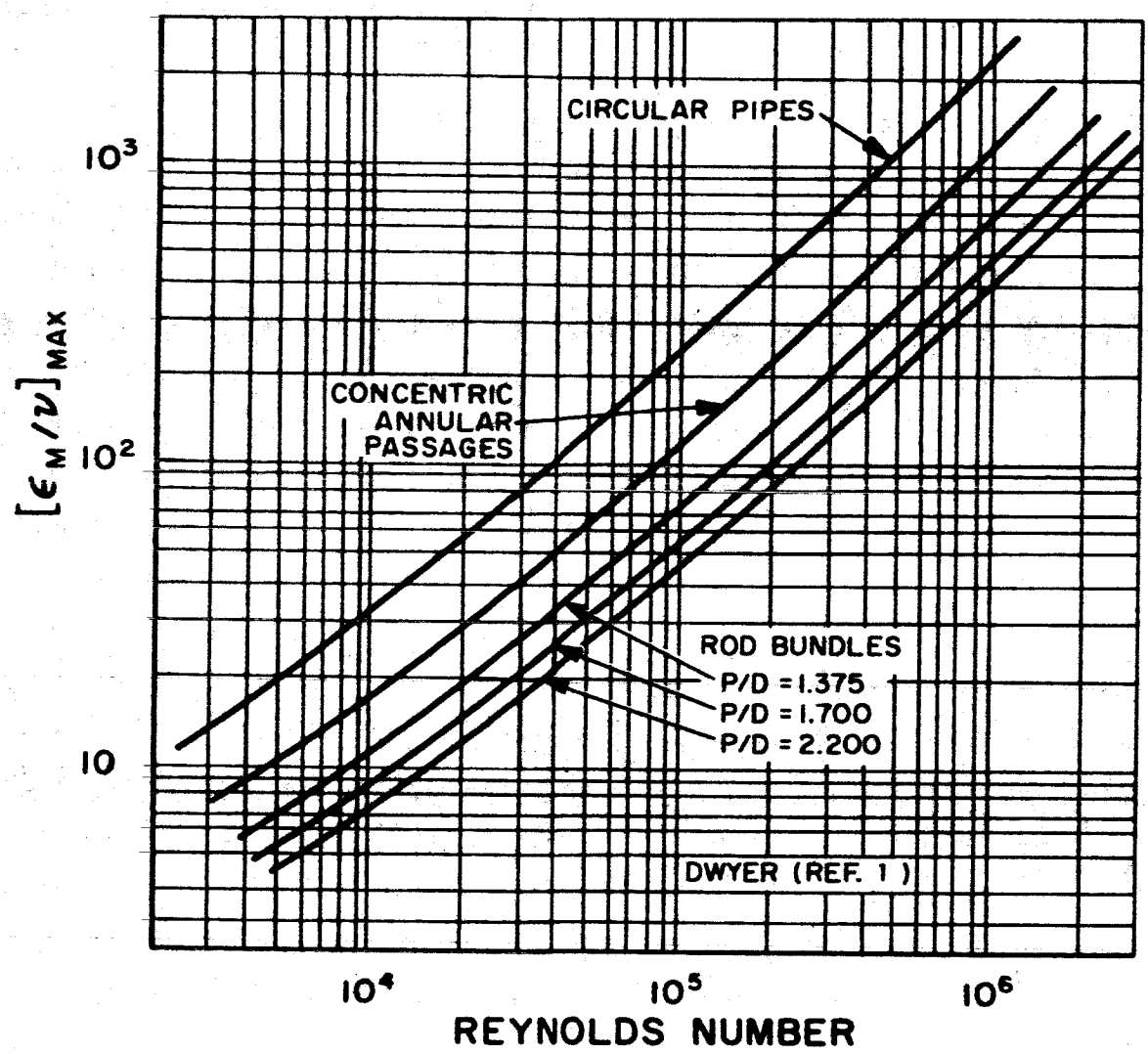

Figure 4 $\left[\frac{\epsilon_M}{\nu}\right]_{max}$ vs Reynolds Number

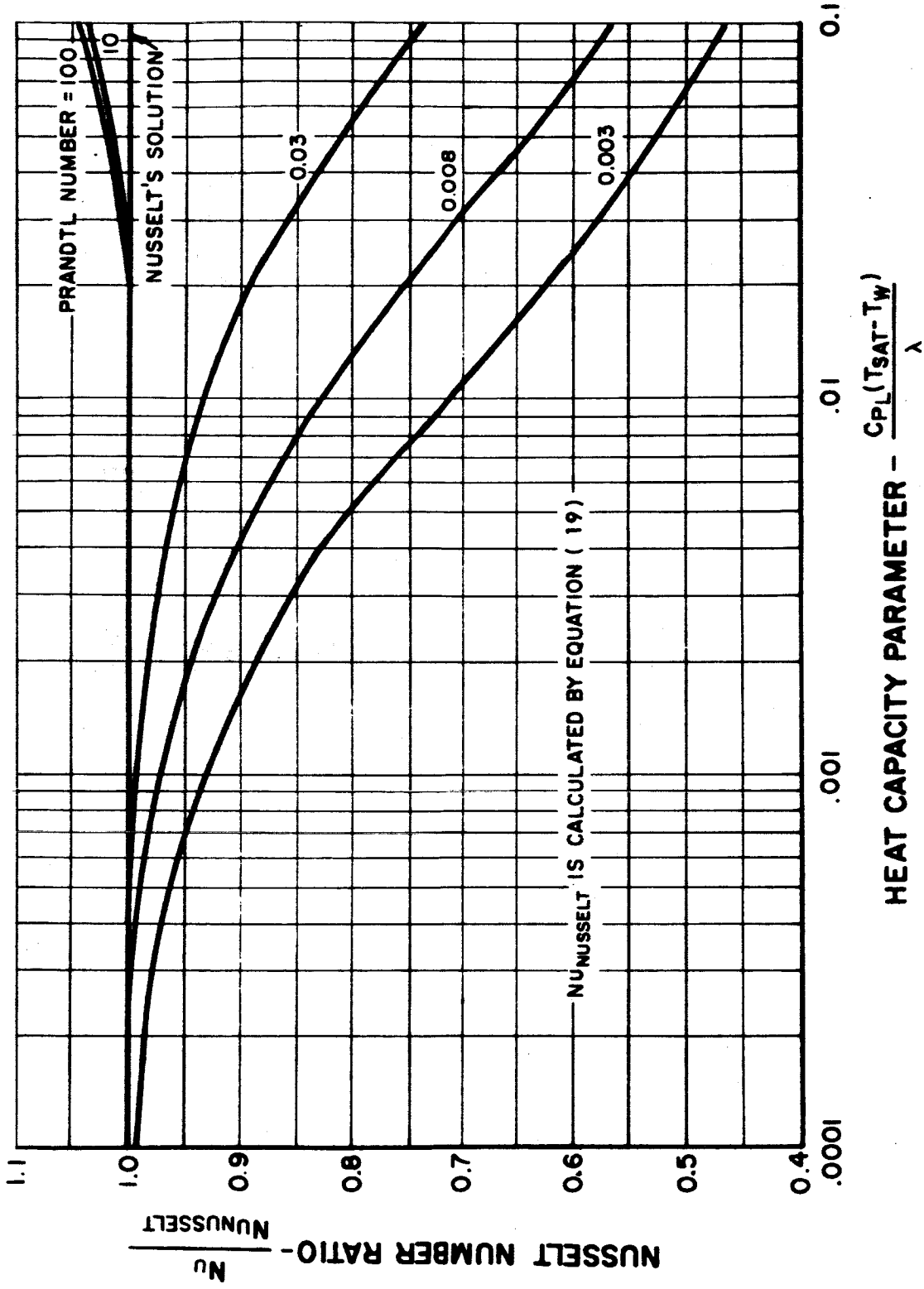

Figure 5 Nusselt Number Ratio vs Heat Capacity Parameter (Koh, Sparrow and Harnett, Ref. 35)

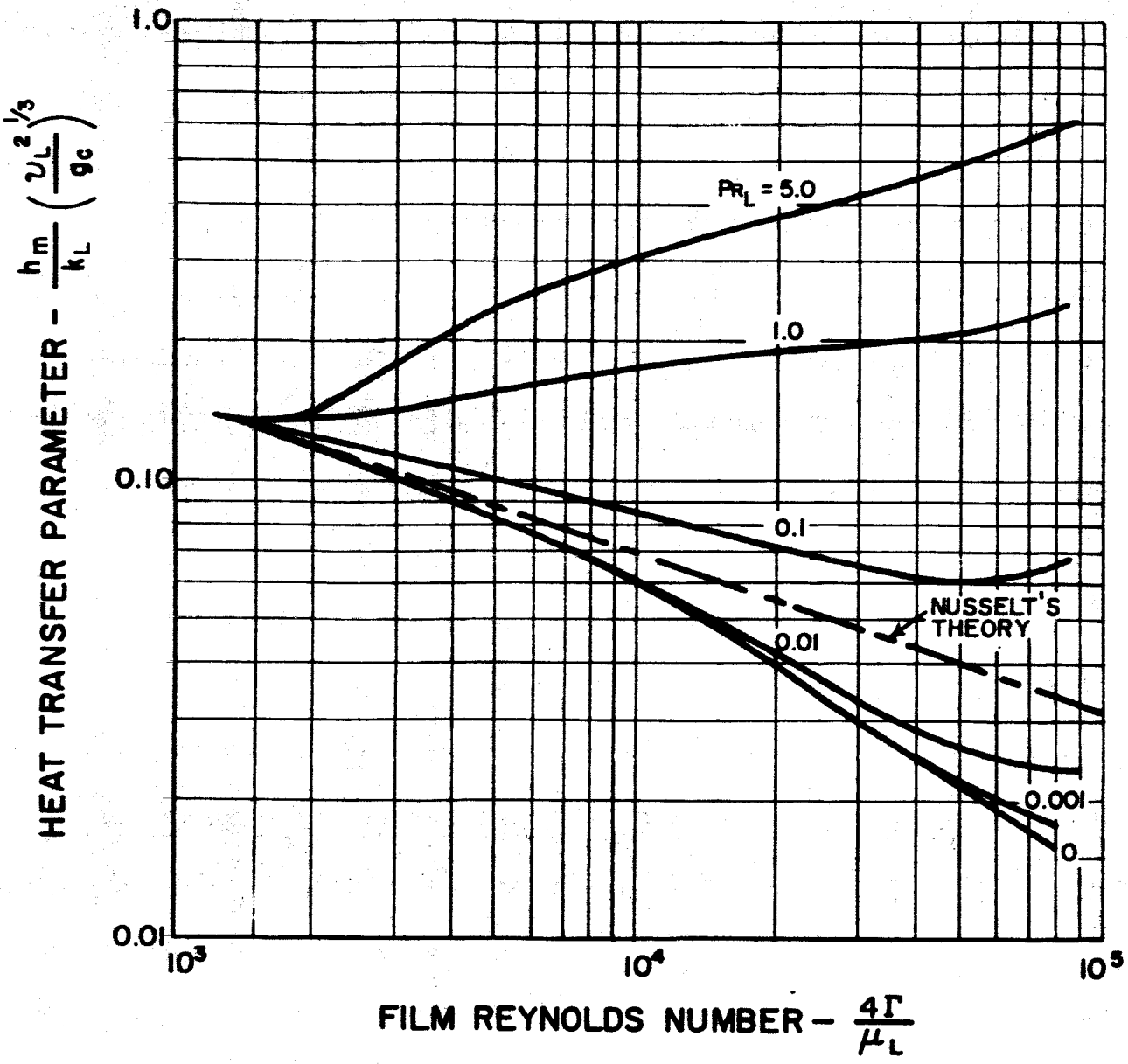

Figure 6 Film Reynolds Number vs Heat Transfer Parameter (Seban, Ref. 40)

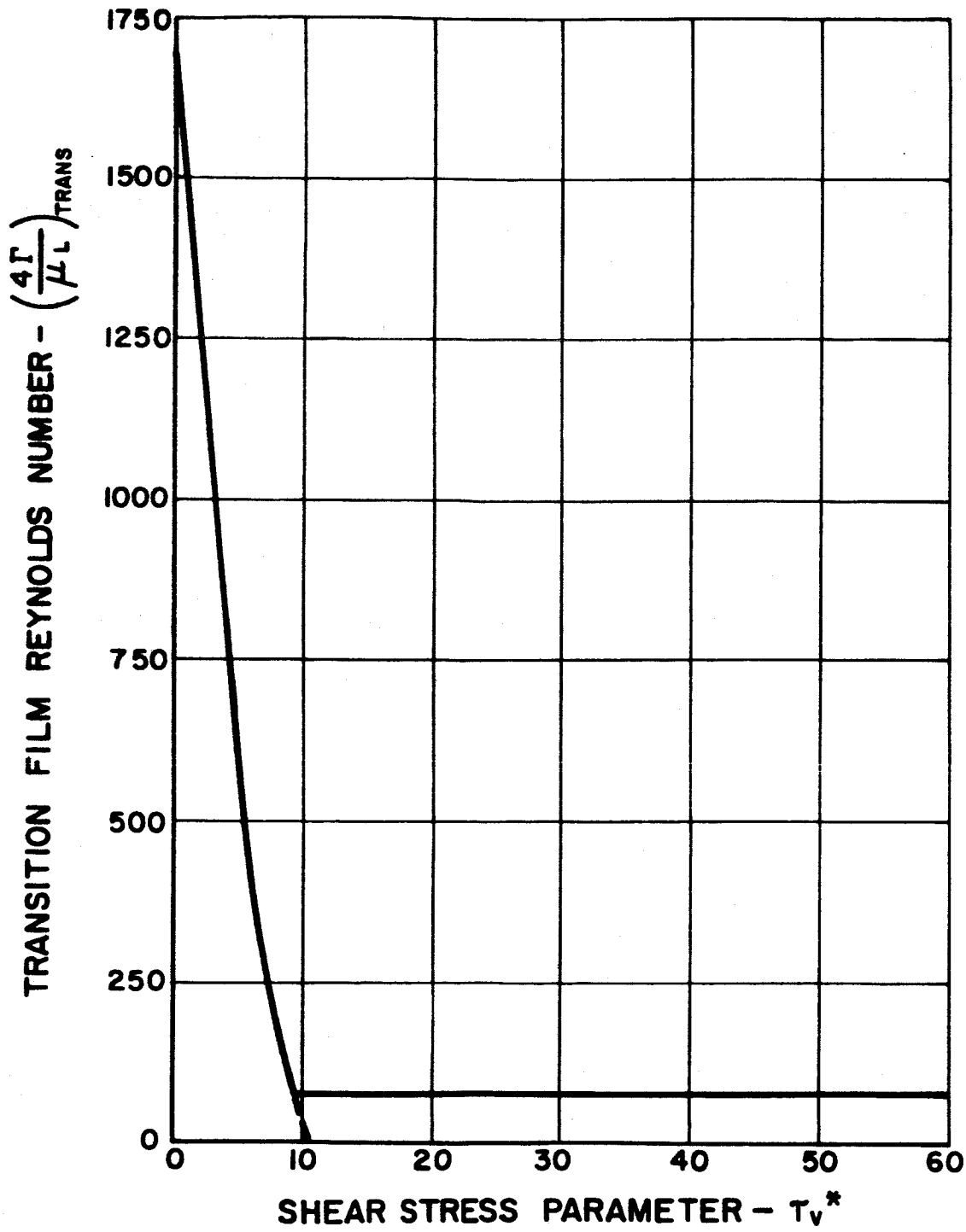

Figure 7 Transition Film Reynolds Number vs Shear Stress Parameter (Rohsenow et al, Ref. 41)

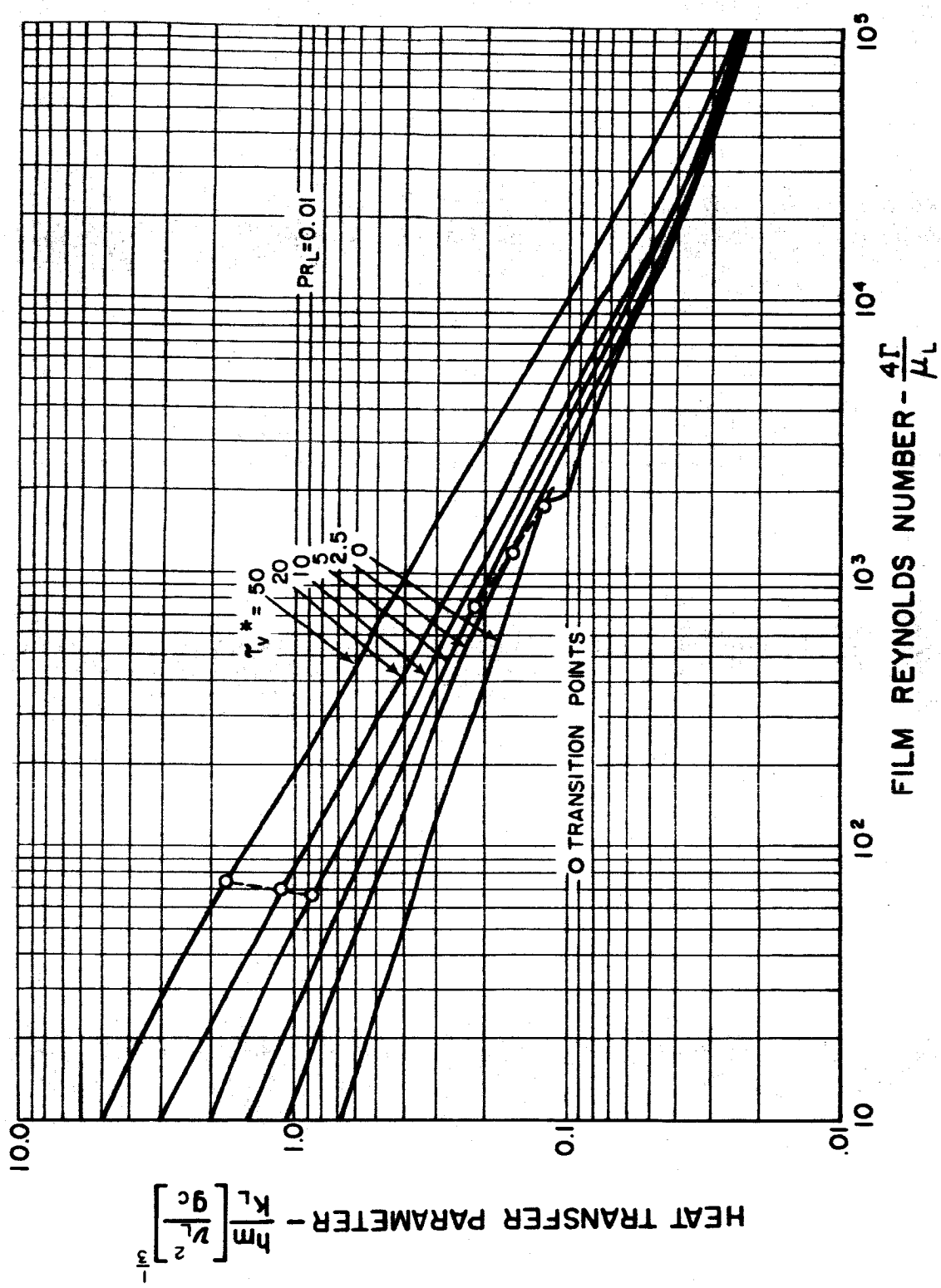

Figure 8 Film Reynolds Number vs Heat Transfer Parameter (Rohsenow, et al, Ref. 41)

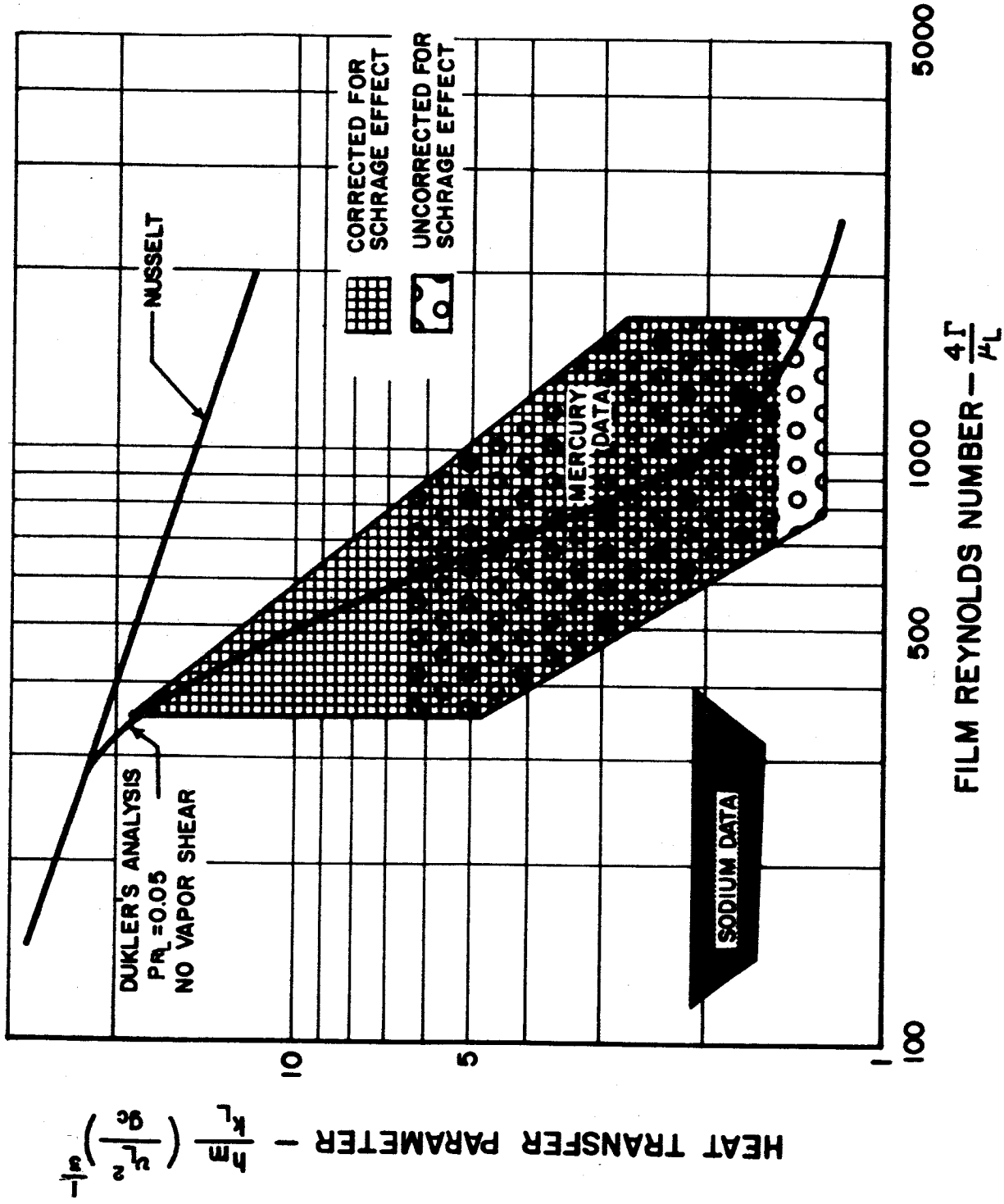

Figure 9 Film Reynolds Number vs Heat Transfer Parameter. Comparison of Theoretical Results with Experimental Data of Misra and Bonilla (Ref. 47)

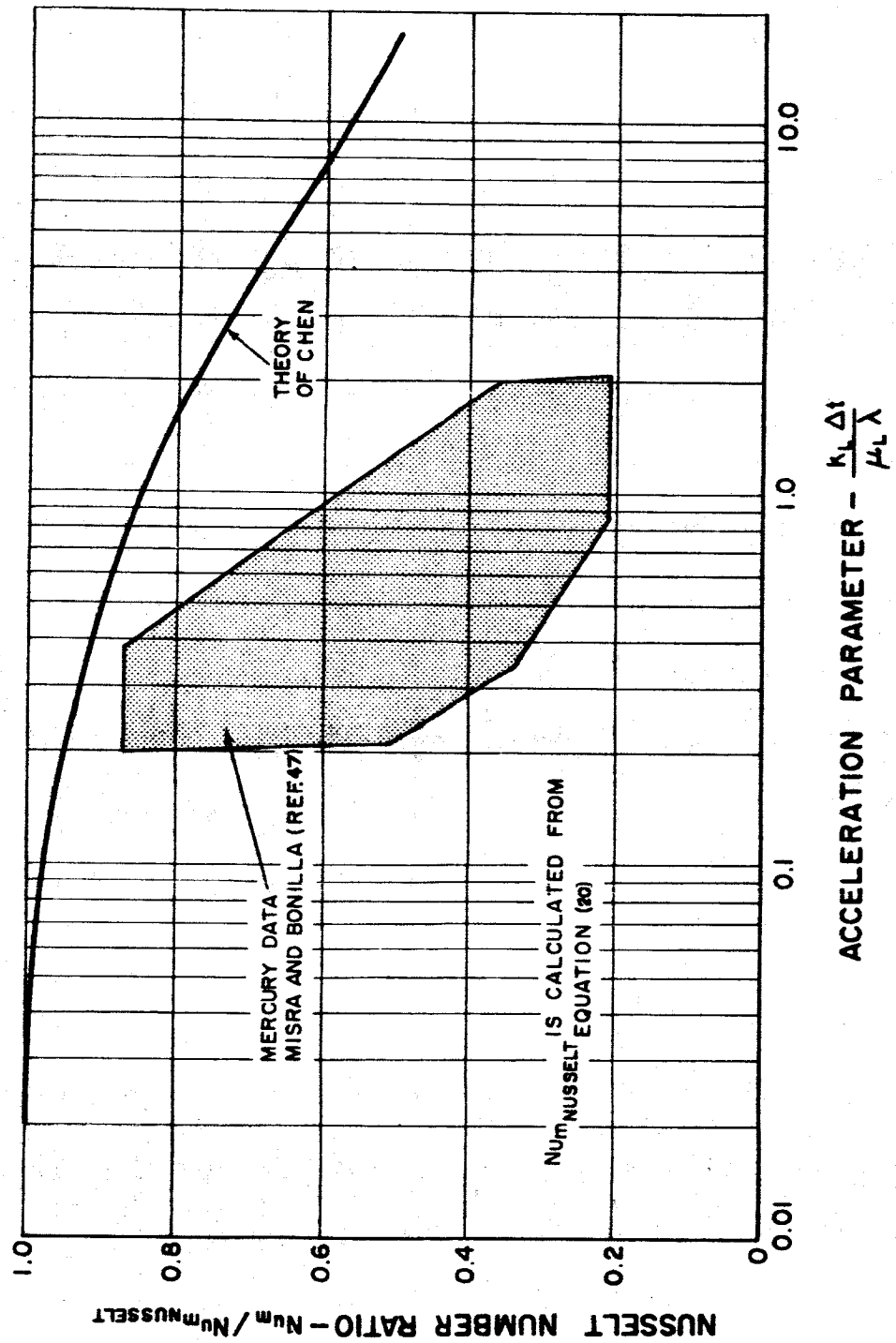

Figure 10 Nusselt Number Ratio vs Acceleration Parameter. Comparison of Theoretical Results of Chen (Ref. 36) with Mercury Data of Misra and Bonilla (Ref. 47)

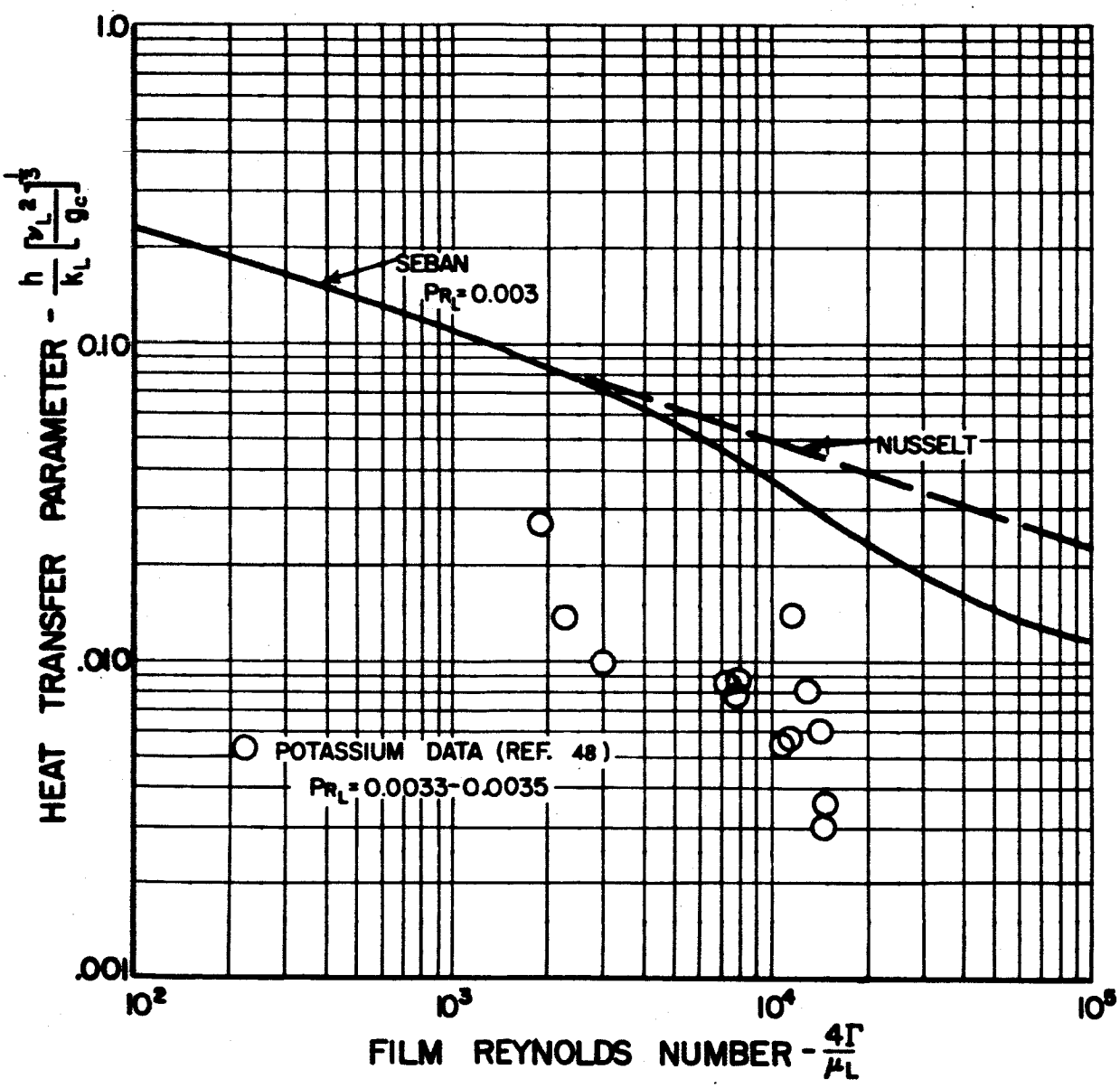

Figure 11 Heat Transfer Parameter vs Film Reynolds Number. Comparison Between Theoretical Results of Seban (Ref. 40) and Nusselt (Ref. 32) and Experimental Data of Brooks and Sawochka (Ref. 48)

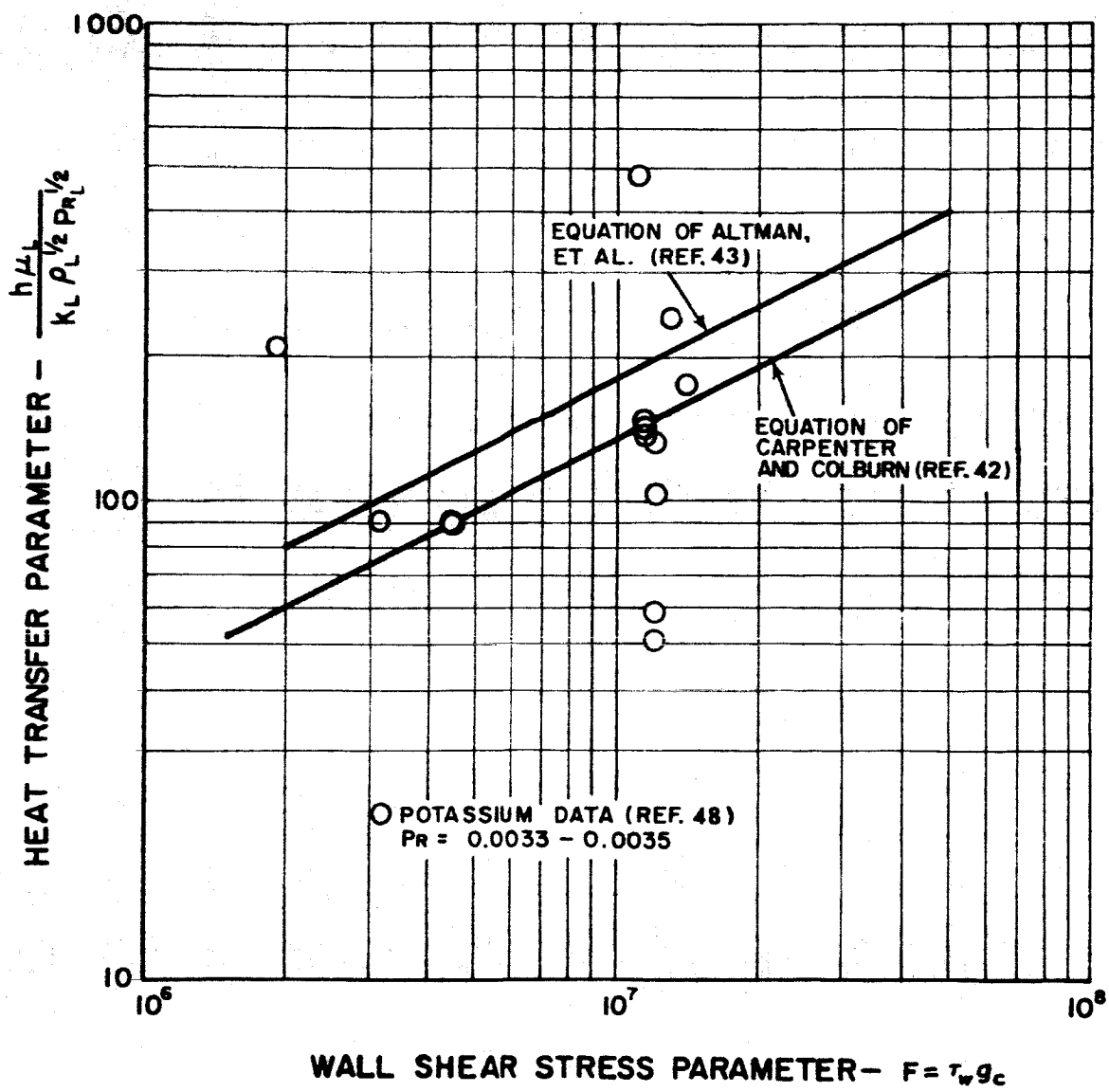

Figure 12 Heat Transfer Parameter vs Wall Shear Stress Parameter. Comparison of Carpenter-Colburn Equation with Condensing Potassium Data

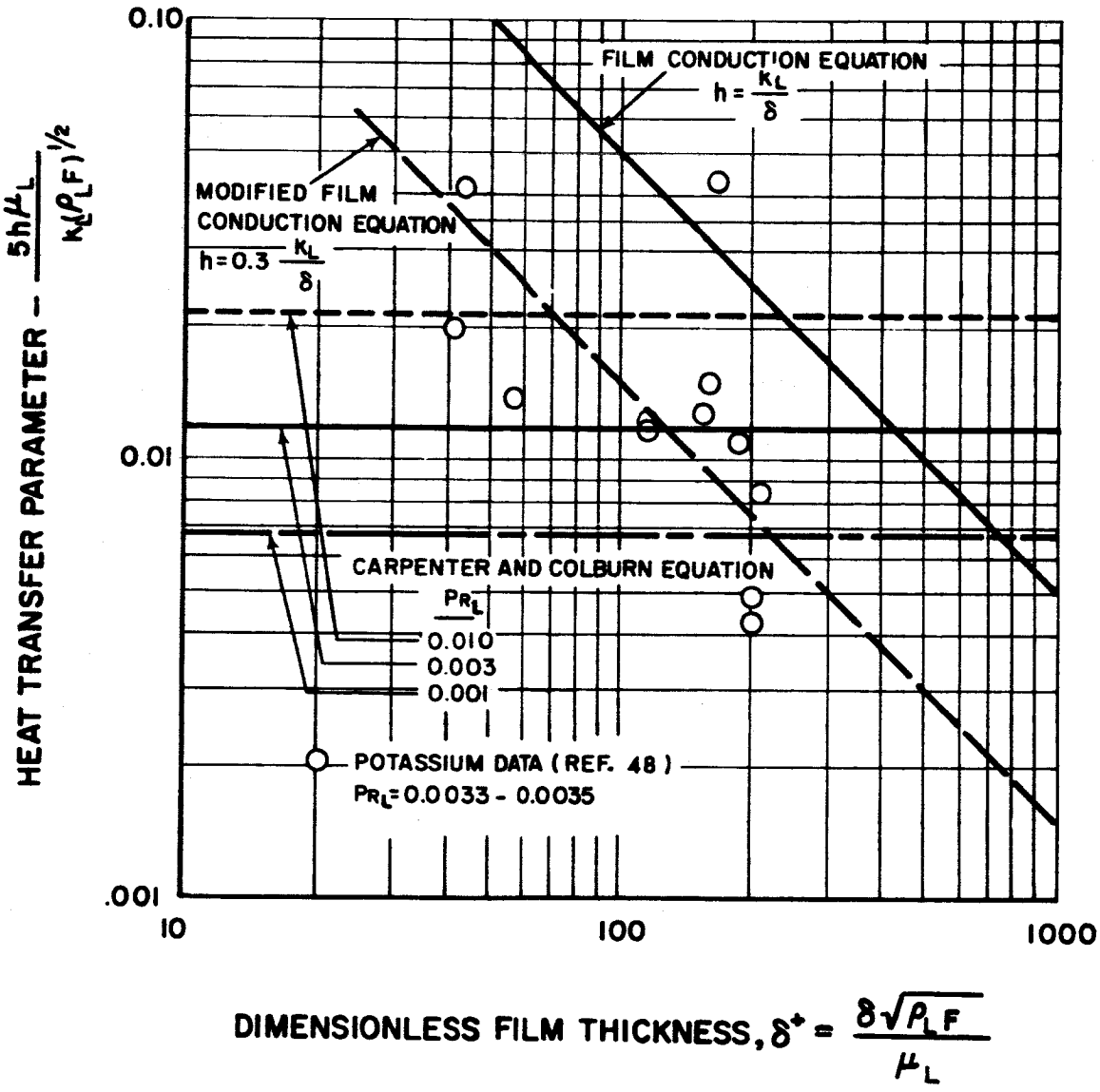

Figure 13 Heat Transfer Parameter vs Dimensionless Film Thickness

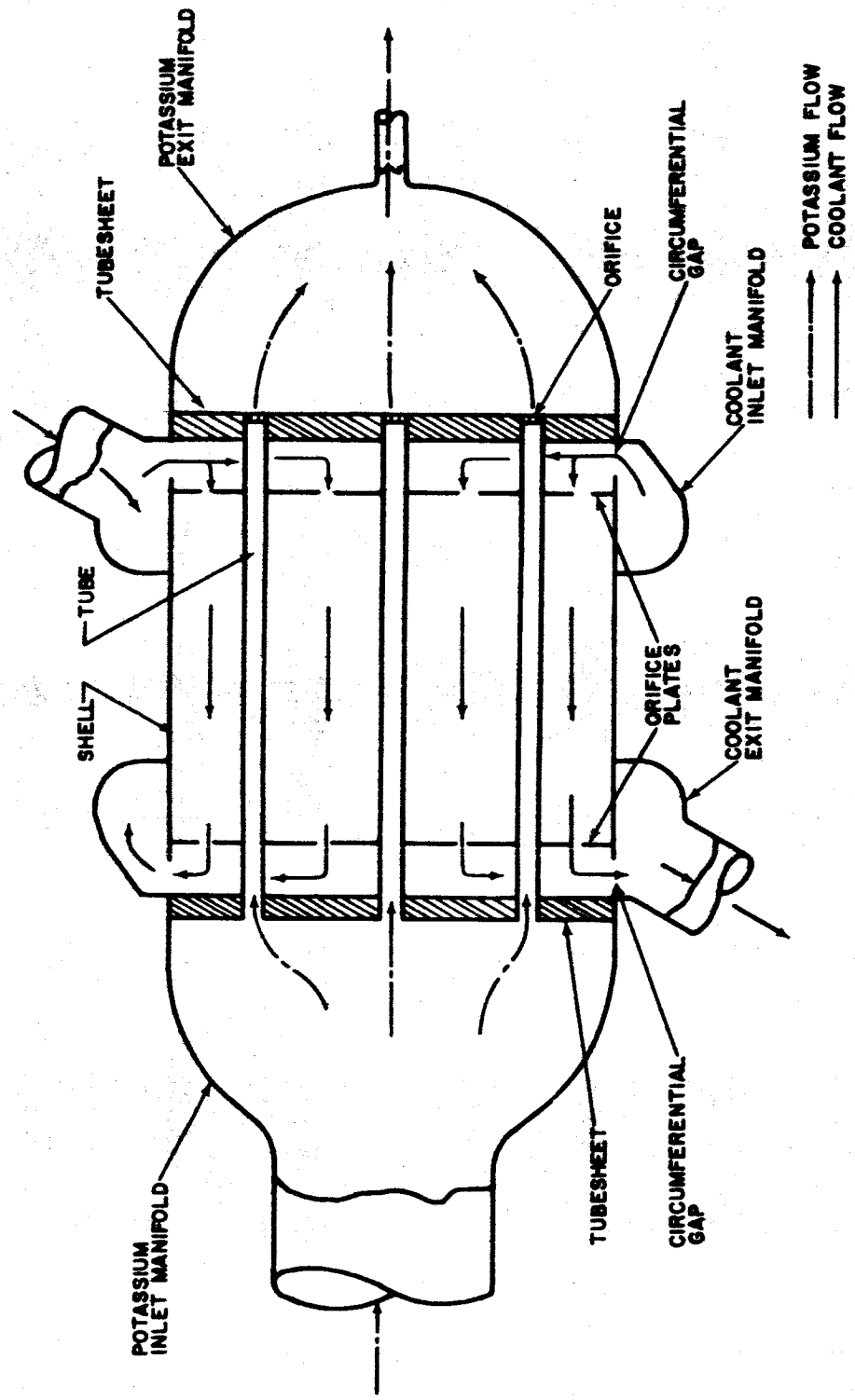

Figure 14 Typical Flow Pattern in Constant-Diameter Shell-and-Tube Condenser for Parallel Arrangement

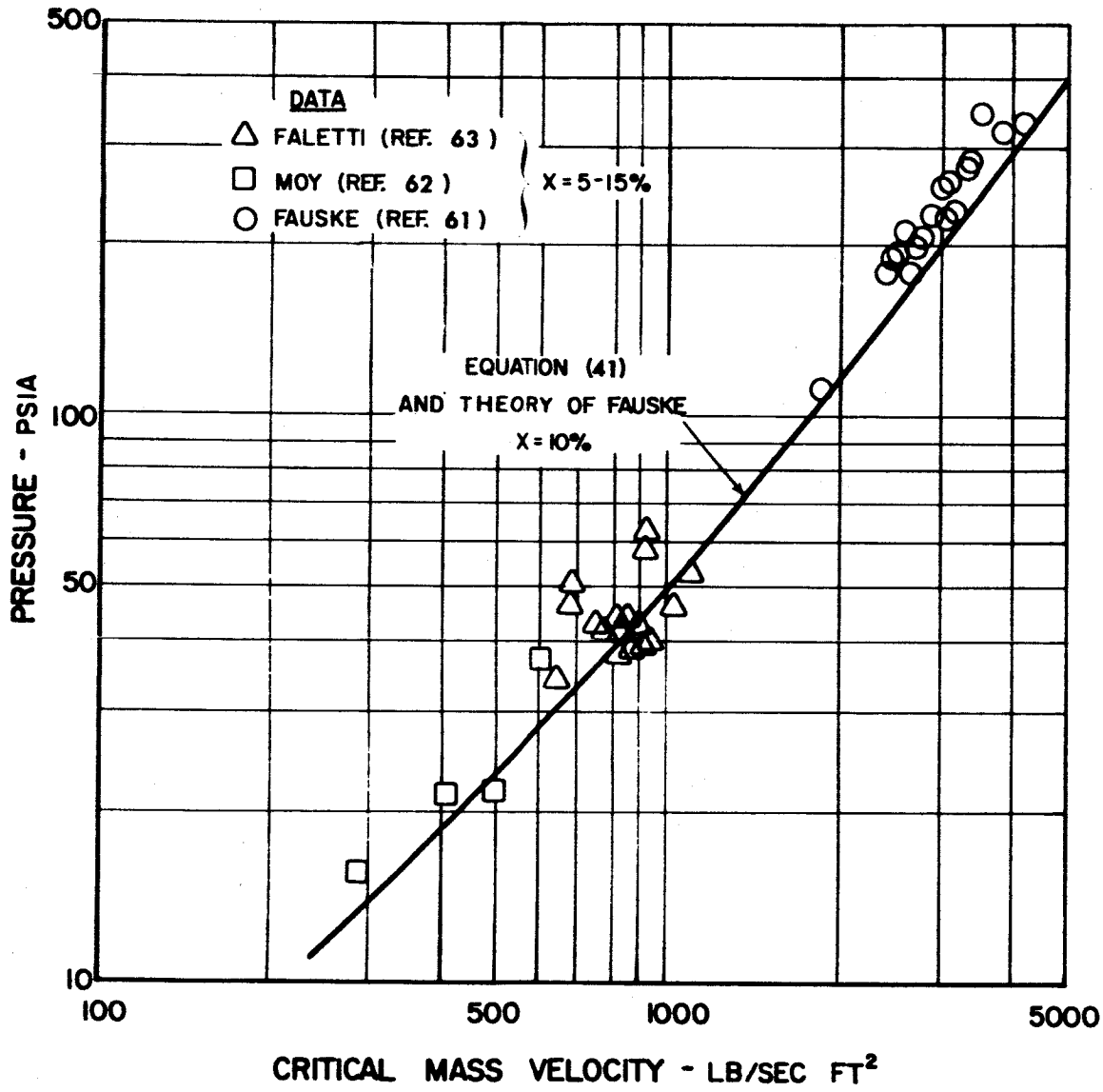

Figure 15 Comparison Between the Critical Mass Velocities Predicted by Equation 41, the Theoretical Results of Fauske, and Experimental Data for a Steam-Water Mixture of 5-15% Quality

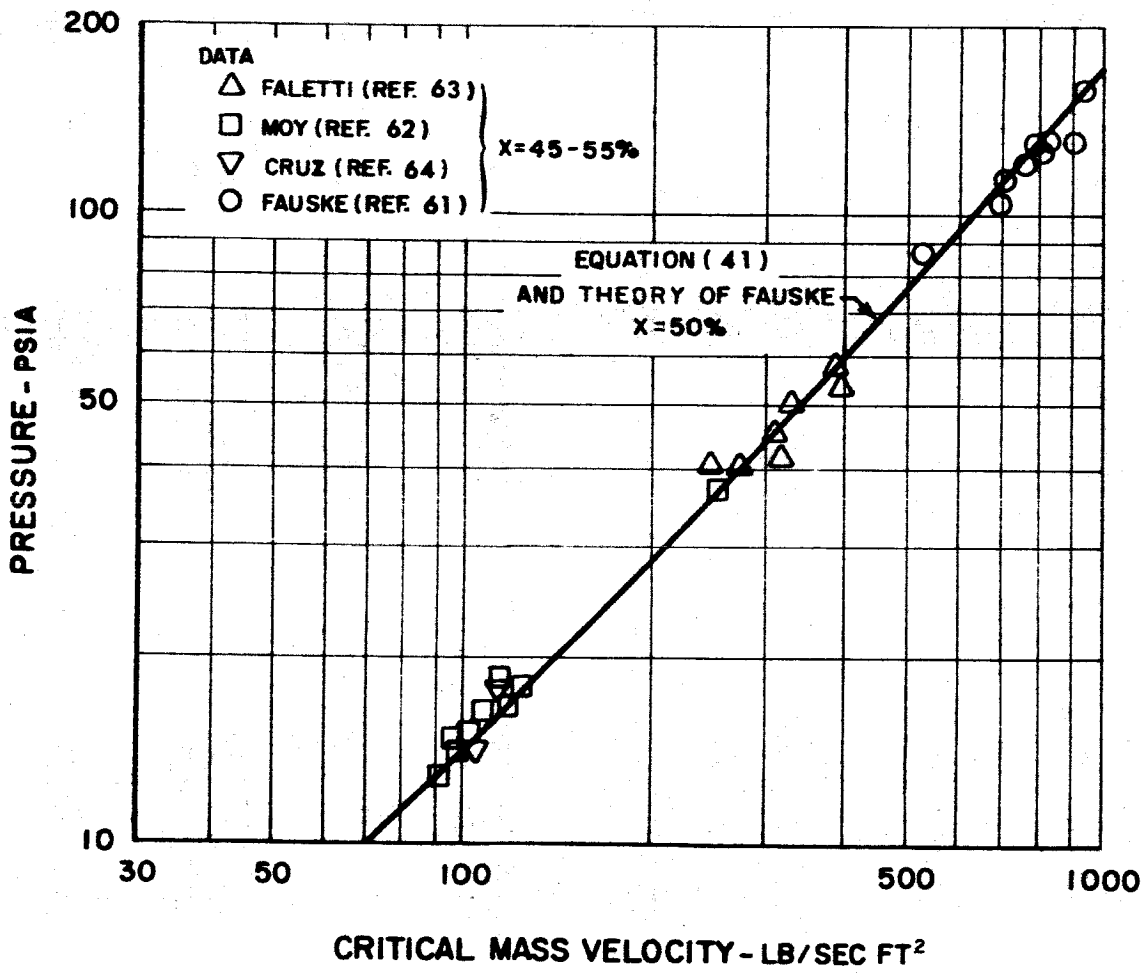

Figure 16 Comparison Between the Critical Mass Velocities Predicted by Equation 41, the Theoretical Results of Fauske, and Experimental Data for a Steam-Water Mixture of 45-55% Quality

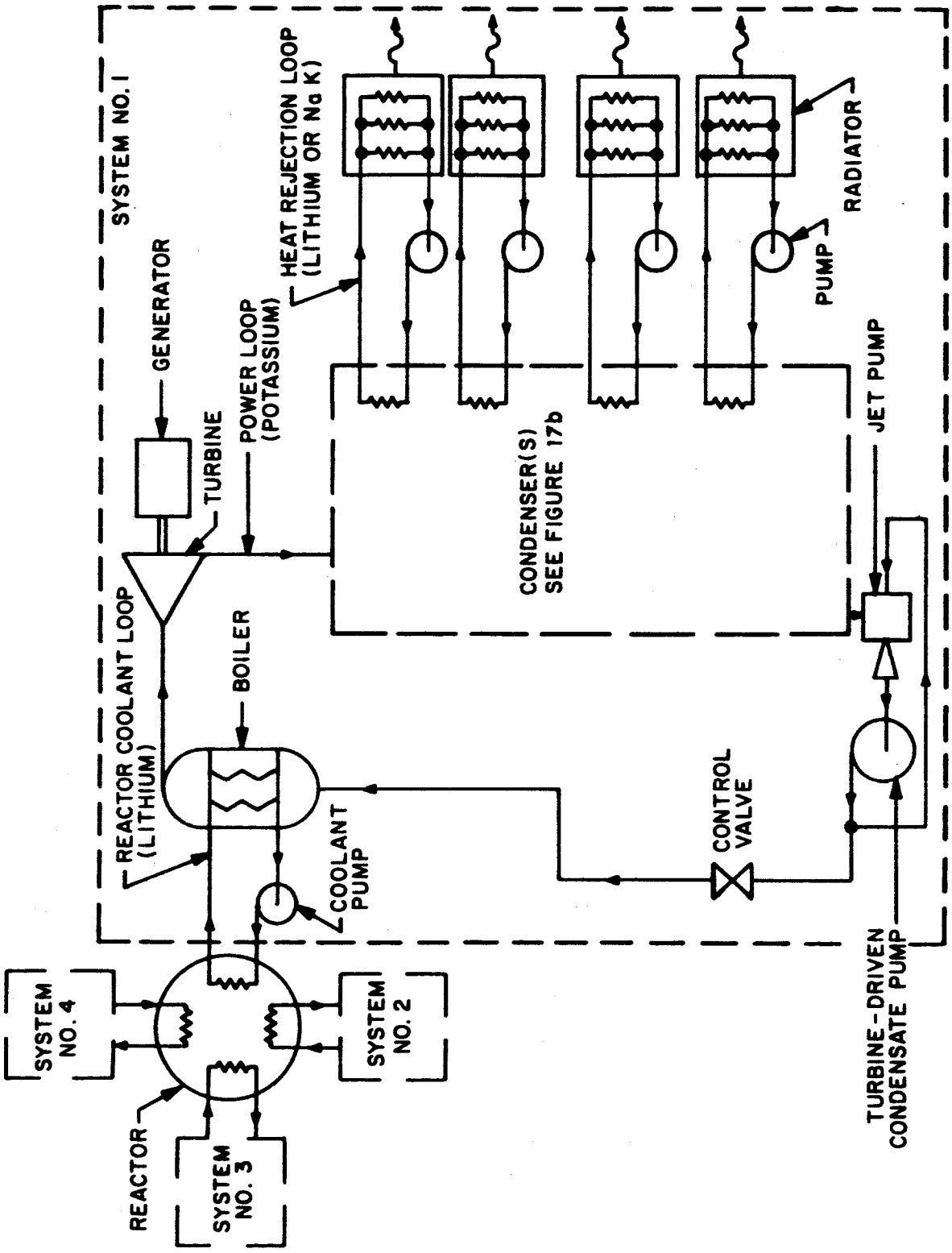

Figure 17a Schematic Diagram of 1MW(e) Nuclear Rankine-Cycle Space Powerplant

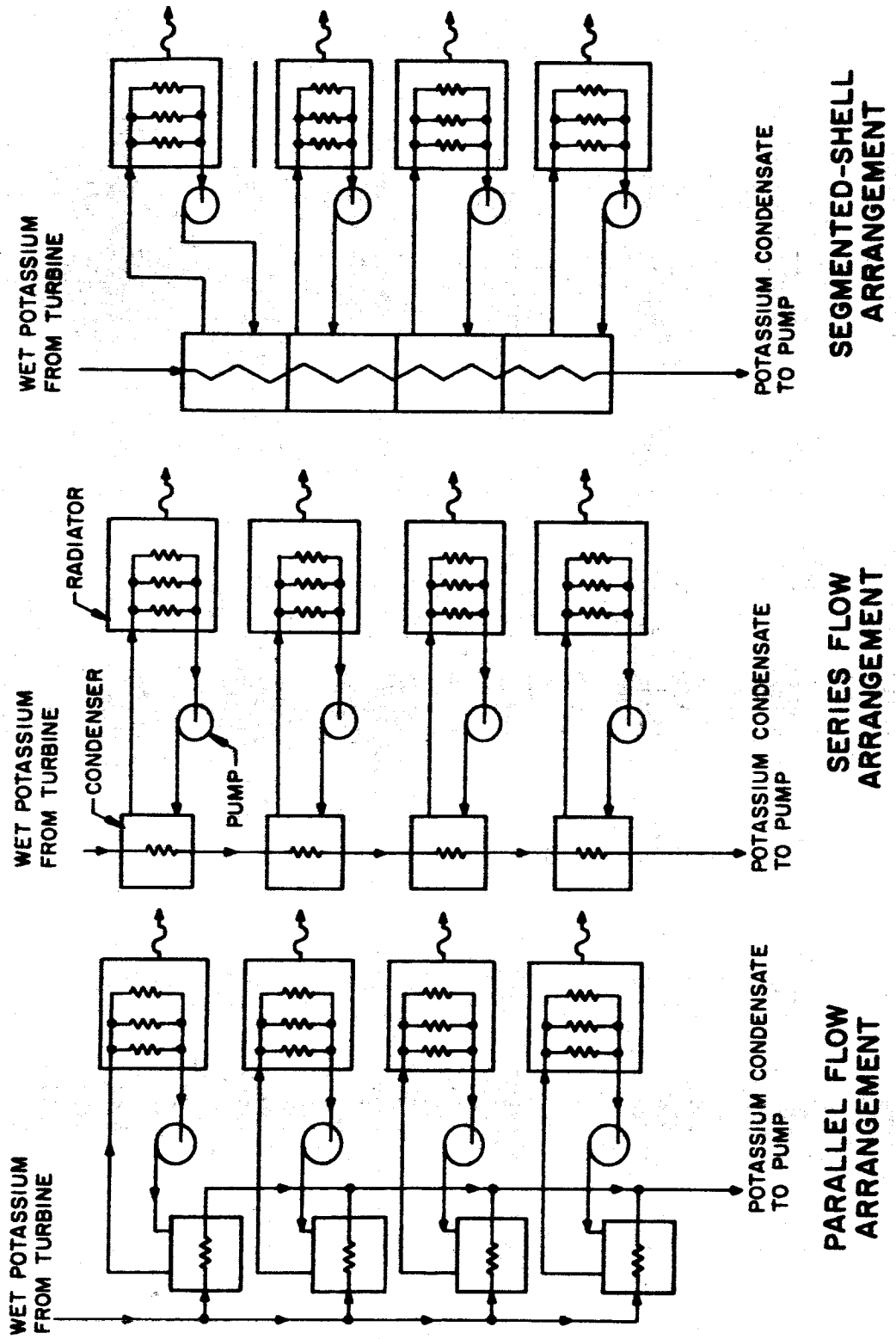

Figure 17b Schematic Diagram of Condenser-Heat Rejection Loop Arrangements

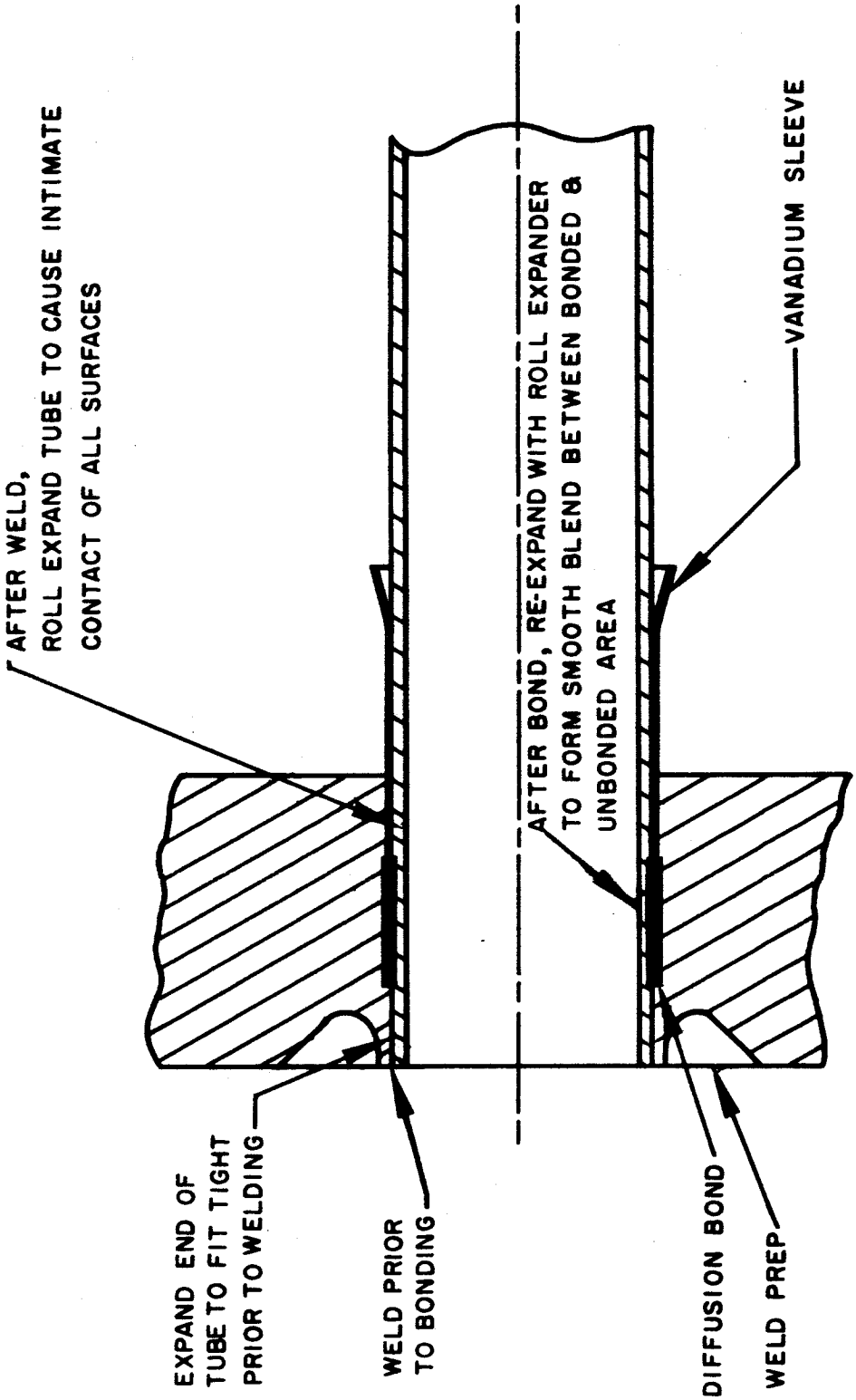

Figure 18 Detail of Tube-to-Tubesheet Joint for Columbium - 1% Zirconium Alloy

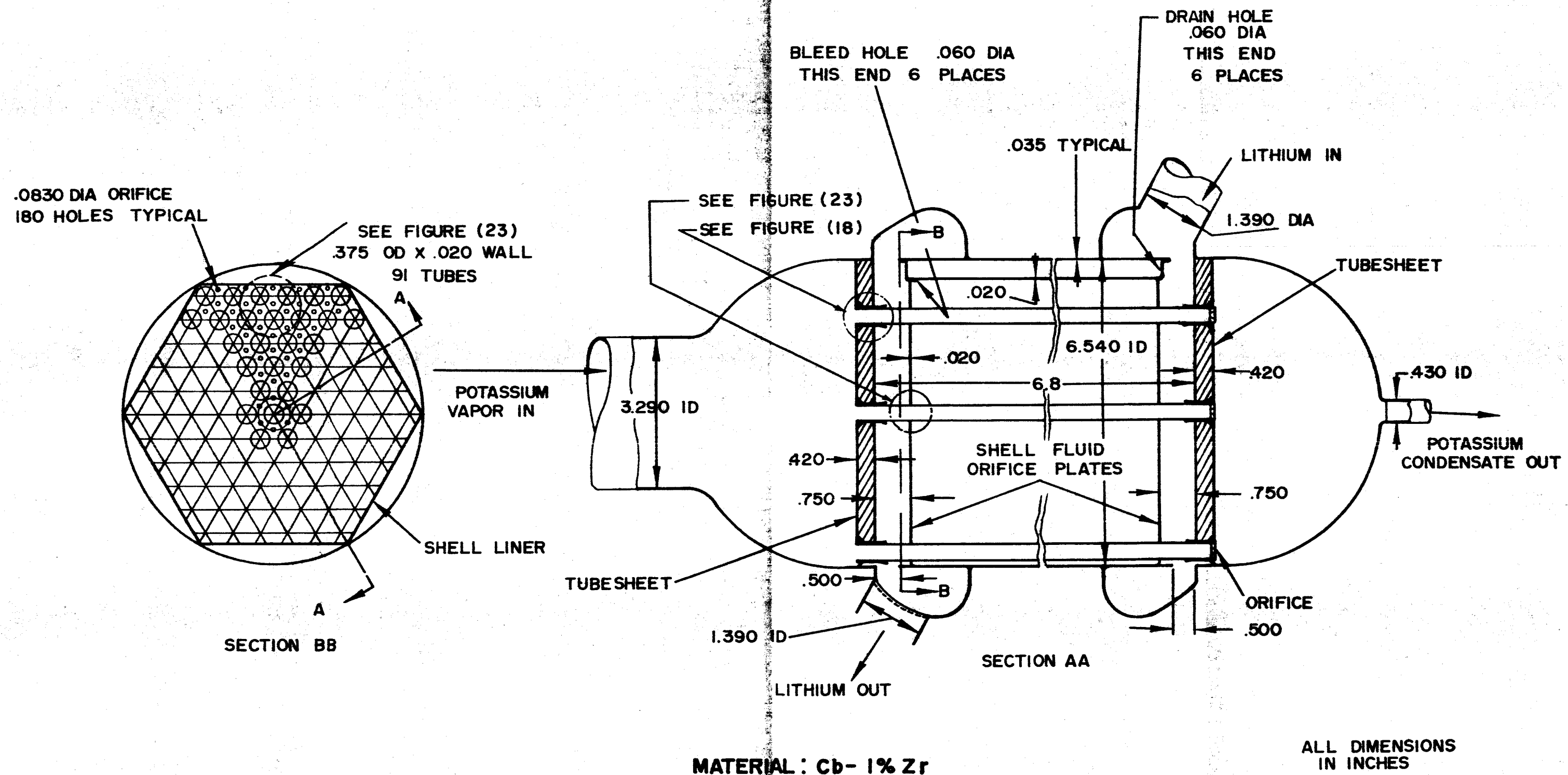

Figure 19 Lithium-Cooled Potassium Condenser for 1 MW(e) Nuclear Space Powerplant. Conventional Shell-Tube Configuration

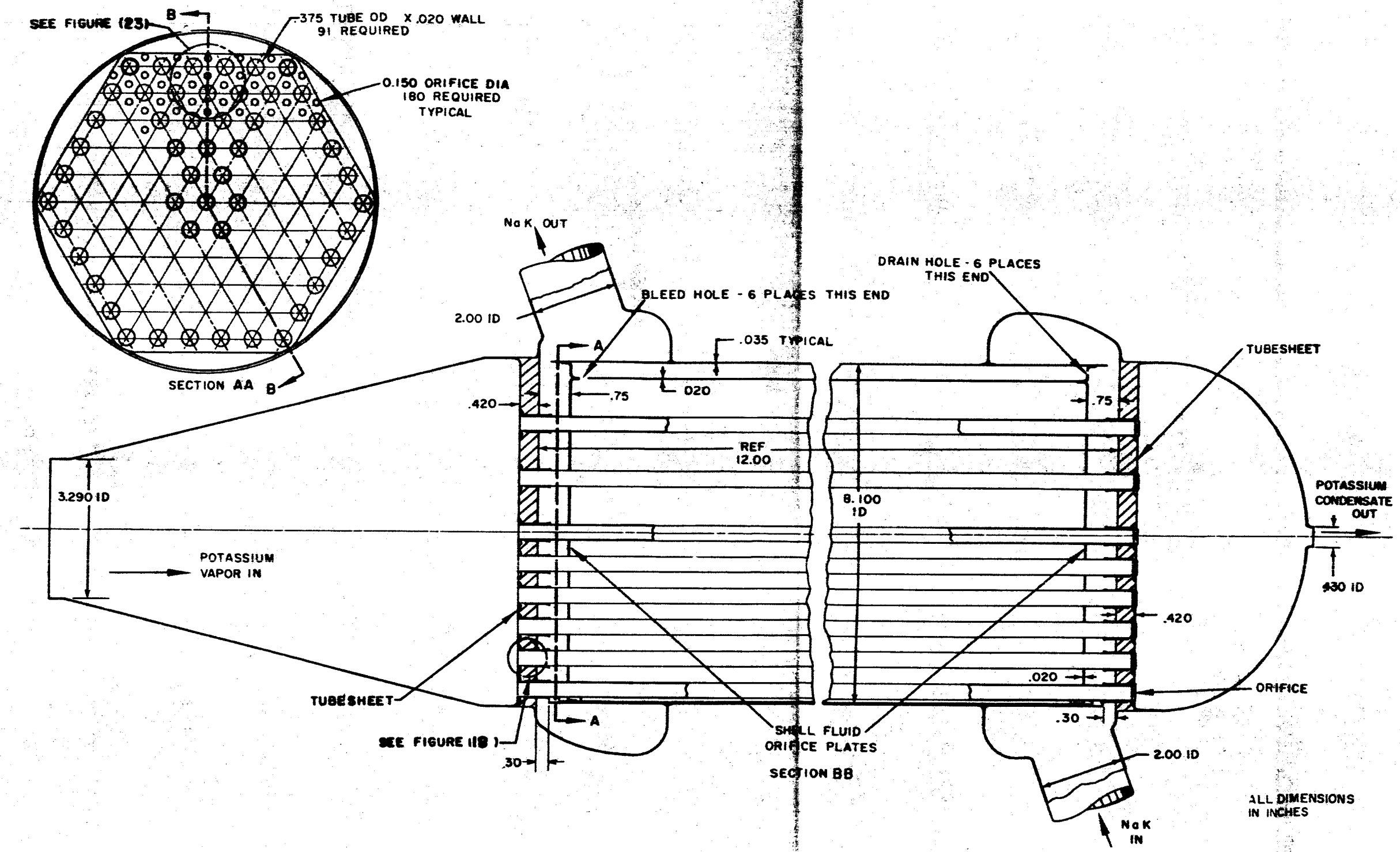

Figure 20 NaK-Cooled Liquid Metal Condenser for 1 MW(e) Nuclear Space Powerplant. Constant Diameter Configuration

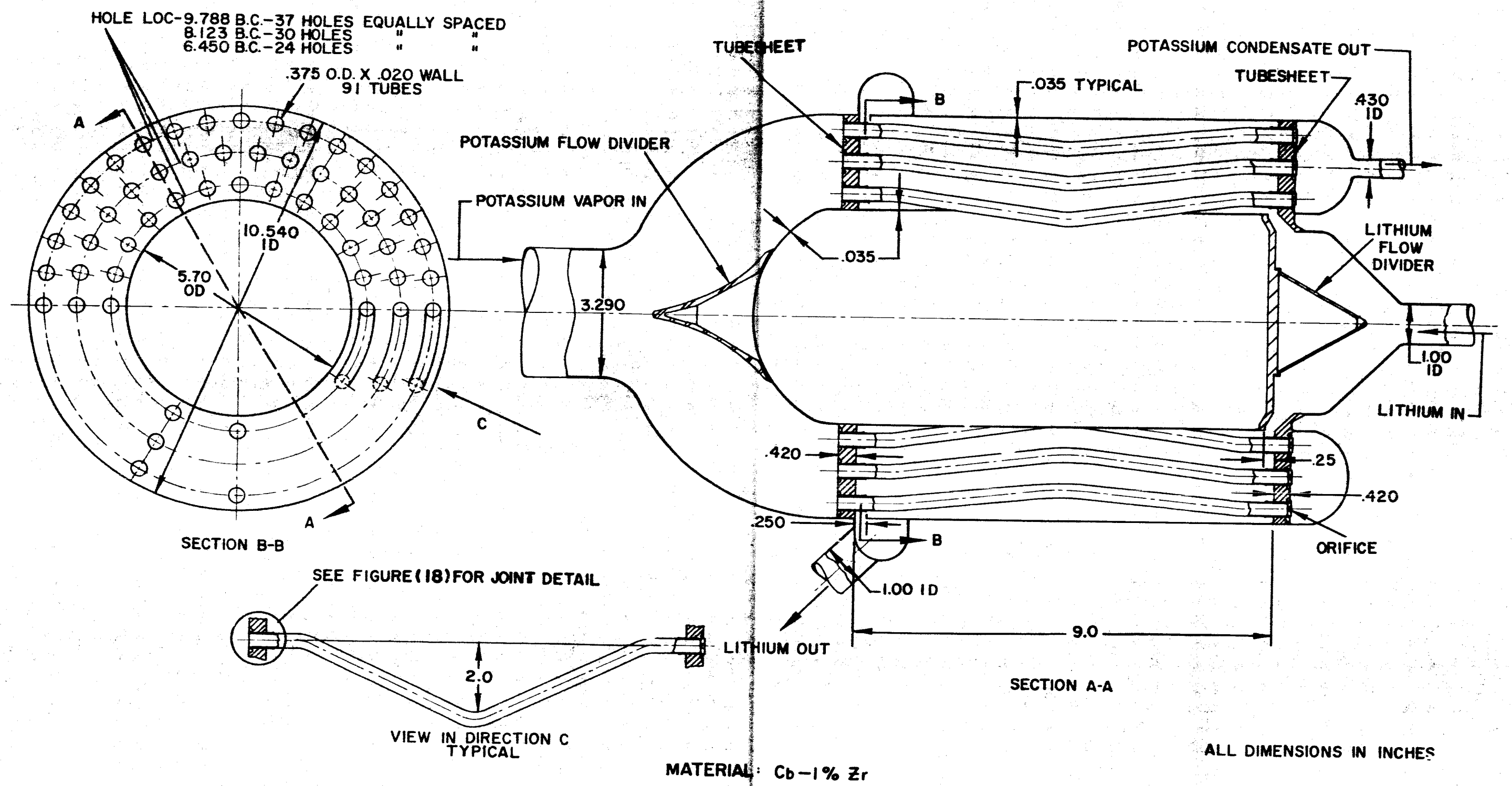

Figure 21 Lithium-Cooled Potassium Condenser for 1 MW(e) Nuclear Space Powerplant. Annular Shell, Bent Tube Configuration

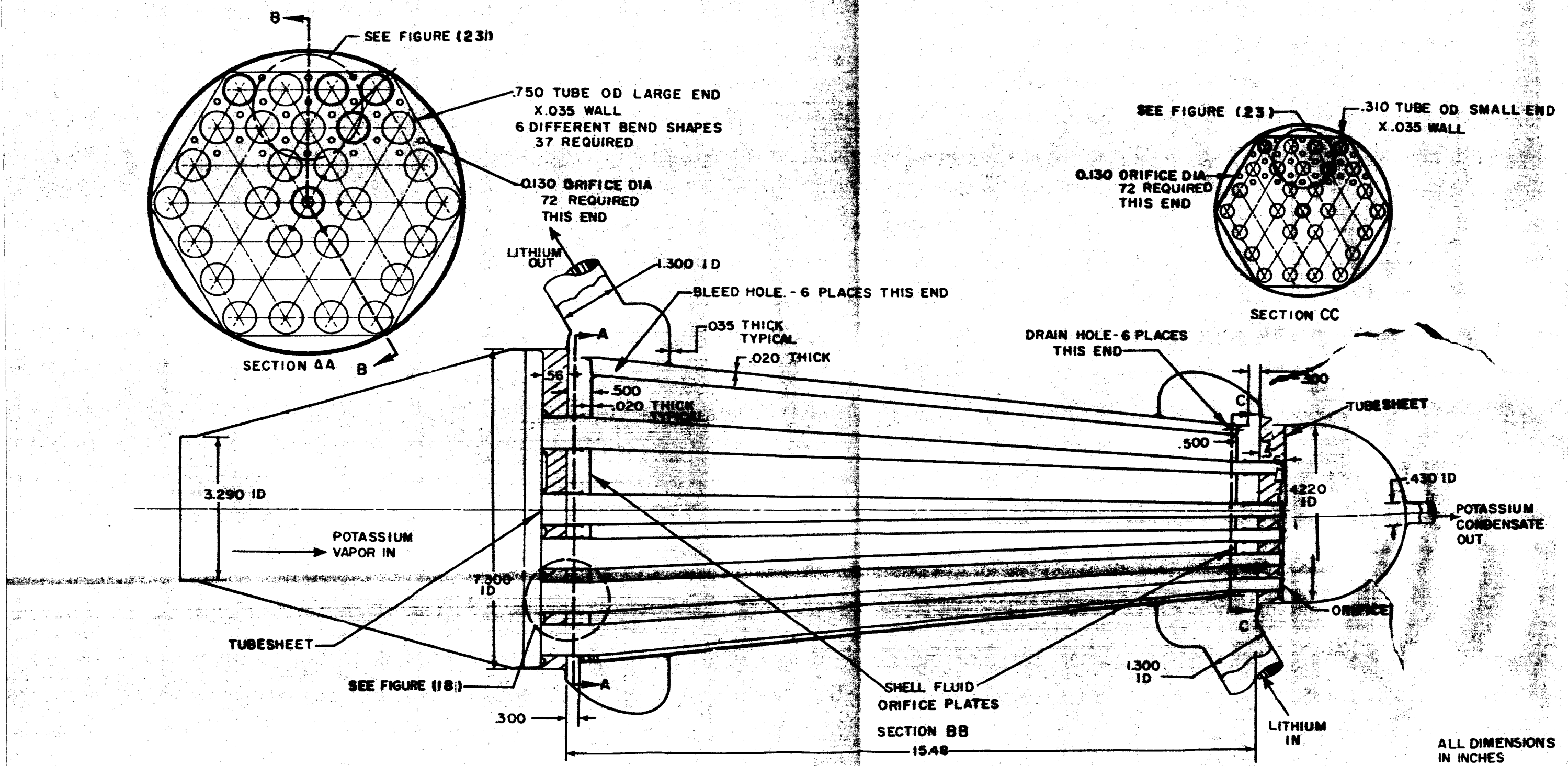

Figure 22 Lithium-Cooled Liquid Metal Condenser for 1 MW(e) Nuclear Space Powerplant. Tapered Configuration

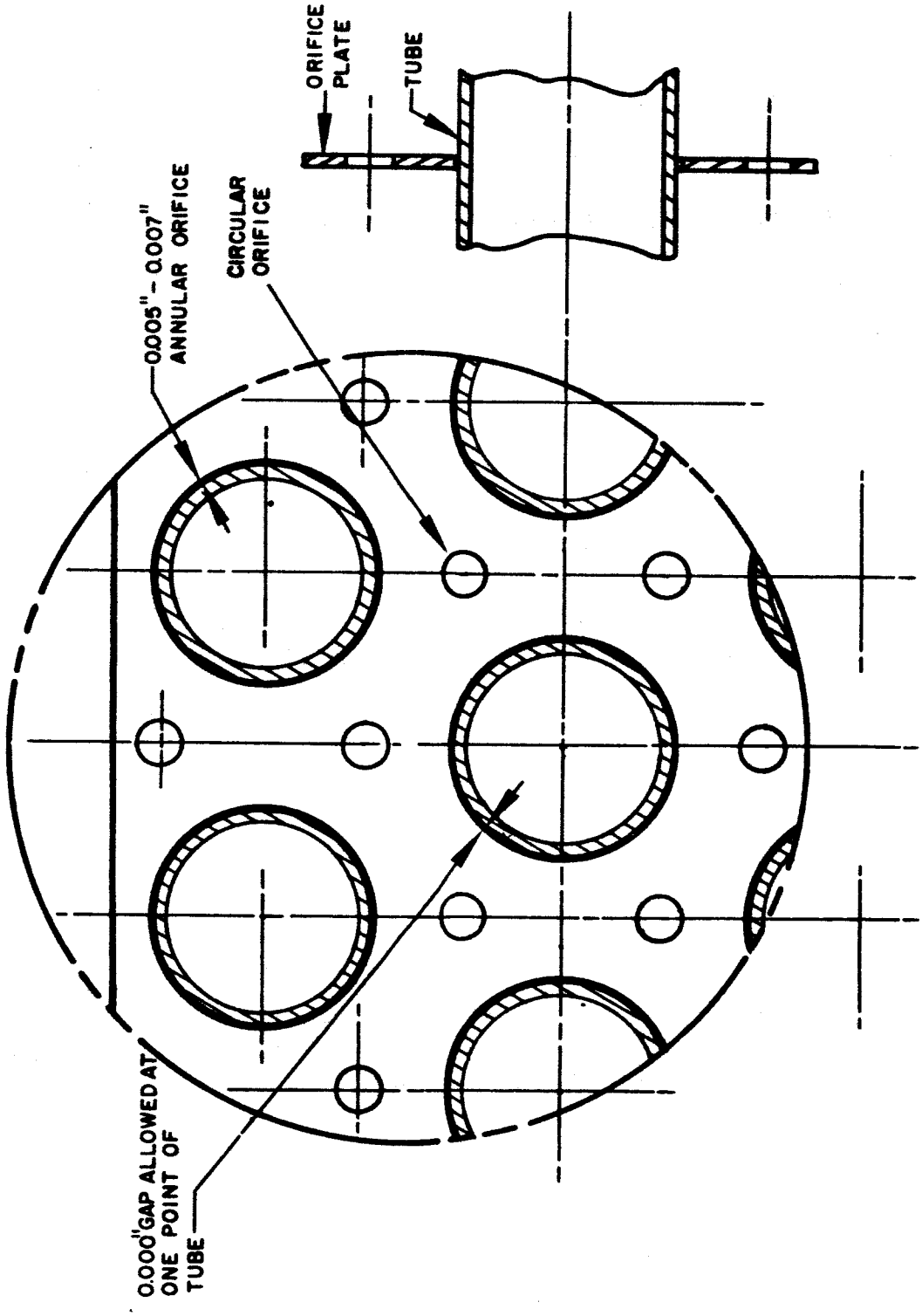

Figure 23 Detail of Hole Pattern in Orifice Plate

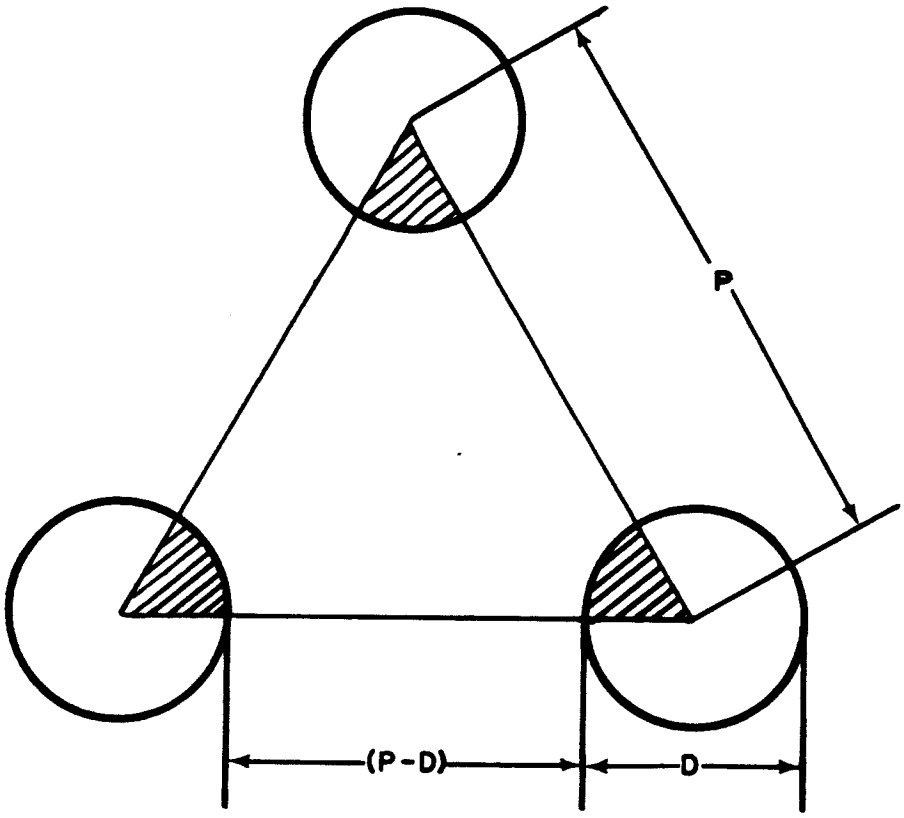

D = OUTSIDE DIAMETER OF TUBE
P = PITCH
(P-D) = TUBE SPACING

Figure 24 Equilateral Triangular Tube Pitch

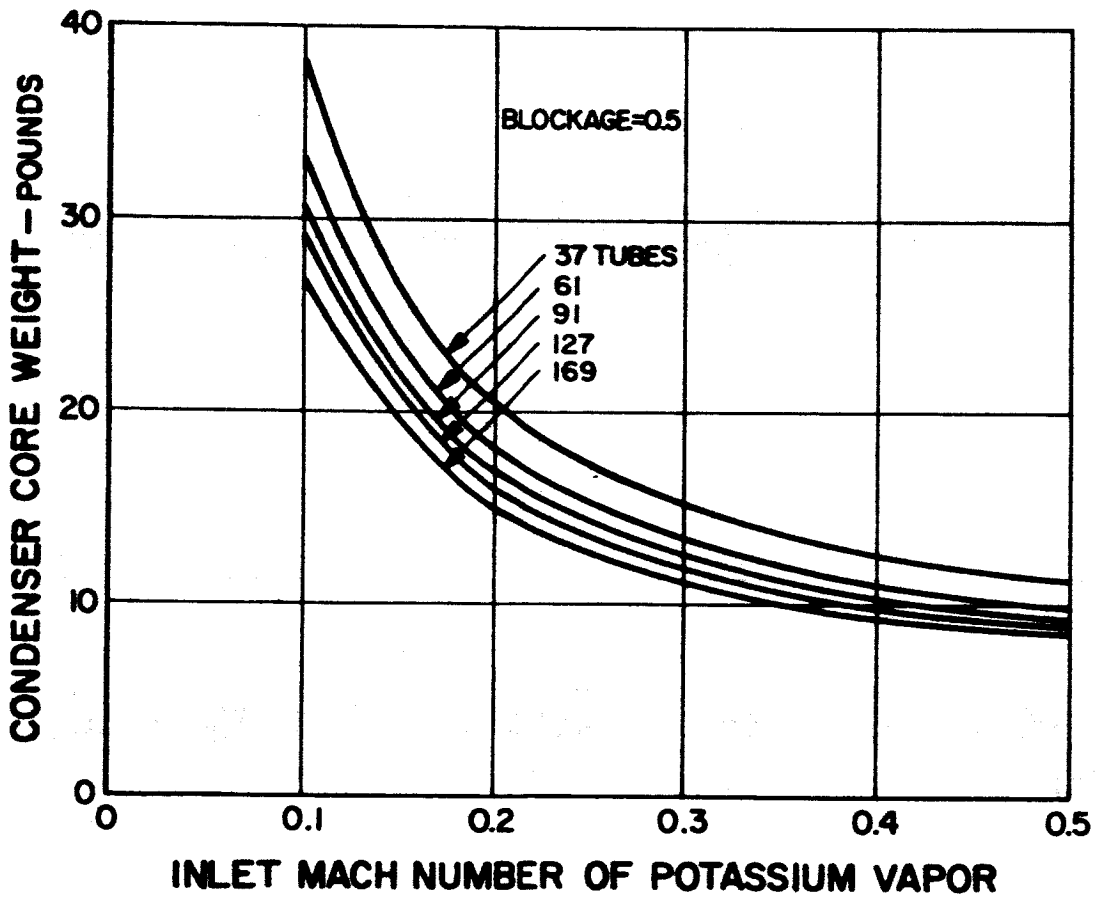

Figure 25 Lithium-Cooled Constant-Diameter Condenser. Effect of Potassium Vapor Inlet Mach Number and Number of Tubes on Condenser Core Weight

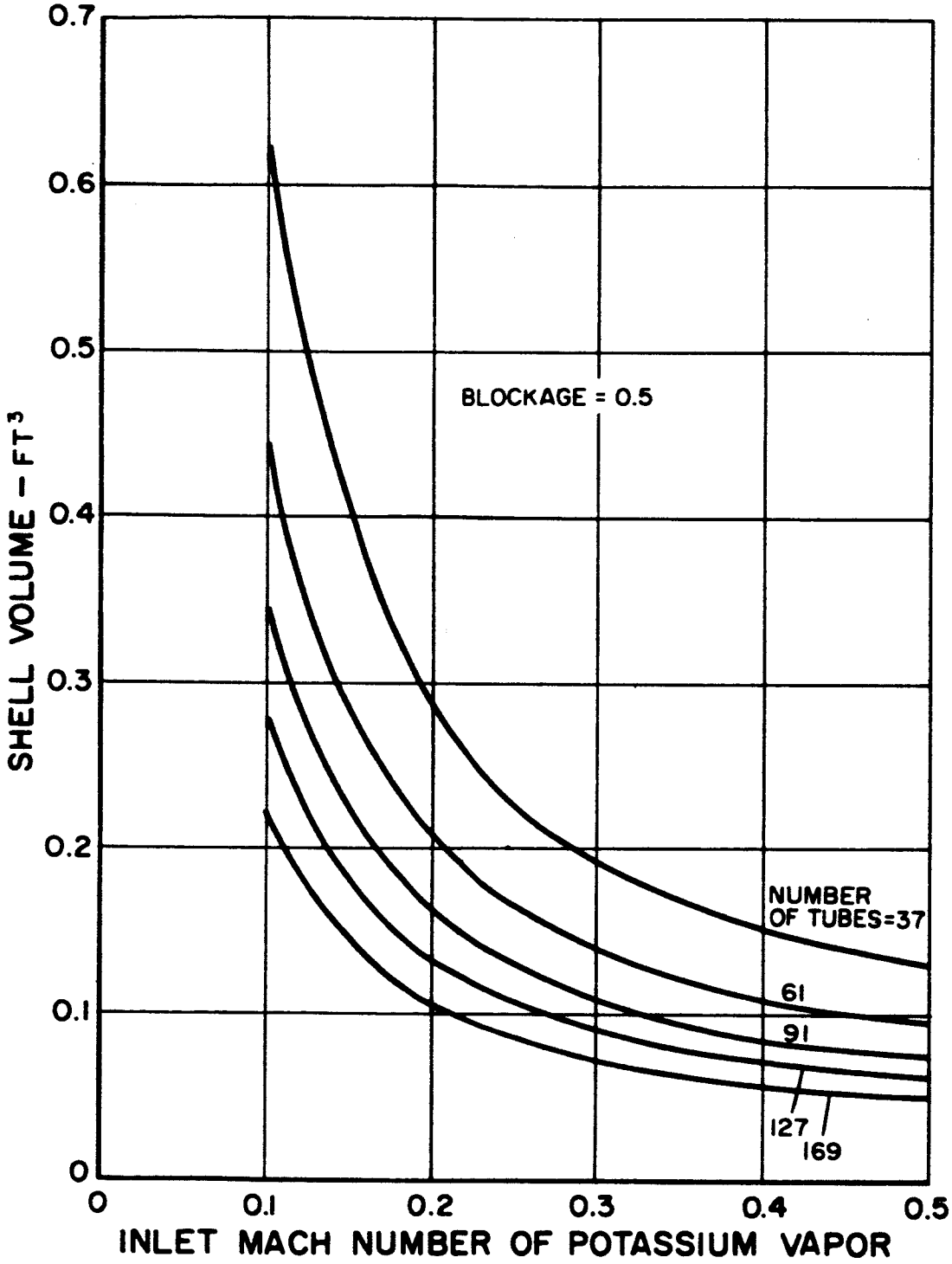

Figure 26 Lithium-Cooled Constant-Diameter Condenser. Effect of Potassium Vapor Inlet Mach Number and Number of Tubes on Shell Volume

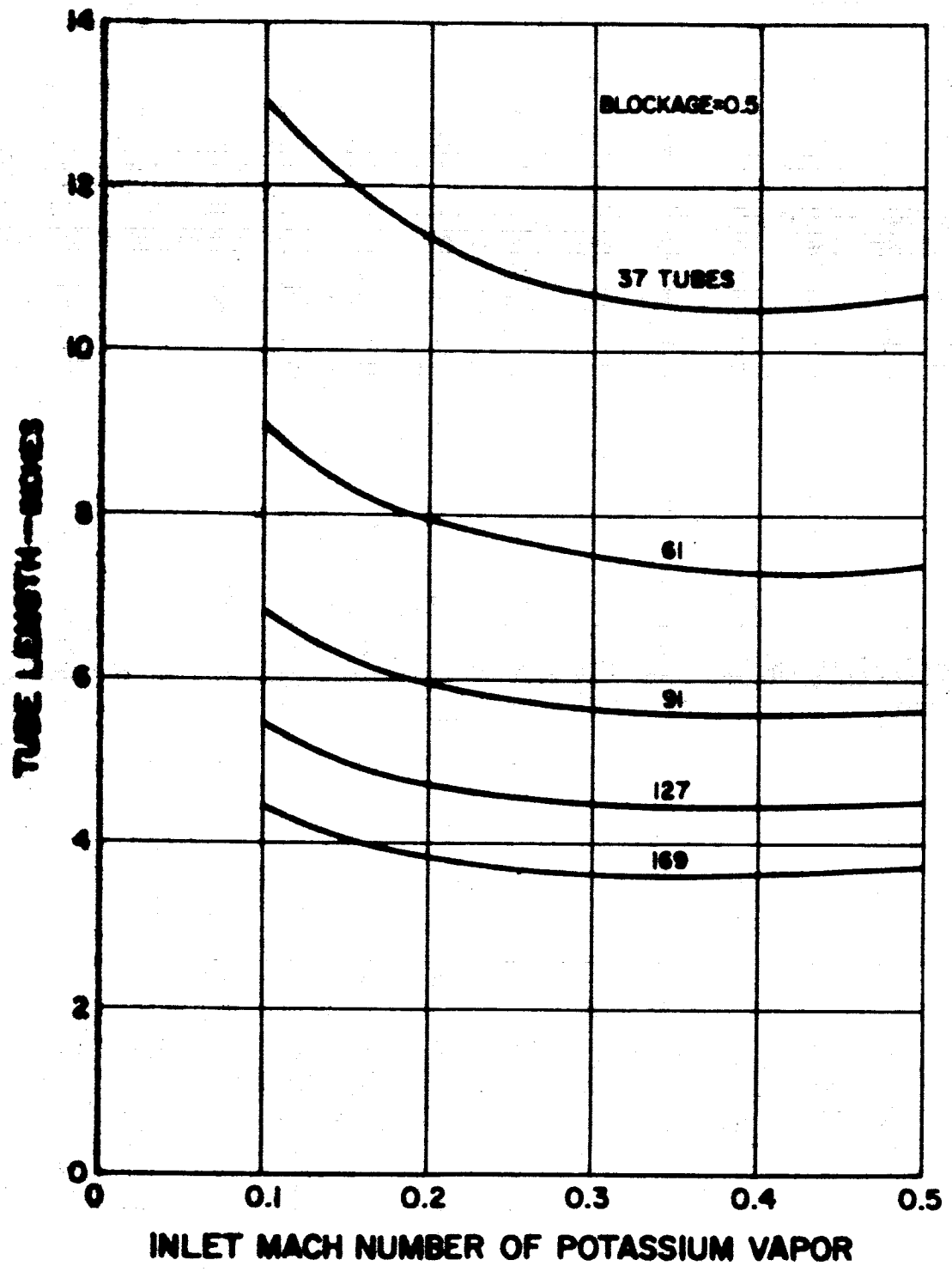

Figure 27 Lithium-Cooled Constant-Diameter Condenser. Effect of Potassium Vapor Inlet Mach Number and Number of Tubes on Tube Length

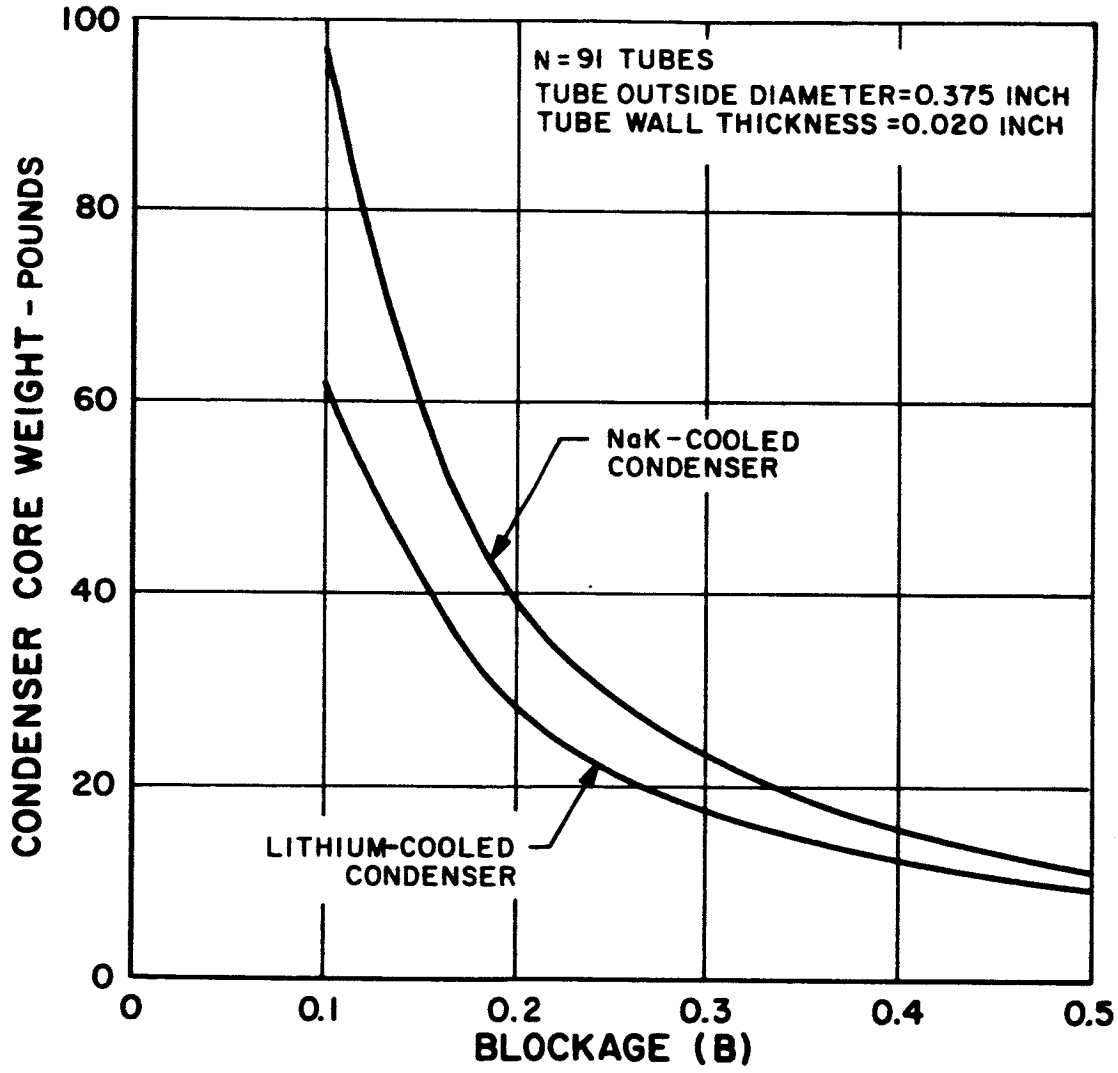

Figure 28 Effect of Blockage on Condenser Core Weight for Lithium-Cooled and NaK-Cooled Constant-Diameter Configurations

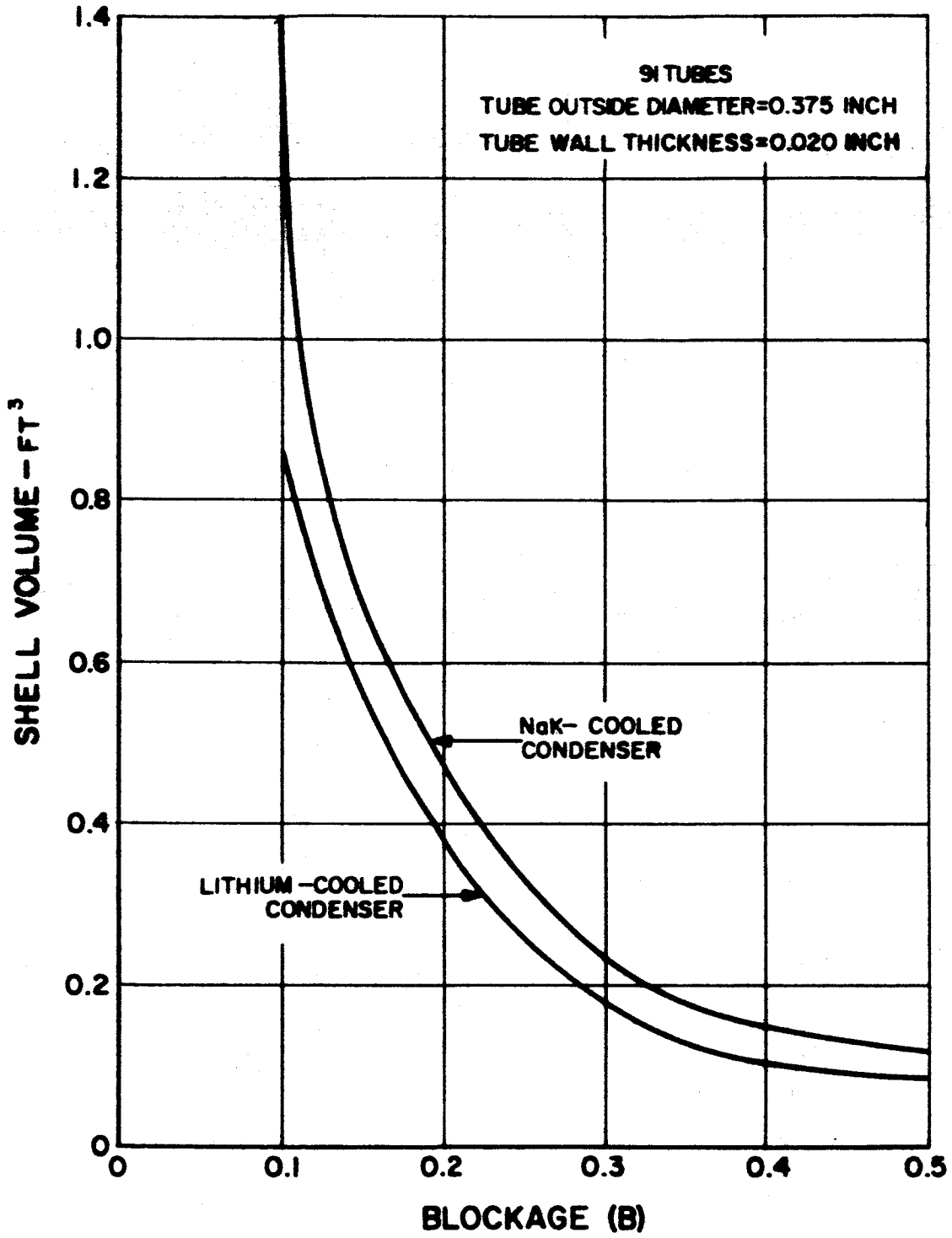

Figure 29 Effect of Blockage on Shell Volume for Lithium-Cooled and NaK-Cooled Constant-Diameter Configurations

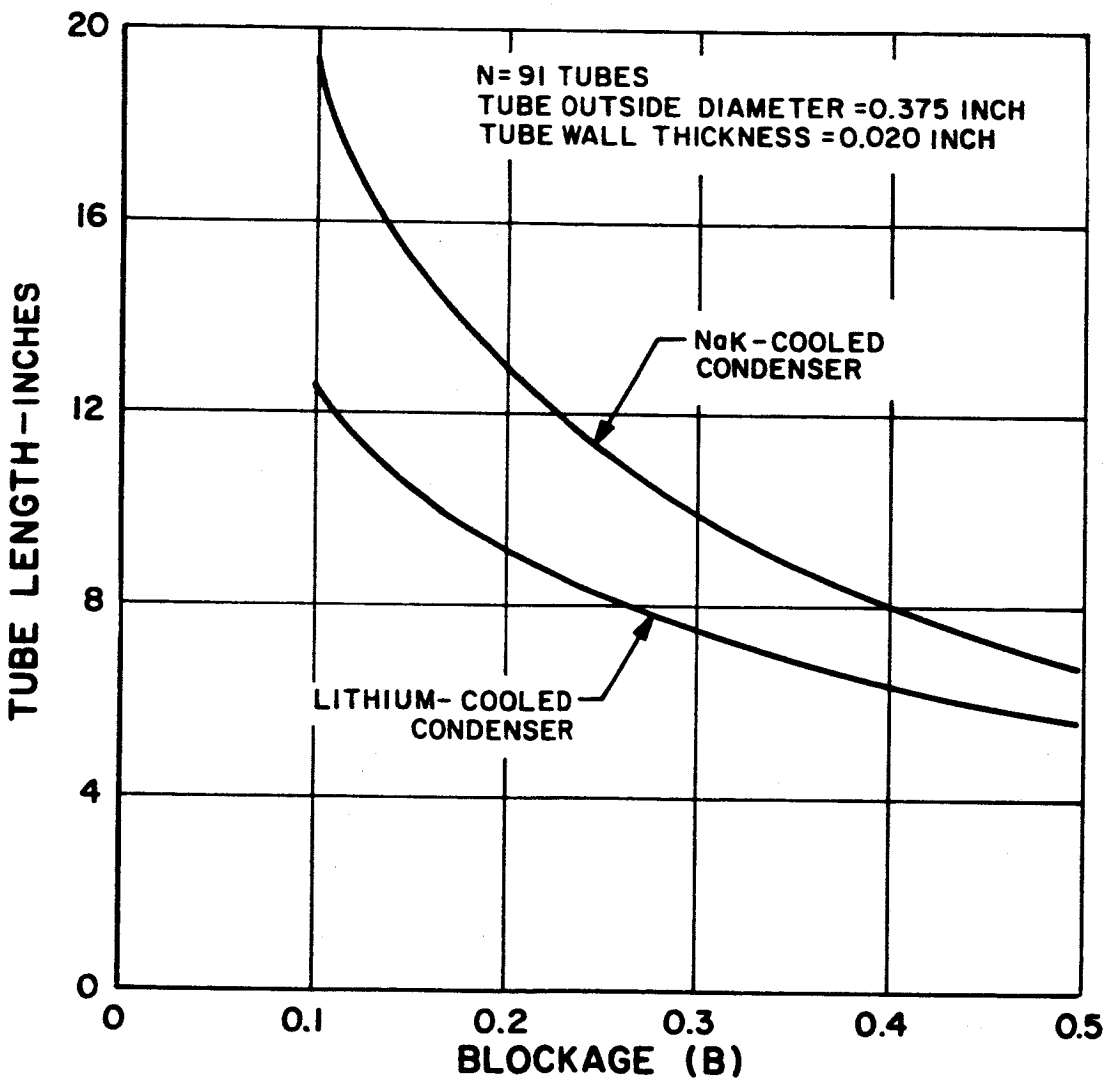

Figure 30 Effect of Blockage on Tube Length for Lithium-Cooled and NaK-Cooled Constant-Diameter Configurations

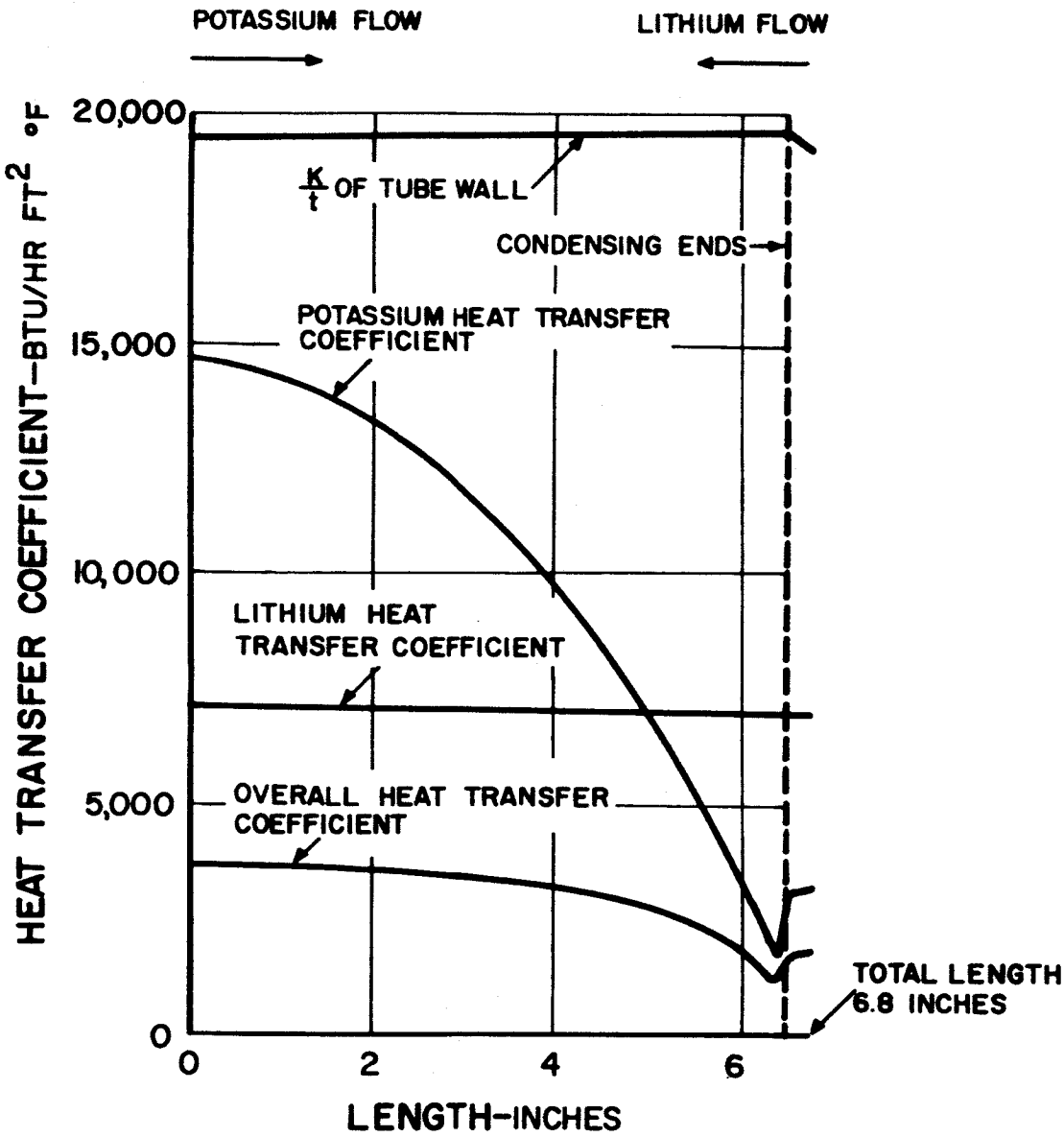

Figure 31a Variation of Heat Transfer Coefficient with Length for Lithium-Cooled Constant-Diameter Shell-and-Tube Configuration

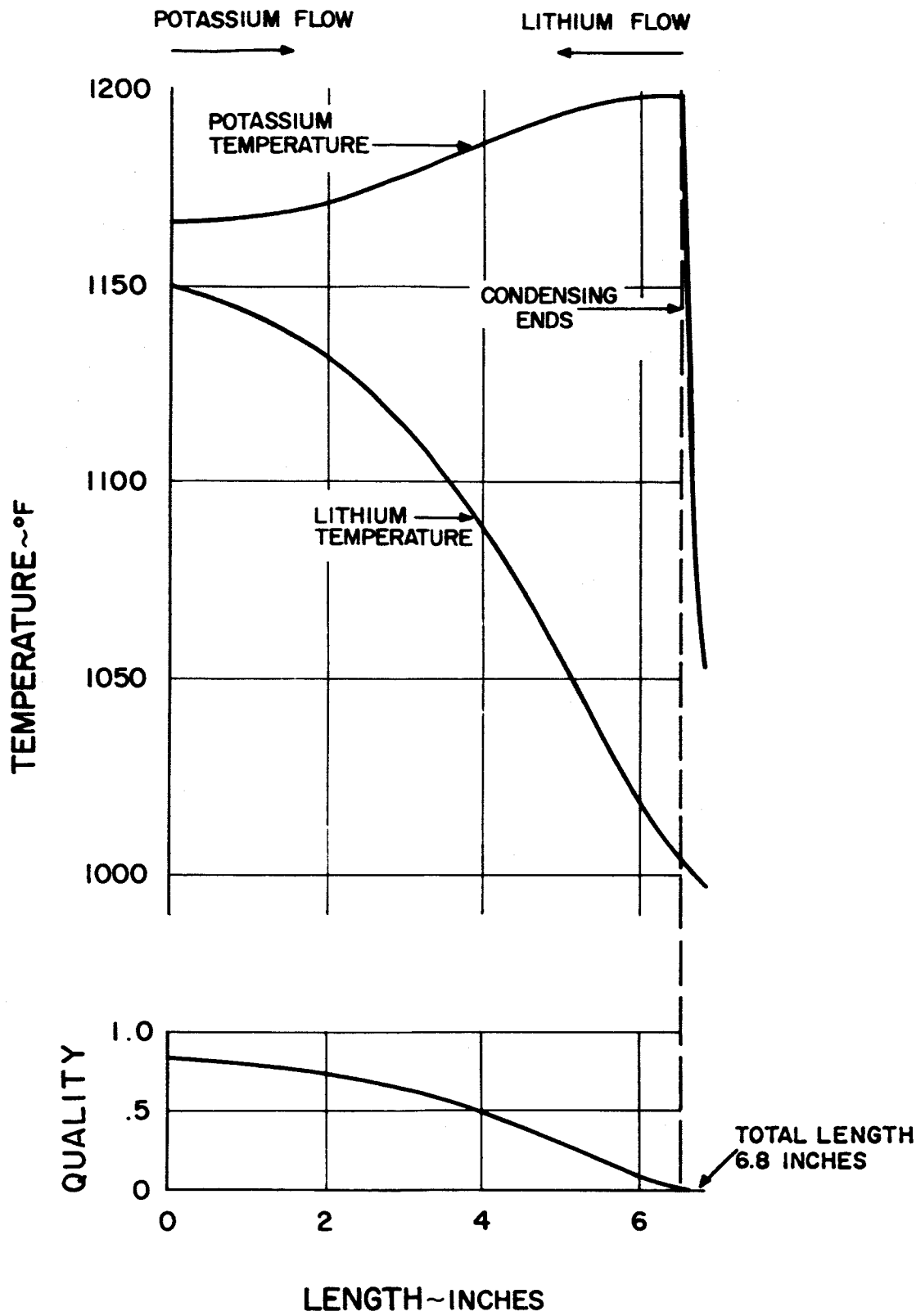

Figure 31b Variation of Fluid Temperatures and Potassium Quality with Length for Lithium-Cooled Constant-Diameter Shell-and-Tube Configuration

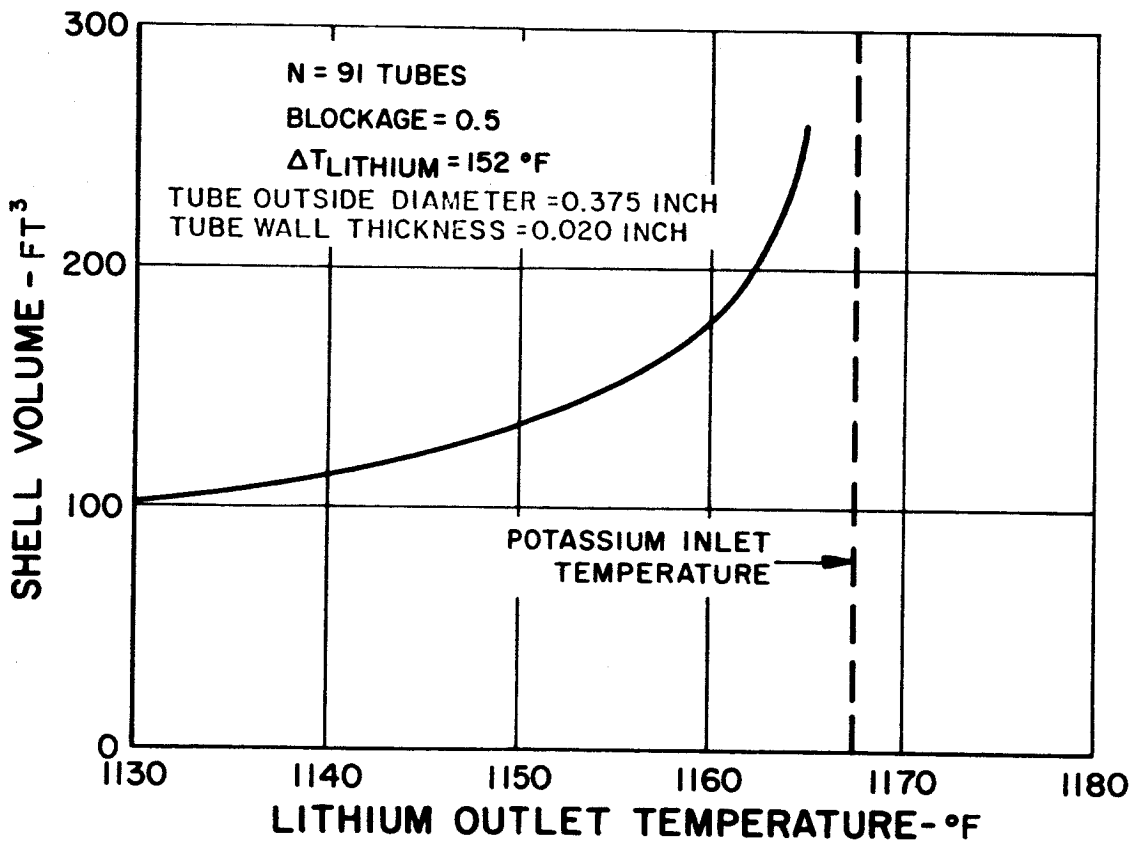

Figure 32a Lithium-Cooled Constant-Diameter Condenser. Effect of Coolant Temperature Level on Shell Volume

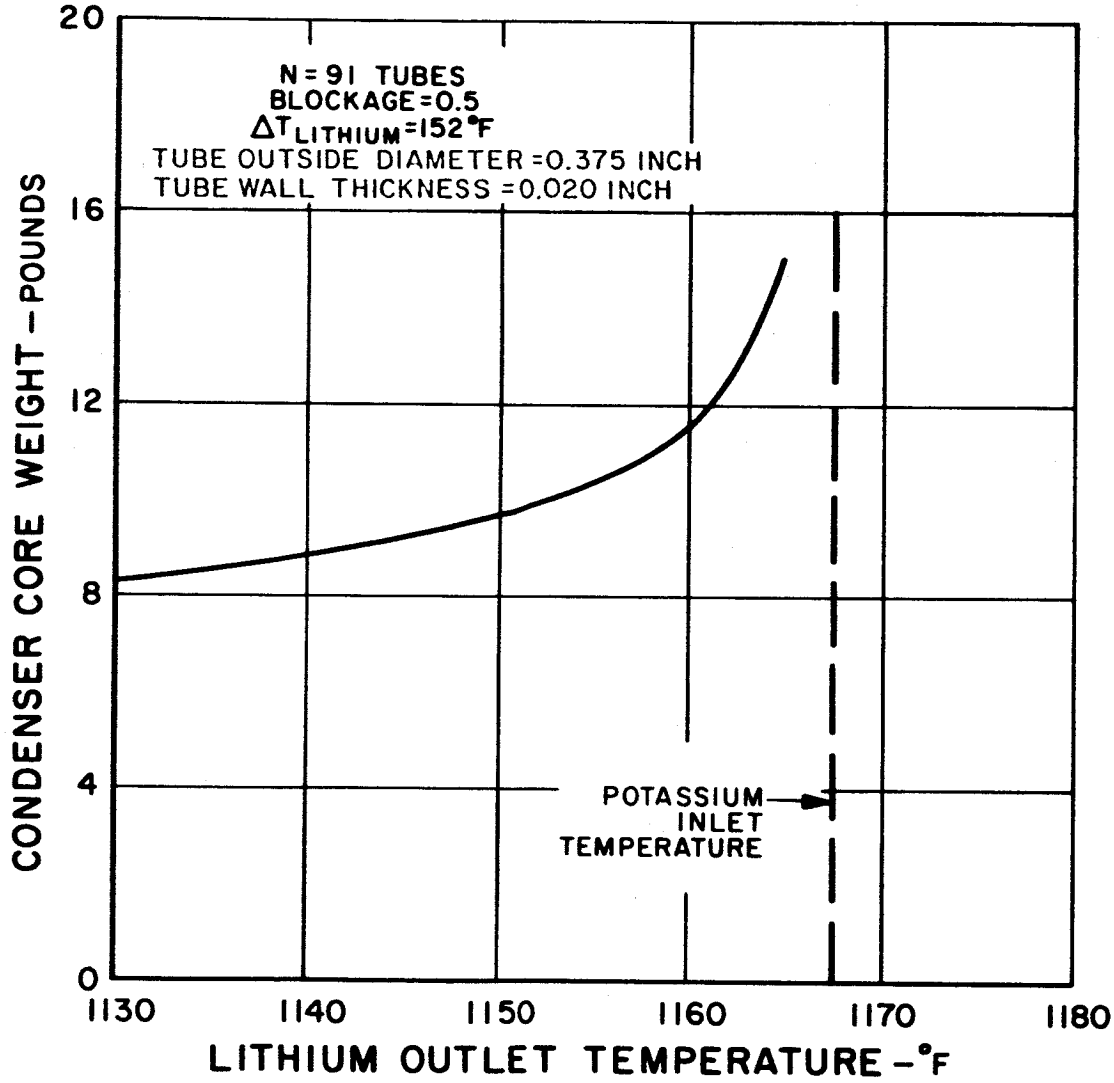

Figure 32b Lithium-Cooled Constant-Diameter Condenser. Effect of Coolant Temperature Level on Condenser Core Weight

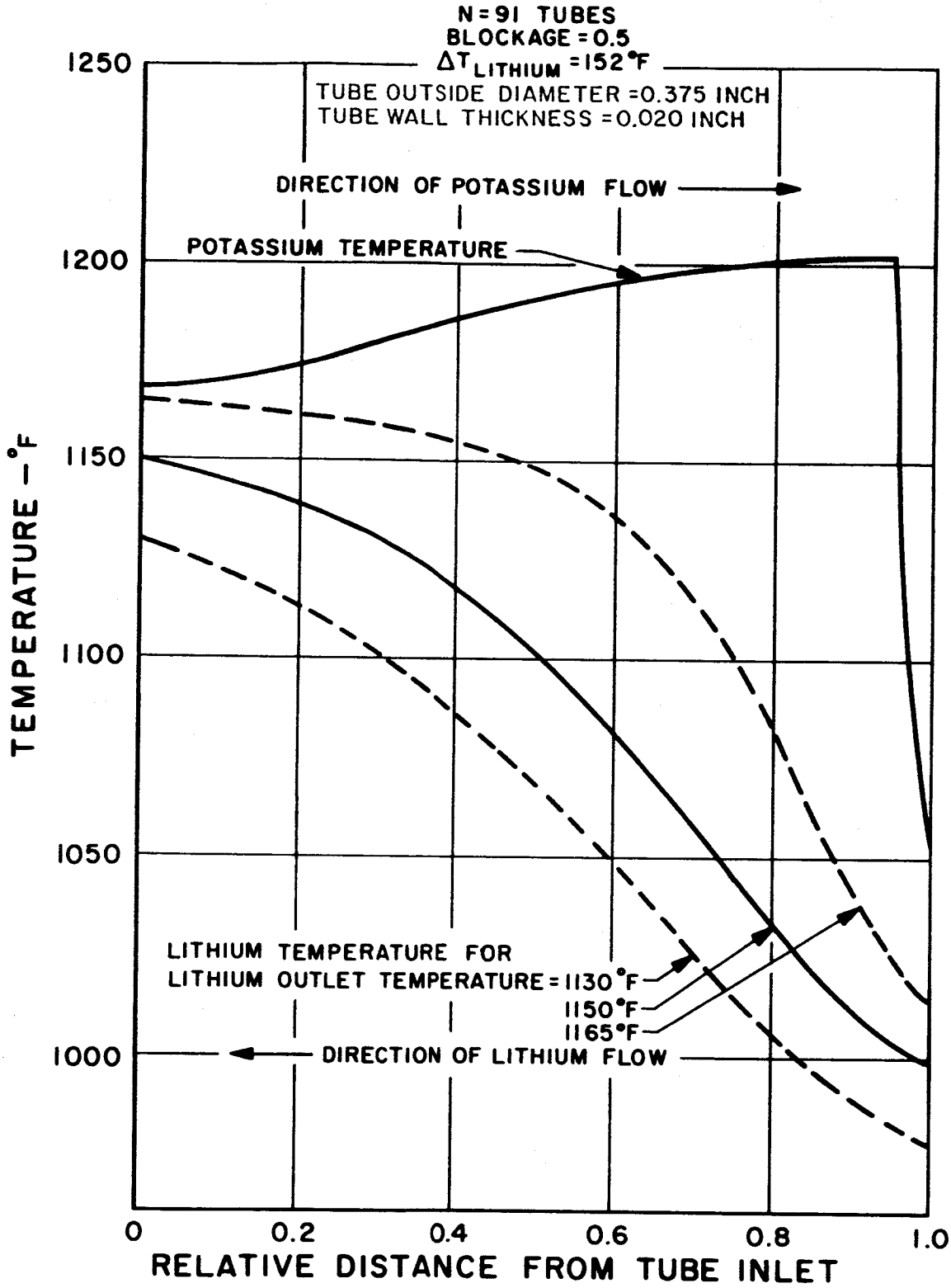

Figure 33 Lithium-Cooled Constant-Diameter Condenser. Fluid Temperature Profile Curves

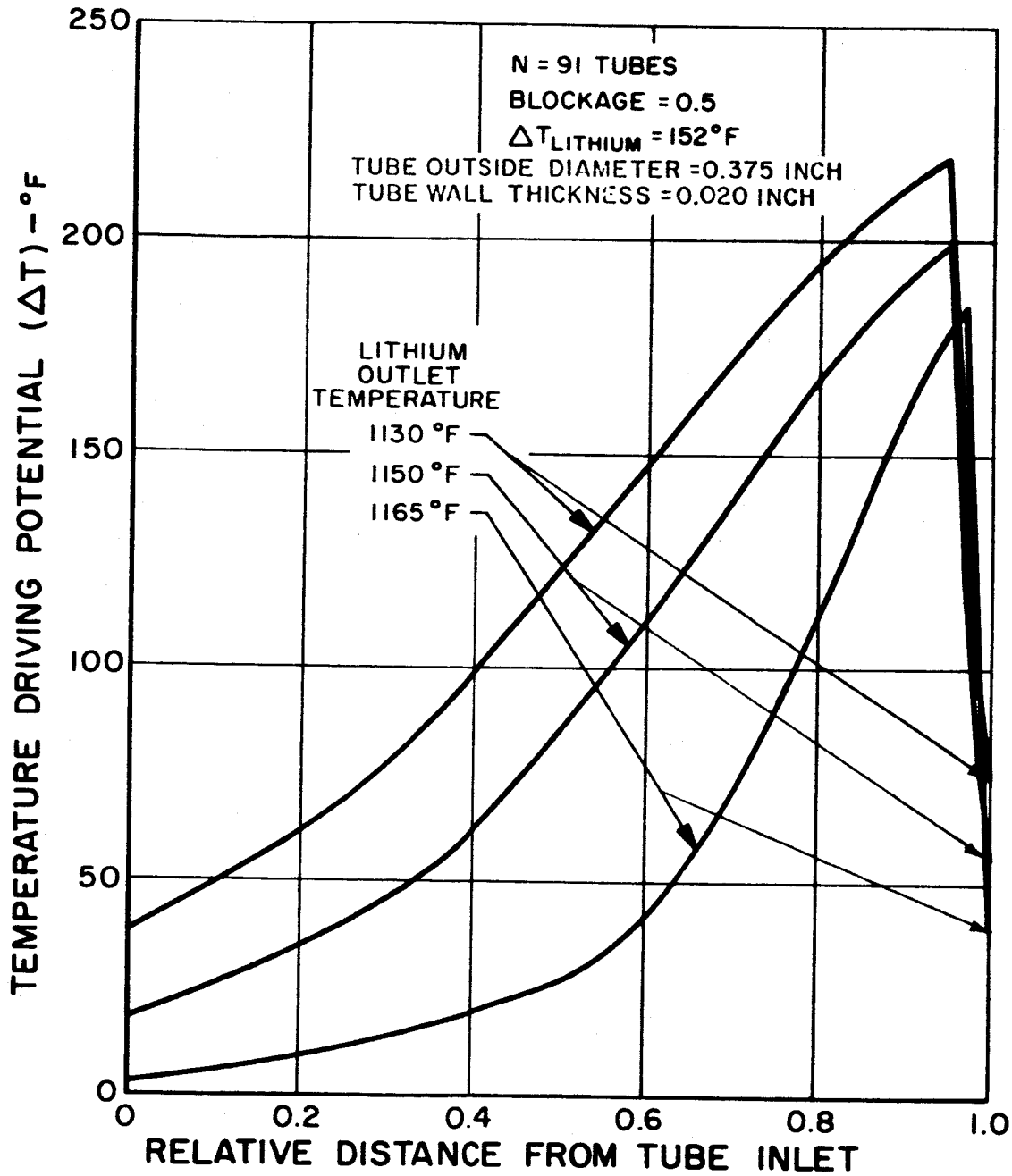

Figure 34 Lithium-Cooled Constant Diameter Condenser. Effect of Coolant Temperature Level on Temperature Driving Potential Distribution Along Condenser

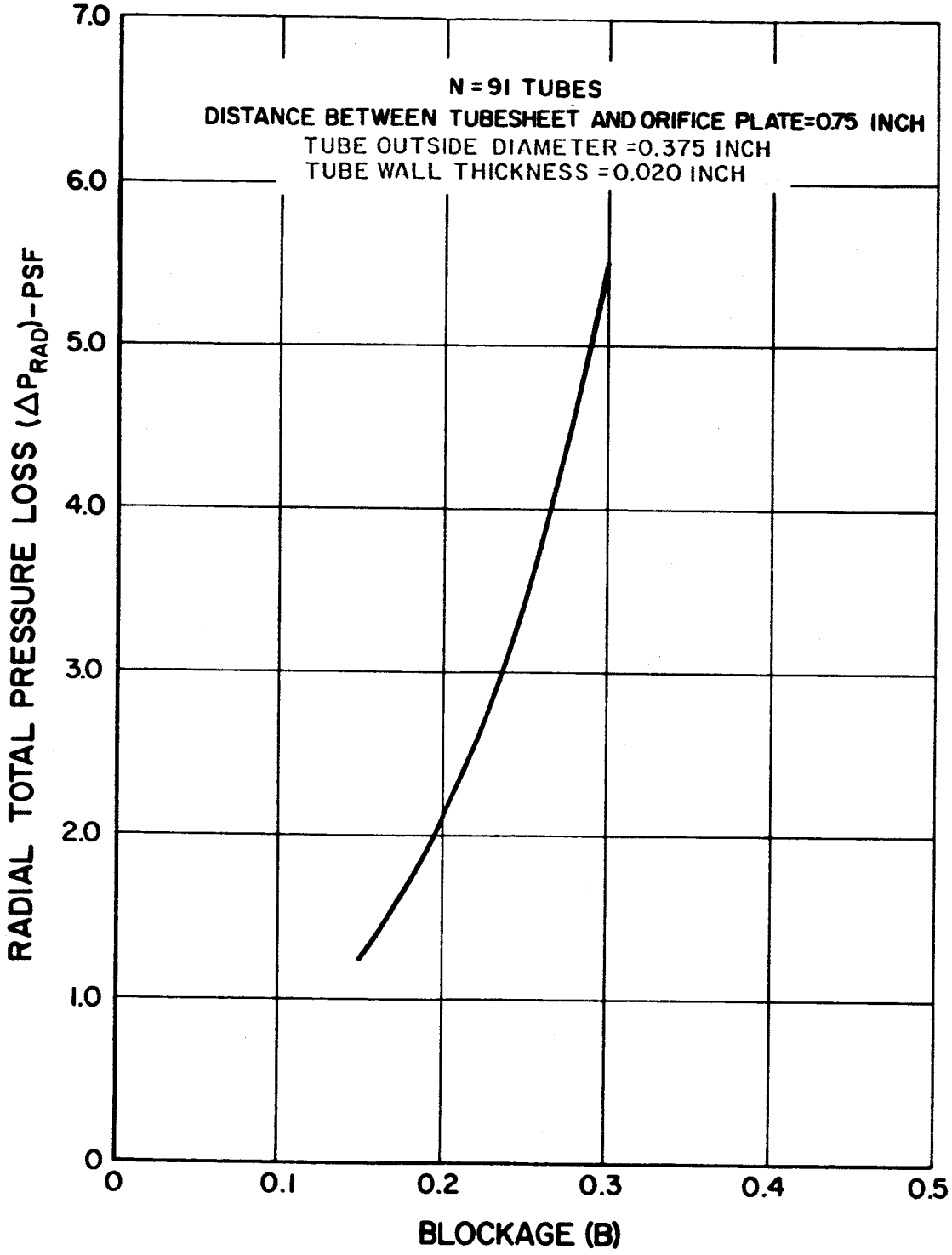

Figure 35 Effect of Blockage on Radial Pressure Loss for NaK-Cooled Constant-Diameter Condenser

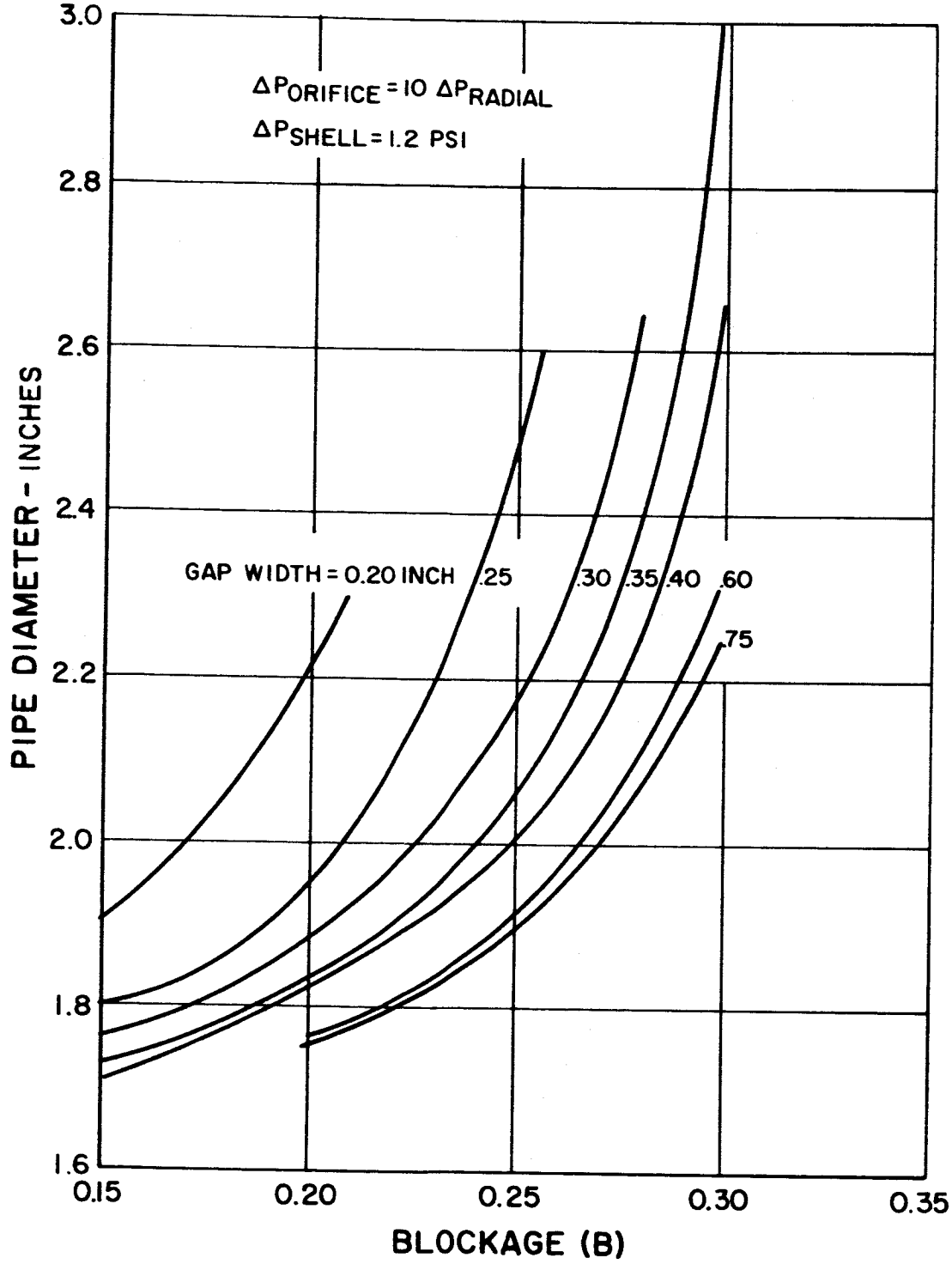

Figure 36 Effect of Gap Width and Blockage on Diameter of Coolant Inlet and Outlet Pipes for NaK-Cooled Constant-Diameter Condenser

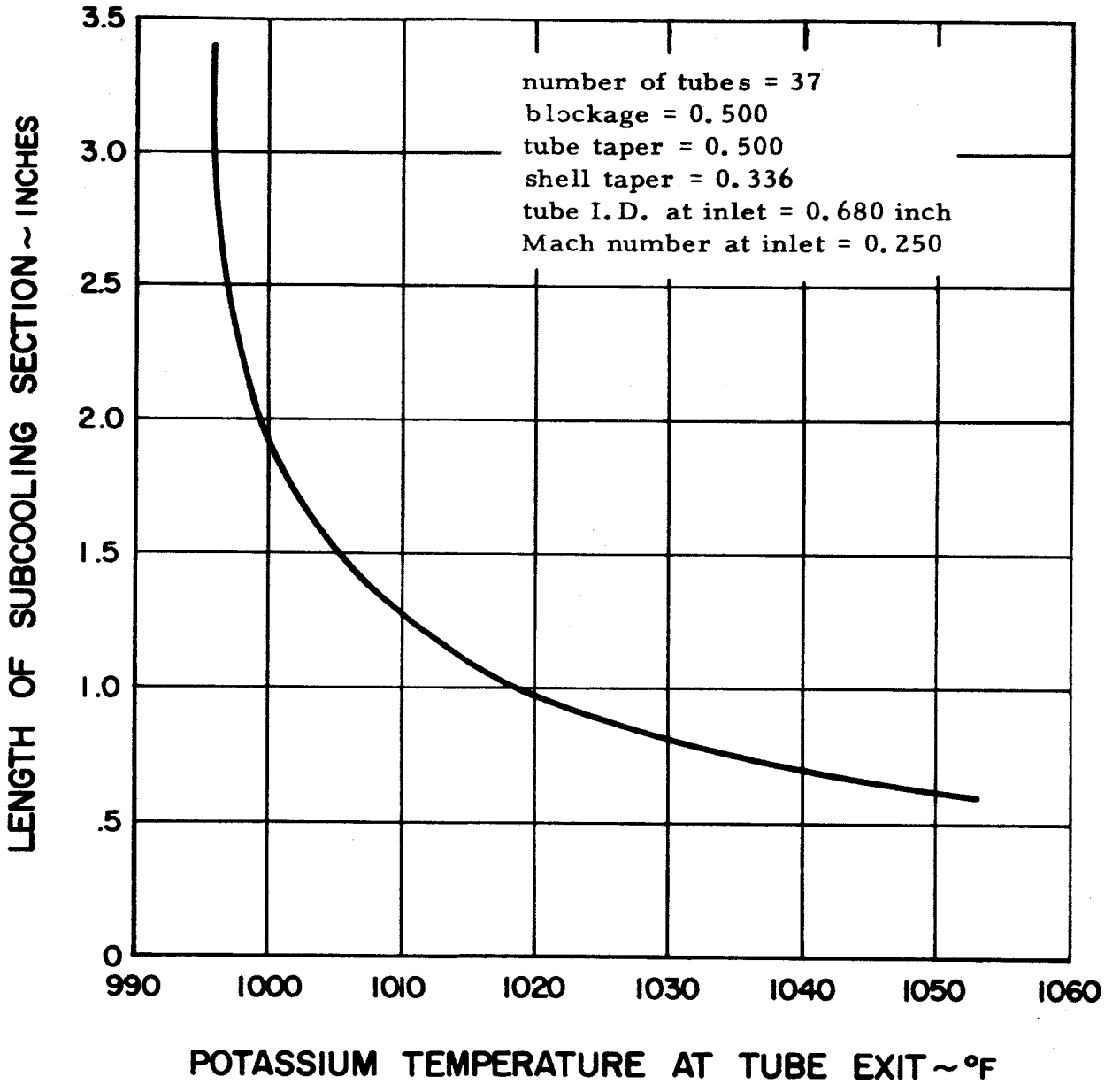

Figure 37 Lithium-Cooled Tapered Condenser. Effect of Potassium Exit Temperature on Subcooling Length

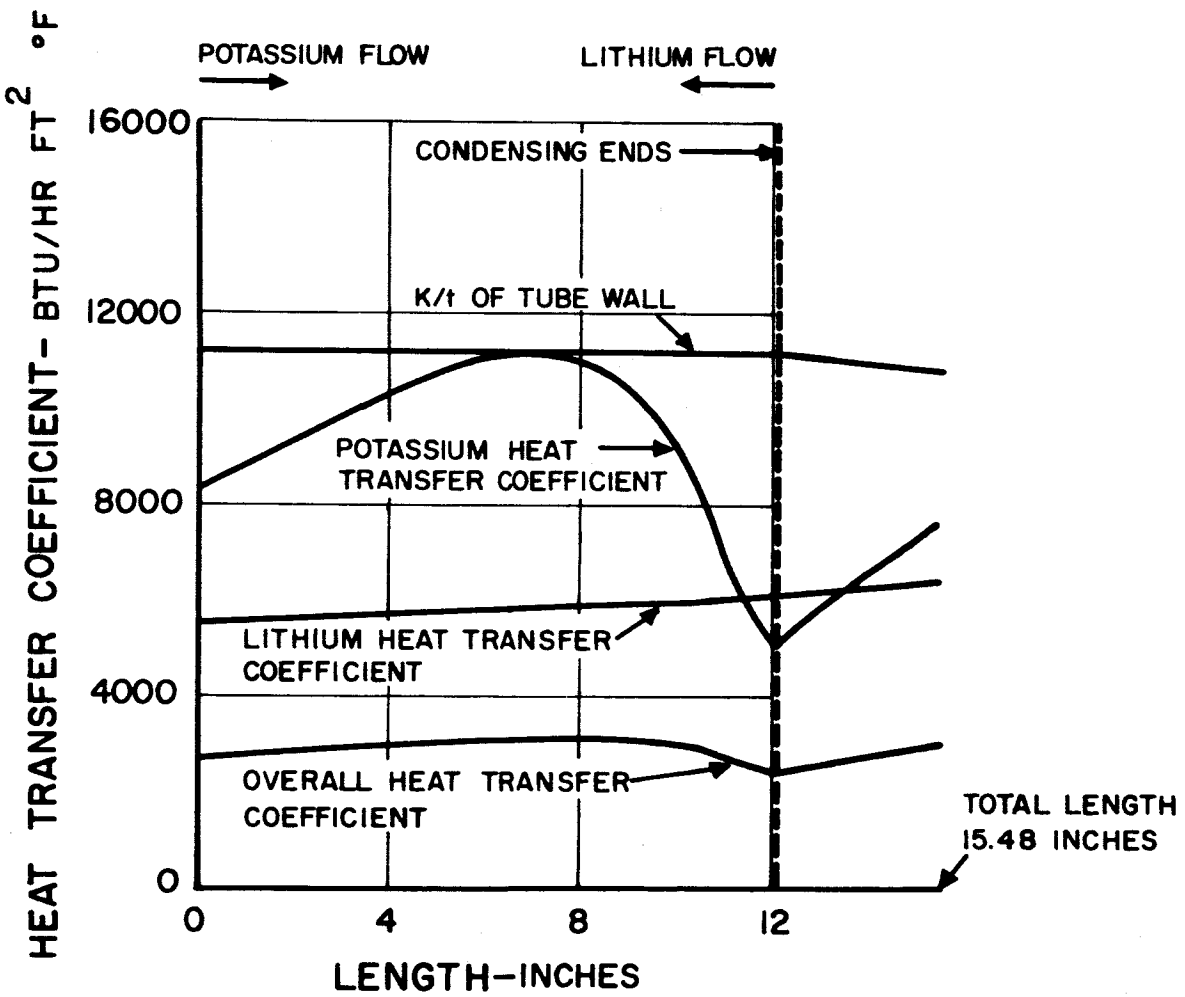

Figure 38 Variation of Heat Transfer Coefficient with Length for Lithium-Cooled Tapered Shell-and-Tube Configuration

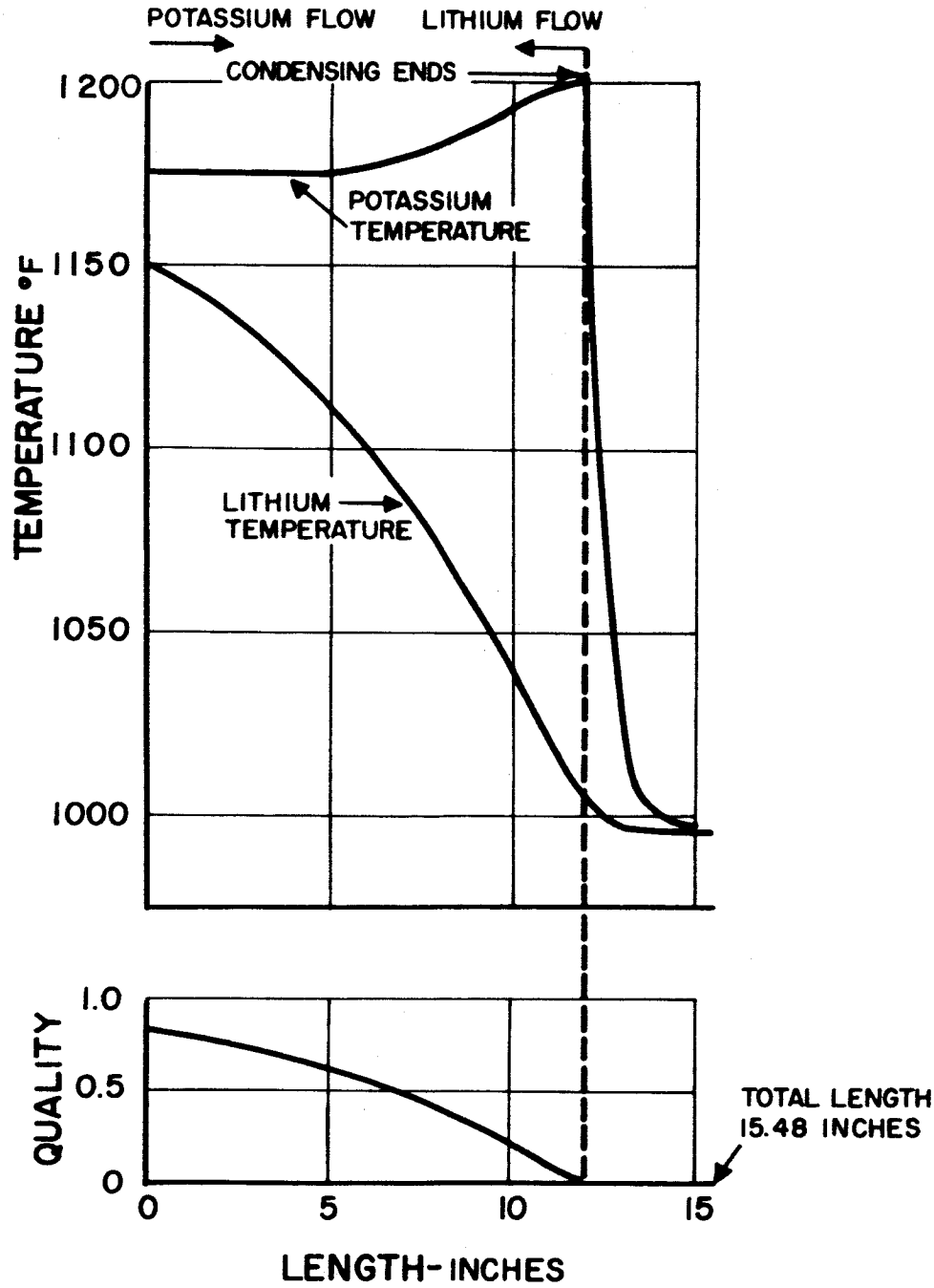

Figure 39 Variation of Fluid Temperatures and Potassium Quality with Length for Lithium-Cooled Tapered Shell-and-Tube Configuration

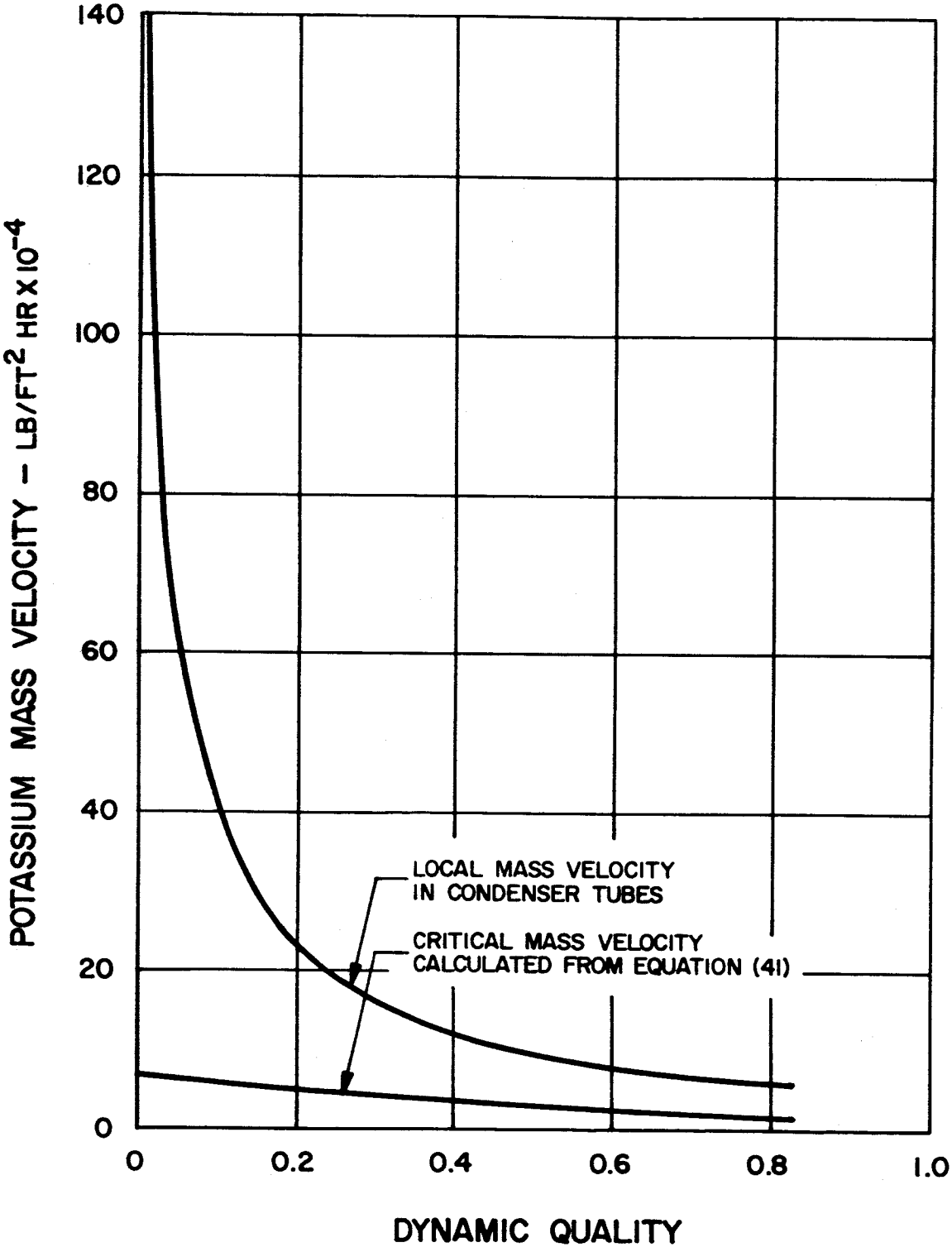

Figure 40 Lithium-Cooled Tapered Condenser. Comparison Between Local Mass Velocity and Critical Mass Velocity of Potassium

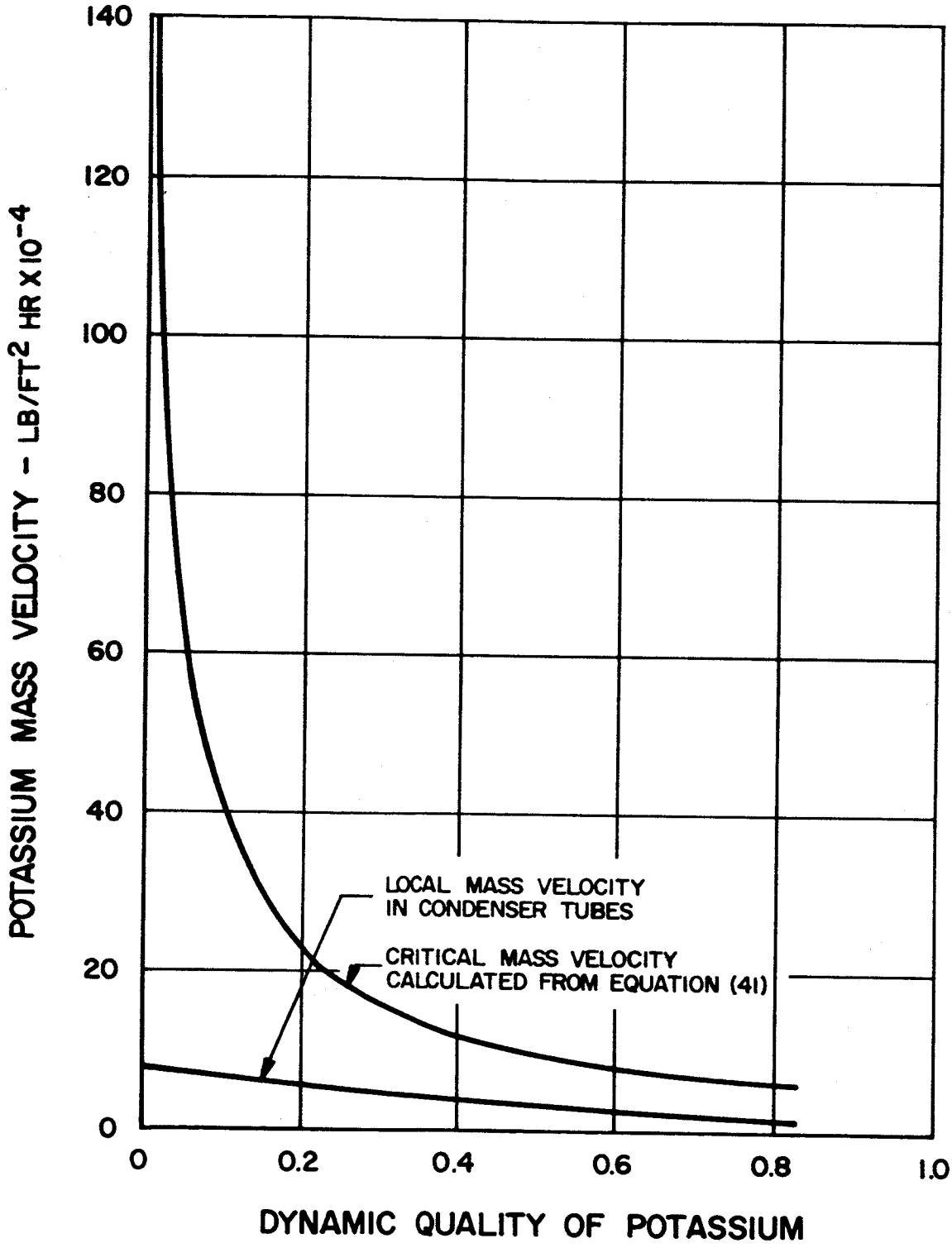

Figure 41 NaK-Cooled Tapered Condenser. Comparison Between Local Mass Velocity and Critical Mass Velocity of Potassium

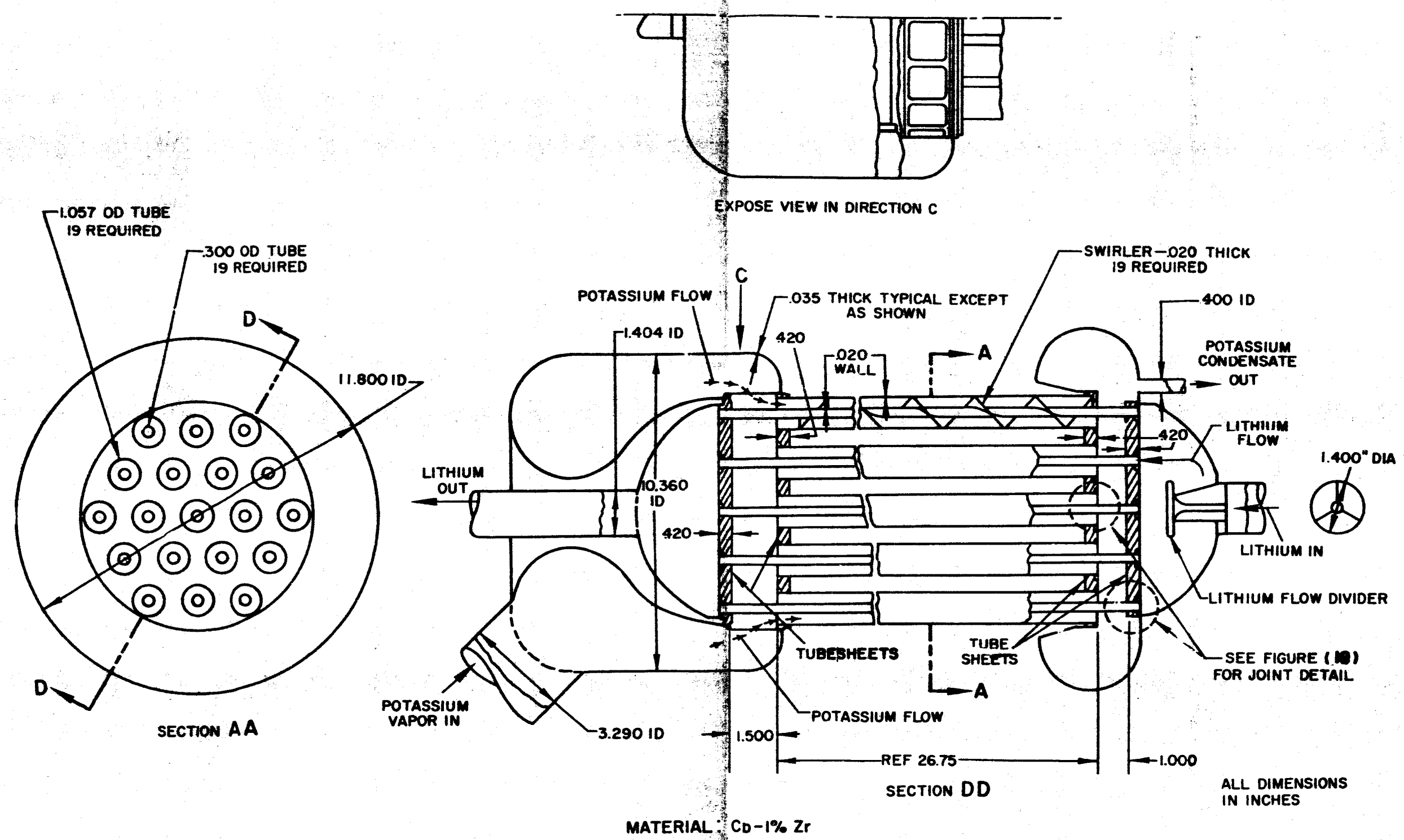

Figure 42 Lithium-Cooled Potassium Condenser for 1 MW(e) Nuclear Space Powerplant with Condensing Flow in Annular Passages

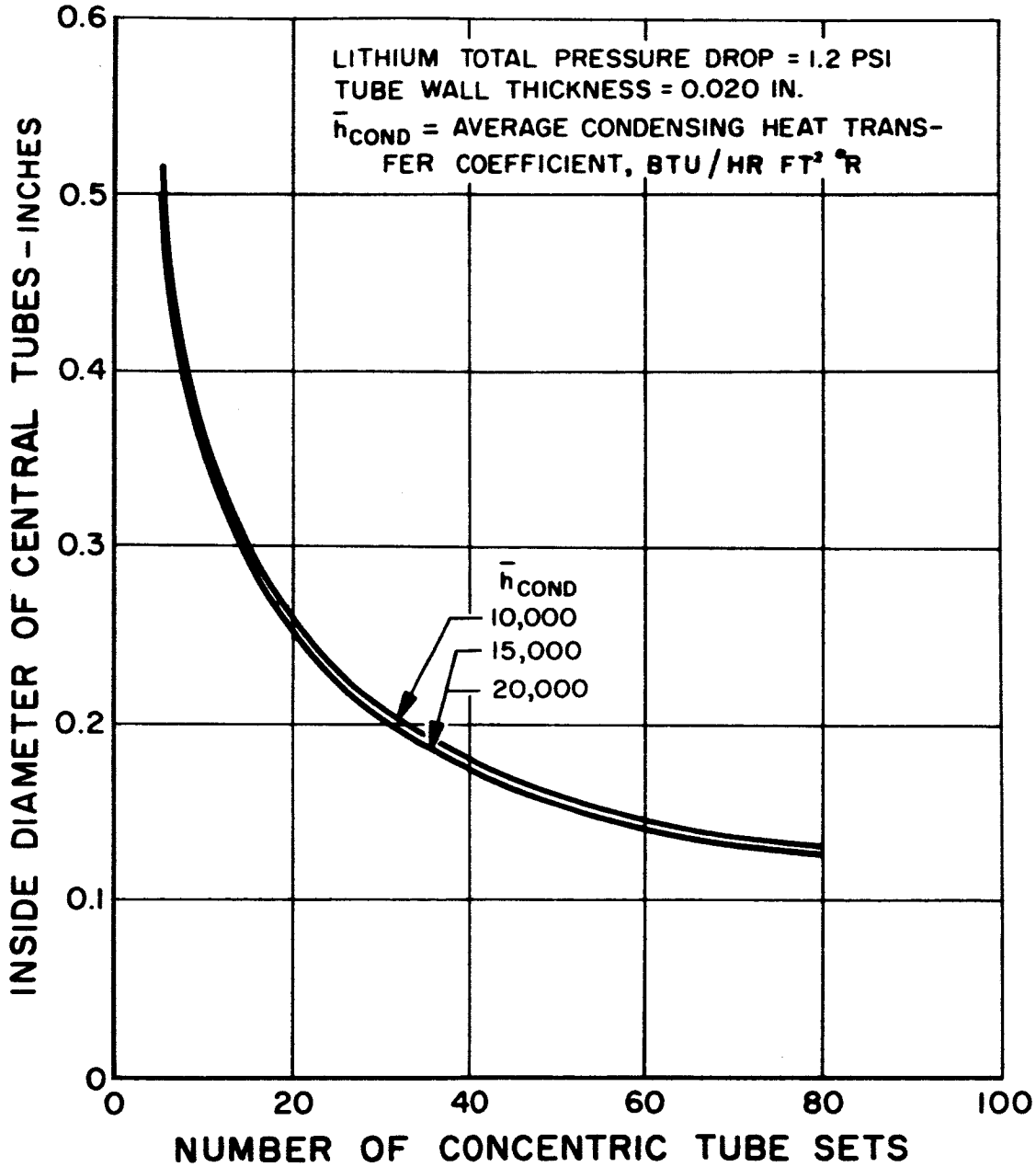

Figure 43 Concentric-Tube Condenser. Effect of Average Condensing Heat Transfer Coefficient and Number of Concentric Tube Sets on Inside Diameter of Central Tubes

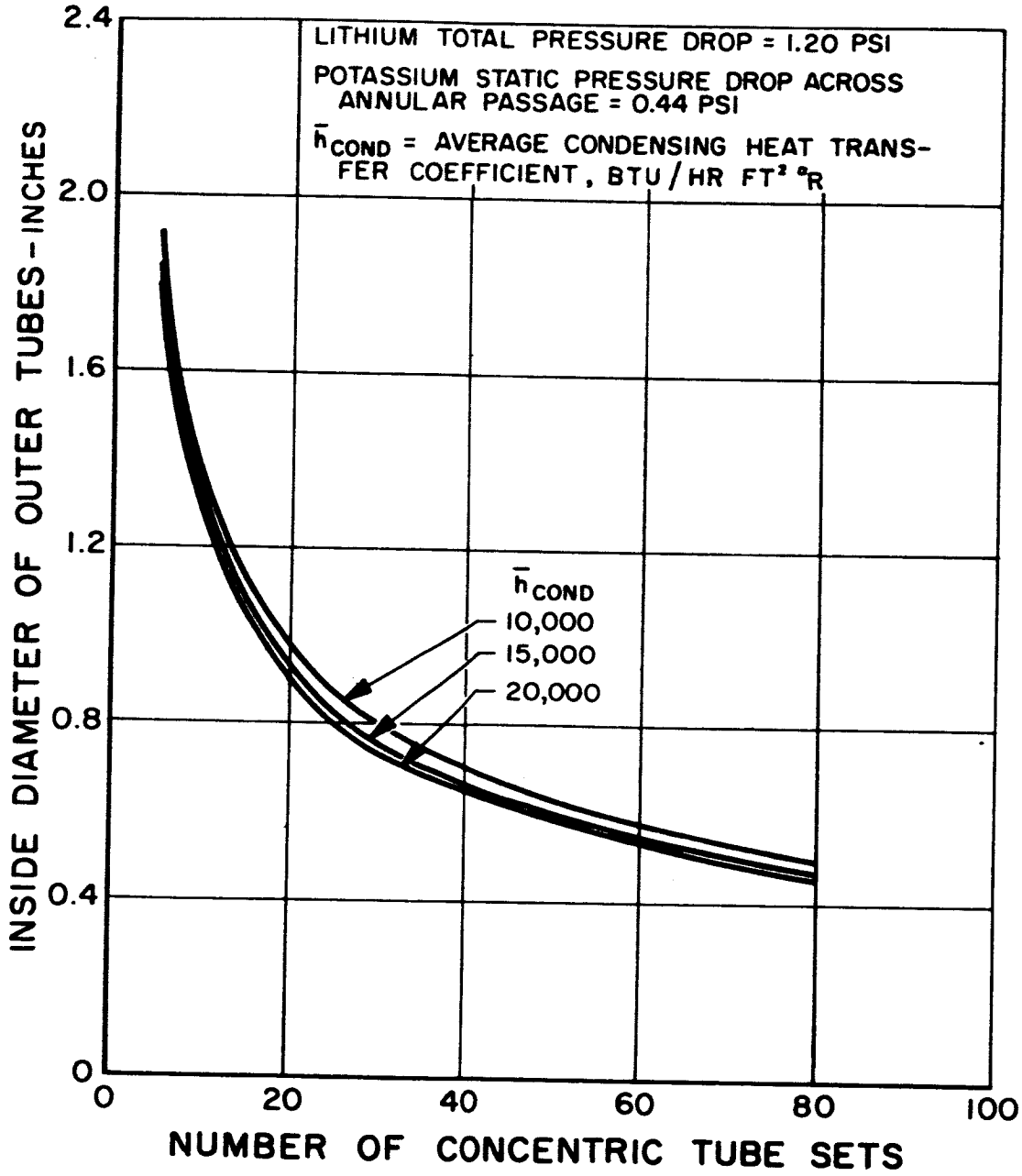

Figure 44 Concentric-Tube Condenser. Effect of Average Condensing Heat Transfer Coefficient and Number of Concentric Tube Sets on Inside Diameter of Outer Tubes

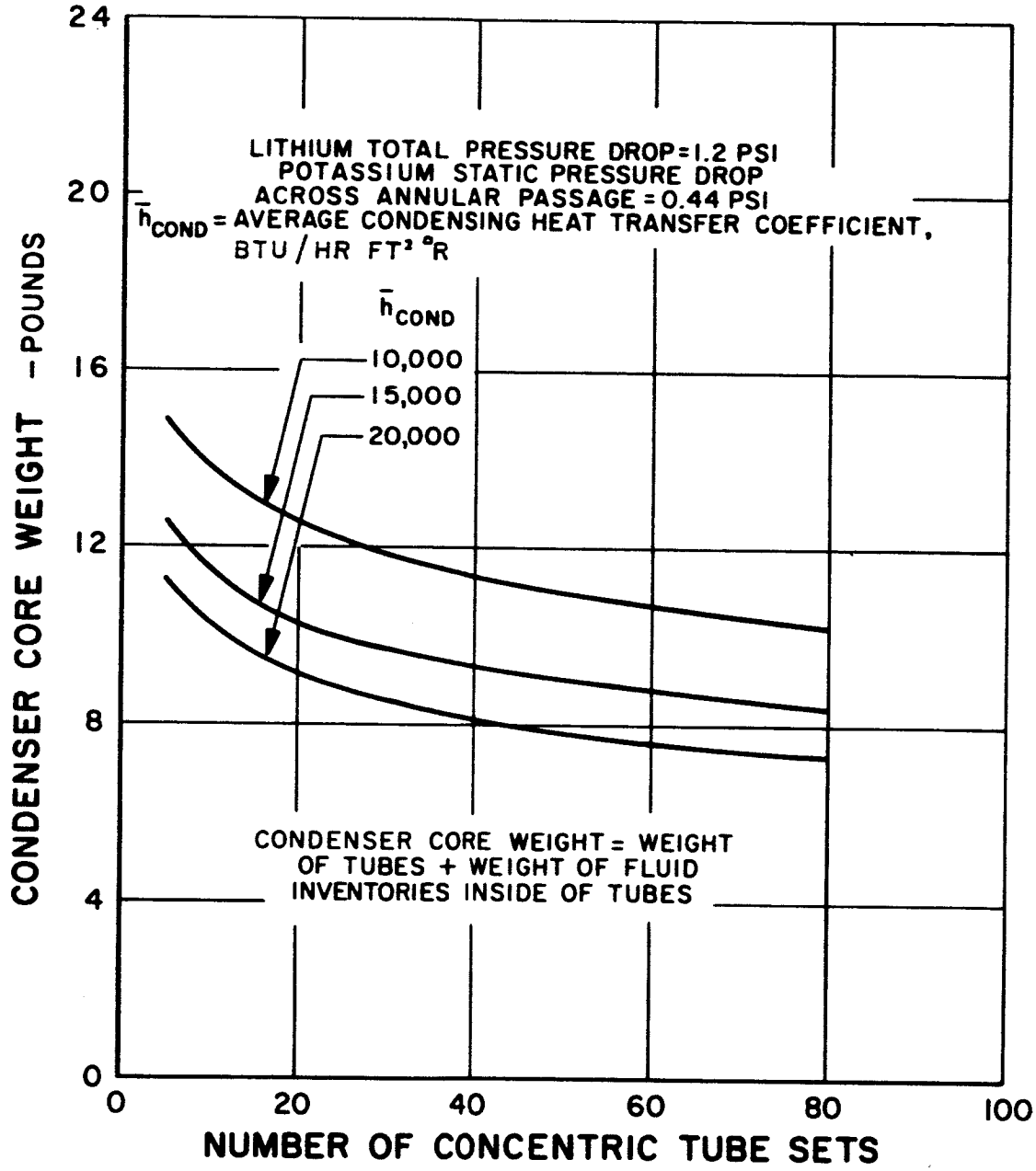

Figure 45 Concentric-Tube Condenser. Effect of Average Condensing Heat Transfer Coefficient and Number of Concentric Tube Sets on Condenser Core Weight

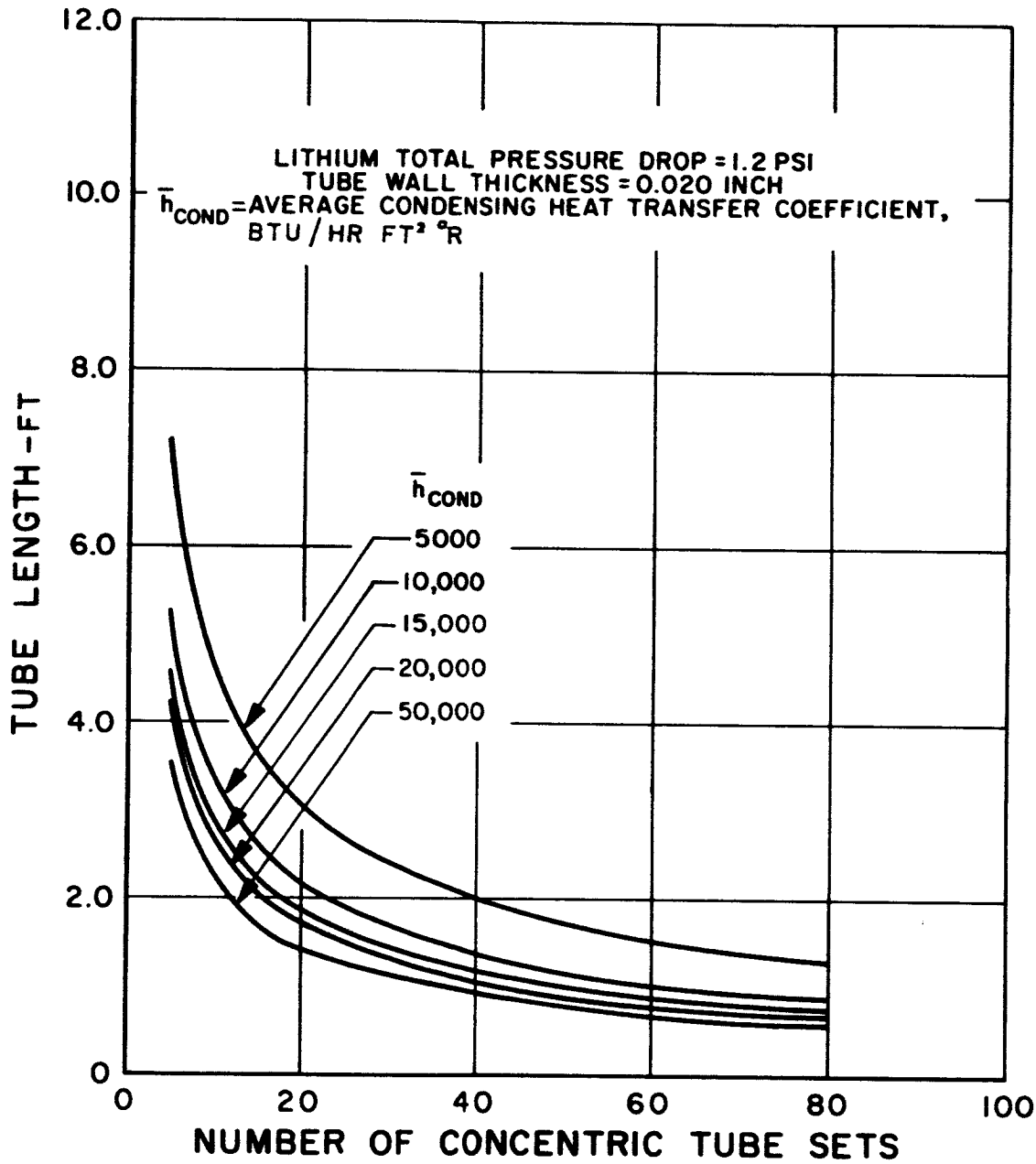

Figure 46 Concentric-Tube Condenser. Effect of Average Condensing Heat Transfer Coefficient and Number of Concentric Tube Sets on Tube Length

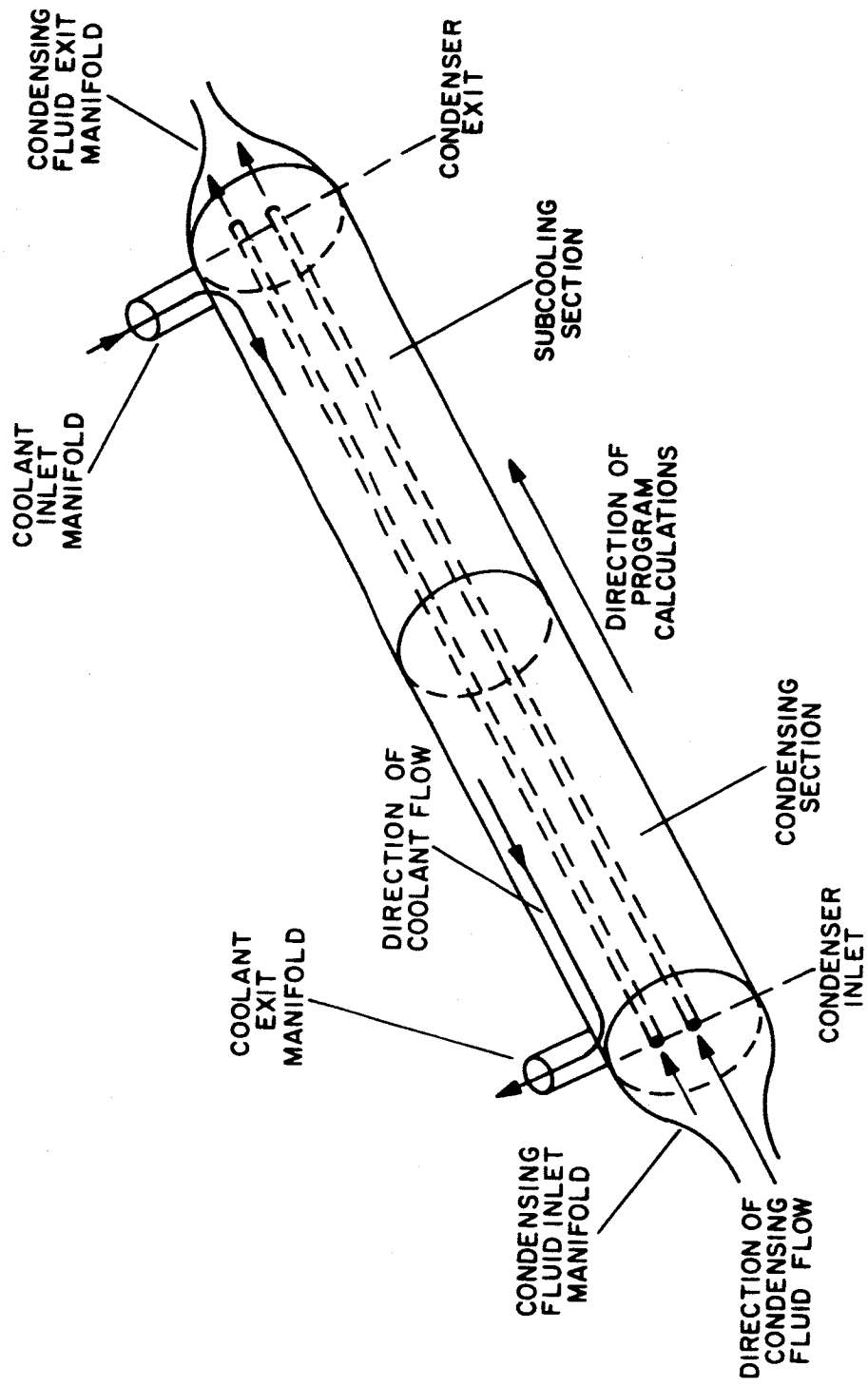

Figure 47. Sketch of Counterflow Condenser

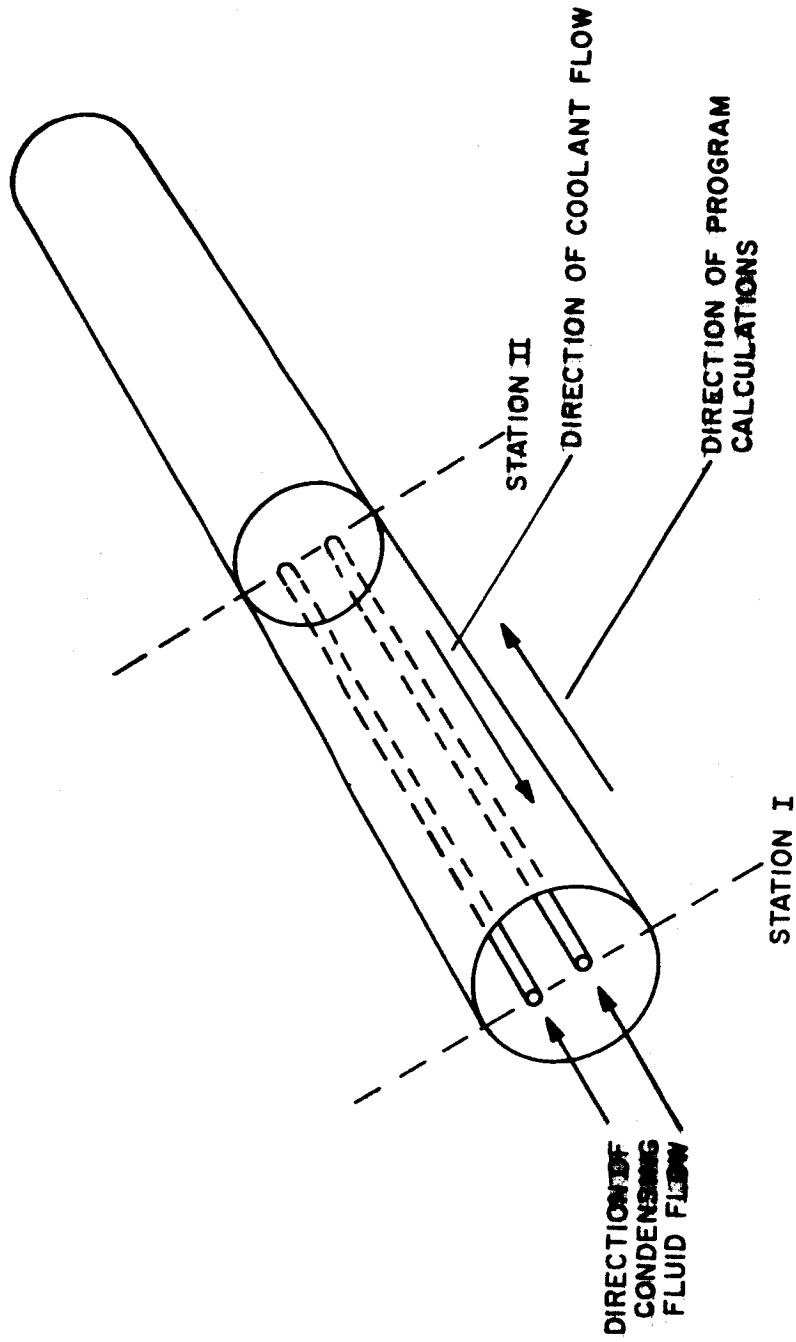

Figure 48 Sketch of Condenser Increment

APPENDIX F

Method of Calculating Incremental Lengths for Tapered Tube Condensers

APPENDIX F

Method of Calculating Incremental Lengths for Tapered Tube Condensers

In Section III. B it was recommended that design calculations for liquid metal condensers be made by subdividing the condenser into a number of small increments that could be considered individually. The solution would be made using an incremental marching procedure that would start at one end of the condenser and proceed increment-by-increment towards the opposite end. Information obtained from the solution of one increment would be used as input for the solution of the following increment. Equations are derived in this appendix that can be applied to the solution of the individual increment lengths for tapered condensers where the cross-sectional dimensions of the condenser vary linearly with axial distance. These equations will account for both the variation of the overall heat transfer coefficient U with axial distance across an increment and the effect of tapering on the heat transfer area of an increment. The derivation will be made for the general case of a counterflow linearly tapered heat exchanger where it will be assumed that the specific heats of both fluids are constants. This derivation will then be applied to a special case where the tube fluid changes phase by making an appropriate assumption concerning the ratio of the specific heat of the shell fluid to the specific heat of the tube fluid.

The tapered heat exchanger considered in this derivation is similar to the condenser illustrated in Figure 22. It employs a counterflow shell-and-tube arrangement where the inside diameter of the tubes D_T and the inside diameter of the shell D_S both vary linearly with axial distance ℓ from the inlet of the tube, according to the relations *

$$D_T = D_{T_o} (1 - \gamma_T \ell) \tag{F1}$$

$$D_S = D_{S_o} (1 - \gamma_S \ell) \tag{F2}$$

*Nomenclature for this appendix is on p. F11

Thus for a given axial location, the inside diameters of the tubes are dependent upon their values at the tube inlet D_{T_o} and the tube taper γ_T, while the inside diameter of the shell is dependent on its value at the tube inlet D_{S_o} and the shell taper γ_S.

The flow pattern, geometry, and temperature distribution for a single increment of a linearly-tapered heat exchanger is illustrated in Figure F1. For this case, the temperature of the tube fluid T_T is higher than the temperature of the shell fluid T_S. As can be seen in Figure F1, the temperatures of both fluids decrease as the axial distance X from the tube inlet end of the increment increases. This is due to the basic counterflow arrangement of the heat exchanger. The variation of the inside diameters of the tubes and the shell across the increment can be described by the relations

$$D_T = D_{T_{Io}} \quad (1 - \beta_T X) \tag{F3}$$

$$D_S = D_{S_{Io}} \quad (1 - \beta_S X) \tag{F4}$$

$D_{T_{Io}}$ and $D_{S_{Io}}$ are the inside diameters of the tubes and the shell respectively at the tube inlet end of the increment (i.e. at X = 0).

The terms β_T and β_S can be related to the tube taper γ_T and the shell taper γ_S of the heat exchanger through the relations

$$\beta_T = \left(\frac{D_{T_o}}{D_{T_{Io}}} \right) \gamma_T \tag{F5}$$

$$\beta_S = \left(\frac{D_{S_o}}{D_{S_{Io}}} \right) \gamma_S \tag{F6}$$

which can be derived from simple geometrical considerations.

Considering a differential element with length dX in the increment, (see Figure F1), the following relation can be written for the heat transferred from the tube fluid to the shell fluid within this differential element

$$dQ = U_I (T_T - T_S)\, dA \tag{F7}$$

where U_I is the overall heat transfer coefficient based on tube inside diameter.

The differential heat transfer area dA can be obtained from the relation

$$dA = N dA_T \tag{F8}$$

where N is the number of tubes and dA_T is the differential area of a single tube. dA_T can be obtained from the relation for the lateral surface area of the frustrum of a cone which has a height dX and a diameter which varies according to Equation (F3). The result is

$$dA_T = D_{T_{Io}} \pi \sqrt{1 + \left(\frac{D_{T_{Io}} \beta_T}{2}\right)^2} (1 - \beta_T X)\, dX \tag{F9}$$

Combining Equations (F7) to (F9) and rearranging, the result is

$$\frac{dQ}{dX} = \pi U_I N D_{T_{Io}} \sqrt{1 + \left(\frac{D_{T_{Io}} \beta_T}{2}\right)^2} (T_T - T_S) (1 - \beta_T X) \tag{F10}$$

Applying the conservation of energy to the differential element of the increment and assuming that the specific heats of the two fluids are constant across the increment, the following relation results

$$\frac{dQ}{dX} = - C_T \frac{dT_T}{dX} = - C_S \frac{dT_S}{dX} \tag{F11}$$

where $C_T = W_t C_{p_T}$

$C_S = W_s C_{p_S}$

C_T and C_S are the capacity rates of the tube and the shell fluids, respectively. The capacity rate represents the product of the weight flow of a fluid and its specific heat.

Combining Equations (F10) and (F11)

$$-C_S \frac{dT_S}{dX} = \pi NU_I D_{T_{Io}} (T_T - T_S) \sqrt{1 + \left(\frac{D_{T_{Io}} \beta_T}{2}\right)^2} (1 - \beta_T X) \tag{F12}$$

Multiplying Equation (F11) by dX and rearranging results in the relation

$$dT_T = \frac{C_S}{C_T} dT_S$$

which upon integration from the tube inlet end of the increment to any position yields the following form

$$T_{T_{(X)}} - T_{To} = \frac{C_S}{C_T} \left(T_{S_{(X)}} - T_{So} \right) \tag{F13}$$

Combining Equations (F12) and (F13) the result is

$$-C_S \frac{dT_S}{dX} = \pi NU_I D_{T_{Io}} \left[T_{To} - \frac{C_S}{C_T} T_{So} - \left(1 - \frac{C_S}{C_T}\right) T_S \right] \sqrt{1 + \left(\frac{D_{T_{Io}} \beta_T}{2}\right)^2} (1 - \beta_T X) \tag{F14}$$

The overall heat transfer coefficient based on tube inside diameter U_I can be obtained from the relation

$$U_I = \frac{1}{\frac{1}{h_T} + \frac{(OD)_T \ln \frac{(OD)_T}{D_T}}{2 k_w} + \frac{(OD)_T}{D_T \; h_S}} \qquad \text{(F15)}$$

where $(OD)_T$ = outside diameter of tube

U_I is dependent upon the heat transfer coefficient of the tube fluid h_T, the heat transfer coefficient of the shell fluid h_S, and the thermal resistance of the tube wall $\frac{OD_T \ln \frac{(OD_T)}{D_T}}{2k_w}$. For given flow rates the heat transfer coefficients of the two fluids are strongly dependent upon the diameters of the tubes and the shell. Since these diameters are dependent upon the axial distance X and the heat transfer coefficients h_T and h_S, the overall heat transfer coefficient U_I will also be dependent upon X. As a result the variation of U_I with length across an increment can be approximated using a Maclaurin series expansion of U_I in terms of X

$$U_I = U_{Io} + \left(\frac{dU_I}{dX}\right)_{X=0} X + \frac{1}{2!}\left(\frac{d^2U_I}{dX^2}\right)_{X=0} X^2 + \frac{1}{3!}\left(\frac{d^3U_I}{dX^3}\right)_{X=0} X^3 + \cdots \qquad \text{(F16)}$$

If U_I does not vary greatly across an increment, the first derivative in Equation (F16) can be approximated by the relation

$$\left(\frac{dU}{dX}\right)_{X=0} = \frac{\Delta U_I}{\Delta X} = \frac{U_{IL} - U_{Io}}{L} \qquad \text{(F17)}$$

where U_{Io} and U_{IL} are the overall heat transfer coefficients at the tube outlet and tube inlet ends of the increment, respectively, and L is the length of the increment.

Combining Equations (F16) and (F17) and neglecting the second and higher order terms in Equation (F16), the result is

$$U_I = U_{Io} - \left(\frac{U_{Io} - U_{IL}}{L}\right) X \qquad \text{(F18)}$$

Equations (F14) and (F18) can then be combined to yield the following expression

$$-C_S \frac{dT_S}{dX} = \pi N D_{T_{Io}} \left[U_{Io} \left(\frac{U_{Io} - U_{IL}}{L} \right) X \right] \left[T_{To} - \frac{C_S}{C_T} T_{So} - \left(1 - \frac{C_S}{C_T} \right) T_S \right] \sqrt{1 + \left(\frac{D_{T_{Io}} \beta_T}{2} \right)^2} \left(1 - \beta_T X \right) \qquad \text{(F19)}$$

Separating the variables in Equation (F19) the result is

$$\frac{-dT_S}{T_{To} - \frac{C_S}{C_T} T_{So} - \left(1 - \frac{C_S}{C_T} \right) T_S} = \frac{\pi N D_{T_{Io}}}{C_S} \sqrt{1 + \left(\frac{D_{T_{Io}} \beta_T}{2} \right)^2} \left[U_{Io} - \left(\frac{U_{Io} - U_{IL}}{L} + \beta_T U_{Io} \right) X + \left(\frac{U_{Io} - U_{IL}}{L} \right) \beta_T X^2 \right] dX \qquad \text{(F20)}$$

Integrating Equation (F20) between the limits X = 0 and X = L yields the relation

$$\frac{\ln \left[\frac{T_{To} - \frac{C_S}{C_T} T_{So} - \left(1 - \frac{C_S}{C_T} \right) T_{SL}}{T_{To} - T_{So}} \right]}{1 - \frac{C_S}{C_T}} =$$

$$\frac{\pi N D_{T_{Io}}}{C_S} \sqrt{1 + \left(\frac{D_{T_{Io}} \beta_T}{2} \right)^2} \left[\frac{U_{Io} + U_{IL}}{2} L - \left(2 U_{IL} + U_{Io} \right) \frac{\beta_T}{6} L^2 \right] \qquad \text{(F21)}$$

Rearranging Equation (F21) the result is

$$\frac{\beta_T}{6}(2U_{IL} + U_{Io})L^2 - \frac{(U_{Io} + U_{IL})}{2}L + H = 0 \qquad \text{(F22)}$$

The term H in Equation (F22) is defined as

$$H \equiv \frac{C_S \ln\left[\dfrac{T_{To} - \dfrac{C_S}{C_T}T_{So} - \left(1 - \dfrac{C_S}{C_T}\right)T_{SL}}{T_{To} - T_{So}}\right]}{\pi N D_{T_{Io}}\left(1 - \dfrac{C_S}{C_T}\right)\sqrt{1 + \left(\dfrac{D_{T_{Io}}\beta_T}{2}\right)^2}} \qquad \text{(F23)}$$

Solving for L the following expression is obtained

$$L = \frac{\dfrac{U_{Io} + U_{IL}}{2} \pm \sqrt{\dfrac{U_{Io} + U_{IL}}{2}^2 - \dfrac{2}{3}H\beta_T(2U_{IL} + U_{Io})}}{\dfrac{\beta_T}{3}(2U_{IL} + U_{Io})} \qquad \text{(F24)}$$

To determine whether the positive or the negative sign must be used in front of the radical in Equation (F24) the case of very slightly tapered tubes, (i.e., β_T approaching zero), can be considered. As β_T approaches zero the right-hand side of Equation (F24) approaches two limits depending on the sign in front of the radical. If the positive sign is used in front of the radical, the right hand side of Equation (F24) approaches infinity. If negative sign is used in front of the radical, the right-hand side of Equation (F24) approaches the limit $H\dfrac{(U_{Io} + U_{IL})}{2}$ which is a finite number. Since the length of an increment must remain finite for slight tapers, the negative sign must be used in front of the radical.

Rearranging Equation (F24) the following relation for the length of an increment is obtained

$$L = \frac{3\,(U_{Io} + U_{IL})}{2\,\beta_T\,(2U_{IL} + U_{Io})} - \sqrt{\left[\frac{3\,(U_{Io} + U_{IL})^2}{2\,\beta_T\,(2U_{IL} + U_{Io})}\right] - \frac{6H}{\beta_T\,(2U_{IL} + U_{Io})}} \qquad \text{(F25)}$$

Equation (F25) was derived for the general case of a counterflow linearly-tapered heat exchanger where it was assumed that the variation of U_I across an increment could be approximated using the first two terms of a Maclaurin series, and that the specific heats of the two fluids remained constant across an increment. In order to calculate the length of an increment using Equation (F25) it is necessary to know the overall heat transfer coefficients based on tube inside diameter at each end of the increment, U_{Io} and U_{IL}, the tube taper of the increment β_T and the parameter H. The parameter H is given by Equation (F23) where it can be seen that H is dependent upon the terminal temperatures of the two fluids T_{To}, T_{TL}, T_{So} and T_{SL}, the capacity rates of the two fluids C_S and C_T, the number of tubes N, the tube taper of the increment β_T, and the inside diameter of the tubes at the tube inlet end of the increment $D_{T_{Io}}$. This equation for H is directly applicable to the case where both fluids are single-phase fluids and have constant specific heats. However, if the tube fluid undergoes a change in phase as it flows through an increment, a number of approximations can be made and a simpler expression for H can be developed.

Equation (F11) can be integrated between the limits X = 0 and X = L to yield the following form

$$Q = C_T\,(T_{To} - T_{TL}) = C_S\,(T_{So} - T_{SL}) \qquad \text{(F26)}$$

Equation (F26) can be rearranged to yield the following form

$$T_{To} - T_{TL} = \frac{C_S}{C_T}\,(T_{So} - T_{SL}) \qquad \text{(F27)}$$

If the tube fluid changes phase as it flows through the condenser, its temperature is dependent upon its pressure due to saturation conditions. Since the pressure of the tube fluid will change only slightly across a single increment, it can be assumed that its temperature remains constant across the increment. The temperature difference $T_{To} - T_{TL}$

can then be assumed to be zero. Since a definite quantity of heat is transferred from the condensing fluid in the tube, conservation of energy requires that inlet-to-outlet temperature difference of the shell fluid $T_{So} - T_{SL}$ cannot be zero. The ratio of the capacity rates C_S/C_T must therefore be assumed to be equal to zero to satisfy Equation (F27). If the ratio of capacity rates C_S/C_T is assumed equal to zero, Equation (F23) is reduced to the following form

$$H = \frac{C_S \ln \left[\dfrac{T_{To} - T_{SL}}{T_{To} - T_{So}} \right]}{\pi N D_{T_{Io}} \sqrt{1 + \left(\dfrac{D_{T_{Io}} \beta_T}{2} \right)^2}} \qquad \text{(F28)}$$

In applying these relations to the analysis of a tapered liquid metal condenser, the condenser must be divided into a condensing section where the tube fluid changes phase, and a subcooling section where the tube fluid is entirely liquid. Equation (F25) can be applied to both sections. However, Equation (F28) must be used to predict H for the condensing section and Equation (F23) must be used to predict H for the subcooling section.

Nomenclature for Appendix F

A	total heat transfer area	ft^2
A_T	heat transfer area of a single tube	ft^2
C_{p_S}	specific heat of shell fluid	Btu/lb-°F
C_{p_T}	specific heat of tube fluid	Btu/lb-°F
C_S	capacity rate of the shell fluid	Btu/hr-°F
C_T	capacity rate of the tube fluid	Btu/hr-°F
D_S	shell inside diameter	ft
D_T	tube inside diameter	ft
$D_{S_{Io}}$	shell inside diameter at X = 0	ft
$D_{T_{Io}}$	tube inside diameter at X = 0	ft
D_{S_o}	shell inside diameter at tube inlet	ft
D_{T_o}	tube inside diameter at tube inlet	ft
H	parameter defined by Equation (F23)	-
h_S	heat transfer coefficient of the shell fluid	Btu/hr-ft^2-°F
h_T	heat transfer coefficient of the tube fluid	Btu/hr-ft^2-°F
k_w	thermal conductivity of tube wall	Btu/hr-ft-°F
L	length of an increment	ft
ℓ	axial distance from the tube inlet end of the heat exchanger	ft
N	number of tubes	-
Q	total heat transferred from hot fluid to cold fluid	Btu/hr
T_{S_o}	shell fluid temperature at X = 0	°F
T_{S_L}	shell fluid temperature at X = L	°F
T_{T_o}	tube fluid temperature at X = 0	°F
T_{T_L}	tube fluid temperature at X = L	°F
t_w	tube wall thickness	ft
U_I	overall heat transfer coefficient based on tube inside diameter	Btu/hr-ft^2-°F
U_{Io}	overall heat transfer coefficient at X = 0 (based on tube I. D.)	Btu/hr-ft^2-°F
U_{IL}	overall heat transfer coefficient at X = L (based on tube I. D.)	Btu/hr-ft^2-°F
W_S	weight flow of shell fluid	lb/hr
W_T	weight flow of tube fluid	lb/hr
X	axial distance from the tube inlet end of an increment of the heat exchanger	ft
β_S	shell taper of an increment of the heat exchanger	ft^{-1}
β_T	tube taper of an increment of the heat exchanger	ft^{-1}
γ_S	shell taper of the heat exchanger	ft^{-1}
γ_T	tube taper of the heat exchanger	ft^{-1}

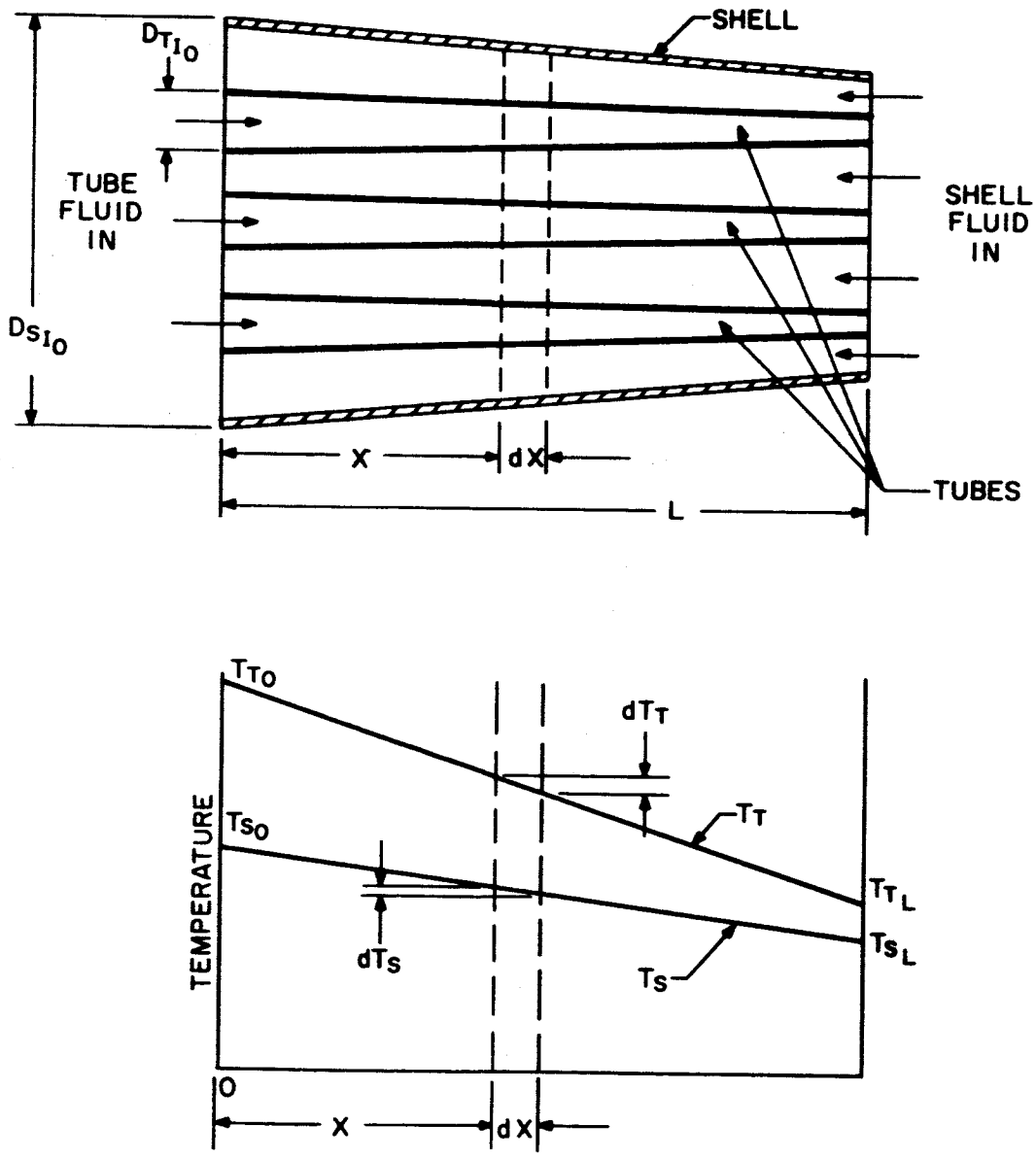

Figure F1 Sketch of Increment for a Counterflow Linearly-Tapered Heat Exchanger

APPENDIX G

Transition Criterion for a Condensing Film

APPENDIX G

Transition Criterion for a Condensing Film

In this appendix a laminar-to-turbulent flow transition criterion will be developed for the flow of a condensing film inside a circular pipe. This criterion will be obtained by analogy with a transition criterion derived for the fully-developed single-phase flow of a liquid through a circular pipe.

For the single-phase flow of a liquid through a circular pipe the wall shear stress is given by the relation*

$$\tau_w = C_f \, \rho_L \, \frac{V^2}{2g_c} \tag{G1}$$

For turbulent flow with Reynolds number $Re = \frac{\rho V D}{\mu}$ close to the transition region, the skin friction coefficient C_f can be obtained from the relation

$$C_f = \frac{0.079}{Re^{0.25}} \tag{G2}$$

The skin friction coefficient C_f differs from the friction factor f defined in Appendix H by a constant factor of 4.0. If it is assumed that transition from laminar to turbulent flow takes place at a Reynolds number of 2000, Equations (G1) and (G2) can be combined to yield the following result which can be used as a transition criterion instead of the Reynolds number

$$\left(\frac{D}{\nu_L} \sqrt{\frac{\tau_w \, g_c}{\rho_L}} \right)_{trans} = 154 \tag{G3}$$

Carpenter** has suggested that a criterion of the form of Equation (G3), which was derived for single-phase flow through a circular pipe, can be applied to the flow of a condensing film through a circular pipe.

*See Appendix B for nomenclature

**Carpenter, F., Heat Transfer and Pressure Drop for Condensing Pure Vapors Inside Vertical Tubes at High Vapor Velocities, PhD Thesis, University of Delaware, 1948

Squaring both sides of Equation (G3) and rearranging yields the following result.

$$\tau_{w_{trans}} = \frac{2.37 \times 10^4}{\rho_L \; g_c} \left(\frac{\mu_L}{D} \right)^2 \tag{G4}$$

Following Carpenter's suggestions, Equation (G4) indicates that for a given liquid and a given pipe diameter, transition from laminar to turbulent flow takes place at the same wall shear stress τ_w for both the fully-developed single-phase flow of a liquid through a pipe and the condensing flow of a liquid film along the pipe wall.

Equation (G3) is similar to that suggested by Carpenter and derived in the paper by Rohsenow, et al*. The development is identical to the derivation of Rohsenow, et al. However, the derivation presented by Rohsenow, et al employed the relation

$$C_f = \frac{0.046}{Re^{0.2}} \tag{G5}$$

for the skin friction coefficient. While this relation is valid for Reynolds numbers in the range of 3.0×10^4 to 3.0×10^5 it is not valid for the low values of Reynolds number occurring within this study.

*Rohsenow, W. M., T. H. Weber, and A. T. Ling, Trans. ASME 78, p. 1637-44, 1956

APPENDIX H

Two-Phase Pressure Drop Calculations

APPENDIX H

Two-Phase Pressure Drop Calculations

The computer program discussed in Section V of this report contains a subroutine for calculating two-phase pressure drops across an increment of the condensing fluid. This appendix describes the details of that subroutine.

The subroutine calculates the static pressure differential across an increment (see sketch) using the equation derived below.

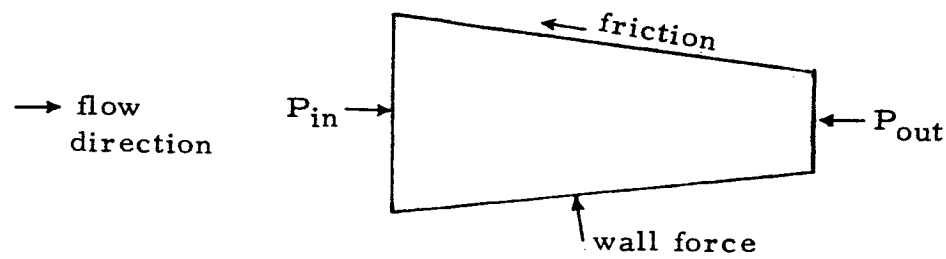

The sum of the forces acting on this increment in the axial direction is equal to the change in momentum flux across the increment in that direction*

$$P_{in} A_{in} - P_{out} A_{out} + \frac{P_{in} + P_{out}}{2} (A_{out} - A_{in}) - \Delta P_{friction} A_{md} = 2 (q_{out} A_{out} - q_{in} A_{in}) \qquad \text{(H1)}$$

where A_{md} = the area based on the mean diameter.

The term $\frac{P_{in} + P_{out}}{2} (A_{out} - A_{in})$ accounts for the wall force.

This equation reduces to

$$P_{in} - P_{out} = \Delta P_{friction} \frac{2A_{md}}{A_{in} + A_{out}} + \frac{4}{A_{in} + A_{out}} (q_{out} A_{out} - q_{in} A_{in}) \qquad \text{(H2)}$$

The method used to obtain frictional pressure loss and the method used to determine pressure drop due to momentum considerations are discussed separately.

Frictional Pressure Loss

The frictional pressure loss calculations used in the computer program were based on the empirical method of Lockhart and Martinelli**. This

*See Appendix B for nomenclature

**Lockhart, R. W. and R. C. Martinelli, Chem. Eng. Prog. Symp. Series, Vol. 45, No. 1, p. 39, 1949

method expresses the two-phase frictional pressure drop per unit length $(\Delta P/\Delta L)_{tpf}$ in terms of the pressure drop per unit length that would exist if the gaseous phase is assumed to flow alone $(\Delta P/\Delta L)_G$ through the definition of a parameter ϕ_G. That is

$$\phi_G^2 = \frac{(\Delta P/\Delta L)_{tpf}}{(\Delta P/\Delta L)_G} \tag{H3}$$

The parameter ϕ_G in turn is a function of a dimensionless variable X which is the square root of the ratio of the liquid to the gaseous pressure drop per unit length when each phase is considered to flow alone. The relationship of ϕ_G to X and the definition of X are dependent upon which of four regimes the flow is considered to have. These four regimes are, 1) turbulent - turbulent (tt) - both liquid and gas phases are in the turbulent flow regime, 2) viscous-viscous (vv) - both liquid and gas phases are in the viscous flow regime, 3) turbulent-viscous (tv) - the liquid phase is turbulent and the gas phase viscous, and 4) viscous-turbulent (vt) - the liquid phase is viscous and the gas phase is turbulent. Lockhart and Martinelli correlated data of ϕ_G vs X for the four regimes. Curves of mean lines through their data are shown in Figure H1. The data was taken for adiabatic flow and not for flow where heat is being transferred as in condensing. However, it was assumed that Equation (H3) can be applied locally in condensing flow after being transformed from a finite difference equation to a differential equation as follows.

$$dP_{tpf} = \phi_G^2 \left(\frac{dP}{d\ell}\right)_G d\ell$$

This equation can then be integrated across an increment in which heat was transferred to obtain the frictional pressure drop across the increment.

$$\Delta P_{tpf} = \int_{\ell}^{\ell+\Delta\ell} \phi_G^2 \left(\frac{dP}{d\ell}\right)_G d\ell \tag{H4}$$

Integration of the right side of Equation (H4) was done by expressing ϕ_G, $(dP/d\ell)$ and ℓ in terms the quality x, a constant tube diameter, the input flow rate, and constant fluid properties.

The quality change across an increment is known in the program and the variation within an increment is assumed to be linear with length. A polynomial equation of ϕ_G^2 in terms of X was made to fit the curves in Figure H1. Another polynomial equation of X in terms of quality was also made. Therefore ϕ_G can be expressed in terms of quality. Table H1 contains the polynomial equations of ϕ_G^2 in terms of X, and X in terms of quality for the four flow mechanisms.

The variable $(dP/d\ell)_G$ can be expressed as $\dfrac{4f_G \; W_T^2 \; x^2}{2g_c \; \rho_G A^2}$.

The friction factor f_G is a function of Reynolds number, which in turn is a function of quality, assuming constant fluid properties. The rest of the terms of the expression of $(dP/d\ell)_G$ except quality would be constant. Thus ϕ^2_G, ℓ, and $(dP/d\ell)_G$ can be expressed in terms of quality and the integral in Equation (H4) can be evaluated directly. Table H2 contains the final equations derived for two-phase frictional drop across an increment for all four flow mechanisms.

Two modifications were made to the Lockhart and Martinelli method for use in this subroutine. The first was to define the point of transition from laminar flow to turbulent flow to occur at a definite condition. The subroutine uses the criteria that if the full-bore Reynolds number* of either phase is less than or equal to 1000, that fluid phase is in viscous flow; and if the full-bore Reynolds number is greater than 1000, that phase is in turbulent flow.

The other modification was made in the functional relationship of friction factor in turbulent flow to full-bore Reynolds number. Lockhart and Martinelli used the following equation

$$f = 0.046\ Re^{-0.2} \tag{H5}$$

and the one used in this subroutine is

$$f = 0.079\ Re^{-0.25} \tag{H6}$$

The latter equation was chosen as it fits the data better for Reynolds numbers of less than 100,000.

Pressure Drop Due to Momentum Considerations

As can be seen from Equations (H1) and (H2), it is necessary to evaluate velocity head at the two end points of an increment in order to determine total and static pressure drop across an increment. The velocity head of a two-phase mixture is defined by the sum of the liquid and gas momentum flux divided by two times the duct cross-sectional area.

$$q = \frac{1}{2g_c A}\left[W_T (1 - x) V_L + W_T x V_G\right] \tag{H7}$$

*The full-bore Reynolds number for a phase is a fictitious Reynolds number calculated as if that phase flow rate occupied the entire pipe cross-sectional area. Thus $Re_L = \frac{W_T (1 - x) D}{A \mu_L}$ and $Re_G = \frac{W_T x D}{A \mu_G}$

The velocities of the two phases can be expressed by the following equations

$$V_L = \frac{W_T (1 - x)}{\rho_L A R_L} \quad \text{and} \quad V_G = \frac{W_T x}{\rho_G A R_G} \tag{H8}$$

where R_L is the local fraction of tube volume that is liquid and R_G is the local fraction of tube volume that is gas.

Thus

$$q = \frac{1}{2} \frac{W_T^2}{A^2 g_c} \left[\frac{(1 - x)^2}{\rho_L R_L} + \frac{x^2}{\rho_G R_G} \right] \tag{H9}$$

The values of W_T, A, ρ_L, ρ_G, and x are determined at the end points from previous routines in the program or are known input values. However, neither R_L nor R_G is known. Once either value is known, then local velocity head can be determined since $R_L + R_G = 1$.

Lockhart and Martinelli correlated data of R_L as a function of the same parameter X used to correlate ϕ_G. This correlation is illustrated in Figure H2. In order to use this correlation in the computer program, the following equation was fitted to a curve in Figure H2.

$$R_L = \frac{0.299\ X^{0.756}}{0.299\ X^{0.756} + 1}$$

The values of X at the two end points of an increment are evaluated from flow rate, quality, local fluid properties, and tube diameter. Thus the velocity heads at the end points of an increment can be calculated. Table H3 contains the final equations derived for local two-phase flow velocity head for all four flow mechanisms.

TABLE H1

$$\Phi^2_{G_{tt}} = 1 + 19.7\, X_{tt} + X^2_{tt}$$

$$\Phi^2_{G_{vv}} = 1 + 6.0\, X_{vv} + X^2_{vv}$$

$$\Phi^2_{G_{tv}} = 1 + 11.0\, X_{tv} + X^2_{tv}$$

$$\Phi^2_{G_{vt}} = 1 + 12.5\, X_{vt} + X^2_{vt}$$

$$X_{tt} = K_3(x^{-0.875} - 0.875x^{0.125} - 0.0547x^{1.125} - 0.0205x^{2.125} - 0.0109x^{3.125} - 0.0389x^{4.125})$$

$$X_{vv} = K_6\,(x^{-0.5} - 0.5x^{0.5} - 0.125x^{1.5} - 0.0625x^{2.5} - 0.0391x^{3.5} - 0.2734x^{4.5})$$

$$X_{tv} = K_5\,(x^{-0.5} - 0.875x^{0.5} - 0.0547x^{1.5} - 0.0205x^{2.5} - 0.0109x^{3.5} - 0.0389x^{4.5})$$

$$X_{vt} = K_2\,(x^{-0.875} - 0.5x^{0.125} - 0.125x^{1.125} - 0.0625x^{2.125} - 0.0391x^{3.125} - 0.2734x^{4.125})$$

$$K_1 = \frac{0.228\,\mu_G^{0.25}\; L\, W_T^{1.75}}{g_c\;\; \rho_G\,(x_e - x_o)\, D^{4.75}}$$

$$K_2 = \frac{13\,\mu_L^{0.5}}{\mu_G^{0.125}}\left(\frac{\rho_G}{\rho_L}\right)^{0.5} \frac{D^{0.375}}{W_T^{0.375}}$$

$$K_3 = \left(\frac{\mu_L}{\mu_G}\right)^{0.125} \left(\frac{\rho_G}{\rho_L}\right)^{0.5}$$

$$K_4 = \frac{41.3\,\mu_G\, L\, W_T}{g_c\;\; \rho_G\,(x_e - x_o) D^4}$$

$$K_5 = \frac{0.0744\,\mu_L^{0.125}}{\mu_G^{0.5}}\left(\frac{\rho_G}{\rho_L}\right)^{0.5} \frac{W_T^{0.375}}{D^{0.375}}$$

$$K_6 = \left(\frac{\mu_L\,\rho_G}{\mu_G\,\rho_L}\right)^{0.5}$$

TABLE H2

Equations for Friction Loss in Two-Phase Flow

$$(\Delta P_{tpf})_{tt} = K_1 \Big\{ 0.364\,(x_e^{2.75} - x_o^{2.75}) + 19.7\,K_3 \big[0.533\,(x_e^{1.875} - x_o^{1.875}) - 0.304\,(x_e^{2.875} - x_o^{2.875}) - 0.0141\,(x_e^{3.875} - x_o^{3.875})$$

$$- 0.0042\,(x_e^{4.875} - x_o^{4.875}) - 0.00186\,(x_e^{5.875} - x_o^{5.875}) - 0.00566\,(x_e^{6.875} - x_o^{6.875}) \big] - 0.364\,K_3^2 \left[(1 - x_e)^{2.75} - (1 - x_o)^{2.75} \right] \Big\}$$

$$(\Delta P_{tpf})_{vv} = K_4 \Big\{ 0.5\,(x_e^2 - x_o^2) + 6.0\,K_6 \big[0.667\,(x_e^{1.5} - x_o^{1.5}) - 0.2\,(x_e^{2.5} - x_o^{2.5}) - 0.0357\,(x_e^{3.5} - x_o^{3.5})$$

$$- 0.0139\,(x_e^{4.5} - x_o^{4.5}) - 0.00711\,(x_e^{5.5} - x_o^{5.5}) - 0.042\,(x_e^{6.5} - x_o^{6.5}) \big] + K_6^2 \left[(x_e - x_o) - 0.5\,(x_e^2 - x_o^2) \right] \Big\}$$

$$(\Delta P_{tpf})_{tv} = K_4 \Big\{ 0.5\,(x_e^2 - x_o^2) + 11.0\,K_5 \big[0.677\,(x_e^{1.5} - x_o^{1.5}) - 0.35\,(x_e^{2.5} - x_o^{2.5}) - 0.01562\,(x_e^{3.5} - x_o^{3.5})$$

$$- 0.00455\,(x_e^{4.5} - x_o^{4.5}) - 0.000198\,(x_e^{5.5} - x_o^{5.5}) - 0.00598\,(x_e^{6.5} - x_o^{6.5}) \big] - 0.364\,K_5^2 \left[(1 - x_e)^{2.75} - (1 - x_o)^{2.75} \right] \Big\}$$

$$(\Delta P_{tpf})_{vt} = K_1 \Big\{ 0.364\,(x_e^{2.75} - x_o^{2.75}) + 12.5\,K_2 \big[0.533\,(x_e^{1.875} - x_o^{1.875}) - 0.174\,(x_e^{2.875} - x_o^{2.875}) - 0.0323\,(x_e^{3.875} - x_o^{3.875})$$

$$- 0.01282\,(x_e^{4.875} - x_o^{4.875}) - 0.00666\,(x_e^{5.875} - x_o^{5.875}) - 0.0398\,(x_e^{6.875} - x_o^{6.875}) \big] + K_2^2 \left[(x_e - x_o) - 0.5\,(x_e^2 - x_o^2) \right] \Big\}$$

See Table H1 for definitions of K_1, K_2, K_3, K_4, K_5, and K_6

TABLE H3

Equations for Equivalent Velocity Head

$$\bar{q}_{tt} = \frac{8\,W_T^2}{g_c\,\pi^2\,D^4}\left\{\frac{x^{1.339}}{\rho_G}\left[0.299K_3^{0.756}\,(1-x)^{0.661} + x^{0.661}\right] + \frac{(1-x)^{1.339}}{\rho_L\,0.299K_3^{0.756}}\left[0.299K_3^{0.756}\,(1-x)^{0.661} + x^{0.661}\right]\right\}$$

$$\bar{q}_{vv} = \frac{8\,W_T^2}{g_c\,\pi^2 D^4}\left\{\frac{x^{1.662}}{\rho_G}\left[0.299K_6^{0.756}\,(1-x)^{0.378} + x^{0.378}\right] + \frac{(1-x)^{1.622}}{\rho_L\,0.299K_6^{0.756}}\left[0.299K_6^{0.756}\,(1-x)^{0.378} + x^{0.378}\right]\right\}$$

$$\bar{q}_{tv} = \frac{8\,W_T^2}{g_c\,\pi^2\,D^4}\left\{\frac{x^{1.622}}{\rho_G}\left[0.299K_5^{0.756}\,(1-x)^{0.661} + x^{0.378}\right] + \frac{(1-x)^{1.339}}{\rho_L\,0.299K_5^{0.756}}\left[0.299K_5^{0.756}\,(1-x)^{0.661} + x^{0.378}\right]\right\}$$

$$\bar{q}_{vt} = \frac{8\,W_T^2}{g_c\,\pi^2 D^4}\left\{\frac{x^{1.339}}{\rho_G}\left[0.299K_2^{0.756}\,(1-x)^{0.378} + x^{0.661}\right] + \frac{(1-x)^{1.622}}{\rho_L\,0.299K_2^{0.756}}\left[0.299K_2^{0.756}\,(1-x)^{0.378} + x^{0.661}\right]\right\}$$

See Table H1 for definitions of K_1, K_2, K_3, K_4, K_5, and K_6

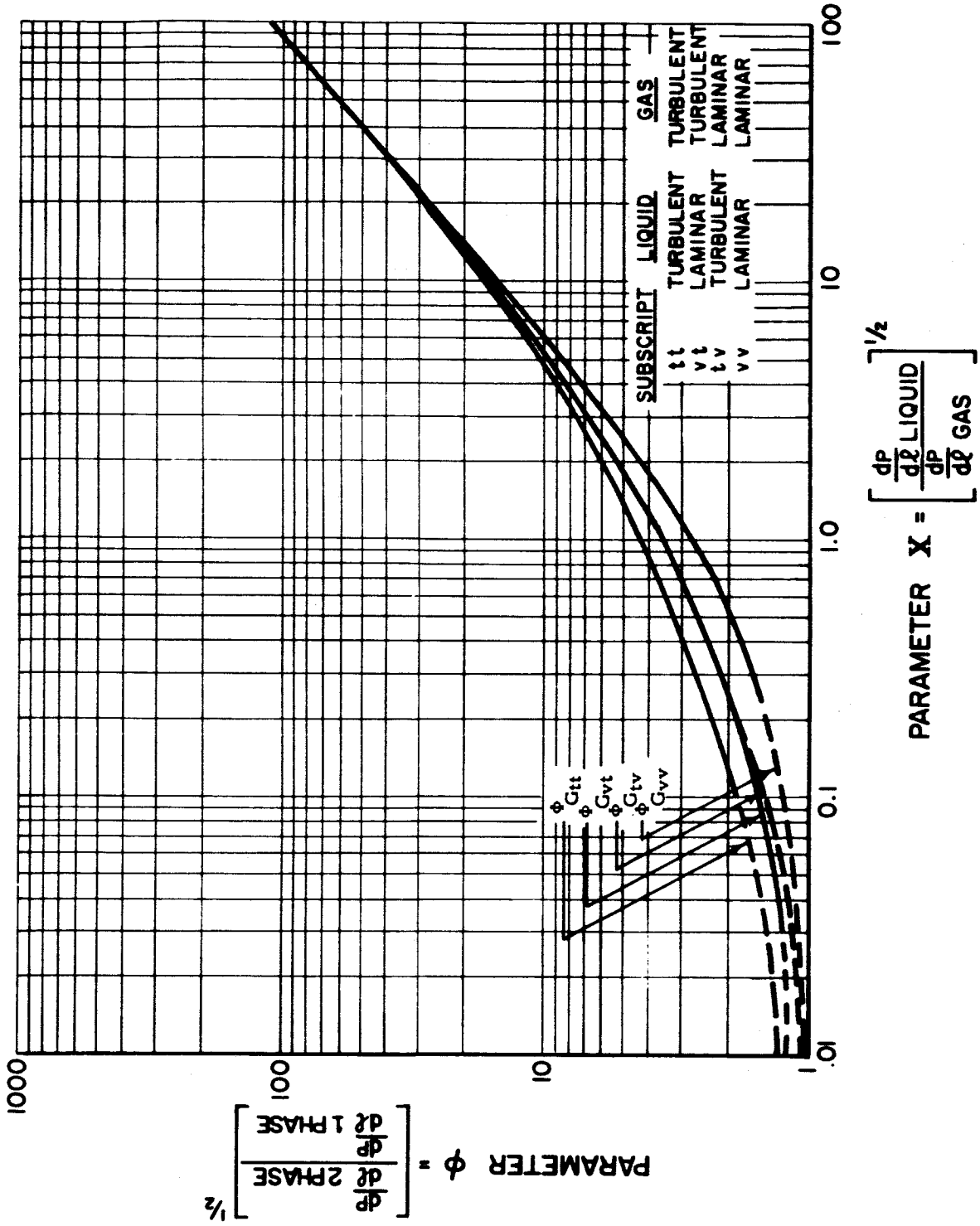

Figure H1 Two-Phase Friction Correlation of Lockhart and Martinelli

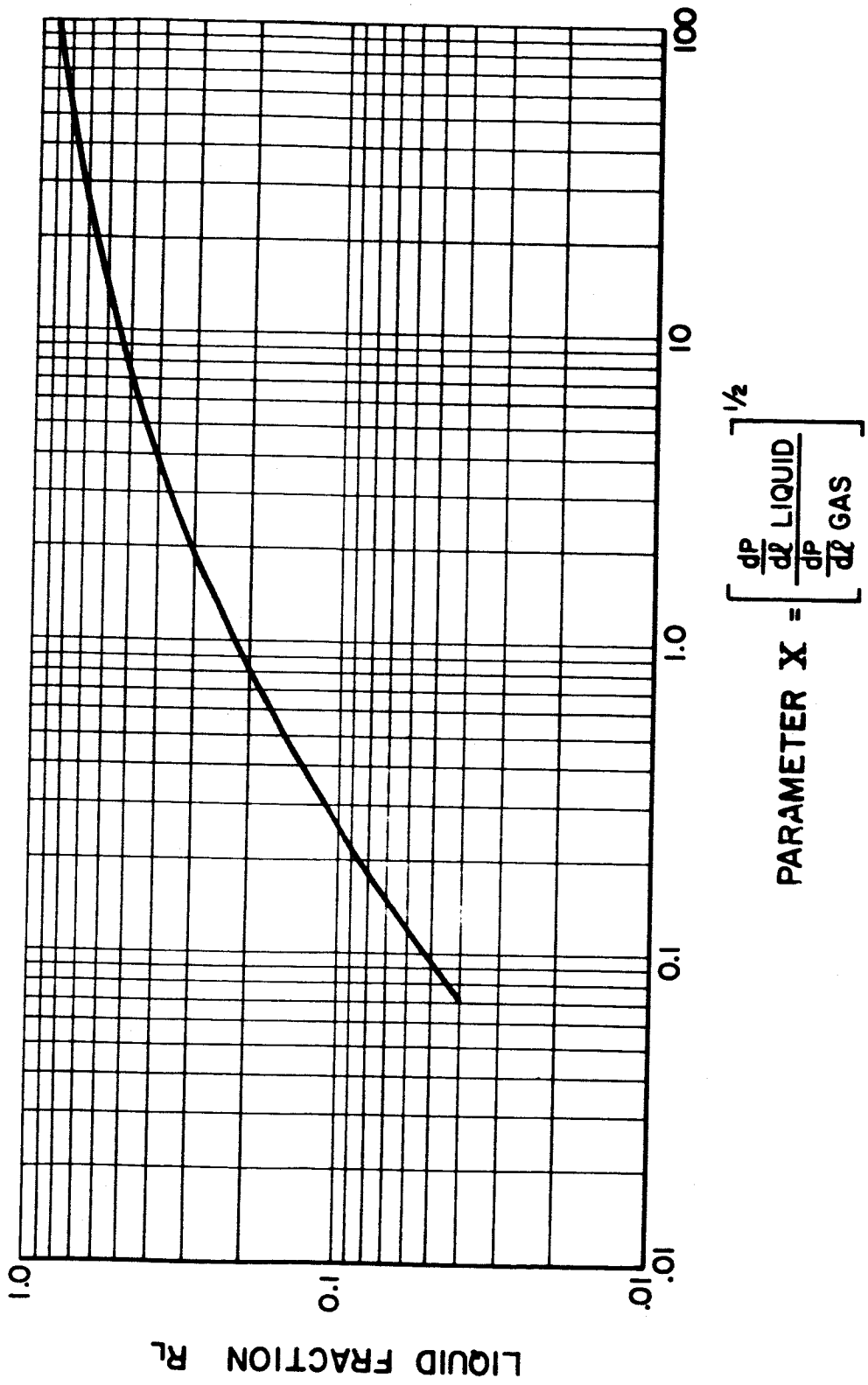

Figure H2 Liquid Fraction Correlation of Lockhart and Martinelli

APPENDIX I

Radial Pressure Losses

APPENDIX I

Radial Pressure Losses

In this appendix equations are derived for calculating the radial pressure losses discussed in Section III. E. These equations are derived for the case of radial inward flow feeding the main shell section of a shell-and-tube condenser. However, they can also be applied to the case of radial outward flow at the shell exit end of a shell-and-tube condenser, or to similar radial flow patterns for other condenser configurations.

The flow geometry considered is illustrated in Figure (I1). The fluid is assumed to enter uniformly along the circumferential gap between the shell and the tubesheet. This fluid then flows radially inward across a bank of tubes arranged in a hexagonal pattern and between a tubesheet and an adjacent orifice plate. As the fluid flows inward it is also dispersed to the main shell section of the condenser through annular orifices formed by the tubes and circular holes in the orifice plate. Thus the flow rate diminishes as it flows towards the center. The pressure drop encountered by this radial flow pattern is a combination of friction and contraction and expansion type losses. At present there is no experimental data for pressure losses for such a flow pattern. The relations presented below are therefore obtained by modifying equations obtained empirically for flow normal to staggered tube banks.

The total radial pressure drop from the outer periphery of the tube bank to the central tube can be determined as the sum of the individual pressure drops across each row of tubes *

$$\Delta P_R = \Delta P_2 + \cdots\cdots + \Delta P_i + \cdots\cdots \Delta P_n \qquad \text{(I1)}$$

The subscripts identifying the individual tube rows follow the convention illustrated in Figure (I2) where row numbers increase with distance from the central tube, and where the central tube is considered to be the first row.

The frictional pressure loss for flow normal to a bank of tubes can be calculated by the following equation given by Kreith**

*See Appendix B for nomenclature

**Kreith, F., Principles of Heat Transfer, International Book Company, Scranton 1959, p. 389

$$\Delta P = \frac{4f' \, G_{max}^{2} \, n}{2 \, \rho \, g_c} \tag{I2}$$

For flow across tube banks arranged in a staggered pattern Jakob* has presented the following equation for the friction factor f'

$$f' = \left[0.25 + \frac{0.118}{\left(\frac{P}{D_o} - 1\right)^{1.08}}\right] \left(\frac{D_o \, G_{max}}{\mu}\right)^{-0.16} \tag{I3}$$

In the above equations

G_{max} = mass velocity at the minimum flow cross-sectional area, $lb_m/hr\ ft^2$
ρ = mass density, lb_m/ft^3
n = number of rows perpendicular to the flow direction
D_o = outside tube diameter, ft
P = pitch or center-to-center distance between tubes, ft
g_c = conversion factor = 4.17×10^8 ft $lb_m/lb_f\ hr^2$

This relation was determined experimentally for Reynolds numbers greater than 1000, using tube banks of at least ten rows deep.

For this analysis it is assumed that Equations (I2) and (I3) which are applicable to tube banks many rows deep can be used to calculate the pressure loss across each individual row of a hexagonal tube pattern.

Combining these equations results in the following expression for the frictional pressure drop across any particular row i

$$\Delta P_i = \frac{4}{2 \rho g_c} \left[0.25 + \frac{0.118}{\left(\frac{P}{D_o} - 1\right)^{1.08}}\right] \left(\frac{D_o}{\mu}\right)^{1.84} G_{max_i}^{-0.16} \tag{I4}$$

*Jakob, M., Heat Transfer and Flow Resistance in Cross Flow of Gases over Tube Banks, Trans. ASME, Vol. 60, 1938, pp. 384-386

Substituting Equation (I4) into Equation (I1) results in

$$\Delta P_R = \frac{4}{2\,\rho\, g_c}\left[0.25 + \frac{0.118}{\left(\frac{P}{D_o} - 1\right)^{1.08}}\right]\left(\frac{D_o}{\mu}\right)^{-0.16} \sum_{i=z}^{n} G_{max_i}^{1.84} \tag{I5}$$

An expression is now derived for the maximum mass velocity associated with any row i. By definition

$$G_{max_i} = \frac{W_i}{A_{min_i}} \tag{I6}$$

where W_i = flow rate in lb_m/hr crossing the hexagonal boundary of row i

A_{min_i} = minimum flow cross-sectional area associated with row i

Since there is an identical annular orifice associated with each tube, the total flow area of the orifices is proportional to the total number of tubes in the shell. This is also true for the portion of the total orifice area enclosed inside a boundary connecting the center of each tube in a hexagonal row. Assuming that there is uniform flow distribution to each orifice (i.e., equal amounts of fluid pass through each orifice) the flow rate across a boundary connecting the tube centers of any row i is then proportional to the number of tubes enclosed within that boundary

$$\begin{aligned} W_i &\sim N_{TOT_i} \\ W_T &\sim N_T \\ \frac{W_i}{W_T} &= \frac{N_{TOT_i}}{N_T} \end{aligned} \tag{I7}$$

where N_{TOT_i} = number of tubes enclosed within the boundary of row i

N_T = total number of tubes in the shell

The number of tubes in any row except the first is given by

$$N_i = 6\,(i - 1)$$

The total number of tubes in the n rows is therefore

$$N_T = 1 + \sum_{i=2}^{n} 6\,(i - 1) = 1 + \frac{6\,(n)\,(n - 1)}{2} = 3\,n^2 - 3n + 1 \quad \text{(I8)}$$

Similarly the total number of tubes in the first i rows is

$$N_{\Sigma i} = 3\,i^2 - 3\,i + 1 \quad \text{(I9)}$$

In the ith row, however, a portion of each tube lies outside the hexagonal boundary of the row. This portion is given as

$$N_{i_{out}} = \frac{1}{2}\,N_i + 1 = \frac{1}{2}\,(6i - 6) + 1 = 3i - 2 \quad \text{(I10)}$$

Thus, the number of tubes enclosed within the boundary is

$$N_{TOT_i} = N_{\Sigma i} - N_{i_{out}}$$

$$N_{TOT_i} = 3i^2 - 3i + 1 - (3i - 2) \quad \text{(I11)}$$

$$N_{TOT_i} = 3i^2 - 6i + 3 = 3\,(i - 1)^2$$

Substituting Equations (I9) and (I11) into Equation (I7) and rearranging, the result is

$$W_i = \frac{3\,(i - 1)^2}{3n^2 - 3n + 1}\,W_T \quad \text{(I12)}$$

The minimum flow cross-sectional area for any row i is the smallest area normal to the direction of flow. This area is equal to the number of flow passages (equal to the number of tubes) times the area of each passage. The area of each passage is equal to the distance between each pair of tubes P-D multiplied by the distance between the orifice plate and the tubesheet, ℓ. The minimum flow area can then be expressed by the equation

$$A_{min_i} = N_i (P - D_o) \ell = 6 (i - 1) \ell (P - D_o) \tag{I13}$$

Substituting Equations (I12) and (I13) into Equation (I6) gives

$$G_{max_i} = \frac{(i - 1) W_T}{(3n^2 - 3n + 1) 2\ell (P - D_o)} \tag{I14}$$

This equation can be rewritten as

$$G_{max_i} = F(i) \frac{W_T}{2\ell (P - D_o)} \tag{I15}$$

where $$F(i) = \frac{i - 1}{3n^2 - 3n + 1} \tag{I16}$$

Substituting the expression for G_{max} from Equation (I15) into Equation (I5) gives

$$\Delta P_R = \frac{4}{2 \rho g_c} \left[.25 + \frac{0.118}{\left(\frac{P}{D_o} - 1\right)^{1.08}} \right] \left(\frac{D_o}{\mu}\right)^{-0.16} \left(\frac{W_T}{2\ell (P - D_o)}\right)^{1.84} \sum_{i=2}^{n} F(i)^{1.84} \tag{I17}$$

Combining like terms and rearranging

$$\Delta P_R = \frac{0.562}{\rho g_c}\left[\frac{0.25}{\left(\frac{P}{D_o} - 1\right)^{1.84}} + \frac{0.118}{\left(\frac{P}{D_o} - 1\right)^{2.92}}\right]\left(\frac{\mu \ell}{W_T}\right)^{0.16}\left(\frac{W_T}{\ell D_o}\right)^2 \sum_{i=2}^{n} F(i)^{1.84} \qquad (I18)$$

Equation (I18) can be put into the following simplified form convenient for making design calculations

$$\Delta P_R = \frac{0.562}{\rho g_c}\,\gamma\left(\frac{P}{D_o}, n\right)\left[\frac{\mu \ell}{W_T}\right]^{0.16}\left[\frac{W_T}{\ell D_o}\right]^2 \qquad (I19)$$

where

$$\gamma\left(\frac{P}{D_o}, n\right) = \left[\frac{0.250}{\left(\frac{P}{D_o} - 1\right)^{1.84}} + \frac{0.118}{\left(\frac{P}{D_o} - 1\right)^{2.92}}\right]\sum_{i=2}^{n} F(i)^{1.84} \qquad (I20)$$

The function γ which depends on geometry alone can be plotted against pitch-to-diameter ratio with number of tubes as a parameter. Such a plot is given in Figure I3 for P/D_o between 1.2 and 2.6 and n between 2 and 15.

These equations were derived for an orifice plate with the hole pattern illustrated in Figure I1. However these relations can be applied to other orifice plate hole patterns, provided that the orifice area enclosed within a hexagonal boundary is proportional to the number of tubes within that boundary.

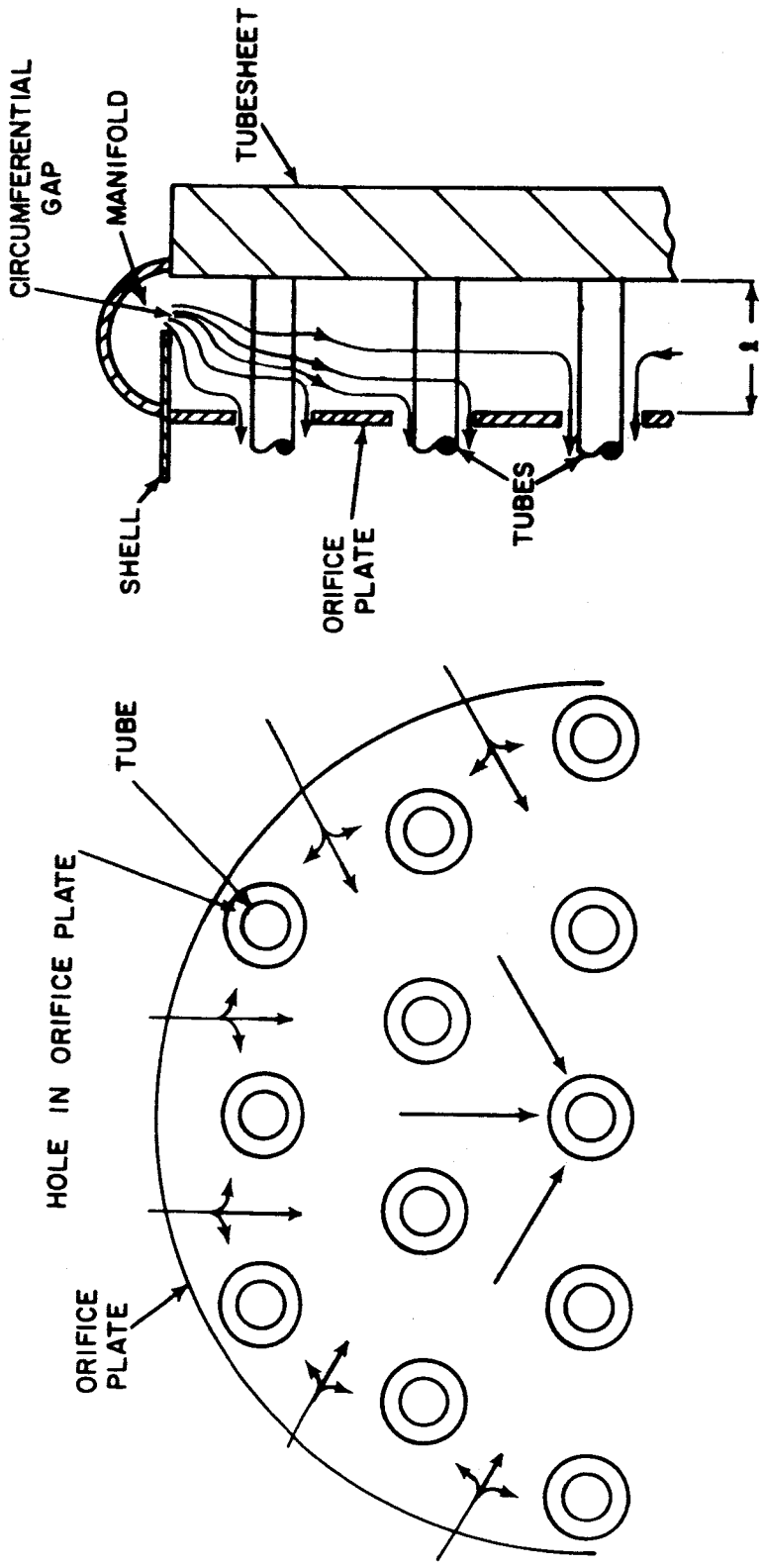

Figure 11 Orifice Plate and Flow Pattern at Inlet End of Shell-and-Tube Condenser

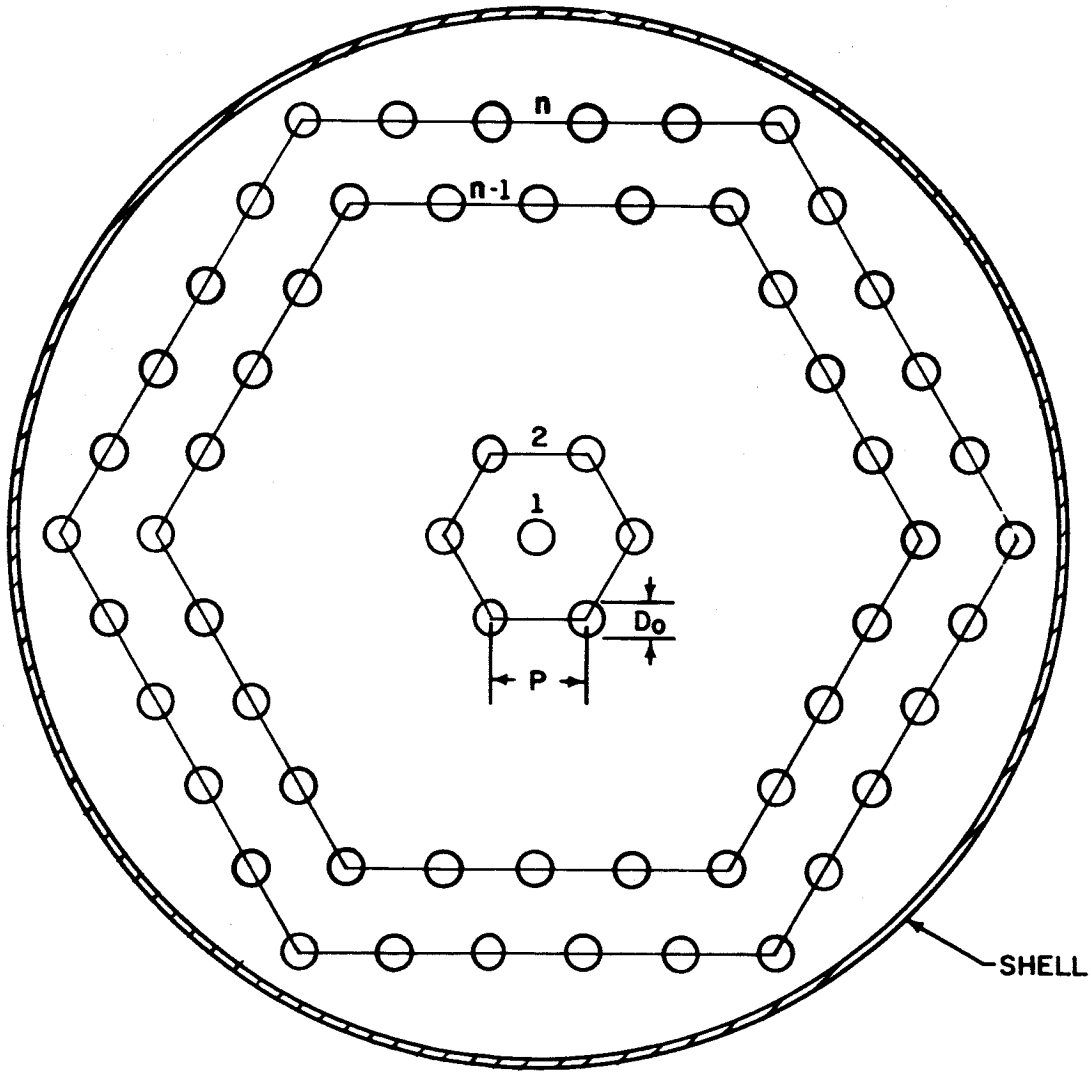

Figure 12 Cross-Section of Condenser Showing Hexagonal Tube Arrangement

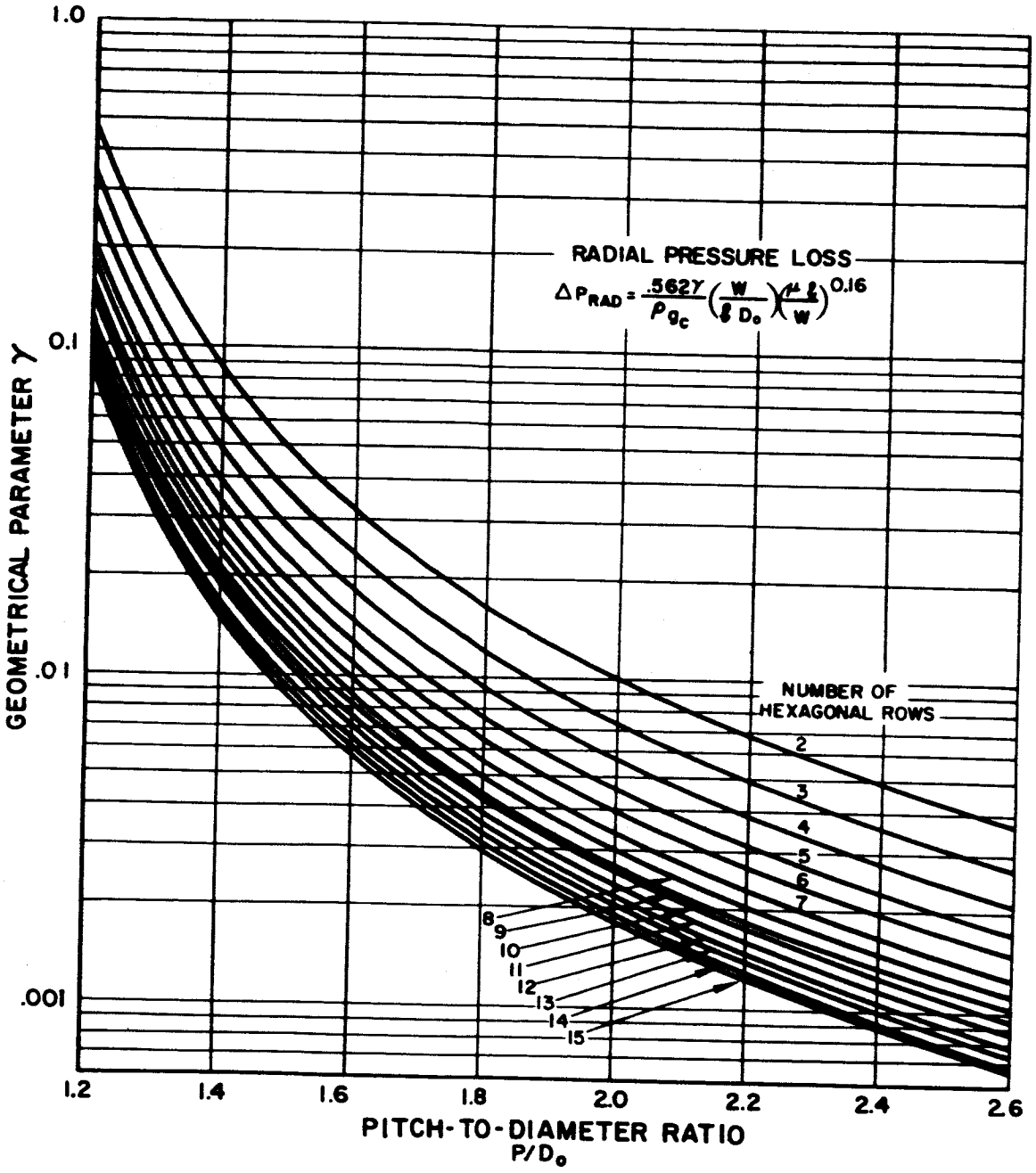

Figure 13 Geometrical Parameter γ vs Pitch-to-Diameter Ratio

APPENDIX J

Critical Mass Velocity for Two-Phase Flow

Appendix J

Critical Mass Velocity for Two-Phase Flow

In this appendix an analytical expression is developed for the critical mass velocity G_{cr} for two-phase annular flow through a constant-area duct with no heat addition. Various flow patterns may exist for a two-phase flow system. Experiments have shown that when the gas velocities are high, an annular flow pattern is often established. The critical flow condition occurs when a further decrease in back pressure, for a fixed inlet duct pressure, does not cause an increase of mass velocity through the duct. The critical condition corresponds to the sonic choking phenomenon of single-phase gas flow. However, in two-phase critical flow, sonic choking of the gas phase does not necessarily occur.

In this analysis, it is assumed that the expression for critical mass velocity at the duct exit in single-phase gas flow*

$$G_{cr} = \left[\frac{-g_c}{\left(\frac{\partial v}{\partial P}\right)_S} \right]^{1/2}$$

is also applicable for critical two-phase flow. However, for two-phase annular flow

$$\left(\frac{\partial v}{\partial P}\right)_S = \left(\frac{\partial v_{tp}}{\partial P}\right)_S$$

where v_{tp}, the equivalent two-phase specific volume, depends on the local static pressure, the quality, and the ratio of gas to liquid velocities k, called the slip. Based upon this effect, Linning** has shown that at the duct exit for critical two-phase flow, the condition

$$\left(\frac{\partial G_{cr}}{\partial k}\right)_{P,x} = 0$$

*See Appendix B for nomenclature

**Linning, D. L., The Adiabatic Flow of Evaporating Fluids in Pipes of Uniform Bore, Proc. Inst. Mech. Engrs., IB, 64-75, 1952-1953

must be satisfied. This condition yields an additional relationship required to develop the expression for critical mass velocity in two-phase flow by relating critical slip to the critical pressure.

The analytical treatment which follows is based on the assumptions that:

1) The two-phase mixture is in fully-developed turbulent flow,
2) The liquid flows along the inner perimeter of the duct and the vapor flows in the core, i. e., an annular flow pattern,
3) The liquid phase is incompressible,
4) At moderate pressures the perfect gas law is applicable,
5) Thermal equilibrium exists between phases,
6) An equivalent specific volume for annular two-phase flow can be defined using the momentum equation by

$$v_{tp} = \left[v_L - x \left(v_L - \frac{v_G}{k} \right) \right] \left[(1 - x) + k\,x \right]$$

7) The critical mass velocity is given by

$$G_{cr} = \left[\frac{-g_c}{\left(\frac{\partial v_{tp}}{\partial P} \right)_S} \right]^{1/2}$$

8) The condition necessary for critical flow at the duct exit is

$$\left(\frac{\partial G_{cr}}{\partial k} \right)_{P,\,x} = 0$$

In order to evaluate the critical mass velocity G_{cr} an expression for $\left(\frac{\partial v_{tp}}{\partial P} \right)_S$ must be obtained. The expression for the equivalent specific volume, v_{tp}, results from a comparison of similar terms in the momentum equation for single-phase flow.

The expression for $\left(\frac{\partial v_{tp}}{\partial P}\right)_S$ can be written as

$$\left(\frac{\partial v_{tp}}{\partial P}\right)_S = \left(\frac{\partial v_{tp}}{\partial x}\right)_{P,k}\left(\frac{\partial x}{\partial P}\right)_S + \left(\frac{\partial v_{tp}}{\partial v_G}\right)_{x,k}\left(\frac{\partial v_G}{\partial P}\right)_S + \left(\frac{\partial v_{tp}}{\partial v_L}\right)_{x,k}\left(\frac{\partial v_L}{\partial P}\right)_S + \left(\frac{\partial v_{tp}}{\partial k}\right)_{P,x}\left(\frac{\partial k}{\partial P}\right)_S \tag{J1}$$

where

$$v_{tp} = v_{tp}\ (x,\ v_G,\ v_L,\ k)$$

The two-phase critical mass velocity is assumed to be

$$G_{cr} = \left[\frac{-g_c}{\left(\frac{\partial v_{tp}}{\partial P}\right)_S}\right]^{1/2} \tag{J2}$$

With pressure and quality held constant, G_{cr} can be differentiated with respect to slip

$$\left(\frac{\partial G_{cr}}{\partial k}\right)_{P,x} = \frac{\partial}{\partial k}\left[\left(\frac{-g_c}{\left(\frac{\partial v_{tp}}{\partial P}\right)_S}\right)^{1/2}\right]_{P,x} = \frac{\frac{1}{2}\ g_c^{1/2}}{\left[-\left(\frac{\partial v_{tp}}{\partial P}\right)_S\right]^{3/2}}\frac{\partial}{\partial k}\left[\left(\frac{\partial v_{tp}}{\partial P}\right)_S\right]_{P,x}$$

At the critical condition $\left(\frac{\partial G_{cr}}{\partial k}\right)_{P,x} = 0$ and G_{cr} is finite. Therefore, the condition for critical flow can also be expressed by

$$\frac{\partial}{\partial k}\left[\left(\frac{\partial v_{tp}}{\partial P}\right)_S\right]_{P,x} = 0$$

Applying the critical condition to Equation (J1)

$$\frac{\partial}{\partial k}\left[\left(\frac{\partial v_{tp}}{\partial P}\right)_S\right]_{P,x} = \frac{\partial}{\partial k}\left[\left(\frac{\partial v_{tp}}{\partial x}\right)_{P,k}\left(\frac{\partial x}{\partial P}\right)_S\right]_{P,x} +$$

$$\frac{\partial}{\partial k}\left[\left(\frac{\partial v_{tp}}{\partial v_G}\right)_{x,k}\left(\frac{\partial v_G}{\partial P}\right)_S\right]_{P,x} + \frac{\partial}{\partial k}\left[\left(\frac{\partial v_{tp}}{\partial v_L}\right)_{x,k}\left(\frac{\partial v_L}{\partial P}\right)_S\right]_{P,x} +$$

$$\frac{\partial}{\partial k}\left[\left(\frac{\partial v_{tp}}{\partial k}\right)_{P,x}\left(\frac{\partial k}{\partial P}\right)_S\right]_{P,x} = 0 \qquad \text{(J3)}$$

Since $\frac{\partial}{\partial k}\left[\left(\frac{\partial x}{\partial P}\right)_S\right]_{P,x} = 0$, $\frac{\partial}{\partial k}\left[\left(\frac{\partial v_G}{\partial P}\right)_S\right]_{P,x} = 0$, and

$$\frac{\partial}{\partial k}\left[\left(\frac{\partial v_L}{\partial P}\right)_S\right]_{P,x} = 0$$

Equation (J3) may be written as

$$\frac{\partial}{\partial k}\left[\left(\frac{\partial v_{tp}}{\partial P}\right)_S\right]_{P,x} = \left(\frac{\partial x}{\partial P}\right)_S \frac{\partial}{\partial k}\left[\left(\frac{\partial v_{tp}}{\partial x}\right)_{P,k}\right]_{P,x} +$$

$$\left(\frac{\partial v_G}{\partial P}\right)_S \frac{\partial}{\partial k}\left[\left(\frac{\partial v_{tp}}{\partial v_G}\right)_{x,k}\right]_{P,x} + \left(\frac{\partial v_L}{\partial P}\right)_S \frac{\partial}{\partial k}\left[\left(\frac{\partial v_{tp}}{\partial v_L}\right)_{x,k}\right]_{P,x} +$$

$$\frac{\partial}{\partial k}\left[\left(\frac{\partial v_{tp}}{\partial k}\right)_{P,x}\left(\frac{\partial k}{\partial P}\right)_S\right]_{P,x} = 0 \qquad \text{(J3a)}$$

Expressions for

$$\frac{\partial}{\partial k}\left[\left(\frac{\partial v_{tp}}{\partial x}\right)_{P,k}\right]_{P,x}, \quad \frac{\partial}{\partial k}\left[\left(\frac{v_{tp}}{\partial v_G}\right)_{x,k}\right]_{P,x},$$

$$\frac{\partial}{\partial k}\left[\left(\frac{\partial v_{tp}}{\partial v_L}\right)_{x,k}\right]_{P,x}, \text{ and } \left(\frac{\partial v_{tp}}{\partial k}\right)_{P,x}$$

are obtained by performing the indicated differentiation on the expression for the two-phase specific volume, $v_{tp} = \left[v_L - x\left(v_L - \frac{v_G}{k}\right)\right]\left[(1 - x) + kx\right]$

The resulting expressions are

$$\frac{\partial}{\partial k}\left[\left(\frac{\partial v_{tp}}{\partial x}\right)_{P,k}\right]_{P,x} = (1-2x)\left(v_L - \frac{v_G}{k^2}\right) \qquad \text{(J4a)}$$

$$\frac{\partial}{\partial k}\left[\left(\frac{\partial v_{tp}}{\partial v_G}\right)_{x,k}\right]_{P,x} = \frac{-(x - x^2)}{k^2} \qquad \text{(J4b)}$$

$$\frac{\partial}{\partial k}\left[\left(\frac{\partial v_{tp}}{\partial v_L}\right)_{x,k}\right]_{P,x} = (x - x^2) \tag{J4c}$$

$$\left(\frac{\partial v_{tp}}{\partial k}\right)_{P,x} = (x - x^2)\left(v_L - \frac{v_G}{k^2}\right) \tag{J4d}$$

Substituting Equations (J4a), (J4b), (J4c) and (J4d) into (J3a) results in

$$\frac{\partial}{\partial k}\left[\left(\frac{\partial v_{tp}}{\partial P}\right)_S\right]_{P,x} = \left(\frac{\partial x}{\partial P}\right)_S (1 - 2x)\left(v_L - \frac{v_G}{k^2}\right) - \left(\frac{\partial v_G}{\partial P}\right)_S \frac{(x - x^2)}{k^2} + \left(\frac{\partial v_L}{\partial P}\right)_S (x - x^2) + \frac{\partial}{\partial k}\left[(x - x^2)\left(v_L - \frac{v_G}{k^2}\right)\left(\frac{\partial k}{\partial P}\right)_S\right]_{P,x} = 0 \tag{J5a}$$

Equation (J5a) can be written as

$$\frac{\partial}{\partial k}\left[\left(\frac{\partial v_{tp}}{\partial P}\right)_S\right]_{P,x} = \left(\frac{\partial x}{\partial P}\right)_S (1 - 2x)\left(v_L - \frac{v_G}{k^2}\right) + (x - x^2)\left[\left(\frac{\partial v_L}{\partial P}\right)_S - \frac{1}{k^2}\left(\frac{\partial v_G}{\partial P}\right)_S\right] + (x - x^2)\left\{\left(v_L - \frac{v_G}{k^2}\right)\frac{\partial}{\partial k}\left[\left(\frac{\partial k}{\partial P}\right)_S\right]_{P,x} + \frac{2 v_G}{k^3}\left(\frac{\partial k}{\partial P}\right)_S\right\} = 0 \tag{J5b}$$

The term $\left[\left(\frac{\partial v_L}{\partial P}\right)_S - \frac{1}{k^2}\left(\frac{\partial v_G}{\partial P}\right)_S\right]$ can be expressed by

$$\left[\left(\frac{\partial v_L}{\partial P}\right)_S - \frac{1}{k^2}\left(\frac{\partial v_G}{\partial P}\right)_S\right] = \frac{\partial}{\partial P}\left[\left(v_L - \frac{v_G}{k^2}\right)\right]_S - \frac{2 v_G}{k^3}\left(\frac{\partial k}{\partial P}\right)_S \qquad \text{(J6)}$$

Substituting Equation (J6) in (J5b) yields

$$\frac{\partial}{\partial k}\left[\left(\frac{\partial v_{tp}}{\partial P}\right)_S\right]_{P,x} = \left(\frac{\partial x}{\partial P}\right)_S (1 - 2x)\left(v_L - \frac{v_G}{k^2}\right) +$$

$$(x - x^2)\frac{\partial}{\partial P}\left[\left(v_L - \frac{v_G}{k^2}\right)\right]_S + v_L - \frac{v_G}{k^2}\frac{\partial}{\partial k}\left[\left(\frac{\partial k}{\partial P}\right)_S\right]_{P,x} = 0 \qquad \text{(J7)}$$

Equation (J7) is satisfied when the following two conditions are met

1) $\frac{\partial}{\partial P}\left[\left(v_L - \frac{v_G}{k^2}\right)\right]_S = 0$

2) $k^2 = \frac{v_G}{v_L}$

Fauske* obtained, from different criteria for the critical outlet condition, the same expression for critical slip. The uniqueness of this solution is not proven. However, its use will be justified by comparison with data.

Since v_G and v_L are functions of pressure only, $\left(\frac{\partial v_G}{\partial P}\right)_S$ and $\left(\frac{\partial v_L}{\partial P}\right)_S$ may be expressed as $\frac{\partial v_G}{\partial P}$ and $\frac{\partial v_L}{\partial P}$.

* Fauske, H. K., Contribution to the Theory of Two-Phase One-Component Critical Flow, PhD. Thesis, University of Minnesota, 1961

At the critical condition $v_L - \frac{v_G}{k^2} = 0$. Therefore Equation (J4d) shows

$\left(\frac{\partial v_{tp}}{\partial k}\right)_{P,x} = 0$ so that Equation (J1) results in

$$\left(\frac{\partial v_{tp}}{\partial P}\right)_S = \left(\frac{\partial v_{tp}}{\partial x}\right)_{P,x} \left(\frac{\partial x}{\partial P}\right)_S + \left(\frac{\partial v_{tp}}{\partial v_G}\right)_{x,k} \left(\frac{\partial v_G}{\partial P}\right) + \left(\frac{\partial v_{tp}}{\partial v_L}\right)_{x,k} \left(\frac{\partial v_L}{\partial P}\right) \tag{J8a}$$

The approximation of liquid incompressibility introduces a negligible error at moderate pressures. Therefore, with $\frac{\partial v_L}{\partial P} = 0$, Equation (J8a) results in

$$\left(\frac{\partial v_{tp}}{\partial P}\right)_S = \left(\frac{\partial v_{tp}}{\partial x}\right)_{P,x} \left(\frac{\partial x}{\partial P}\right)_S + \left(\frac{\partial v_{tp}}{\partial v_G}\right)_{x,k} \left(\frac{\partial v_G}{\partial P}\right) \tag{J8b}$$

Expressions for $\left(\frac{\partial v_{tp}}{\partial x}\right)_{P,k}$ and $\left(\frac{\partial v_{tp}}{\partial v_G}\right)_{x,k}$ are

$$\left(\frac{\partial v_{tp}}{\partial x}\right)_{P,x} = v_L \left[(k-1)(1-2x) - 1\right] + \frac{v_G}{k}\left[2x(k-1) + 1\right] \tag{J9a}$$

and

$$\left(\frac{\partial v_{tp}}{\partial v_G}\right)_{x,k} = \frac{x}{k}\left[x(k-1) + 1\right] \tag{J9b}$$

Substituting Equations (J9a) and (J9b) into (J8b) yields

$$\left(\frac{\partial v_{tp}}{\partial P}\right)_S = \left(\frac{\partial x}{\partial P}\right)_S \left\{ v_L \left[(k-1)(1-2x)-1\right] + \frac{v_G}{k}\left[2x(k-1)+1\right]\right\} + \frac{x}{k}\left[x(k-1)+1\right]\left(\frac{\partial v_G}{\partial P}\right) \tag{J9c}$$

Expressions for $\left(\frac{\partial x}{\partial P}\right)_S$ and $\left(\frac{\partial v_G}{\partial P}\right)$ are developed below:

A. <u>Determination of $\left(\frac{\partial x}{\partial P}\right)_S$</u>

Since $S_{tp} = S_{tp}(x, p)$, from the chain rule

$$\left(\frac{\partial x}{\partial P}\right)_S \left(\frac{\partial S_{tp}}{\partial x}\right)_P \left(\frac{\partial P}{\partial S_{tp}}\right)_x = -1$$

so that

$$\left(\frac{\partial x}{\partial P}\right)_S = -\frac{\left(\frac{\partial S_{tp}}{\partial P}\right)_x}{\left(\frac{\partial S_{tp}}{\partial x}\right)_P} \tag{J10a}$$

where

$$S_{tp} = xS_G + (1-x)S_L \tag{J10b}$$

Since S_G and S_L are functions of pressure only

$$\left(\frac{\partial S_{tp}}{\partial P}\right)_x = \frac{x\,dS_G}{dP} + (1-x)\frac{dS_L}{dP}$$

and

$$\left(\frac{\partial S_{tp}}{\partial x}\right)_P = S_G - S_L = S_{fg}$$

Substituting the expressions for $\left(\frac{\partial S_{tp}}{\partial P}\right)_x$ and $\left(\frac{\partial S_{tp}}{\partial x}\right)_P$ into (J10a) yields

$$\left(\frac{\partial x}{\partial P}\right)_S = -\frac{x}{S_{fg}}\frac{dS_G}{dP} - \frac{(1-x)}{S_{fg}}\frac{dS_L}{dP} \qquad \text{(J11a)}$$

Multiply $\frac{dS_G}{dP}$ and $\frac{dS_L}{dP}$ by $\left(\frac{T}{T}\right)\left(\frac{dT}{dT}\right)$

$$\frac{dS_G}{dP} = \frac{dS_G}{dP}\frac{T}{T}\frac{dT}{dT} = \left(\frac{TdS_G}{dT}\right)\frac{1}{T}\frac{dT}{dP} = \frac{C_{s_G}}{T}\frac{dT}{dP}$$

$$\frac{dS_L}{dP} = \frac{dS_L}{dP}\frac{T}{T}\frac{dT}{dT} = \left(\frac{TdS_L}{dT}\right)\frac{1}{T}\frac{dT}{dP} = \frac{C_{s_L}}{T}\frac{dT}{dP}$$

where C_s is the saturated specific heat.

Use of the Clausius-Clapeyron equation $\frac{dT}{dP} = \frac{Tv_{fg}}{\lambda}$ yields

$$\frac{dS_G}{dP} = C_{s_G}\frac{v_{fg}}{\lambda} \quad \text{and} \quad \frac{dS_L}{dP} = C_{s_L}\frac{v_{fg}}{\lambda}$$

Equation (J11a) can therefore be written as

$$\left(\frac{\partial x}{\partial P}\right)_S = -\frac{xC_{s_G}v_{fg}}{S_{fg}\lambda} - \frac{(1-x)C_{s_L}v_{fg}}{S_{fg}\lambda} \qquad \text{(J11b)}$$

The saturated specific heat C_s can also be expressed as

$$C_s = C_p - \frac{\lambda}{v_{fg}}\left(\frac{\partial v}{\partial T}\right)_P$$

and Equation (J11b) becomes

$$\left(\frac{\partial x}{\partial P}\right)_S = - \frac{x v_{fg}}{S_{fg} \lambda} \left[C_{p_G} - \frac{\lambda}{v_{fg}} \left(\frac{\partial v_G}{\partial T}\right)_P \right] -$$

$$\frac{(1 - x)\ v_{fg}}{S_{fg} \lambda} \left[C_{p_L} - \frac{\lambda}{v_{fg}} \left(\frac{\partial v_L}{\partial T}\right)_P \right] \qquad \text{(J11c)}$$

Since the liquid phase was assumed to be incompressible, Equation (J11c) results in

$$\left(\frac{\partial x}{\partial P}\right)_S = - \frac{v_{fg}}{S_{fg} \lambda} \left[x C_{p_G} + (1 - x)\ C_{p_L} \right] + \frac{x}{S_{fg}} \left(\frac{\partial v_G}{\partial T}\right)_P \qquad \text{(J11d)}$$

The perfect gas law can be expressed by $P\ v_G = RT$. Use of the perfect gas law and the approximation of liquid incompressibility introduces a negligible error at moderate pressures. At higher pressures, account should be taken of liquid compressibility and the deviation from the perfect gas law. Differentiating the expression for specific volume from the perfect gas law with respect to temperature at constant pressure yields

$$\left(\frac{\partial v_G}{\partial T}\right)_P = \frac{R}{P}$$

Substituting the above expression into (J11d) results in

$$\left(\frac{\partial x}{\partial P}\right)_S = - \frac{v_{fg}}{S_{fg} \lambda} \left[x C_{p_G} + (1 - x)\ C_{p_L} \right] + \frac{x R}{S_{fg} P} \qquad \text{(J11e)}$$

B. <u>Determination of $\frac{d v_G}{d P}$</u>

Differentiating the expression for specific volume from the perfect gas law with respect to pressure yields

At the critical condition, k is equal to $\left(\frac{v_G}{v_L}\right)^{\frac{1}{2}}$.

The expression for critical mass velocity in Equation (J13) is similar to that obtained by Fauske. The difference between the expressions is that Fauske evaluates $\left(\frac{\partial v_{tp}}{\partial P}\right)$ at constant enthalpy instead of at constant entropy. In addition, analytical expressions for $\left(\frac{\partial x}{\partial P}\right)_S$ and $\left(\frac{dv_G}{dP}\right)$ are developed here so that graphical interpolation need not be used for their evaluation.